

ADVERTIMENT. La consulta d'aquesta tesi queda condicionada a l'acceptació de les següents condicions d'ús: La difusió d'aquesta tesi per mitjà del servei TDX (www.tesisenxarxa.net) ha estat autoritzada pels titulars dels drets de propietat intel·lectual únicament per a usos privats emmarcats en activitats d'investigació i docència. No s'autoritza la seva reproducció amb finalitats de lucre ni la seva difusió i posada a disposició des d'un lloc aliè al servei TDX. No s'autoritza la presentació del seu contingut en una finestra o marc aliè a TDX (framing). Aquesta reserva de drets afecta tant al resum de presentació de la tesi com als seus continguts. En la utilització o cita de parts de la tesi és obligat indicar el nom de la persona autora.

ADVERTENCIA. La consulta de esta tesis queda condicionada a la aceptación de las siguientes condiciones de uso: La difusión de esta tesis por medio del servicio TDR (www.tesisenred.net) ha sido autorizada por los titulares de los derechos de propiedad intelectual únicamente para usos privados enmarcados en actividades de investigación y docencia. No se autoriza su reproducción con finalidades de lucro ni su difusión y puesta a disposición desde un sitio ajeno al servicio TDR. No se autoriza la presentación de su contenido en una ventana o marco ajeno a TDR (framing). Esta reserva de derechos afecta tanto al resumen de presentación de la tesis como a sus contenidos. En la utilización o cita de partes de la tesis es obligado indicar el nombre de la persona autora.

WARNING. On having consulted this thesis you're accepting the following use conditions: Spreading this thesis by the TDX (www.tesisenxarxa.net) service has been authorized by the titular of the intellectual property rights only for private uses placed in investigation and teaching activities. Reproduction with lucrative aims is not authorized neither its spreading and availability from a site foreign to the TDX service. Introducing its content in a window or frame foreign to the TDX service is not authorized (framing). This rights affect to the presentation summary of the thesis as well as to its contents. In the using or citation of parts of the thesis it's obliged to indicate the name of the author

EXPERIMENTAL INVESTIGATION OF INDUCED SUPERSONIC BOUNDARY LAYER TRANSITION

*A thesis submitted in partial fulfilment for the degree of
Doctor in Engineering*

PhD with European recognition

by

Henny Bottini

Directed by

Salvador de las Heras (UPC)

Guillermo Paniagua (VKI)



**UNIVERSITAT POLITÈCNICA DE CATALUNYA
BARCELONATECH**

Departament de Mecànica de Fluids



von KARMAN INSTITUTE
FOR FLUID DYNAMICS

Terrassa, 2.014

Abstract

Turbulence onset within an initially laminar flow is one of the most common phenomenon in Fluid Mechanics, yet is an open field of research. This is due to the many and diverse causes that can trigger turbulence, which often add to each other, change their effect upon the flow velocity, and are difficult to single out in real-world situations. This is why laminar-to-turbulent transition experiments have been and still are a fundamental tool for the researcher.

This thesis work has addressed the study of turbulence onset in supersonic flows from an experimental point of view. Two test campaigns have been carried out each in a dedicated supersonic wind tunnel. The first aimed at tracking turbulence onset triggered by a single tetrahedral roughness element. It has been carried out in a multiple-Mach-number supersonic wind tunnel whose qualification campaign has been completed within this thesis work. Two roughness heights were tested, both for two Mach numbers, 1.6 and 2.3. The second test campaign has investigated the effects of an oblique shock wave impinging onto a Mach-2 transitional boundary layer. The transitional state of a boundary layer is that state during which the boundary layer passes from fully laminar to fully turbulent. This passage can be either induced or natural, and it was represented in this thesis work by the trigger wake and by the boundary layer flow downstream of the release point of an electric spark, respectively.

Surface sensors, as thin-films and piezoelectric pressure transducers, were used to measure steady and unsteady high-frequency flow evolutions. Different wall temperatures were set for the thin-films insert as to allow the experimental estimation of the recovery temperature. Convective heat-flux trends have been extracted from the steady measurements, which, together with the recovery temperature trends, allowed the calculation of the Stanton number trends. All these quantities let to conclude on the general state of the boundary layer investigated in the first test campaign.

The post-processing of the unsteady measurements yielded temperature and pressure fluctuations spectra and RMS streamwise evolutions, along with spectral time evolution at a given position. For the first test campaign, they allowed the characterization of the unsteadiness produced by the roughness within the supersonic boundary layer at different downstream locations. In so doing, they helped conclude on the state of the boundary layer, thus on the effectiveness of the roughness in triggering transition to turbulence. For the second test campaign, they allowed to single out the unsteady effects of the shock impinging downstream of the single roughness and downstream of the electric spark release point. In this way, differences in the shock effect between the roughness configuration and the clean-plate configuration have been highlighted, and the effects of different spark release frequencies compared.

Resumen

El desarrollo de la turbulencia en el interior de un flujo inicialmente laminar, a pesar de ser uno de los fenómenos más comunes en la mecánica de fluidos, continúa siendo un campo abierto de investigación. Esto es debido a las muchas y diversas causas que condicionan la transición de flujo laminar a régimen turbulento, a menudo actuando de modo combinado, cuyo efecto cambia con la velocidad del flujo y las cuales son difíciles de aislar en situaciones reales. Este es el motivo por el cual los experimentos que estudian la transición de régimen laminar a turbulento han sido y continúan siendo una herramienta fundamental para el investigador.

Esta tesis doctoral ha abordado el estudio del comienzo de la turbulencia en flujos supersónicos desde un punto de vista experimental. Dos series de experimentos fueron realizados, cada uno en un túnel de viento supersónico específico. La primera serie tuvo como objetivo el seguimiento del inicio de la turbulencia causado por un único elemento de rugosidad de forma hexaédrica. Este tipo de experimentos fue realizado en un túnel de viento supersónico capaz de operar en un cierto rango de números de Mach, cuya caracterización fue completada en paralelo a esta investigación. Los experimentos fueron realizados a dos números de Mach, 1.6 y 2.3, y dos niveles de rugosidad diferentes variando la temperatura de pared.

El objetivo de la segunda serie de medidas consistió en investigar los efectos del impacto de una onda de choque oblicua en una capa límite transitoria, en un flujo a Mach 2. El estado transitorio de una capa límite es aquel durante el cual la capa límite pasa de enteramente laminar a enteramente turbulenta. Esta transformación puede ser tanto natural como inducida. Ambos escenarios han sido reproducidos en esta tesis. La transformación natural ha sido representada mediante la presencia de un elemento de rugosidad, mientras que la transformación inducida se corresponde con el desarrollo de la capa límite aguas abajo del punto de liberación de chispas eléctricas.

Para medir la evolución de flujos estacionarios y no estacionarios de alta frecuencia se emplearon sensores superficiales tales como *thin-films* y transductores piezoeléctricos de presión. Para determinar experimentalmente la temperatura de recuperación (*recovery temperature*) se aplicaron distintas temperaturas de pared a la pieza contenedora de los *thin-films*. De las medidas estacionarias se extrajeron las diferentes distribuciones del flujo de calor por convección, las cuales, junto con la distribución de la temperatura de recuperación, permitieron el cálculo de la distribución espacial del número de Stanton. Estos resultados permitieron llegar a una conclusión sobre el estado general de la capa límite investigada en la primera serie de experimentos.

Las medidas no estacionarias proporcionaron espectros de fluctuación de temperatura y presión, y evoluciones longitudinales de residuos cuadráticos medios (MSR), así como espectros de evolución temporal en una posición dada. Estos datos permitieron caracterizar, en la primera serie de experimentos, la inestabilidad producida por la rugosidad en la capa límite supersónica en distintas posiciones aguas abajo. Ayudaron, por tanto, a determinar el estado de la capa límite y, con ello, concluir en la efectividad de la rugosidad para provocar la transición a régimen turbulento. En la segunda serie de experimentos se pudieron señalar los efectos no estacionarios de la onda de choque incidiendo aguas debajo del elemento de rugosidad, y los efectos no estacionarios de la onda incidente aguas abajo del punto de liberación de chispas eléctricas. De este modo, se han identificado las diferencias entre el efecto de una onda de choque en presencia de un elemento de rugosidad y en el caso de la configuración limpia, y se han comparado los efectos del uso de diferentes frecuencias de descargas eléctricas.

Ὁ βίος βραχύς,
ἡ δὲ τέχνη μακρή,
ὁ δὲ καιρὸς ὄξυς,
ἡ δὲ πεῖρα σφαλερή,
ἡ δὲ κρίσις χαλεπή.

Hippocrates, c. 460 BC-c. 370 BC

*[Life is short,
and art long,
opportunity fleeting,
experience perilous,
and judgment difficult.]*

Contents

| | |
|--|-----------|
| Nomenclature | xv |
| 1 Introduction | 1 |
| 1.1 Introduction | 1 |
| 1.2 Objectives of the research | 2 |
| 1.3 Research methodology | 3 |
| 1.4 Thesis outline | 5 |
| 2 Design and qualification of a multi-M_∞ supersonic wind tunnel | 7 |
| 2.1 Description of the wind tunnel test section | 7 |
| 2.1.1 The suction slots and the aspiration system | 9 |
| 2.1.2 Surface treatment of the nozzle walls | 13 |
| 2.1.3 Typical test cycle operation | 15 |
| 2.1.4 Parameters regulation | 16 |
| 2.1.5 Wind-tunnel standard equipment | 19 |
| 2.2 Test section qualification | 21 |
| 2.2.1 Practical Mach range achievable | 22 |
| 2.2.2 Assessment of wind-tunnel noise | 25 |
| 2.3 Conclusions | 32 |
| 3 Single-roughness effects on supersonic laminar boundary layers | 35 |
| 3.1 Wall-temperature high-frequency measurement system | 39 |
| 3.1.1 Thin-films calibration | 40 |
| 3.1.2 Sensitivity and uncertainty analysis of the heat-flux measurements | 43 |
| 3.2 Wall-pressure high-frequency measurement system | 45 |
| 3.2.1 PCB calibration setup | 46 |
| 3.2.2 Pressure sensitivity computation | 48 |
| 3.3 Boundary layer state at the roughness location | 51 |
| 3.3.1 $\frac{dp}{dx}$ and T_{wall} effects on a supersonic boundary-layer profile | 53 |
| 3.4 Time-averaged heat-flux measurements | 55 |
| 3.4.1 Streamwise and spanwise heat-flux trends | 55 |
| 3.4.2 Streamwise and spanwise heat-flux trends: wall tem- perature effects | 63 |
| 3.5 Time-averaged adiabatic-wall temperature measurements | 70 |

| | | |
|----------|---|------------|
| 3.5.1 | Adiabatic-wall temperature trends along the thin-films insert | 70 |
| 3.5.2 | Uncertainty estimation of the adiabatic-wall temperature measurements | 74 |
| 3.5.3 | Stanton number streamwise trends | 75 |
| 3.6 | Time-resolved wall-temperature measurements | 78 |
| 3.6.1 | Frequency analysis of the wall-temperature fluctuations | 78 |
| 3.6.2 | Signals RMS streamwise evolution | 85 |
| 3.6.3 | Wall-temperature fluctuations evolution in the (<i>frequency,time</i>) domain | 94 |
| 3.7 | Cross-correlation analysis of thin-films signals | 106 |
| 3.7.1 | Cross-correlation results | 106 |
| 3.8 | Time-resolved wall-pressure measurements | 111 |
| 3.8.1 | Fourier analysis of unsteady pressure signal | 112 |
| 3.8.2 | Conclusions on the unsteady pressure measurements | 114 |
| 3.9 | Transition criteria and conclusions | 117 |
| 3.9.1 | Transition criteria | 117 |
| 3.9.2 | Conclusions | 120 |
| 4 | Shock-wave/transitional-boundary-layer interaction | 127 |
| 4.1 | Instrumentation and apparatus | 128 |
| 4.1.1 | Hardware for the generation of electric sparks | 128 |
| 4.2 | Preliminary test campaigns | 131 |
| 4.3 | Mach-2 test campaign | 141 |
| 4.3.1 | Mach-2 facility and experimental set-up | 142 |
| 4.3.2 | Thin-film data processing | 144 |
| 4.3.3 | Effects of oblique-shock-wave impingement on the wake of a single roughness element | 150 |
| 4.3.4 | Effects of an electric spark within a supersonic laminar boundary layer with and without oblique-shock-wave impingement | 162 |
| 4.4 | Conclusions | 170 |
| 5 | Conclusions | 175 |

List of Figures

| | | |
|------|--|----|
| 2.1 | The facility of the supersonic multiple-Mach-number wind tunnel | 8 |
| 2.2 | The test section with the mechanical arrangement of its movable ramps, and the bleed slots detail | 9 |
| 2.3 | Example of 2-D CFD computations made to investigate the effectiveness of the suction-slot lip design (divergent angle of 4.7° , Mach number =2.3) | 11 |
| 2.4 | Detail of the structured mesh around the central part of the wind tunnel (divergent angle of 4.7°) | 12 |
| 2.5 | Detail of the structured mesh around the suction-slot lip (divergent angle of 4.7°) | 13 |
| 2.6 | Top row: typical flows around the lip of a suction slot; bottom row: streamlines and velocity contours around the lip tip for $\alpha = 1.2^\circ$ (left) and $\alpha = 4.7^\circ$ (right) | 14 |
| 2.7 | The roughness meter Mitutoyo SJ-201P on one of the nozzle ramps | 15 |
| 2.8 | Static-pressure time evolution during a wind tunnel run (Mach =2.3 at 90 cm from the sonic throat) | 16 |
| 2.9 | The unit Reynolds number evolution through the divergent at different total temperatures (top plot: $\alpha=1.2^\circ$); bottom plot: $\alpha=4.7^\circ$) | 18 |
| 2.10 | The theoretical test time versus the throat height at different total temperatures | 20 |
| 2.11 | The front view of the four static pressure L-shaped taps and the thermocouple that instrument each of the aspiration system four tubes | 21 |
| 2.12 | The two ramps instrumented for the qualification test campaign: the upper ramp features five pressure taps, the lower ramp ten | 21 |
| 2.13 | Typical static pressure axial evolution throughout the whole nozzle divergent ($p_0=4.2$ bar) | 22 |
| 2.14 | Typical Mach number axial evolution throughout the whole nozzle divergent ($p_0=4.2$ bar) | 23 |
| 2.15 | Static pressure axial evolution in case of un-started wind tunnel ($p_0= 3$ bar) | 24 |
| 2.16 | Static pressure evolution from divergent centerline to wall at three different positions | 25 |

| | | |
|------|---|----|
| 2.17 | The double hot-wire in the test section | 26 |
| 2.18 | The flat plate with the accelerometer in the test section, and a detail of the accelerometer position beneath the plate | 27 |
| 2.19 | Frequency spectrum of the mechanical vibrations of a flat plate cantilever-mounted in the wind tunnel divergent | 28 |
| 2.20 | Variation of mass-flow fluctuations with freestream Mach number | 29 |
| 2.21 | Detail of the rear part of the compression tube (the two 300-bar-line inlets are horizontal and side by side) | 30 |
| 2.22 | Spectrum of measured mass-flow fluctuations with estimated range of first-mode self-sustained-oscillations frequency, $M=1.7$ ($\frac{U_c}{U_j} \in [0.6 \div 0.89]$ $\Delta U_j = \pm 15\%$) | 32 |
| 2.23 | Spectrum of measured mass-flow fluctuations with estimated range of first-mode self-sustained-oscillations frequency, $M=1.9$ ($\frac{U_c}{U_j} \in [0.6 \div 0.89]$ $\Delta U_j = \pm 15\%$) | 33 |
| 3.1 | The thin-films insert on the bottom ramp of the supersonic wind tunnel divergent | 36 |
| 3.2 | The PCBs insert on the bottom ramp of the supersonic wind tunnel divergent | 37 |
| 3.3 | General view of the supersonic wind tunnel divergent with the inserts location highlighted | 38 |
| 3.4 | A magnified view of a thin-film sensor | 39 |
| 3.5 | The arrangement of the electric heaters on the bottom of the thin-films insert | 41 |
| 3.6 | The thin-films insert embedded in the lower ramp of the supersonic wind tunnel | 42 |
| 3.7 | Infrared image of the thin-films insert top heated up by Joule heaters glued on its bottom | 42 |
| 3.8 | Example of thin-film calibrations: voltage vs. electric resistance, electric resistance vs. temperature | 43 |
| 3.9 | PCB amplifier frequency response | 46 |
| 3.10 | PCB balloon calibration setup | 47 |
| 3.11 | Static calibration curve of the Kulite used as reference in the balloon-calibration procedure | 47 |
| 3.12 | Normalized raw output voltages of PCB (∇) and reference Kulite (\square) | 48 |
| 3.13 | Electronic model of a first-order high-pass filter | 49 |
| 3.14 | Frequency response (magnitude) of an inverted high-pass filter and the PCB's transfer function | 50 |
| 3.15 | Example of signal reconstruction using the PCB transfer function | 51 |
| 3.16 | CFD computation of the velocity field throughout the whole compression-tube (2D, only the upper half is resolved) | 53 |

| | | |
|------|--|----|
| 3.17 | The velocity, density, and dynamic viscosity profiles of the supersonic boundary layer along a wind-tunnel ramp as from CFD computations ($M=2.3$, $T_{wall}=28^\circ\text{C}$) | 54 |
| 3.18 | The thin-films insert into the lower ramp of the supersonic wind tunnel | 55 |
| 3.19 | The thin-films layout | 56 |
| 3.20 | Heat-flux RMS reduction by filtering out the signal above $\frac{1.2}{T_{test}}$ Hz ($T_w = 41^\circ\text{C}$, $k=1$ mm) | 56 |
| 3.21 | Typical heat-flux spanwise evolution on the insert without roughness ($M=2.3$, $T_w=26^\circ\text{C}$) | 57 |
| 3.22 | Heat-flux streamwise evolution downstream of the 0.1-mm high single roughness ($M=2.3$, wall heating off) | 58 |
| 3.23 | Heat-flux streamwise evolution downstream of the 1-mm high single roughness ($M=2.3$, wall heating off) | 59 |
| 3.24 | Heat-flux streamwise evolution downstream of the 1-mm high single roughness ($M=1.6$, wall heating off) | 59 |
| 3.25 | Heat-flux streamwise evolutions downstream of a spherical single roughness of varying height | 60 |
| 3.26 | Heat-flux streamwise evolutions along the clean insert ($M=2.3$, $T_w=26^\circ\text{C}$) | 61 |
| 3.27 | Heat-flux spanwise trends ($M=2.3$, $k=0.1$ mm, $T_w=24.5^\circ\text{C}$) | 62 |
| 3.28 | Heat-flux spanwise trends ($M=2.3$, $k=1$ mm, $T_w=15^\circ\text{C}$) . . | 62 |
| 3.29 | Heat-flux spanwise trends ($M=1.6$, $k=1$ mm, $T_w=26^\circ\text{C}$) . . | 63 |
| 3.30 | Heat-flux streamwise evolutions at different wall temperatures ($M=2.3$, roughness height 0.1 mm) | 64 |
| 3.31 | Heat-flux streamwise evolutions at different wall temperatures ($M=2.3$, roughness height 1 mm) | 65 |
| 3.32 | Heat-flux streamwise evolutions at different wall temperatures ($M=1.6$, roughness height 1 mm) | 65 |
| 3.33 | Heat-flux spanwise trends at different wall temperatures ($M=2.3$, $k=0.1$ mm) | 67 |
| 3.34 | Heat-flux spanwise trends at different wall temperatures ($M=2.3$, $k=1$ mm) | 67 |
| 3.35 | Heat-flux spanwise trends at different wall temperatures ($M=1.6$, $k=1$ mm) | 68 |
| 3.36 | The (q_w, T_w) pairs from five tests at different wall temperatures for thin-film nr. 4 ($M=2.3$, clean configuration) | 71 |
| 3.37 | The (q_w, T_w) pairs and the interpolated T_{ad} value for thin-film nr. 4 ($M=2.3$, clean configuration) | 71 |
| 3.38 | The experimental adiabatic-wall temperature trend along the thin-films insert ($M=2.3$, $k=0.1$ mm) | 72 |
| 3.39 | The experimental adiabatic-wall temperature trend along the thin-films insert ($M=2.3$, $k=1$ mm) | 73 |
| 3.40 | The experimental adiabatic-wall temperature trend along the thin-films insert ($M=1.6$, $k=1$ mm) | 73 |

| | | |
|------|---|----|
| 3.41 | Comparison among analytical and 2D-CFD numerical adiabatic-wall temperature trends along the thin-films insert (M=2.3) . | 74 |
| 3.42 | Estimation of the uncertainty on the adiabatic-wall temperature value | 75 |
| 3.43 | Experimental Stanton number trends along the thin-films insert (M=2.3, k=1 mm) | 77 |
| 3.44 | Typical signal and noise frequency spectra of a thin-film correctly working (M=2.3, k=1 mm) | 79 |
| 3.45 | Frequency spectrum streamwise evolution (M=2.3, clean configuration, coldest T_{wall}) | 79 |
| 3.46 | Frequency spectrum streamwise evolution (M=2.3, clean configuration, warmest T_{wall}) | 80 |
| 3.47 | Frequency spectrum streamwise evolution (M=2.3, k=0.1 mm, coldest T_{wall}) | 81 |
| 3.48 | Frequency spectrum streamwise evolution (M=2.3, k=0.1 mm, warmest T_{wall}) | 81 |
| 3.49 | Frequency spectrum streamwise evolution (M=2.3, k=1 mm, coldest $T_{wall}=15^\circ C$) | 82 |
| 3.50 | Frequency spectrum streamwise evolution (M=2.3, k=1 mm, warmest $T_{wall}=43^\circ C$) | 83 |
| 3.51 | Frequency spectrum streamwise evolution (M=1.6, k=1 mm, coldest $T_{wall}=26^\circ C$) | 84 |
| 3.52 | Frequency spectrum streamwise evolution (M=1.6, k=1 mm, warmest $T_{wall}=38^\circ C$) | 84 |
| 3.53 | Three streamwise evolutions of noise RMS from the beginning of different tests (M=2.3, $T_{wall} \simeq 25^\circ C$) | 86 |
| 3.54 | Three streamwise evolutions of noise RMS from the beginning of different tests (M=2.3, $T_{wall} \simeq 41^\circ C$) | 87 |
| 3.55 | Streamwise evolutions of filtered and unfiltered RMS (M=2.3, clean configuration, $T_{wall} = 26^\circ C$) | 87 |
| 3.56 | Thin-films RMS streamwise evolution (M=2.3, clean insert, $T_{wall} = 26^\circ C$, $f_{LP} = 20$ kHz) | 89 |
| 3.57 | Thin-films RMS streamwise evolution (M=2.3, k=0.1 mm, $T_{wall} = 26^\circ C$, $f_{LP} = 20$ kHz) | 89 |
| 3.58 | Thin-films RMS streamwise evolution (M=2.3, k=0.1 mm, $T_{wall} = 33.5^\circ C$, $f_{LP} = 20$ kHz) | 90 |
| 3.59 | Thin-films RMS streamwise evolution (M=2.3, k=1 mm, $T_{wall} = 15^\circ C$, $f_{LP} = 20$ kHz) | 91 |
| 3.60 | Thin-films RMS streamwise evolution (M=2.3, k=1 mm, $T_{wall} = 42.5^\circ C$, $f_{LP} = 20$ kHz) | 91 |
| 3.61 | Thin-films RMS streamwise evolution (M=1.6, k=1 mm, $T_{wall} = 26^\circ C$, $f_{LP} = 20$ kHz) | 92 |
| 3.62 | Thin-films RMS streamwise evolution (M=1.6, k=1 mm, $T_{wall} = 38^\circ C$, $f_{LP} = 20$ kHz) | 93 |
| 3.63 | Typical spectrogram of an unsteady signal: $A = A(f, t)$. . . | 95 |

| | |
|--|-----|
| 3.64 Spectrogram of TF nr. 5 signal (M=2.3, clean insert, $T_w=27^\circ$ C) | 96 |
| 3.65 Spectrogram of TF nr. 5 signal (M=2.3, k=0.1 mm, $T_w=28^\circ$ C) | 96 |
| 3.66 Spectrogram of TF nr. 14 signal (M=2.3, clean insert, $T_w=27^\circ$ C) | 97 |
| 3.67 Spectrogram of TF nr. 14 signal (M=2.3, k=0.1 mm, $T_w=28^\circ$ C) | 97 |
| 3.68 Spectrogram of TF nr. 4 signal (M=2.3, clean insert, $T_w=41^\circ$ C) | 98 |
| 3.69 Spectrogram of TF nr. 4 signal (M=2.3, k=1 mm, $T_w=41.5^\circ$ C) | 98 |
| 3.70 Spectrogram of TF nr. 6 signal (M=2.3, clean insert, $T_w=41^\circ$ C) | 99 |
| 3.71 Spectrogram of TF nr. 6 signal (M=2.3, k=1 mm, $T_w=41.5^\circ$ C) | 100 |
| 3.72 Spectrogram of TF nr. 5 signal (M=1.6, clean insert, $T_w=27^\circ$ C) | 101 |
| 3.73 Spectrogram of thin-film 5 signal (M=1.6, k=1 mm, $T_w=26^\circ$ C) | 101 |
| 3.74 Spectrogram of TF nr. 14 signal (M=1.6, clean insert, $T_w=27^\circ$ C) | 102 |
| 3.75 Spectrogram of TF nr. 14 signal (M=1.6, k=1 mm, $T_w=26^\circ$ C) | 102 |
| 3.76 Spectrogram of TF nr. 4 signal (M=2.3, k=0.1 mm, $T_w=24.5^\circ$ C) | 103 |
| 3.77 Spectrogram of TF nr. 4 signal (M=2.3, k=0.1 mm, $T_w=33.5^\circ$ C) | 103 |
| 3.78 Spectrogram of TF nr. 5 signal (M=1.6, k=1 mm, $T_w=26^\circ$ C) | 104 |
| 3.79 Spectrogram of TF nr. 5 signal (M=1.6, k=1 mm, $T_w=38^\circ$ C) | 105 |
| 3.80 Typical cross-correlation outputs from no-flow signals (signal band pass=[0.5 ÷ 20] kHz) | 107 |
| 3.81 Typical cross-correlation outputs from signals at Mach 2.3 in clean-insert configuration (signal band pass=[0.5 ÷ 20] kHz) . | 107 |
| 3.82 Propagation velocities from the cross-correlations between pairs of signals from thin-films along the insert (Mach 2.3, clean-insert configuration) | 108 |
| 3.83 Propagation velocities from the cross-correlations between pairs of signals from thin-films along the insert (Mach 2.3, $h = 1 \text{ mm}$) | 108 |
| 3.84 Propagation velocities from the cross-correlations between pairs of signals from thin-films along the insert (Mach 1.6, $h = 0.1 \text{ mm}$) | 109 |
| 3.85 The PCB insert mounted into the lower ramp of the super- sonic wind tunnel | 111 |

| | | |
|------|---|-----|
| 3.86 | The broadband spectra of PCB sensors for the test at $M=2.3$ with 0.1 mm roughness | 112 |
| 3.87 | The low frequency spectra of third PCB sensors downstream of the roughness element for all test conditions | 113 |
| 3.88 | Time-resolved frequency spectra of third PCB sensor downstream of the roughness element for all test conditions | 116 |
| 3.89 | the Reda transition criterion applied to numerical and experimental results | 117 |
| 3.90 | the Shuttle transition criterion applied to numerical and experimental results | 118 |
| 3.91 | The Reda transition criterion applied to the results of the present thin-film experiments | 119 |
| 3.92 | The Shuttle transition criterion applied to the results of the present thin-film experiments | 121 |
| 4.1 | The layout of the thin-films on the insert used for the Mach-2 test campaign (dimensions are in <i>mm</i>) | 129 |
| 4.2 | The schematics of the two circuits used to generate the electric spark | 130 |
| 4.3 | The spark plug activated and recorded by high speed camera (the gap between the electrodes is 6 mm) | 130 |
| 4.4 | The cross section of the spark plug with its two convergent passages for the electrodes | 131 |
| 4.5 | The relation between electrodes tip gap (d), pressure (p), and voltage for spark release (Paschen law) | 132 |
| 4.6 | A view of the low-speed wind-tunnel with the set up for smoke-sheet visualizations | 133 |
| 4.7 | A view of the smoke sheet generated on the bottom of the low-speed wind-tunnel test section. The cabling for electrodes and Nicrom heater is visible through the transparent bottom | 134 |
| 4.8 | The effect of one spark release on the smoke sheet (spark frequency=1 Hz, electrode gap=6 mm, the flow comes from above) | 135 |
| 4.9 | The effect of one transformer burst on the smoke sheet (spark frequency= 100 Hz, electrode gap=6 mm, the flow comes from above) | 136 |
| 4.10 | The effect of sparks generated by the battery-coil circuit on the smoke sheet (spark frequency continuously increased from 1 to 8 Hz, electrode gap=6 mm) | 137 |
| 4.11 | Smoke sheet visualization of the naturally-occurring turbulent boundary layer along the bottom of the L2A low-speed wind tunnel | 138 |
| 4.12 | The spark plug within the vacuum chamber for testing at very low pressures | 139 |

| | | |
|------|---|-----|
| 4.13 | The spark released at three different static pressures: ambient, 0.5 atm, 0.01 atm, from left to right | 140 |
| 4.14 | The duration of the spark glow generated by the battery-coil circuit versus air pressure | 141 |
| 4.15 | Schlieren visualization of an oblique shock wave impinging downstream of the roughness position (the electrodes for the spark tests are also visible upstream of the roughness) | 142 |
| 4.16 | The Mach-2 S-1 Wind tunnel | 142 |
| 4.17 | The test section with the shock generator, and the convergent-divergent 2-D nozzle for Mach 2 | 143 |
| 4.18 | The layout of the two instrumented inserts on the plate (the PCBs insert is on the left, the thin-films insert is on the right) 144 | |
| 4.19 | Zoomed view on the two instrumented inserts on the plate: each of them has a dedicated electrodes plug or roughness . . | 145 |
| 4.20 | Example of thin-film signal affected by the Electro-Magnetic Interference of the spark release ($f_{spark} = 20$ Hz, no shock wave impinging) | 146 |
| 4.21 | Example of the spectrum of a thin-film signal affected by the Electro-Magnetic Interference of the spark release ($f_{spark} = 20$ Hz, no shock wave impinging) | 147 |
| 4.22 | Example of the effect on a thin-film time series of EMI removal ($f_{spark} = 20$ Hz, no shock wave impinging) | 148 |
| 4.23 | Example of the effect on the spectrum of a thin-film signal of EMI removal ($f_{spark} = 20$ Hz, no shock wave impinging) . . . | 149 |
| 4.24 | Comparison among trends of RMS wall-temperature fluctuations with (3 tests) and without (1 test) the single roughness element ($f_{LP} = 500$ Hz) | 151 |
| 4.25 | Comparison among trends of RMS wall-temperature fluctuations with and without shock wave impingement (no-roughness configuration, $f_{LP} = 600$ Hz) | 153 |
| 4.26 | Comparison among trends of RMS wall-temperature fluctuations with (2 tests) and without (3 tests)shock wave impingement (1-mm roughness, $f_{LP} = 500$ Hz) | 154 |
| 4.27 | Sketch of shock-wave/laminar-boundary-layer interaction in case of separation with skin friction coefficient and static pressure evolutions | 155 |
| 4.28 | Comparison between the spectrograms of the signal by the most upstream thin-film (nr. 32): shock impingement vs. no shock impingement | 157 |
| 4.29 | Comparison between the spectrograms of the signal by the second most upstream thin-film (nr. 4): shock impingement vs. no shock impingement | 158 |
| 4.30 | Comparison between the spectrograms of the signal by a thin-film on the last row (nr. 15): shock impingement vs. no shock impingement | 159 |

| | | |
|------|--|-----|
| 4.31 | Comparison between the spectrograms of the signal by the most upstream thin-film (nr. 32), 1-mm-high roughness case: no shock impingement vs. shock impingement | 161 |
| 4.32 | Comparison between the spectrograms of the signal by the second most upstream thin-film (nr. 4), 1-mm-high roughness case: no shock impingement vs. shock impingement | 162 |
| 4.33 | Comparison between the spectrograms of the signal by a thin-film on the last row (nr. 15), 1-mm-high roughness case: no shock impingement vs. shock impingement | 163 |
| 4.34 | Comparison between the RMS trends of the wall-temperature fluctuations for $f_{spark} = 100$ Hz and for a reference state ($f \in [20/div60]$ kHz) | 165 |
| 4.35 | Comparison between the RMS trends of the wall-temperature fluctuations for $f_{spark} = 1, 10, 20, 100$ Hz and with shock wave impingement | 166 |
| 4.36 | Comparison between the spectrograms of the signal by the most upstream thin-film (nr. 32): 100-Hz spark vs. no-spark-effect reference state; no shock impingement (transformer operated in “burst mode”) | 167 |
| 4.37 | Comparison between the spectrograms of the signal by a thin-film on the second row (nr. 22): 100-Hz spark vs. no-spark-effect reference state; no shock impingement (transformer operated in “burst mode”) | 168 |
| 4.38 | Comparison between the spectrograms of the signal by the second most upstream thin-film (nr. 4); spark frequencies are 1, 10, 20, 100 Hz (tests with shock impingement; transformer operated throughout the test time) | 169 |
| 4.39 | The spectrogram of the signal by the most upstream thin-film (nr. 32); spark frequency=100 Hz; with shock impingement (transformer operated throughout the test time) | 170 |

List of Tables

- 2.1 Mach number range, unit Reynolds numbers and total pressure for the multiple-Mach-number wind tunnel 23
- 2.2 Freestream mass-flow fluctuations and the corresponding Mach and unit Reynolds numbers 28

- 3.1 Sensitivities of the heat flux measurements to the uncertainties of four parameters 44
- 3.2 Specifications of PCB 132A31 piezoelectric pressure transducers 46
- 3.3 PCB transducer pressure sensitivities from manufacturer (S_{specs}) and from present evaluation (S_{cal}), including 100× amplification) 51
- 3.4 Range of Re_k values for the two Mach numbers and two roughness heights (k) tested 52
- 3.5 RMS values of the pressure fluctuations measured by PCB nr.3114

- 4.1 S-1 main test conditions for $M = 2$ 144

Nomenclature

Roman Symbols

| | | |
|-----------|--|-------------------------------------|
| A | area | $[\text{m}^2]$ |
| C | specific heat | $[\text{J}/\text{kg}\cdot\text{K}]$ |
| C_p | isobaric specific heat | $[\text{Jkg}^{-1}\text{K}^{-1}]$ |
| C_f | skin-friction coefficient | $[-]$ |
| D | diameter | $[\text{m}]$ |
| E | voltage | $[\text{V}]$ |
| f | frequency | $[\text{Hz}]$ |
| f_s | sampling frequency | $[\text{Hz}]$ |
| h | static enthalpy | $[\text{J}/\text{m}^3]$ |
| h_{aw} | adiabatic convective heat transfer coefficient | $[\text{Wm}^{-2}\text{K}^{-1}]$ |
| h | roughness height | $[\text{m}]$ |
| j | imaginary unit | $[-]$ |
| k | thermal conductivity | $[\text{Wm}^{-1}\text{K}^{-1}]$ |
| k | roughness height | $[\text{m}]$ |
| \dot{m} | mass flow | $[\text{kgs}^{-1}]$ |
| L | length | $[\text{m}]$ |
| M | Mach number | $[-]$ |
| Nu | Nusselt number | $[-]$ |
| p | pressure | $[\text{Pa}]$ |
| Pr | Prandtl number | $[-]$ |
| \dot{q} | heat flux | $[\text{Wm}^{-2}]$ |
| r | recovery factor | $[-]$ |
| Re | Reynolds number | $[-]$ |
| R_a | distributed roughness average height | $[\text{m}]$ |
| R_a | hot-wire el. resistance at ambient conds. | $[\text{Ohm}]$ |
| R_q | RMS of distributed roughness height | $[\text{m}]$ |
| R_w | hot-wire electric resistance | $[\text{Ohm}]$ |
| R^2 | coefficient of determination | $[-]$ |
| Re | Reynolds number | $[-]$ |
| St | Stanton number | $[-]$ |
| S_i | Sensitivity | variable unit of measure |
| t | time | $[\text{s}]$ |
| T | temperature | $[\text{K}]$ |
| Tu | turbulence intensity | $[\%]$ |

| | | |
|-----|---------------|--------------------|
| U | mean velocity | $[\text{ms}^{-1}]$ |
|-----|---------------|--------------------|

Greek Symbols

| | | |
|----------|--------------------------|-----------------------------|
| α | thermal diffusivity | $[\text{m}^2\text{s}^{-1}]$ |
| γ | specific heat ratio | $[-]$ |
| δ | boundary layer thickness | $[\text{m}]$ |
| Δ | variation, difference | $[\]$ |
| μ | dynamic viscosity | $[\text{Pa}\cdot\text{s}]$ |
| ν | kinematic viscosity | $[\text{m}^2/\text{s}]$ |
| ρ | density | $[\text{kgm}^{-3}]$ |
| σ | standard deviation | $[\]$ |
| τ | time | $[\text{s}]$ |
| τ | shear stress | $[\text{Pa}]$ |
| ω | circular frequency | $[\text{Hz}]$ |

Subscript

| | |
|-----------|---|
| a | ambient conditions (like for hot-wire R_a) |
| ad | adiabatic wall |
| adv | advection |
| air | air |
| amb | ambient conditions |
| $char$ | characteristic |
| eff | effective |
| f | final |
| in | initial |
| is | isentropic |
| j | relative to the jet |
| k | relative to the roughness |
| lam | laminar |
| max | maximum value |
| $mean$ | mean value |
| r | recovery |
| ref | reference value |
| $tube$ | relative to the compression tube |
| $turb$ | turbulent |
| τ | friction (like the friction velocity v_τ) |
| u | unit |
| $w, wall$ | wall, relative to the surface |
| x | relative to the freestream direction |
| x_k | relative to the axial position of the roughness element |

| | |
|----------|----------------------|
| 0 | total quantity |
| 1 | initial |
| ∞ | infinite, freestream |

Superscript

| | |
|---|---|
| + | plus (like for y-plus y^+) |
| * | critical |
| * | reference (like for reference temperature T^*) |
| ' | fluctuating component |

Acronyms

| | |
|---------|--|
| 1-D | one-dimensional |
| 2-D | two-dimensional |
| CFD | Computational Fluid Dynamics |
| DC | Direct Current |
| EMI | Electro-Magnetic Interference |
| FFT | Fast Fourier Transform |
| LE | Leading Edge |
| PCB | (name of the producer of) piezoelectric pressure transducers |
| RMS | Root Mean Square |
| SR-CMOS | Single-Reflex Complementary Metal Oxide Semiconductor |
| TC | ThermoCouple |
| TF | Thin-Film |
| VKI | von Karman Institute for Fluid Dynamics |

Chapter 1

Introduction

1.1 Introduction

Long range flights around the world must be relied upon more and more frequently as our planet becomes more economically, politically, and culturally multi-polar. As the frequency of long-range flights increases, practical and economical considerations have raised the need of a sensible decrease of their duration. And matching long ranges with short flight inevitably amounts to the use of faster airplanes. That is, supersonic or even hypersonic airplanes. This means that their velocity will be sensibly higher than that of the current airplanes, and, to achieve it, more powerful propulsion systems have to be designed. This implies more advanced, or entirely novel, engine components.

Among the main components of an air-breathing propulsion system, the intake has a key role to compress the incoming air stream into the engine core. In supersonic flight, this compression is accomplished partly outside of the intake by means of oblique shock waves generated upstream of the inlet entrance. After their generation they usually impinge and get reflected along the intake [e.g., 1, 2].

To ensure an efficient engine operation, boundary layer separation must be avoided, and laminar boundary layers are more prone to separation than turbulent boundary layers [e.g., 3, 4]. One of the most dangerous causes of separation is found to be the impingement of a shock wave. Thus, a turbulent boundary layer has to be preferred along the inlet ramps, and, if it does not occur naturally, has to be promoted to assure inlet performance. This promotion can be done with turbulence triggers [e.g., 5]. These triggers usually generate the turbulent boundary layer at some distance downstream of their location, or, if properly designed, just downstream of it. Hence, the designer can locate them only upstream of that part of the inlet where separation is more likely. In so doing, the drawbacks of a turbulent boundary layer, like increased friction and heat transfer, more and more severe as flight speed increase, can be kept at a minimum.

Turbulence triggers are designed by the means of wind-tunnel testing, flight testing, and CFD computations (notably, DNS simulations). However, the last two means show important drawbacks.

Flight tests, would be the optimal solution, since, in principle, they can reproduce exactly the flight conditions of the airplane. But they are usually very expensive, rather complex and risky, and at present reserved only to few research groups for the supersonic or hypersonic regimes.

DNS computations, on the other hand, may often fall short in dealing with the high Reynolds numbers of supersonic inlet flows. This is because of the dramatic increase in the required computational power, that often cannot be coped with.

Therefore, wind tunnel testing often times, if not usually, cannot be dispensed of in the design of effective boundary layer turbulence triggers for high speed applications.

1.2 Objectives of the research

Supersonic wind-tunnel testing requires specific facilities with specific features. And the fundamental feature of a supersonic wind tunnel is its correct start. This means that a shock-free expansion to supersonic velocity has to happen within the wind tunnel divergent part. If this is not the case, test conditions are not reached, and the facility cannot be used for supersonic flow experiments. If this is the case, instead, the wind tunnel will inevitably produce some degree of disturbances on the measurement of the flow quantities of interest [e.g., 6, 7]. This means that there will be a difference between the values obtained from the wind tunnel tests and those in real flight. It is important to quantify these disturbances as to be able to estimate this difference. The verification of the wind tunnel correct start and the quantification of its disturbances are the main parts of the qualification of a supersonic wind tunnel. A multiple-Mach-number supersonic wind tunnel for induced boundary-layer transition experiments has been designed and built at the von Karman Institute. And **the qualification of such multiple-Mach-number wind tunnel** has been the first objective of the present research. Since, this wind tunnel has been designed to operate at different Mach numbers, the correct start verification and the disturbances assessment have been carried out for more than one Mach number.

The effects of single or multiple roughness elements in boundary layer transition have been so far studied extensively only in some ranges of Mach numbers [e.g., 5, 8, 9]. Therefore, a dearth of data in the low-supersonic Mach range is felt in the aerospace community, especially in Europe. Furthermore, the interplay of wall temperature and single roughness presence is an aspect of roughness induced transition not yet fully addressed, but of design interest. Finally, most of the studies so far produced on roughness-induced transition were based almost exclusively on steady data, thus neglecting the unsteady characteristics of the roughness effects. Once qualified, the multiple-Mach-number wind tunnel has been used for an **experimental study of the steady and unsteady effects of a single roughness**

element on supersonic laminar boundary layers at different wall temperatures.

It is often the case that the turbulent boundary layer induced by the roughness does not start at the roughness location, but further downstream of it [e.g., 5, 10, 11]. Then, in case of natural transition to turbulence, the turbulent part and the laminar part of the boundary layer are not separated by a well defined line. Instead, they are separated by a zone, where lumps of turbulent flow (turbulent spots) are generated and evolve within disturbed, but still laminar, surroundings. In this zone, and in the roughness wake between the roughness position and the start of full turbulence, the boundary layer is in the transitional state, which is an intermediate state between the fully laminar and the fully turbulent [e.g., 12]. Since such transitional boundary layers may be found along the external part of a supersonic jet-engine inlet, it was considered of interest to experimentally assess the effects of an oblique shock wave impinging onto them. Therefore, the third objective of the present research has been **the experimental study of the effects on a Mach-2 transitional boundary layer of an impinging oblique shock wave.**

1.3 Research methodology

In order to accomplish the three research objectives above presented, steady and unsteady measurements were taken in two different supersonic wind tunnels, and visualizations were made in a low-speed facility.

The qualification of the multiple-Mach-number wind tunnel consisted in a test campaign carried out to assess the range of the facility Mach numbers, and to measure the freestream disturbances in the test section. The Mach range assessment has been carried out by measuring the streamwise evolution of the static pressure within the divergent. These measurements were made by fifteen piezoresistive pressure transducers. The measured static-pressure streamwise trend was checked against the analytical, isentropic-expansion trend for the same test conditions. Two-dimensional CFD of the whole wind tunnel supported these pressure measurements. The multiple-Mach-number wind tunnel was designed with two specific features to reduce its freestream disturbances: suction slots at the wind-tunnel throat, and mirror-polishing of all the internal surfaces. The effectiveness of such features was assessed by two-dimensional CFD computations of the whole wind tunnel, and by hot-wire measurements of freestream fluctuations. The computations verified the absence of a recirculation bubble in the proximity of the bleed slot lip, while the hot-wire measurements yielded the RMS intensity and the spectrum of the freestream mass-flow fluctuations. Both the computations and the hot-wire measurements were repeated for two different Mach numbers. The inspection of the fluctuations frequency spectrum gave some hints about the possible causes of the freestream noise.

To assess the effects of the single roughness element on two different supersonic boundary layers, steady and unsteady wall-temperature measurements, and unsteady wall-pressure measurements, were taken. Joule heaters at the bottom of one instrumented insert varied the temperature of the wall downstream and around the single roughness. All measurements were made at first for a reference clean configuration, and then repeated for the configurations with the roughness. The steady wall-temperature measurements made possible the calculation of the convective heat-flux at each sensor location, hence of its streamwise trend. This, in turn, allowed the calculation of the adiabatic-wall temperature and the Stanton number trends. The adiabatic-wall temperature trend, verified against analytical results for fully laminar and fully turbulent regimes, has been used to conclude on the general state of the roughness wake. CFD computations verified the correctness of these analytical trends for the test cases under evaluation. Also the Stanton number trends gave the picture of the general state of the roughness wake, but, more specifically, without accounting for the wall-temperature effects. The unsteady wall-temperature and -pressure measurements allowed the characterization of the roughness wake unsteadiness; they complemented the results from the steady measurements. This characterization was made by tracing the streamwise evolutions of the fluctuations RMS and frequency spectrum downstream of the roughness, by cross-correlating wall-temperature signals from consecutive sensors, and by calculating the frequency-time evolution of the signals at each sensor location.

To evaluate the effects of shock impingement on transitional boundary layers, the single-roughness wake and the naturally occurring transitional boundary layer have been reproduced along a flat plate in a Mach-2 facility. The single roughness was one of the two used in the test campaign in the multiple-Mach-number wind tunnel. The naturally transitional boundary layer, instead, was simulated by the release of electric sparks within the supersonic laminar boundary layer to try to produce turbulent spots. An oblique-shock generator above an instrumented flat plate produced the oblique shock. The impact location was such as to assure the presence of some sensors upstream of it to capture the differences induced by the shock impingement. The sensors used for these measurements were of the same type as for the test campaign in the multiple-Mach-number wind tunnel. However, no steady data from the wall-temperature measurements were acquired, but only unsteady wall-temperature data. For this reason, the RMS streamwise trends and the frequency-time signal evolutions at the sensors locations were used to draw conclusions. The set-up for the electric spark release was conceived, designed, built, and tested during the present research project. These preliminary tests were carried out in a low-speed wind tunnel, where high-speed-camera visualizations of an incompressible boundary layer flow were taken. The examination of the spark effects on this boundary layer allowed to decide the best gap between the electrodes and their best distance from the wall. Since the spark release was designed to be tun-

able, the visualizations also verified the multiple-frequency capability of the set-up, and, finally, the presence of distinguishable effects on the boundary layer for different spark frequencies.

1.4 Thesis outline

This dissertation consists of five chapters, three main chapters plus this introduction and the chapter for the general conclusions. Each of the three main chapters is dedicated to one of the thesis objectives. They have the same structure: a general introduction to the chapter topic; a main body, where the chapter topic is dealt with; and a final section dedicated to the conclusions.

Chapter 2 begins with the description of the multiple-Mach-number wind tunnel in Section 2.1. This includes the description of the facility low-noise features, typical cycle operation, and instrumentation. The presentation and discussion of the qualification campaign results follows in Section 2.2. This comprises the facility Mach range successfully span, the freestream noise quantification, and the investigation of its possible causes.

Chapter 3 begins with the description of the measurements techniques for wall-temperature and wall-pressure in Sections 3.1 and 3.2. Specifically, calibrations for both thin-films and piezo-electric pressure transducers are described, along with the sensitivity analysis of the thin-films. Section 3.3 follows by describing the use of CFD for the test campaign, and the insights on the boundary layer flow that its results have provided. Then, the results from the steady data post-processing are presented and commented in Sections 3.4 to 3.5, while the results from the unsteady data post-processing are presented and commented in Sections 3.6 to 3.8.

Chapter 4 begins with the description of the electric set-up for the spark generation (Section 4.1), and proceeds with the description of the preliminary tests made to ready it for the main Mach-2 test campaign (Section 4.2). Following Section 4.3 is dedicated to the Mach-2 test campaign, and describes the facility used, the specific data post-processing required by the signals from the spark tests, and the results from the unsteady measurements.

Finally, Chapter 5 summarizes all the results of this work and outlines the main conclusions.

Chapter 2

Design and qualification of a multiple-Mach-number supersonic wind tunnel

This Chapter describes the design and the qualification test campaign of a multiple-Mach-number supersonic wind tunnel conceived at the von Karman Institute for Fluid Dynamics (Fig. 2.1). This wind tunnel allows supersonic testing at different Mach number in the same facility by the sole setting of the divergent angle. This divergent, in fact, is made of two movable straight ramps and two fixed vertical walls. Not only the divergent of the wind tunnel is shaped along the movable ramps but also its throat and the part of the convergent between the throat and the suction-slot lip. Since also the rest of its convergent is comprised of two contoured part between two vertical walls, the whole wind tunnel features a rectangular cross section.

The suction slots are a feature introduced in the design to limit its noise, and for this purpose are complemented by an accurate mirror polishing of all the wind tunnel internal metal surfaces. They prevent that the boundary layer coming from far upstream through the convergent can flow along the divergent as thick and highly perturbed as it usually becomes [13, and references therein]. In so doing, they also let the instrumentation of the lower ramp so to carry on experiments directly on it.

This supersonic wind tunnel is fed by a compression tube and evacuates into the atmosphere. In this Chapter after the description of the wind tunnel characteristics, the operation of the facility is described, and finally the results of the qualification test campaign are presented.

2.1 Description of the wind tunnel test section

The supersonic wind tunnel is realized by removing or substituting some parts of a compression-tube short-duration blow-down facility designed and used to test turbo-machinery airfoils. The main modifications are the addition of the divergent-convergent nozzle to generate the supersonic flow, and the removal of the piston used to compress the air in the compression tube. To these modifications add the evacuation into atmosphere instead of into a

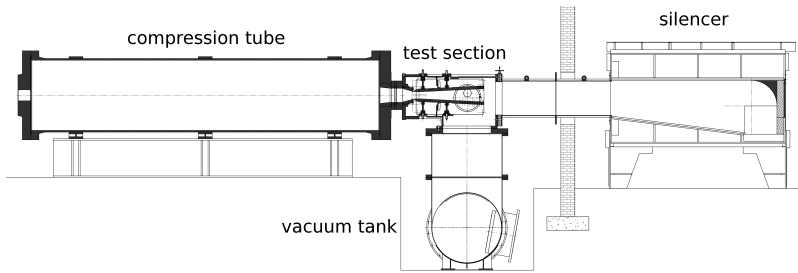


Figure 2.1: *The facility of the supersonic multiple-Mach-number wind tunnel*

vacuum tank, and the use of this vacuum tank as part of the boundary-layer aspiration system. The air enters the nozzle convergent from the compression tube by the opening of a slide/shutter valve and is finally vented out to atmosphere through a silencer. Figure 2.1 shows the wind tunnel general arrangement.

Since the original function of the facility had to be preserved, all of the overall dimensions had to be kept. This yielded a series of constraints on the design of the supersonic wind tunnel, whose most evident are the fixed test section width and length. These constraints, along with the requirement of a movable divergent to allow different Mach numbers, prevented the presence of a constant-section zone to be used as constant-freestream-properties test section. Therefore, the divergent itself had to be used as test section with consequent freestream properties varying streamwise (Fig. 2.2). Specifically, the lower of the two movable ramps have been equipped with instrumented inserts and test articles.

The movable ramps constitute the divergent part of the supersonic nozzle. Changing their angle allows to control the degree of the supersonic expansion, hence the Mach number values through the divergent. This angle change is made operating on two screws per ramp that allow vertical movements in two distinct positions. In this way the throat area, thus the mass flow, can be kept constant as the Mach number changes (Fig. 2.2).

To avoid strong pressure disturbances in the test section the boundary layer must be laminar on those parts of the wind tunnel from where it could radiate noise onto the test article. In the present case this rationale applies to the upper ramp, but becomes a compelling requirement for the lower ramp, because it is along this ramp that transition tests are carried out. The boundary layer along the ramps, then, is kept laminar by using suction slots just upstream of the nozzle throat, and by accurate wall polishing. These are

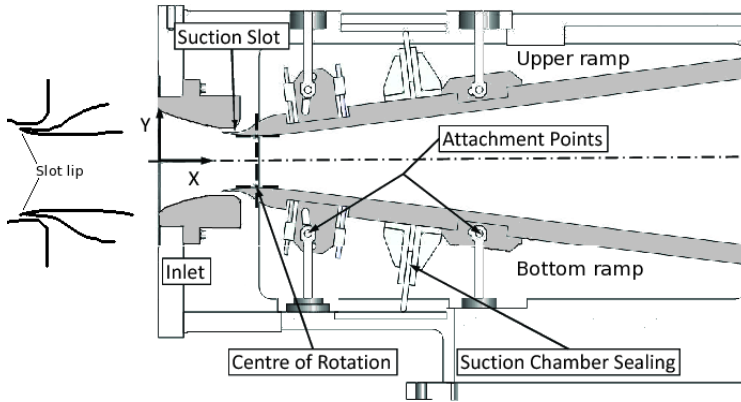


Figure 2.2: *The test section with the mechanical arrangement of its movable ramps, and the bleed slots detail*

the two main solutions currently used in quiet wind tunnels used for research in natural (i.e., not induced) boundary layer transition to turbulence [9, 14].

2.1.1 The suction slots and the aspiration system

Suction slots (Fig. 2.2) are openings upstream of the throat of the wind tunnel that ingest the boundary layer formed and grown along the walls of the convergent. In this way, the boundary layer that enters the supersonic part of the wind tunnel arises as new at the leading edge of the suction slot (the lip). And it is much less contaminated by disturbances than the ingested boundary layer. Therefore, it is much more prone to stay laminar throughout the test section [14]. In the present design it has been possible to apply a suction slot only to two sides of the wind tunnel throat: the upper and the lower, that is the two movable ramps.

The boundary layer ingestion in the present arrangement is activated by an aspiration system downstream of the suction slots. This system is comprised of a large vacuum tank beneath the test section of the wind tunnel (Fig.2.1), connected to the suction slots through a total of four tubes. The tank is complemented by the void part between ramps and the casing downstream of the slots throat (Fig. 2.2). When the valves of the tubes open, the vacuum tank starts aspirating air from the slots at a flow rate that chokes the slots throat and make the flow highly supersonic downstream of them.

It is clear that the slots themselves should not produce sensible disturbances in the newly created laminar boundary layer. The possible sources for these disturbances are recirculation bubbles on the slots surface along which the boundary layer grows (inner wall), and/or recirculation bubbles on the surfaces of the remaining parts of the suction system (outer wall).

For this latter case, the remedy is to assure a sonic throat in the duct downstream of the slot entrance so that no disturbances generated in the suction system can move up into the wind tunnel flow. To avoid recirculation bubbles along the inner walls, instead, a special contour of the slot lip must be designed.

A recirculation bubble can be generated by two different suction regimes, strong and weak, and both of them have to be dealt with to avoid disturbances within the boundary layer (Fig. 2.6, top row) [14].

In the case of strong suction, a stagnation point will occur on the side of the suction-slot lip toward the wind tunnel center-line (inner wall). Thus the subsonic boundary layer flow to be ingested by the slot experiences an acceleration around the lip just followed by a deceleration flowing downstream along the straight surface of the outer wall. In the case of weak suction, on the other hand, the stagnation point moves to the outer surface of the lip, leading to a recirculation bubble on the inner wall. Both of these configurations can cause dangerous perturbations in the boundary layer flow heading to the divergent. The configuration due to the weak suction may be particularly harmful because it creates noise directly in the downstream flow increasing the risk of early transition of the boundary layer on the tunnel walls. The case of strong suction could also cause perturbations in the main flow, if the mass flow through the slot becomes unsteady and produces oscillations on the stagnation point on the suction lip.

To avoid both dangerous regimes, an *adapted suction* regime has to be achieved by designing the suction lips with a specific shape [14]. In fact, a perfectly round lip as in Fig. 2.6 (the most straightforward shape, and historically one of the first configurations used) was soon found too prone to form highly unsteady recirculation bubbles, and new contours were investigated. The most promising resulted the *modified super ellipse* contour described by the following equation

$$\left(\frac{y}{b}\right)^2 + \left(\frac{a-x}{a}\right)^m = 1 \quad (2.1)$$

$$m = 2 + \left(\frac{x}{a}\right)^2 \quad (2.2)$$

where a and b are the major and minor axes of the ellipse. With this profile, the curvature goes continuously to zero as $x \rightarrow a$ [15]. This contour has been selected for the suction lips of the wind tunnel here presented, and, to verify its effectiveness, 2-D CFD computations of the flow field around them have been performed. They are presented in the following paragraph.

2.1.1.1 Numerical verification of the suction lip design

The verification of the correctness of the suction lip design required laminar computations to be performed, since this is the state of the boundary layer

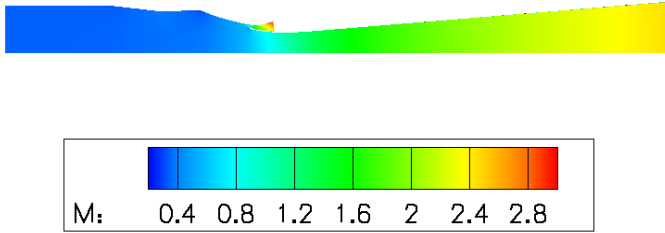


Figure 2.3: Example of 2-D CFD computations made to investigate the effectiveness of the suction-slot lip design (divergent angle of 4.7° , Mach number = 2.3)

that the suction slots are designed to preserve. To perform such computations the commercial software *CFD++* was selected because of its proven reliability in dealing with supersonic flows. Considering the geometry of the whole wind tunnel, 2-D computations were set up. Measured quantities as total pressure, total temperature, wall temperature, and nozzle exit static pressure were used as boundary conditions for all these laminar computations. Along with the whole suction slot, the entire supersonic wind tunnel was resolved from the compression tube downstream to the main divergent exit (Fig. 2.3).

In view of the test campaign to be discussed in Chapter 3, the computations were made at two Mach numbers, 1.6 and 2.3. Figure 2.4 shows the detail of the structured mesh in the central part of the wind tunnel with the suction lip upstream of the sonic throat. Figure 2.5, instead, zooms in on the mesh structure around the suction-slot lip. From this picture one can also appreciate the mesh refinement used for the boundary layer: 200 nodes are allocated normally within 2 mm from the wall along the entire boundary layer developing from the lip tip downstream through the main divergent on one side, and the suction-slot divergent on the other side. This refinement resulted in y^+ values always below 1.

The bottom row in Fig. 2.6 shows the results of the computations performed to verify the lip design. The plot on the right refers to the widest possible ramp angle, 4.7° , that corresponds to Mach 2.3. It shows the flow streamlines and the field of the velocity axial component around the modified super-elliptical tip.

The streamlines pattern shows that no laminar recirculation bubble is caused by the elliptical suction tip; neither on the immediate outer wall nor on the inner wall. It also explains why negative values of the axial

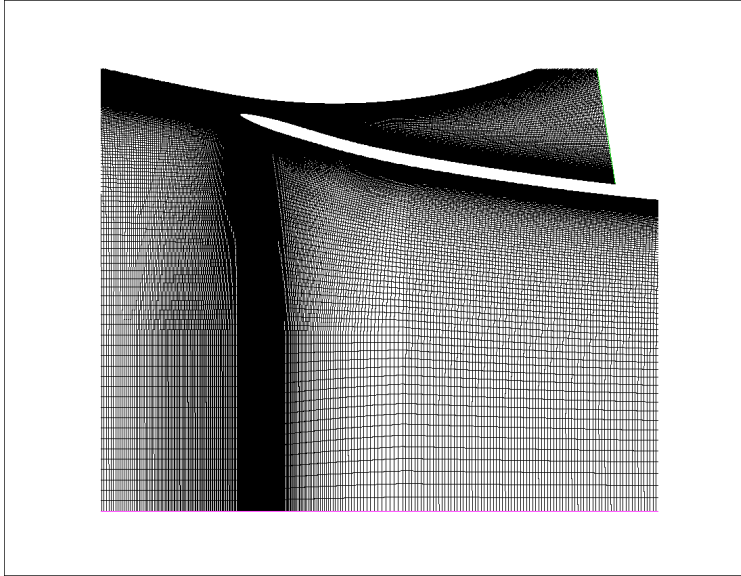


Figure 2.4: *Detail of the structured mesh around the central part of the wind tunnel (divergent angle of 4.7°)*

component of the flow velocity appear in the field: the flow moves up from the stagnation point around the tip, and, in so doing, moves back a short axial distance.

Practically, the same flow picture comes from the plot on the left, which is for the smallest ramp angle qualified, 1.2° , corresponding to Mach 1.6. Again streamlines and the field of the velocity axial component are presented, and they show no sign of a recirculation bubble. In the end, the CFD computations show that no recirculation bubble is present around the slot tips for the largest and smallest divergent angle qualified, thus for the two most extreme tip positions possible. Now, recirculation bubbles are usually formed because of strong adverse pressure gradient in the boundary layer. In the present situation these adverse pressure gradient can come only from the tip angle of attack respect to the flow. This in turn is determined only by the ramp angle. Thus proving that no recirculation bubble appears for the smallest and the largest ramp angles possible, one can plausibly conclude that it will not appear neither for all the intermediate ramp angles, and that the tip design is finally effective for all the Mach numbers possible by the facility.

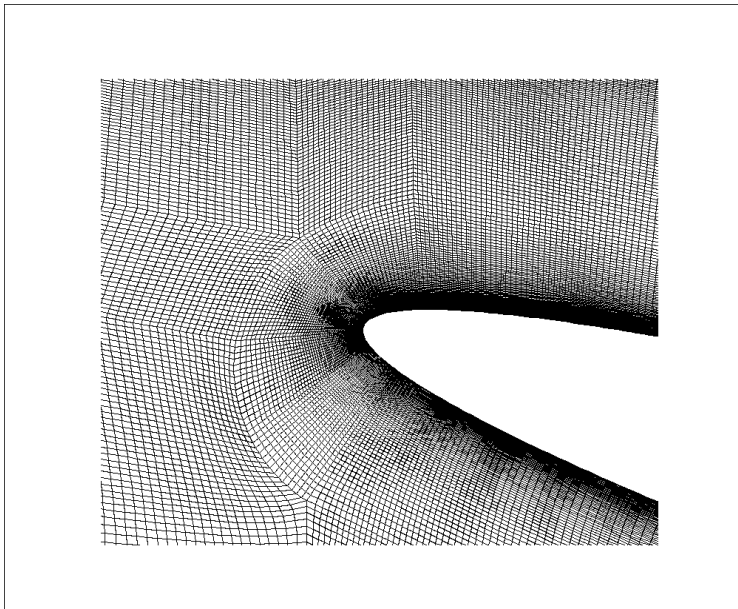


Figure 2.5: *Detail of the structured mesh around the suction-slot lip (divergent angle of 4.7°)*

2.1.2 Surface treatment of the nozzle walls

Even the most sophisticated and performing boundary layer removal technique can result useless if not complemented by very highly polished nozzle surfaces. In fact tests showed that the wall and freestream pressure fluctuations were found to scale with the mean wall shear for all Mach numbers [16]. Refining the smoothness of the nozzle from a RMS of 2-10 $\mu\text{in.}$ to a RMS of 1-3 $\mu\text{in.}$ improved the Reynolds number at which the NASA- Langley Mach-3.5 tunnel is quiet by a factor of two. *Quiet* is usually called that wind tunnel whose interference to the boundary layer flow along the test article is so low that it allows the fair reproduction of the natural transition process as in flight conditions. Therefore, high aerodynamic smoothness is deemed important, especially for the throat surface, and has been achieved throughout the internal walls of the present wind tunnel.

The "aerodynamic smoothness" of a surface can be judged taking as a reference the thickness of the laminar sub-layer of a hypothetical turbulent boundary layer at the location of interest. This hypothetical turbulent boundary layer has to be compatible with the properties of the flow under exam. Then, a surface can be considered smooth if the RMS value of its roughness height is less than the thickness of the laminar sub-layer of the hypothetical turbulent boundary layer [17].

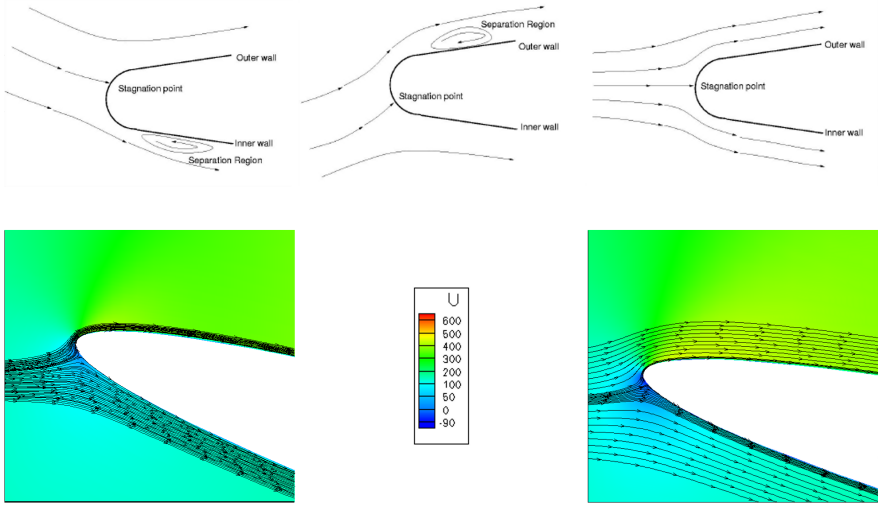


Figure 2.6: Top row: typical flows around the lip of a suction slot; bottom row: streamlines and velocity contours around the lip tip for $\alpha = 1.2^\circ$ (left) and $\alpha = 4.7^\circ$ (right)

Usually the thickness of the laminar sub-layer is $y^+ = 5 - 6$ [18] with

$$y^+ = \frac{y \cdot u_\tau}{\nu} \quad (2.3)$$

$$u_\tau = \sqrt{\frac{\tau_w}{\rho}} \quad (2.4)$$

$$\tau_w = \frac{\rho_\infty u_\infty^2}{2} C_f \quad (2.5)$$

and the approximate maximum value for the C_f to be expected for $M_\infty \in [1 \div 3]$ can be evaluated as $5 \cdot 10^{-3}$, taking into account the expected total temperature, thus the expected Reynolds number. This corresponds to a height of the laminar sub-layer in the range $6 - 11 \mu m$, and this range was taken as reference for the wall polishing.

Both ramps, the convergent walls, and the divergent lateral walls have been mirror-polished, and their degree of smoothness was measured. These measurements were taken on one of the ramps by a roughness-meter Mitutoyo SJ-201P in five different locations across its entire width (see Fig. 2.7). More than one roughness measurement was taken as to check repeatability, and two quantities have been recorded: the RMS, R_q , and the average value, R_a , of the roughness height. The roughness standard selected was ISO. The measurements yielded an average value in the range $[0.06 \div 0.11] \mu m$ and

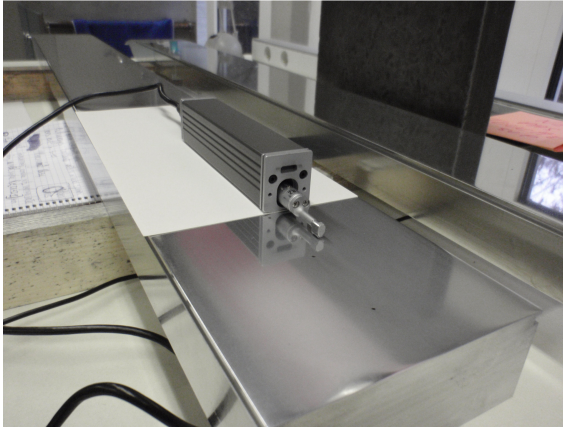


Figure 2.7: *The roughness meter Mitutoyo SJ-201P on one of the nozzle ramps*

an RMS in the range $[0.08 \div 0.14] \mu\text{m}$, i.e. two orders of magnitude less than the calculated laminar sub-layer thickness. These measurements lead to the conclusion that the ramps resulted smooth enough to prevent turbulence onset due to distributed roughness. Eventually, no quantification of the roughness height has been possible for the vertical side walls. This is because the roughness-meter works only on horizontal surfaces, while these walls were kept vertical during the polishing. Their weight and integration in the facility prevented the necessary displacement and horizontal positioning for the measurement.

2.1.3 Typical test cycle operation

Here it is now described the procedure by which the new supersonic wind tunnel has been operated. Initially the shutter valve is closed isolating the test section from the compression tube. Air is fed into this tube as to reach the total pressure required for the test. Total temperature increases in consequence of the compression process.

As the total pressure reaches the desired value the shutter is opened, and air starts its expansion through the convergent-divergent nozzle to the wanted test conditions. However, these conditions would not stay steady if only the air compressed at the beginning were used for the test. In fact, the air flow out of the compression tube would automatically decrease the pressure in it, and reduce the total pressure of the test. This, in turn, would prevent any interval of time long enough to allow measurements at steady total conditions. This situation is avoided by throttling a second air-feeding system that lets high-pressure air into the compression tube, and keeps the pressure inside it (thus the total pressure of the test) as constant as possible

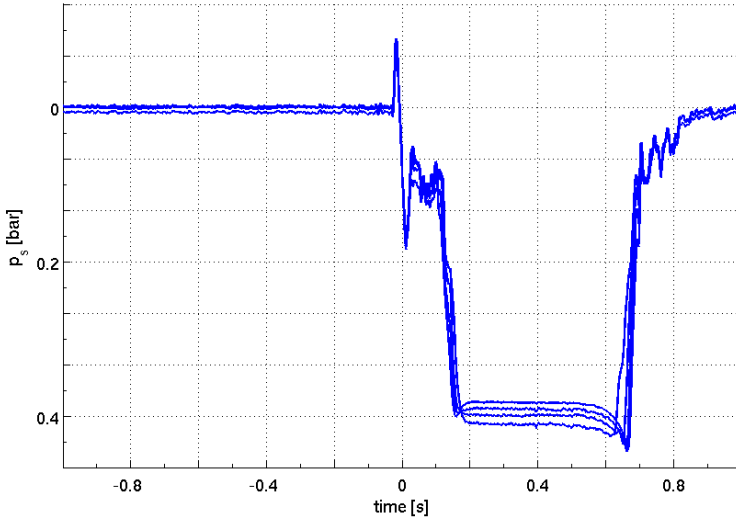


Figure 2.8: *Static-pressure time evolution during a wind tunnel run ($Mach = 2.3$ at 90 cm from the sonic throat)*

throughout the wind tunnel run.

The supersonic wind tunnel takes a finite time to start and establish the isentropic supersonic flow throughout the divergent. At the end of the run, then, air conditions come back to initial values also in a finite time. Figure 2.8 illustrates this process showing the signals of four pressure taps flush-mounted at the end of the upper ramp (see Fig. 2.12). There appears how the flow starts at 0 seconds and how steady signals establish after about 0.2 seconds. They stay steady for about 0.3 seconds, then they start decreasing, and at about 0.65 seconds start gaining back the pre-test values. After 0.9 seconds the run is practically over.

Finally, the valves of the aspiration system open 0.1 seconds before the shutter so that the boundary layer removal is already operative before the supersonic test conditions are reached.

2.1.4 Parameters regulation

The unit Reynolds number of each test depends on the setting of the total pressure (p_0) and total temperature (T_0). This dependency happens through the variations of freestream density and viscosity. The supersonic Mach number, instead, once the throat is choked, depends only on the divergent angle. Therefore, in principle, one can test for a given divergent angle in a range of Reynolds numbers just varying the values of total pressure and

total temperature.

The total pressure value for each divergent angle has been assigned upon the successful starting of the wind tunnel. That is, the value of the total pressure for a test at a given divergent angle is the minimum value among those that succeeded in starting the wind tunnel during the qualification test campaign (Section 2.2). The mechanical limits of the facility, then, set the highest safe total pressure at 5 bar. This value turned out to be the one needed to operate the wind tunnel at the widest divergent angle, that is, for the highest Mach number possible. This signals that the total pressure change becomes more and more limited with the required Mach number.

On the other hand, the total temperature can be varied more extensively acting on the initial pressure (p_{in}) of the compression process that builds up the test total pressure value. The facility, in fact, allows initial pressure values either lower or higher than ambient, thus the same compression process can yield different total temperatures as from

$$\frac{T_f}{T_{in}} = \left(\frac{p_f}{p_{in}}\right)^{\frac{\gamma-1}{\gamma}} \quad (2.6)$$

Here $p_f = 0.995 \cdot p_0$, $T_{in} = T_{amb}$ and $T_f = 1.11 \cdot T_0$, with 0.995 and 1.11 empirical coefficients that account for the deviation from the ideal isentropic compression.

The two plots in Fig. 2.9 are for the smallest and largest ramp angles qualified, and show the unit Reynolds number evolution throughout the divergent for five T_0 values. The maximum total temperature is such that the lowest p_{in} is about 0.4 bar, an usual value for turbo-machinery testing, whilst the minimum is such that the lowest possible freestream temperature is always higher than 90 K. Reynolds numbers are plotted against the axial direction spanning the length of the lower ramp section that can be instrumented ([720 ÷ 1120] mm).

Both plots show that the unit Reynolds number decreases with total temperature and with the length flown, if T_0 is fixed. This is because at fixed total pressure, an increase of total temperature yields an increase of dynamic viscosity and a decrease of density, both leading to the decrease of the unit Reynolds number. Then, as the flow expands through the divergent, at fixed total temperature and pressure, density and viscosity decrease, and the Reynolds number also decreases because density changes are more important than viscosity changes. However, the streamwise decrement is not very large: +19% at maximum, which happens for the widest divergent angle (4.7°) and the highest total temperature ($T_0 = 610$ K). The minimum is +6% for the narrowest angle (1.2°) and the lowest total temperature ($T_0 = 210$ K). This is the difference in percentage between values of the unit Reynolds number at the beginning of the instrumented section and at its end.

Another parameter that can be varied is the test time. It can be increased

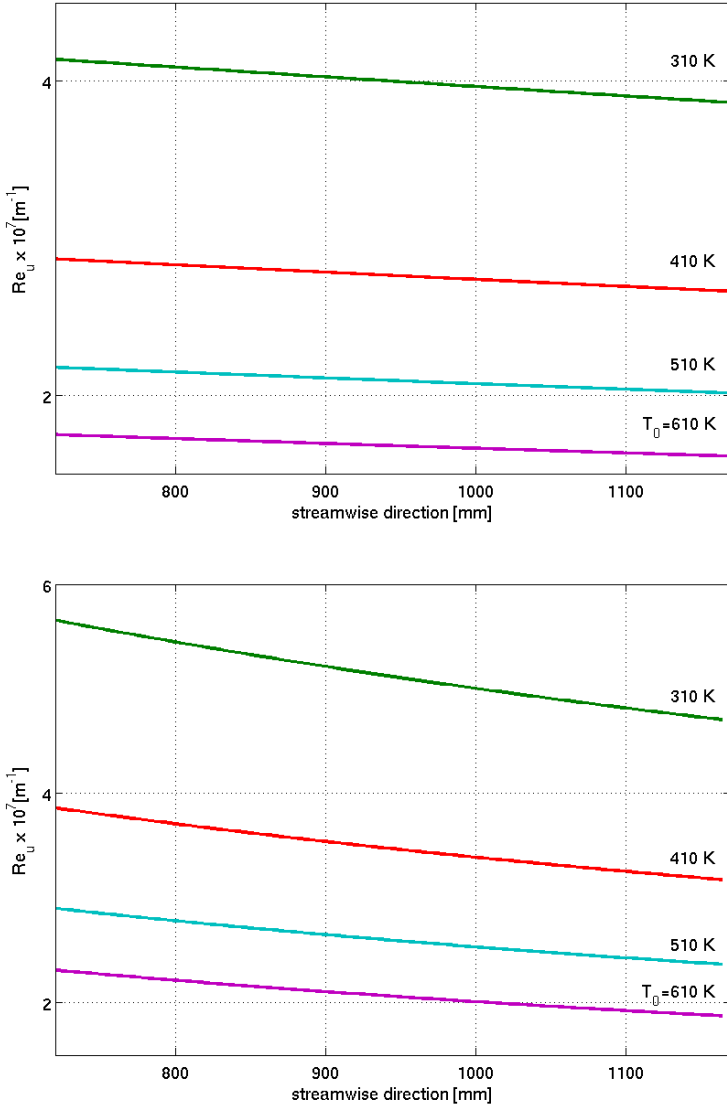


Figure 2.9: The unit Reynolds number evolution through the divergent at different total temperatures (top plot: $\alpha = 1.2^\circ$; bottom plot: $\alpha = 4.7^\circ$)

by reducing the throat area, for the same initial conditions. In fact, it can be estimated upon the mass flow through the nozzle and the mass of air prepared for the test inside the compression tube. The mass flow through

the supersonic nozzle is the critical mass flow of the throat section (i.e. the mass flow for sonic velocity at the throat) and depends on the throat area, the total pressure, the total temperature, and the ratio of specific heats:

$$\dot{m}^* = (h \cdot w)^* \left[\left(\frac{2}{\gamma + 1} \right)^{\frac{1}{\gamma - 1}} \cdot \sqrt{\frac{2\gamma}{\gamma + 1}} \right] \frac{p_0}{RT_0} \quad (2.7)$$

where h and w are the throat height and width, respectively. Given $m_{tube} = \rho_0 \cdot V_{tube}$ as the mass of air inside the compression tube ready to be blown through the nozzle, the test time depends inversely on the throat area as

$$\dot{m}^* \simeq \frac{m_{tube}}{t_{test}} \Rightarrow t_{test} \propto \frac{m_{tube}}{A^*} \propto \frac{V_{tube}}{\sqrt{T_0} A^*} \quad (2.8)$$

Thus reducing the throat area will increase the test time. (Note also that the test time does not depend on the total pressure because of the linear dependency on total pressure of both m_{tube} and \dot{m}^* .) Since the width of the entire wind tunnel is fixed, the only way to reduce the throat area is to reduce its height. Figure 2.10 shows the theoretical test time versus the possible throat heights in the same range of total temperatures as for the plots in Fig. 2.9.

This figure shows that the test time decreases with the throat height for a given total temperature, as expected, while it decreases with total temperature for a given throat height. This latter behavior is also expected as from Equation 2.8.

2.1.5 Wind-tunnel standard equipment

To command the correct function of the wind tunnel and to check the correct establishment of the supersonic flow, the compression tube, the boundary-layer injection system, and the wind tunnel divergent are permanently instrumented.

The total pressure in the compression tube is monitored by a Valydine DP15 variable-reluctance differential pressure transducer, and the total temperature by two type-K thermocouples. The pressure sensor is relied upon for opening the shutter as the wanted total pressure is reached, and thus starting the flow, and for controlling the total pressure steadiness through the test time. Thermocouples are used to measure the total temperature, and to track its time evolution during the test. One thermocouple is located very near the total-pressure sensor, the other is flush-mounted on the front of the compression tube.

The four pipes that connect the vacuum tank to the suction slots are also instrumented to measure the mass flow. Each pipe is equipped with four total pressure piezoresistive probes, three static-pressure piezoresistive

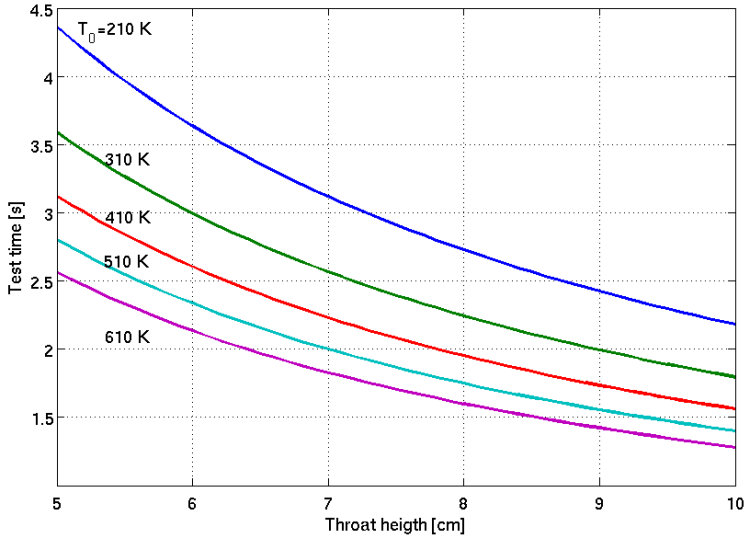


Figure 2.10: *The theoretical test time versus the throat height at different total temperatures*

probes, and one type-K thermocouple. The four total pressure probes are arranged at the same depth inside the pipe and are spaced by 90 degrees to each other. This arrangement allows to have a fair representation of the inflow total pressure from the average of the probes measurements. The three static pressure probes are flush-mounted pressure taps located at the same distance from the pipe inlet as the total-pressure probes. The thermocouple, then, being exposed to the freestream, measures the total temperature of the flow. It is located at the same depth and same distance from pipe inlet as the pressure probes (Fig. 2.11). Monitoring the mass flow of each pipe allows to control how the upper and the lower suction slots work, and whether they do work in the same correct way.

The same piezoresistive sensors used to instrument the aspiration system are used to sense the static pressure inside the nozzle divergent. Their response time is 0.1 ms. The upper ramp of the divergent is equipped with five pressure taps, each one connected to one piezoresistive sensor (Fig. 2.12). These taps are located close to the end of the ramp as to avoid acoustic radiation onto the instrumented part on the lower ramp.

Only for the qualification test campaign, also the lower ramp was instrumented with ten pressure taps that allowed to plot the static pressure evolution throughout most of the instrumented insert. These plots were used to judge the successful start of the wind tunnel (Section 2.2).



Figure 2.11: *The front view of the four static pressure L-shaped taps and the thermocouple that instrument each of the aspiration system four tubes*



Figure 2.12: *The two ramps instrumented for the qualification test campaign: the upper ramp features five pressure taps, the lower ramp ten*

2.2 Test section qualification

The wind tunnel qualification consisted firstly in proving the correctness of the wind tunnel starting, i.e. the presence of a shock-free supersonic expansion in the divergent. Secondly, the qualification campaign focused on measurement of the wind tunnel noise to assess experimentally the wind tunnel degree of quietness.

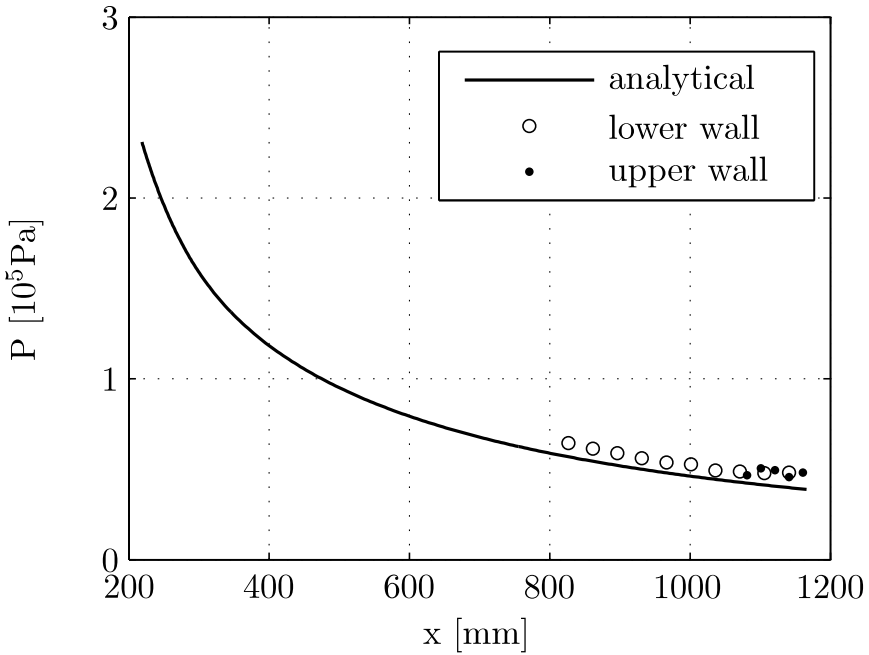


Figure 2.13: Typical static pressure axial evolution throughout the whole nozzle divergent ($p_0=4.2$ bar)

2.2.1 Practical Mach range achievable

The wind tunnel was designed to operate at different Mach numbers, therefore its starting was verified for a range of Mach numbers. The absence of the shock was verified by the use of the fifteen pressure taps described in the preceding. The evolution of the static pressure at the wall along an axial length of 36 cm was measured. These measurements, in turn, were compared with pressure and Mach number axial evolutions of a supersonic shock-free expansion produced by quasi-1-D calculations. These calculations had as inputs the measured total quantities of the run. An example of comparison between the calculations and the measurements is illustrated by Fig. 2.13 for the static pressure and by Fig. 2.14 for the Mach number.

These two Figures show how the measured pressure and Mach number evolution along the divergent matches the theoretical evolution. This means that no shock wave is present in the divergent, that is the wind tunnel is correctly started for the total pressure value selected for the test. For the sake of comparison, Fig. 2.15 shows the static pressure measurements for a case when the wind tunnel failed to start. Between 800 and about 900 mm measurements are in fair agreement with the theoretical trend, as in Fig. 2.13, but behind 900 mm they rapidly diverge to a higher value that

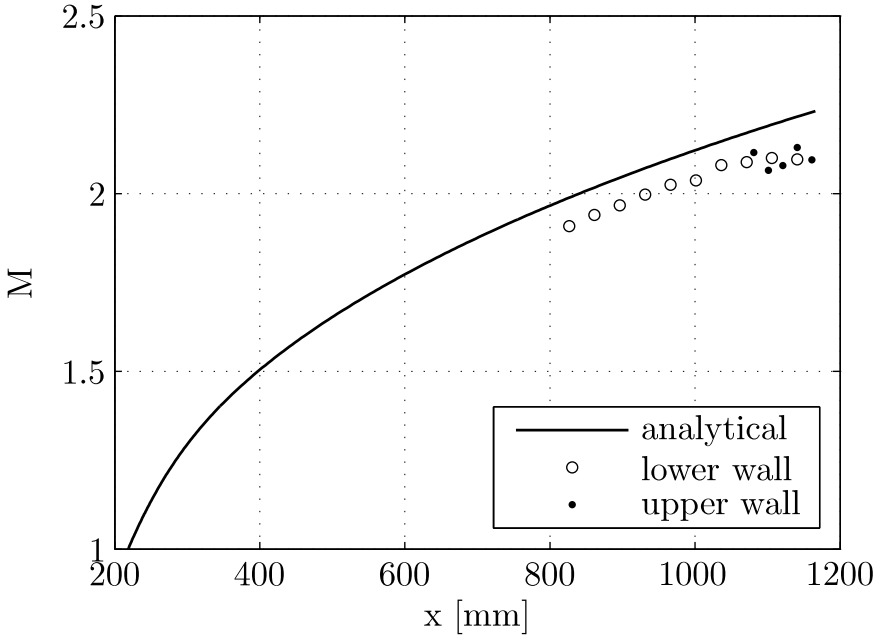


Figure 2.14: Typical Mach number axial evolution throughout the whole nozzle divergent ($p_0=4.2$ bar)

seems to increase slightly and linearly after 100 mm. This rapid increase in pressure is due to the shock wave sitting within the divergent. This shock wave forces the flow to adapt to the nozzle back pressure, that is, the ambient pressure. This happened because the ratio between the total pressure of the test and the nozzle back pressure was not high enough as for Fig. 2.13.

This type of verification succeeded for the Mach numbers presented by Table 2.1. Here are also presented the corresponding unit Reynolds numbers, and total pressures for each Mach number.

| MACH NUMBER [-] | UNIT Re 10^7 m^{-1} | p_0 [bar] |
|--------------------|----------------------------------|----------------|
| 1.6 | 4.1 | 3 |
| 1.7 | 3.8 | 3 |
| 1.9 | 5 | 4.2 |
| 2.3 | 5.4 | 5 |

Table 2.1: Mach number range, unit Reynolds numbers and total pressure for the multiple-Mach-number wind tunnel

Note that, since the tests are made in the divergent of the supersonic wind

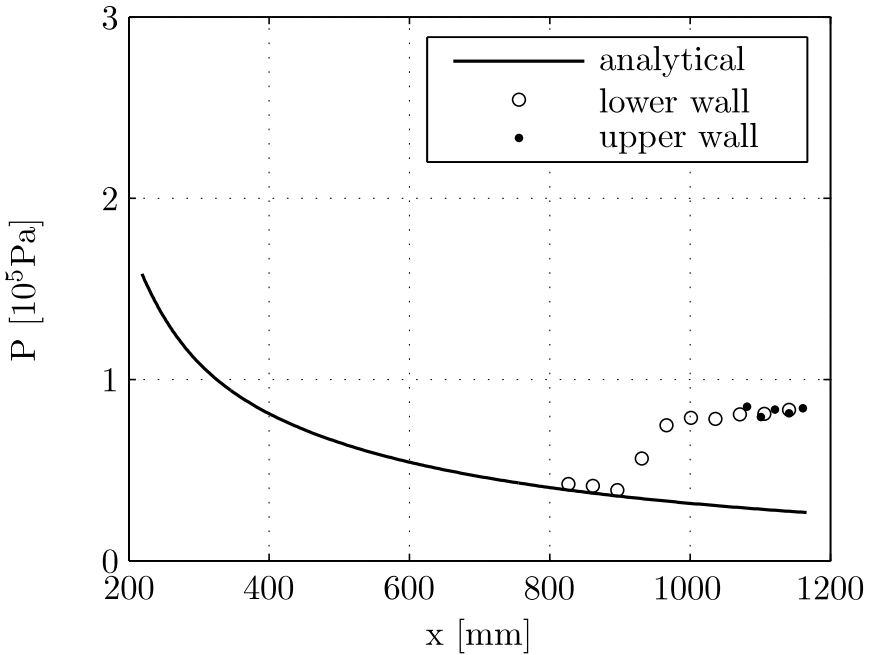


Figure 2.15: *Static pressure axial evolution in case of un-started wind tunnel ($p_0 = 3$ bar)*

tunnel, an axial location had to be selected to which refer the test Mach number. This was 80 cm from the ramp (suction slot) tip, corresponding more or less to the middle of the instrumented part of the lower ramp.

2.2.1.1 Vertical evolution of the static pressure within the divergent

The correctness of the wind tunnel operations was judged upon the axial pressure evolution measured by sensors flush mounted on the divergent wall, that is, away from the centerline. Quasi-one-dimensional supersonic flow theory states that the static pressure should not change appreciably across a divergent section whose angle is small. In the present case the largest angle possible is 4.7° , hence the pressure taps on the divergent ramps should give sufficiently reliable measurements of the centerline values. Nonetheless, numerical simulations of the flow throughout the entire wind tunnel were performed to support the experimental campaign, and their results were used to check also this aspect. In this respect, Fig. 2.16 shows the trends of the static pressure with the distance from the centerline at three different positions in the divergent, and for a freestream Mach number of 1.7.

The maximum absolute difference between the centerline and the wall values is about 0.45% of the centerline value (~ 200 Pa) at the location

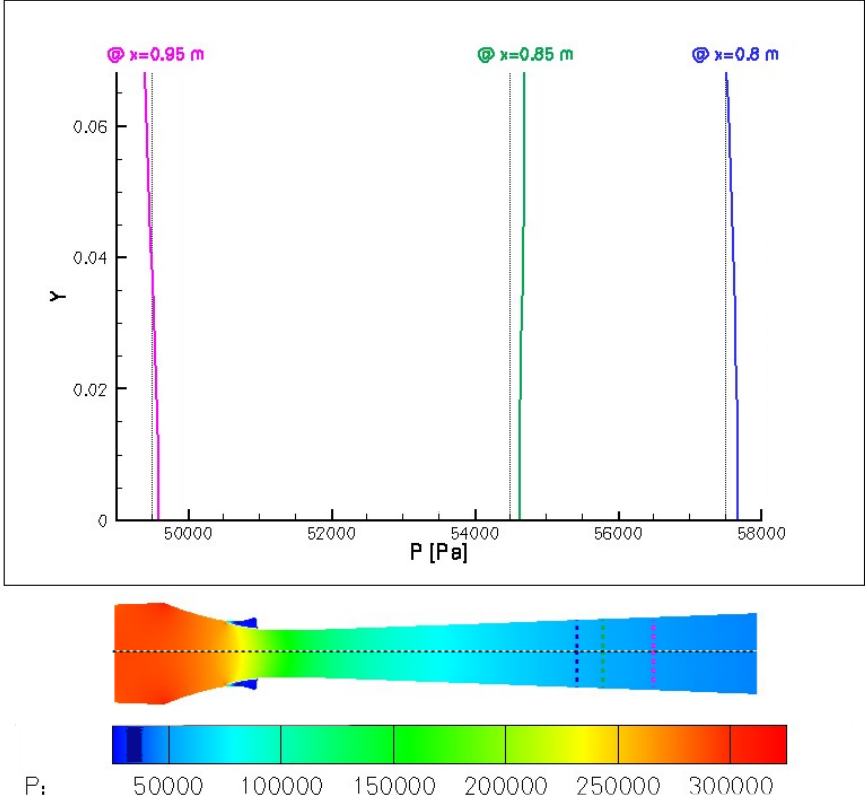


Figure 2.16: Static pressure evolution from divergent centerline to wall at three different positions

marked 0.95 cm. It is thus evident how the pressure variations normal to the centerline are very feeble and do not endanger the conclusions on the flow drawn by the wall measurements.

2.2.2 Assessment of wind-tunnel noise by hot-wire measurements

Quiet wind tunnels must generate very low disturbances, and these are mainly due to the turbulent boundary layer along the wind tunnel walls. However, also freestream fluctuations play a role at supersonic Mach numbers [19] and they are generated in the most upstream parts of the facility. Hence, a complete assessment of wind tunnel quietness has to comprise freestream turbulence quantification as well.

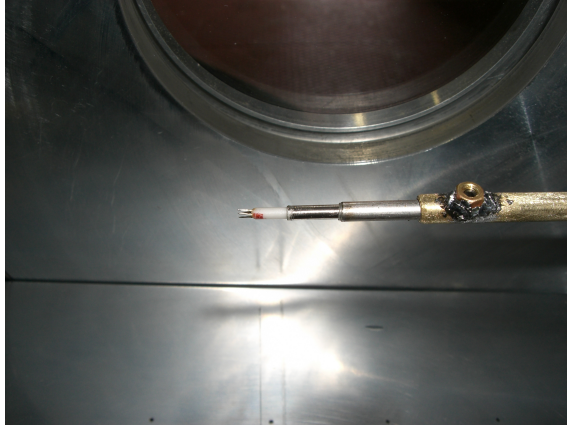


Figure 2.17: *The double hot-wire in the test section*

The freestream turbulence measurements consisted in the measurements of the mass-flow fluctuations, and were made with a double hot-wire probe mounted on a boom on the axis of the test section (see Fig. 2.17). The hot-wires were of the constant-temperature type, platinum-coated, 3-mm long, and had a diameter of $9\ \mu\text{m}$. Only the wire with the highest over-heating ratio ($R_w/R_a = 1.6$) was used for the measurements. The hot-wire electronics allowed a maximum frequency resolution of $20\ \text{kHz}$.

The hot-wire calibration was made *in situ*, i.e. at the same time as the measurements, in the following way. The mean flow quantities in each test were calculated from p_0 , p and T_0 measurements, and time intervals in which they were mostly constant were singled out of the entire test duration. Then, the mean values of ρU were plotted against the corresponding hot-wire voltage outputs so to have for each test a calibration curve of the type

$$E^2 = A + B(\rho U)^{0.5} \quad (2.9)$$

for each test. From this calibration function, the inverse function ($\rho U = f(E)$) was obtained and applied to the time-dependent hot-wire output to yield the values of the mass-flow fluctuations $\rho U'$.

As stated in the preceding, the upper limit of the fluctuations frequency range was set at $20\ \text{kHz}$ by the electronics, and for the lower limit some considerations had to be done. It has been soon evident that the entire facility vibrated during each test, and so did the boom hosting the hot-wire. These low-frequency mechanical vibrations were recorded by the hot-wire as flow fluctuations and thus had to be removed from the hot-wire signals during the post-processing. An estimation of the range of these vibrations has been possible thanks to some previous tests made with a flat plate mounted as a cantilever in the test section and equipped with

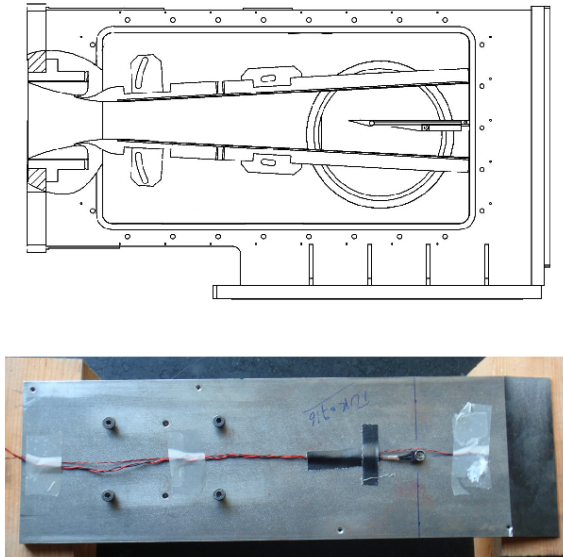


Figure 2.18: *The flat plate with the accelerometer in the test section, and a detail of the accelerometer position beneath the plate*

an accelerometer (Fig. 2.18). This accelerometer (ENDEVCO 2250AM1-10) recorded the vertical components of the plate vibrations. Even if the mechanical system composed by the plate and its supporting beams differed from that comprised of the boom and its support (the attachment to the wind tunnel was the same, instead), we considered the accelerometer data still as a good estimation of the mechanical vibrations suffered by the hot-wire. The frequency spectrum of the plate mechanical vibrations is reported in Fig. 2.19.

There appears how the strongest vibrations occur for a frequency less than 700 Hz. Hence, this value has been used as the lower limit for the frequency range of the mass-flow fluctuations.

In conclusion, the intensities of the freestream mass-flow fluctuations measured in the frequency range $[700 \div 20000]$ Hz are reported in Table 2.2 for two different Mach numbers. These intensities are expressed as the ratio between the RMS and the average value.

These RMS values are included in Fig. 2.20 where they can be compared with data from other supersonic facilities. Here are shown (linked by lines) data measured in the 1960' in a JPL supersonic quiet wind tunnel as reported in [5], plus additional data about freestream mass-flow disturbances in the Russian ITAM wind tunnels T313 and T325 [20]. The JPL wind-tunnel

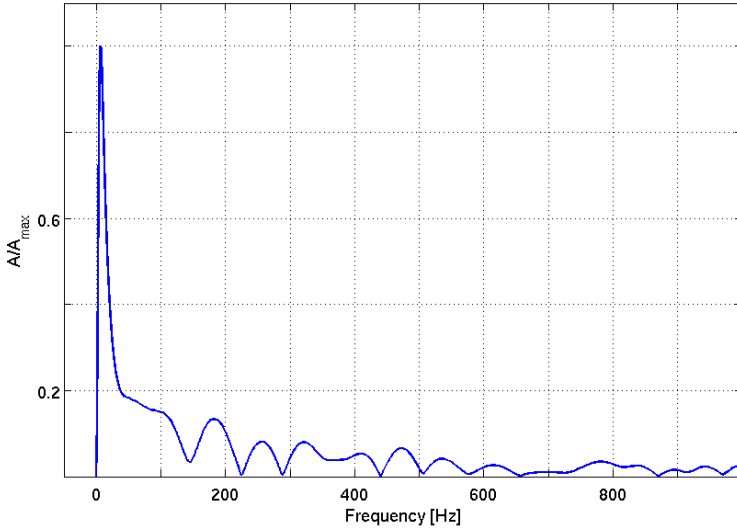


Figure 2.19: *Frequency spectrum of the mechanical vibrations of a flat plate cantilever-mounted in the wind tunnel divergent*

| M_∞ | UNIT RE | $\rho U'$ |
|------------|---------------|----------------------|
| [-] | $10^7 m^{-1}$ | $\frac{RMS}{\rho U}$ |
| 1.72 | 3.8 | 0.63% |
| 1.93 | 5 | 1.14% |

Table 2.2: *Freestream mass-flow fluctuations and the corresponding Mach and unit Reynolds numbers*

features a 1%-turbulence-intensity settling chamber with four screens and one air filter; the ITAM T325 features a settling chamber with honeycomb, ten screens, and a noise-reduction system not specified; finally, the T313 is reported as conventional.

Regarding the JPL data, the curve of interest for the comparison is that for the unit Reynolds number equal to $(1.3 \cdot 10^7 m^{-1})$ that features an interpolated value of about 0.1% for the Mach numbers tested in the present work. This means that the values measured in the VKI facility are six to ten times those of this quiet wind tunnel, i.e. typical of non-quiet wind tunnels. This is confirmed by the value from the ITAM T313 (even if for a higher Mach number), and by the values of the ITAM T325 used at transonic conditions. In this latter case, the ITAM T325 is reported as noisier than as operated at supersonic conditions.

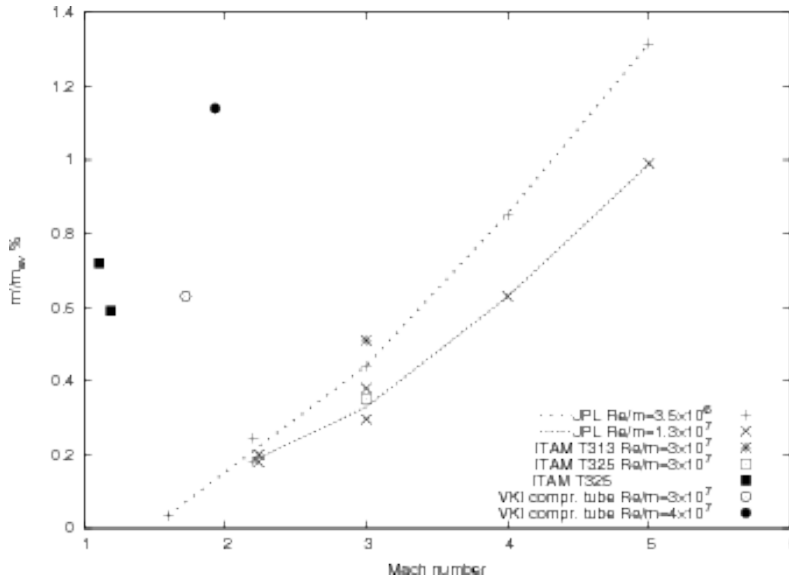


Figure 2.20: *Variation of mass-flow fluctuations with freestream Mach number [5]*

In this comparison, however, it must be kept in mind that in the present wind tunnel there are none of the noise/turbulence-reduction devices that the JPL and ITAM facilities feature in their settling chambers. In this respect, the next paragraph presents an estimation of the possible sources of noise within the compression tube of the present facility. Its aim is to offer some support to the hypothesis that this lack of noise/turbulence-suppression devices can be the cause of the difference in the intensity of mass-flow fluctuations found in Fig. 2.20.

2.2.2.1 Spectral analysis of the mass-flow fluctuations and possible cause of their intensity

As stated in the section 2.1, the supersonic wind tunnel is fed by a compression tube upstream of its convergent (Fig. 2.1), which, in turn, is directly linked to a 300-bar pressurized line that provides the air for the tests. This line feeds the compression tube at the back through two inlets, from where air expands into the tube. This expansion is followed by flow impingement onto a circular plate located about 30 cm in front of the inlets (Fig. 2.21). The purpose of such plate is to give a resting location to the piston that usually slides within the compression tube when operated for turbo-machinery testing. This piston is removed for supersonic testing, hence the compression tube is completely empty, except for the resting plate, and, therefore,

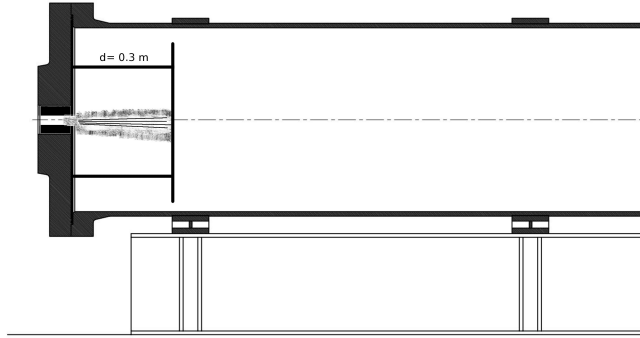


Figure 2.21: *Detail of the rear part of the compression tube (the two 300-bar-line inlets are horizontal and side by side)*

can be assimilated to a settling chamber.

This paragraph presents an analysis of the possible noise frequencies generated by the flow impinging onto this resting plate. These frequencies once calculated have been checked against mass-flow fluctuation spectra. This check wanted to find some possible support to the hypothesis of a cause/effect link between phenomena within the compression tube and the freestream fluctuations measured within the test section.

From the point of view of noise generation, the shear layer created by the jet out of its inlet is more important than the jet itself. This layer, in fact, is naturally unsteady and comprised of eddies and rolls of fluid advected along the jet direction with an advection velocity different from the jet-core velocity. If the shear layer impinges onto a solid surface (like the resting plate of the present case) acoustic noise is generated at the impingement location and radiated all around. And, if the advection velocity is subsonic, it is also radiated backward through the shear layer. This backward radiation results in a positive energy input to the fluid oscillations next onto the solid surface, which, in turn, produce other noise as they impinge the surface, and this noise is again radiated also backward, and so on. This continuous loop transformation of fluid oscillations into acoustic power and of acoustic power back into fluid oscillations makes the shear layer associated to the jet a self-sustained primary source of jet noise [21].

It is possible to evaluate the frequencies of the main modes of such self-sustained oscillations exploiting the following Rossiter's equation:

$$f = \left(\frac{U_j}{L}\right) \frac{(n - \beta)}{\frac{U_j}{U_{adv}} + \frac{M_j}{\sqrt{\left(1 + \frac{(\gamma - 1)M_j^2}{2}\right)}}} \quad (2.10)$$

here the subscripts j and adv stand for *jet* and *advection*, respectively; U is velocity; L is the characteristic distance between the shear layer impingement point and the jet outlet; n is a characteristic integer number for each mode of oscillation ($n = 1$ for first mode, $n = 2$ for second mode, etc.); β is a phase lag constant; M is the Mach number; and γ is the ratio of the specific heats.

For high-speed flows it is found $\beta = 0.25$ in [22], and $U_{adv}/U_j \in [0.6 \div 0.89]$ in [23].

In the present analysis the jet Mach numbers have been estimated by considering the air expanding isentropically from the pressurized-line value to the value within the compression tube just before the hot-wire test (i.e. the test total pressure); both these values were measured during the hot-wire test campaign. From the Mach numbers the jet velocities have been derived through the velocity of sound, which, in turn, is calculated with the temperature value within the compression tube before the test (i.e. the test total temperature).

This approximated estimation implies an uncertainty on the calculated jet-core velocities. This is tentatively put at $\pm 15\%$, and also accounts for the reading-error of the pressurized-line gauge, and the error in the temperature calculations. This uncertainty is transferred to the Rossiter's frequency values, and adds up to the uncertainty due to the eddies advection velocity. In the following plots both uncertainties are shown as vertical bands differently colored: the uncertainty from the eddies advection velocity value is colored in light-blue, while the uncertainty from the jet-core velocity value is colored in light-green. They both refer to the frequency of the first oscillation mode.

Figures 2.23 and 2.22 show the spectra of the measured mass-flow fluctuations within the range as for the RMS calculations ($[700 \div 20000]Hz$), and with the amplitude normalized by its maximum value. Both Figures feature the highest peaks below 1500 Hz, and these peaks are of the single-frequency type. Note, as well, how the number of such peaks increases with the freestream Mach number through the whole frequency spectrum.

It is evident at once that all the highest peaks in Fig. 2.23 fall within the bands of the first-mode self-oscillation frequency as from Eq. 2.10. The same is in Fig. 2.22, except for the highest peak that, however, falls very close to the rightmost edge of the uncertainty band.

These frequency correspondences may support the hypothesis that at least one of the peaks measured by the hot-wire in the freestream of the test section may be generated by the shear layer impingement onto the resting plate.

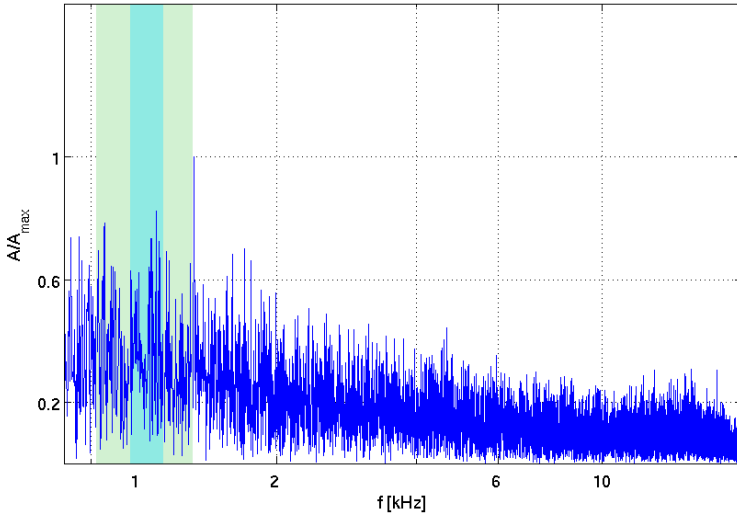


Figure 2.22: *Spectrum of measured mass-flow fluctuations with estimated range of first-mode self-sustained-oscillations frequency, $M=1.7$ ($\frac{U_c}{U_j} \in [0.6 \div 0.89]$ $\Delta U_j = \pm 15\%$)*

In conclusion, the estimations presented in this paragraph do not want to be an exhaustive analysis of the noise generation by the jet impinging on the resting plate. This would be a rather complicated problem and was not in the objectives of the present work. These estimations, instead, are here presented with the only purpose of giving some support to the possibility that the absence of any noise/turbulence-suppression devices within the compression tube can be one of the causes of the freestream fluctuations as measured within the test section. Whence, one may also infer that this lack of suppressors may be the cause of the difference in fluctuations intensity found in Fig. 2.20.

2.3 Conclusions

The multiple-Mach-number supersonic wind tunnel designed at the von Karman Institute has been successfully started in a Mach range going from 1.6 to 2.3, thus proving the effectiveness of its design. The shift from one Mach number to another during the qualification campaign resulted rather quick, about ten minutes from the end of one test to the beginning of the next one, thus allowing as many as twelve tests per day.

The suction-slot lip design resulted correct from the numerical computa-

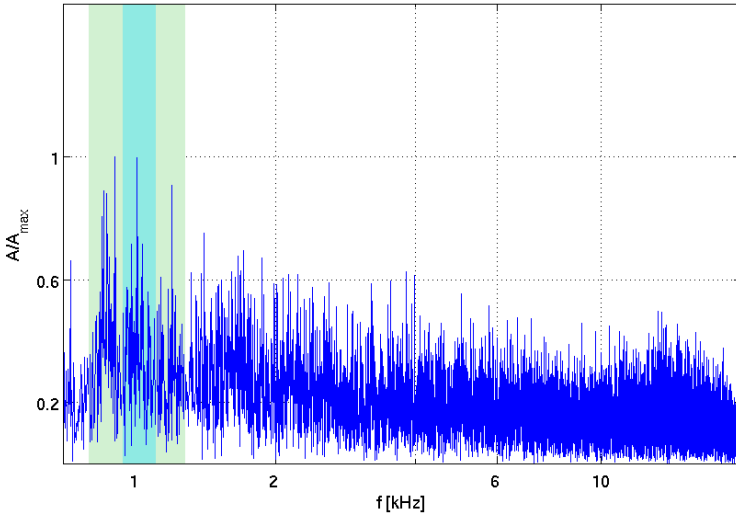


Figure 2.23: *Spectrum of measured mass-flow fluctuations with estimated range of first-mode self-sustained-oscillations frequency, $M=1.9$ ($\frac{U_c}{U_j} \in [0.6 \div 0.89]$ $\Delta U_j = \pm 15\%$)*

tions performed on the whole wind tunnel flow field. In fact, no recirculation bubble has been found for the lowest as well as for the highest Mach numbers tested, thus encompassing all the possible divergent angles. The measurements of the test campaign to be discussed in the next Chapter 3 gave further confirmations on the state of the boundary layer along the ramps.

From the point of view of the freestream noise, the hot-wire measurements gave mass-flow fluctuations intensity comparable to those of non-quiet supersonic wind tunnel, thus larger than those of quiet wind tunnels. It must be said, however, that the realization of a fully quiet wind tunnel has been so far accomplished as a sum of decade-long improvements and refinements of a base design. And yet very few facilities in the world can be labelled as quiet, especially for high flow velocities [24]. Therefore, there should be no surprise that this brand new supersonic facility does not feature very low freestream disturbance levels from its very first operations. And especially so considering the specific features of the wind tunnels used as comparison in Fig. 2.20. In fact, they have their settling chambers equipped with specific devices to suppress freestream turbulence and/or acoustic noise, while the present wind tunnel has none. And the analysis in paragraph 2.2.2.1 gave some support to the possibility that some peaks in the measured freestream fluctuation may indeed originate from phenomena generated and evolving within the compression tube.

It must be noted that the absence of any turbulence/noise suppressor within the compression tube is due essentially to its dual purpose as a supersonic test section and as a transonic test section for turbo-machinery airfoils. The modifications to the general facility layout needed to implement any of these suppressors would affect the compression tube itself, its air inlet from the high-pressure supply system, and its outlet to the test section. But mostly the functioning of the piston would be affected. Therefore, these changes could heavily conflict with the actual primary purpose of the wind tunnel that consists in turbo-machinery air-foil testing.

However, it must be emphasized that the very stringent quietness standards that have been tried to achieve with the present design, apply for wind tunnel intended to reproduce *natural* boundary layer transition to turbulence. They become less stringent if the tests are for *induced* boundary layer transition to turbulence. In fact it is now accepted [10, 25] that disturbances purposely introduced into the laminar boundary layer (as those produced by a big single roughness) have such a high intensity to outplay the effect of the disturbances induced by the facility, thus reducing to a bearable level their bias effect on the experimental results.

Chapter 3

Effects of a single roughness element on a supersonic laminar boundary layer for different wall temperatures

The goal of the experimental campaign here presented is the study of the effects of a single roughness element on a supersonic laminar boundary layer at different wall temperatures. Tests were performed at Mach numbers 2.3 and 1.6 in the multiple-Mach-number wind tunnel whose qualification has been presented in the preceding Chapter. Two roughness heights were tested, 0.1 mm and 1 mm, and the length and width of the roughness were 2 mm for both heights. Five wall temperatures were tested.

Two types of sensors have been used for the measurements: thin-films and piezoelectric pressure transducers (PCBs). Thin-films were used to measure the wall temperature time evolution during the tests, and the PCBs to measure the pressure fluctuations at the wall. Both types of sensors were hosted into inserts flush mounted onto the bottom ramp of the supersonic wind tunnel (Figs. 3.1 and 3.2). Figure 3.3 shows the whole wind tunnel divergent, and the yellow line highlights the position of the instrumented inserts; they replaced the line of pressure sensors used to qualify the wind tunnel. Thin-films and piezoelectric pressure transducers (PCBs) will be discussed in detail in the following Sub-sections 3.1 and 3.2. The five pressure taps at the end of the top ramp were kept and provided the verification of the test conditions. Furthermore, the time evolution of their signals was used to evaluate the duration of each test as described in Sub-section 2.1.

Thin-films signals were low-pass- and high-pass-filtered before being acquired. The low passed signals (≤ 750 Hz) were used for the measurements of the flow mean temperature at the wall, from which the convective heat flux was numerically computed. This computation was repeated for different wall temperatures, and all the results were used to calculate the adiabatic wall temperature trends along the insert. These trends were used to evaluate the state of the boundary layer downstream of the roughness by comparison with reference analytical trends. The high-passed signals were used



Figure 3.1: *The thin-films insert on the bottom ramp of the supersonic wind tunnel divergent*

to analyze the temperature fluctuations from 100 Hz up to the maximum frequency allowed by the thin-films electronics (60 kHz).

The PCBs signals were also high-passed with the same filter as for the thin-films. Because of their remarkably high frequency response, they were used to analyze the pressure fluctuations. This analysis complemented that of the temperature fluctuations in detailing the effects of the roughness on the boundary layer flow. The wall temperature was not varied for the PCBs measurements.

Results of the measurements made with thin-films and PCBs are presented and commented from Section 3.4 to Section 3.8. The numerical computations that provided benchmarks for the measurements results are presented in Sub-section 3.3. They provided as well insights on the flow along the instrumented insert that were not possible to the flush-mounted instruments.



Figure 3.2: *The PCBs insert on the bottom ramp of the supersonic wind tunnel divergent*



Figure 3.3: *General view of the supersonic wind tunnel divergent with the inserts location highlighted*

3.1 Wall-temperature high-frequency measurement system

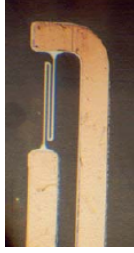


Figure 3.4: *A magnified view of a thin-film sensor*

The thin-film (Fig. 3.4) is a thin serpentine of nickel fed with constant current by two copper wires. The thermal strain induced by the flow on the serpentine changes its electric resistance, thus the voltage across. Voltage changes, in turn, are recorded and, after the application of a calibration, yield the wall temperature measurement. The measurement provides not only the average temperature but also its fluctuations; in fact the thin-film features a rather good frequency response to the thermal inputs. This is because of the serpentine thinness ($O(10^{-1})\mu m$), that makes the characteristic time response to thermal inputs

$$\tau_{char} = \frac{t_{TF}^2}{\alpha}$$

of the order of 10^{-9} s, and the corresponding frequency response

$$f_{3dB} = \frac{1}{2\pi\tau_{char}}$$

of the order of 10^7 Hz. However, this is the ideal response of the sole sensor and is limited by the practical frequency range of the electronic components of the measurement chain. In the present case the system of thin-films and dedicated electronics was limited to about 60 kHz.

The insert used for the tests (Fig. 3.6) is equipped with sixteen thin-films, each comprised of a single resistance element made in nickel evaporated on a thin Upilex sheet. Each sensor is connected to copper leads (also applied onto the Upilex layer), and, through them, to electrical connections that provide the final link to the acquisition electronics outside of the test section. A two-sided adhesive bonds the Upilex sheet to the metallic insert, which was machined as to have the sheet flush once glued.

The thin-films are arranged on the plate according to the likely flow evolution downstream of the single roughness elements to be tested. This arrangement was designed taking into account turbulent-spot characteristics

in supersonic boundary layers as in [26], and past experience on roughness-induced transition experiments in hypersonic boundary layers [27]. Once found the characteristic spreading angles of both the turbulent spot and the roughness wake, the thin-film arrangement was designed as to cover as much of the expected wake area as allowed by the number of sensors available.

To make tests at different wall temperatures, resistive heaters have been applied to the bottom of the insert to uniformly increase its temperature. The requirements for the heating are high power-density, in order to minimize the heating period, and minimum thickness, to avoid fitting problems into the nozzle ramp. Considering those specifications, *Minco Ther-mofoilTM* heaters were chosen. They consist of a flexible etched-foil resistive heating element, which is laminated between two Polyimide layers. An aluminum backing foil combined with a layer of acrylic pressure-sensitive adhesive allowed a simple application directly to the bottom of the insert. The maximum operating temperature of this heater configuration is 150°C , but the maximum temperature reachable in testing is determined by the Upilex adhesive properties. According to the company specifications, they should not experience a dramatic degradation if 120°C are exceeded. However, past experience with Upilex sheet has proven that the glue can already form bubbles below the sheet if heated to temperatures much lower than 120°C . These bubbles resulted in deformations of the flat surface, which, in turn, affected the boundary layer flow. In the end, to avoid such bubbles the heaters power was kept always as low as not to give a wall temperature larger than 50°C . Four heaters have been applied to the bottom of the plate, one big quadratic element on the front, and three rectangular ones on the aft covering as much as possible the surface around six screw holes (Fig. 3.5).

Finally, the effectiveness of the heaters layout was verified by infrared thermography which showed the uniformity of the wall temperature on a similar thin-films insert used as a flat plate in hypersonic experiments (Fig. 3.7). This figure shows, that, due to the high thermal conductivity of the steel, the heaters can produce an acceptably uniform surface temperature distribution. Note also how the metallic parts on the insert surface seem to be colder. This is due to their poor emission characteristics in the infrared spectrum.

3.1.1 Thin-films calibration

The relation between the temperature of the thin-film and its induced electric-resistance change has to be established for each sensor by a calibration procedure. This calibration has consisted in putting the whole insert into an oven, which allowed an accurate setting of its internal temperature, and in recording the electric-resistance of each thin-film at six different oven temperatures. Since each of these temperatures was kept constant for one hour, thermal equilibrium inside the oven was ensured, and the thin-films insert temperature became the same as the selected oven temperature. This then

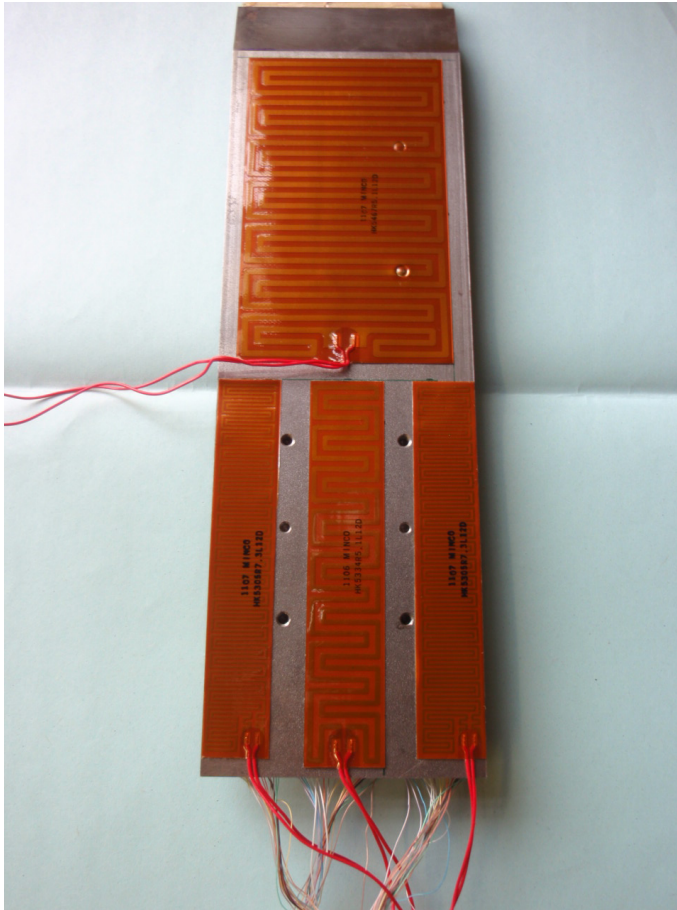


Figure 3.5: *The arrangement of the electric heaters on the bottom of the thin-films insert*

was accurately measured by a thermocouple placed on the insert surface. The right plot in Fig. 3.8 shows the results of this calibration for some of the sixteen thin-films used. There appears how the electric resistance of the thin-film varies practically linearly with the temperature; in fact, the R^2 of the linear approximation resulted between 0.999 and 0.9999.

Also the relation between electric-resistance change and voltage change imparted by the electronics of the thin-films had to be calibrated. This calibration consisted in applying a given electric resistance in input to each channel of the two electronic boxes used for the experiments, and in recording the output voltage. These electronic boxes can either operate in absolute or relative mode. The relative mode provides only the temperature change



Figure 3.6: *The thin-films insert embedded in the lower ramp of the supersonic wind tunnel*



Figure 3.7: *Infrared image of the thin-films insert top heated up by Joule heaters glued on its bottom*

compared to an initial value, and for this reason it is used to measure fluctuations. The absolute mode, instead, provides the mean-temperature time evolution, thus it is used to measure the wall temperature just before the test, and to calculate the convective heat flux during the test. Because of this two-mode character of the electronic boxes, distinct calibrations had to be made for each operation mode. Eleven different electric-resistance values were input to each channel of the boxes for the absolute mode, and ten for the relative mode. The left plot in Fig. 3.8 shows typical calibration trends

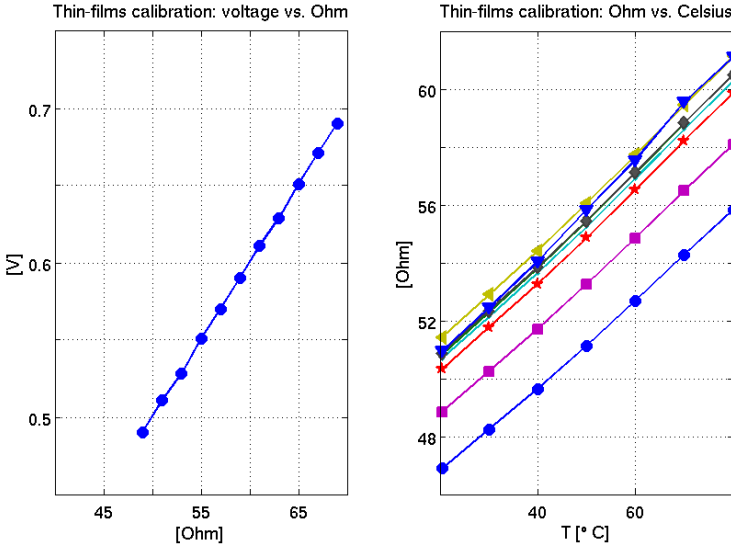


Figure 3.8: Example of thin-film calibrations: voltage vs. electric resistance, electric resistance vs. temperature

for both modes, and how they result practically linear. For these calibrations the R^2 of the linear approximation was better for the relative mode than for the absolute mode: between 0.999 and 0.99999 for the former and between 0.999 and 0.9998 for the latter.

In practice, the linear relations above presented were reversed and used in sequence to extract a temperature value from the thin-film final voltage signal.

3.1.2 Sensitivity and uncertainty analysis of the heat-flux measurements

The wall temperature values obtained as explained above were used as inputs for convective heat flux calculations. The calculations were performed through the numerical solution of the 1-D heat-conduction equation normal to the wall. The heat is considered to be conducted through the Upilex sheet hosting the thin-films and the metal below it. This is because the glue between the two is usually assimilated to the Upilex sheet from the point of view of the thermal properties [28]. The assumption of semi-infinite slab is taken, and the temperature of the metal far from the surface is assumed constant and equal to the temperature of the wall just before the blow down. This semi-infinite-slab assumption is supported by the blow-down character of the wind tunnel that hinders the temperature equilibrium of massive

| PARAMETER | UNCERTAINTY | q_w | SENSITIVITY |
|-----------------------------|-------------|-------|-------------|
| [-] | [-] | | S_i [%] |
| $(\sqrt{\rho Ck})_{Upilex}$ | 5% | | 0.13 |
| $(\sqrt{\rho Ck})_{metal}$ | 5% | | 0.19 |
| T_w | 0.5 deg. | | 0.0 |
| t | 2.3% | | -1.2% |

Table 3.1: Sensitivities of the heat flux measurements to the uncertainties of four parameters

metal parts to be reached within the short test time.

The parameters playing a role in the heat-flux computation were: the thermal properties of the Upilex sheet, $(\sqrt{\rho Ck})_{Upilex}$; the thermal properties of the metal insert, $(\sqrt{\rho Ck})_{metal}$; the accuracy of the temperature measurements; and the accuracy of the measurement of the Upilex (plus glue) sheet thickness (t). Uncertainties in the values of these parameters sum up and cause the overall uncertainty on the final value of the heat flux, thus they had to be quantified. This quantification consisted in the analysis of the sensitivity of the heat-flux values to each of these parameters.

The sensitivity (S_i) of the heat flux value on a single parameter ($\theta_i, i = 1, 2, 3, 4$) is considered to be the ratio between the change in the heat flux and the change in the parameter, while the other three are kept constant:

$$S_i = \frac{\Delta q_w \%}{\Delta \theta_i \%} \quad (3.1)$$

Hence, the sensitivity analysis consisted in: varying the values of each parameter in input to the code used for the solution of the 1-D heat conduction equation, $(\theta_i)_{mod}$, keeping all the other parameters constant; running the code for both the lowest and the highest wall temperature tested; recording the heat flux in output, $(q_w)_{mod}$; and calculating equation 3.1 with $\Delta q_w = (q_w)_{mod} - q_w$ and $\Delta \theta_i = (\theta_i)_{mod} - \theta_i$. In so doing more than one sensitivity was found, and, as a conservative approach, the highest was taken into account. The uncertainties on the thermal properties of the Upilex and of the metal were taken both to be 5%, that is a conservative 1% more than in [29]; the uncertainty on the thin-film temperature measurement was taken to be 0.5 degrees, again more conservative than in [29]; and the uncertainty on the Upilex sheet thickness was taken to be 2.3%. The latter uncertainty was calculated, for want of a better method, as the difference between the measured thickness and the value reported on the Upilex specifications sheet.

Table 3.1 shows the results of the sensitivity analysis. The highest sensitivity is to the thickness of the Upilex sheet, and is negative. This means that a decrease in heat-flux corresponds to an increase in Upilex thickness

and vice versa. This is a sound conclusion as the heat flux is inversely proportional to the thickness of the slab through which it is calculated.

The overall uncertainty on the heat flux values was eventually calculated from the changes induced by each of the four parameters with the following formula:

$$(\Delta \dot{q}_w)\% = \frac{100}{\dot{q}_w} \cdot \sqrt{(\Delta \dot{q}_w)_{U_{pilex}}^2 + (\Delta \dot{q}_w)_{metal}^2 + (\Delta \dot{q}_w)_{T_w}^2 + (\Delta \dot{q}_w)_t^2} \quad (3.2)$$

Again, as for the sensitivity only the highest value from the computations was retained, and this ended up to be 5%.

However, since these uncertainty calculations were made just for few sensors and, in general, other hardly quantifiable factors can affect thin-films measurements, a more conservative value of 7% was considered. This was applied to the measurements to be shown in the following of the chapter, and for the calculations based on them. Consequently, error bars corresponding to this uncertainty level appear in the plots when their range is larger than the vertical dimension of the symbol used.

3.2 Wall-pressure high-frequency measurement system

The high frequency pressure fluctuations were sensed using PCB 132A31 piezoelectric pressure transducers. The characteristics of this PCB are listed in Table 3.2. Piezoelectric pressure transducers rely on the piezoelectric property of some solids to measure pressure fluctuations. The piezoelectric property consists in generating electricity under mechanical stress. The mechanical stress acts at microscopic level on the crystal structure of the ceramic material by altering the spatial symmetry among its cations and anions [e.g. 30]. In so doing it polarizes the crystal, and a voltage difference is set across the crystal external surfaces [e.g., 31]. The electric effect of this mechanical stress is ephemeral and the produced charges eventually annihilate [32]. This is why these sensors are best used to measure fluctuations rather than steady quantities. Commonly, the piezoelectric material is placed inside the sensor below and parallel to a flexible membrane. In this way the piezoelectric material can feel pressure fluctuations from outside through this membrane. Since the piezoelectric material is very stiff, even feeble stresses yield a sensible electric output, so that sensors made with this kind of crystals can have a remarkable dynamic amplitude range.

The transducers used for the present test campaign were operated with two PCB 482C05 signal conditioners. Each conditioner has four channels and serves as a power supply for the internal sensor electronics. The PCB output was amplified with an eight-channel amplifier. The gain is 100 and the nominal upper cut-off frequency is 1 MHz. The frequency response of this amplifier was tested with an artificial sinusoidal input. The results of

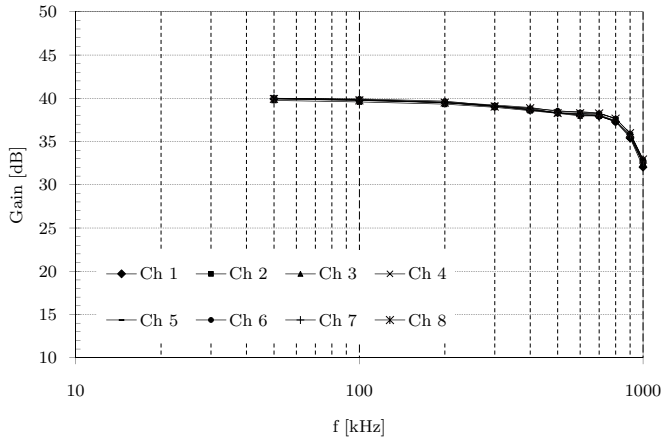


Figure 3.9: *PCB amplifier frequency response*

such tests are presented in Fig. 3.9, where it appears how all the channels perform practically the same in terms of gain versus frequency.

The amplifier output was digitized at a sampling frequency of 1 MHz by the data acquisition system.

| | |
|---|-------------------------------|
| Measurement range | 345 kPa |
| Sensitivity ($\pm 30\%$) | 20.3 mV/kPa |
| Maximum pressure (dynamic) | 5516 kPa |
| Resolution | 7 Pa |
| Resonant frequency | $\geq 1000\text{kHz}$ |
| Rise time (incident) | $\leq 3 \mu\text{s}$ |
| Low frequency response (-5%) | 11 kHz |
| Operating temperature range | $(-18... + 79)^\circ\text{C}$ |
| Discharge time constant (@ 20°C) | $\geq 45\mu\text{s}$ |
| Diameter | $\varnothing 3.18 \text{ mm}$ |
| Length | 7.6 mm |
| Weight | 0.52 g |

Table 3.2: *Specifications of PCB 132A31 piezoelectric pressure transducers*

3.2.1 PCB calibration setup

As for the thin-films, the voltage output of the piezoelectric sensors had to be related to a specific pressure value by a calibration. However, unlike for the thin-films, this time no steady pressure value could have been input to the sensor because of its characteristics discussed above. Therefore, to

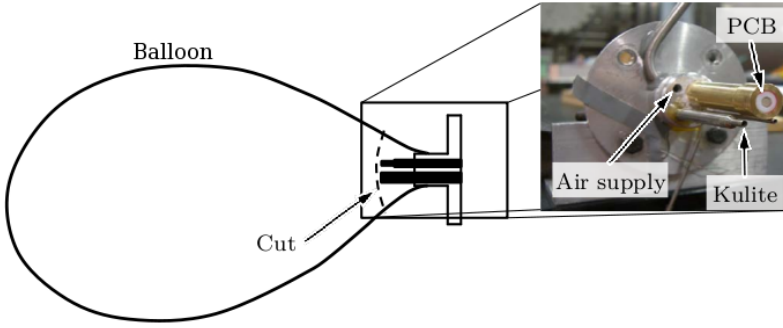


Figure 3.10: *PCB balloon calibration setup*

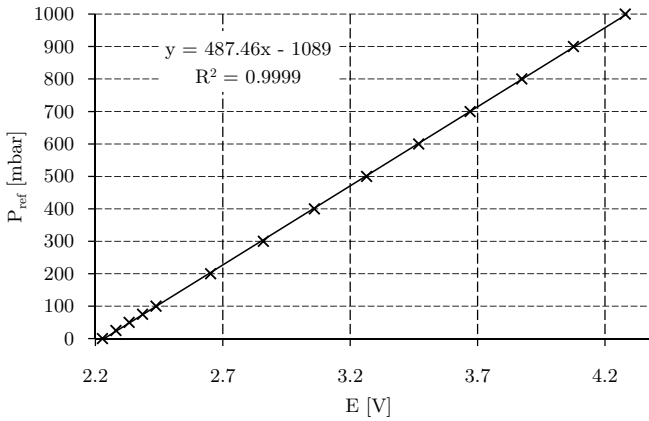


Figure 3.11: *Static calibration curve of the Kulite used as reference in the balloon-calibration procedure*

simulate as much as possible the rise of a pressure fluctuation, a sudden pressure change was chosen as calibration input.

The calibration input was achieved by applying the “balloon technique” to each transducer. This technique consisted in placing the PCB and a fast reference transducer inside a rubber balloon (Fig. 3.10). This balloon was then inflated with pressurized air and sealed, as to have both sensors at a pressure higher than ambient. At this point the balloon was cut with a razor blade and burst. This burst made both sensors sense a sudden return to ambient pressure that wanted to simulate a peak signal due to a pressure fluctuation.

The fast reference transducer was a Kulite XCQ-062. Figure 3.11 shows its static calibration.

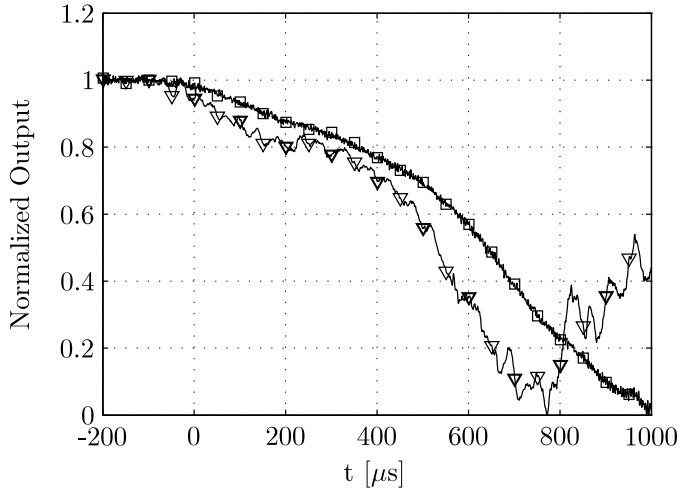


Figure 3.12: Normalized raw output voltages of PCB (∇) and reference Kulite (\square)

3.2.2 Computation of the pressure sensitivity from the balloon calibration

Since the PCBs cannot sense a steady pressure value but only fluctuations, i.e. rapid, feeble pressure changes, its calibration should provide a relation between the change in the pressure input and the change in the voltage output. This reduces to finding the sensitivity of the PCB, S . The sensitivity of an instrument is defined as the ratio between the indicated output and the given change in the input that generated it [e.g. 7]. Therefore, the sensitivity corresponds to the slope of the calibration curve in the $(x,y)=(\text{input}, \text{output})$ plane.

The Kulite had a known pressure sensitivity that was used to find the pressure sensitivity of each PCB. An example of the normalized raw output voltages by the Kulite and the PCB is shown in Fig. 3.12. This figure shows the signals for a time intervals starting 200 μs and ending 1000 μs after the balloon burst. Both transducers react very rapidly to the change of pressure, but, unlike the Kulite, the PCB tries to return to its initial value if the pressure transient is not sufficiently fast. This is seen in the increase of just the PCB output voltage at about 800 μs .

As a first attempt to obtain the pressure sensitivity of the PCB, a direct comparison of the initial slopes of the two signals was performed. Knowing the change of output voltage over time and the pressure sensitivity of the reference sensor, the actual pressure change can be calculated. This in turn can be used to compute the PCB sensitivity to pressure as

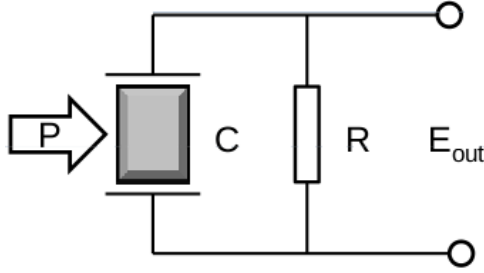


Figure 3.13: *Electronic model of a first-order high-pass filter*

$$S_{PCB} = S_{Kulite} \frac{\partial E_{PCB}}{\partial t} \frac{\partial t}{\partial E_{Kulite}} \quad (3.3)$$

However, since the pressure change was not fast enough, this comparison yielded pressure sensitivities about one order of magnitude lower than the manufacturer values. This difference was considered unacceptably high and led to discard these calculations, and to introduce a temporal compensation of the PCB output. The purpose of this compensation is to allow a more correct comparison between the Kulite and the PCB signals, despite their differences in properties, notably in high-pass frequency threshold. Such compensation was implemented in the frequency domain. In fact, due to its internal electronics, the PCB can be assimilated to a first-order high-pass filter, consisting of a capacitor and a resistance [32] (Fig. 3.13). As such, the PCB cuts to (practically) zero the amplitude of all the pressure fluctuations, whose frequencies are below a given threshold (i.e. 11 kHz). In the frequency domain its transfer function is:

$$H(j\omega) = \frac{j\omega\tau}{1 + j\omega\tau} \quad (3.4)$$

where the time constant is equal to the product of resistance R and capacitance C , $\tau = RC$. For the PCB these values are known from the manufacturer specifications, and yield a time constant $\tau \geq 45\mu s$ [32]. Now, this transfer function can be modeled numerically in Matlab, and this allowed the temporal compensation to be performed in the frequency domain. The compensation consisted in applying the inverse of the transfer function to the PCB signal as to invert the effect of the high-pass filter: instead of lowering to zero the amplitude of low-frequency signals, it amplifies it (Fig. 3.14) [6].

The best compensations were obtained by limiting the amplification at very low frequencies. This was done by adding in series to the inverted high-pass filter another high-pass filter with a much larger time constant τ_2 . In conclusions, the PCB compensated output is:

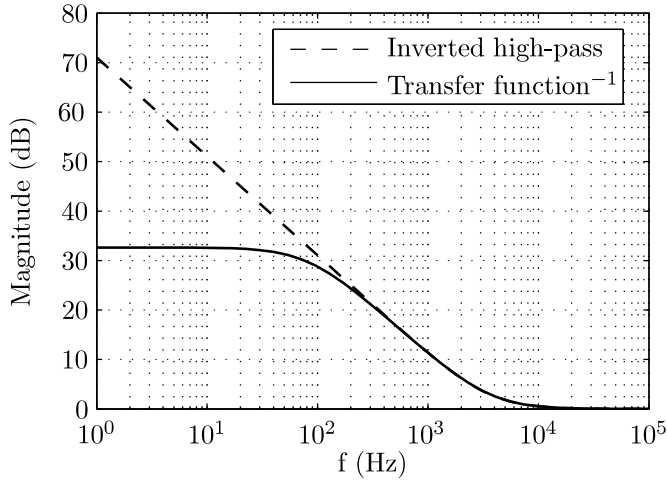


Figure 3.14: Frequency response (magnitude) of an inverted high-pass filter and the PCB's transfer function

$$\hat{E}_{out} = \frac{1 + j\omega\tau}{j\omega\tau} \cdot \frac{j\omega\tau_2}{1 + j\omega\tau_2} \cdot \hat{E}_{in} \quad (3.5)$$

where \hat{E}_{out} is the Fourier transform of the PCB compensated output, and \hat{E}_{in} is the Fourier transform of the raw PCB output voltage to be compensated.

As the PCB signals and the Kulite signals could be compared meaningfully, the PCB sensitivity was found by trial and error, i.e. varying it manually until a good agreement with the Kulite measurements was achieved. As matching criterion the correlation factor of both signals was used. For each transducer five balloon calibrations were carried out. The resulting data have been used for an estimation of the random calibration error based on the standard deviation. That is, the standard deviation of the difference between the Kulite signal and the PCB compensated signal was computed at each time step after the rupture of the balloon, for each of the five tests. In so doing, the $\pm 2\sigma$ envelope of the final PCB output approximates the 95% confidence interval of the calibration. Finally, this interval can also be used to estimate the uncertainty of the PCB's pressure sensitivity.

Figures 3.15a and 3.15b show two examples of corrected pressure measurements. Figure 3.15a shows the PCB compensated signal (called “correct” in the legend) including the uncertainty estimate. It is seen that the 95% confidence interval might be approximated by a $\pm 15\%$ uncertainty of the PCB's pressure sensitivity. As a proof-check, Fig. 3.15b shows that the inverted transfer function applied to the Kulite raw signal yields the raw, i.e. not

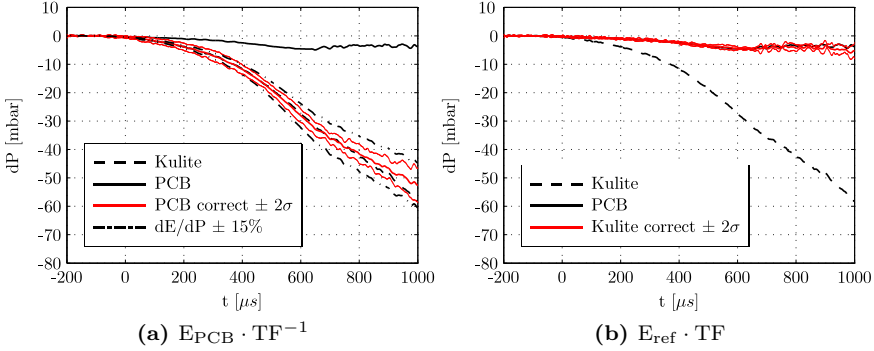


Figure 3.15: Example of signal reconstruction using the PCB transfer function

compensated, PCB output. It is seen that, in general, the transfer function allows the reconstruction of the majority of the signal.

In the end, the PCB sensitivities resulting from the balloon calibration are listed in Table 3.3 along with the manufacturer sensitivities.

| LOCATION | SERIAL NUMBER | S_{specs} [V/mbar] | S_{cal} [V/mbar] |
|----------|---------------|-------------------------|-----------------------|
| 1 | SN5273 | 0.259 | 0.220 |
| 2 | SN5275 | 0.257 | 0.225 |
| 3 | SN5274 | 0.245 | 0.205 |
| 4 | SN5272 | 0.241 | 0.225 |
| 5 | SN5271 | 0.253 | 0.185 |
| 6 | SN5277 | 0.220 | 0.145 |
| 7 | SN5270 | 0.179 | 0.180 |
| 8 | SN5276 | 0.234 | 0.175 |

Table 3.3: PCB transducer pressure sensitivities from manufacturer (S_{specs}) and from present evaluation (S_{cal}), including $100\times$ amplification

3.3 Boundary layer state at the roughness location

Numerical computations of the two-dimensional flow field in the supersonic wind tunnel have been performed to support the measurements. The same mesh and commercial package as for the wind-tunnel qualification test campaign presented in Chapter 2 were used; thus, computations were made for

| MACH NUMBER [-] | k [mm] | Re_k [-] |
|--------------------|-------------|-------------------------------|
| 2.3 | 0.1 | [570 ÷ 620] |
| | 1 | [5.1 ÷ 5.3] · 10 ⁴ |
| 1.6 | 1 | [5.4 ÷ 5.6] · 10 ⁴ |

Table 3.4: Range of Re_k values for the two Mach numbers and two roughness heights (k) tested

the entire compression tube (Fig. 3.16). The pressure and temperature values measured by the sensors on the wind tunnel during the tests were used as boundary conditions.

Numerical outputs were used to calculate the unit Reynolds number for each Mach number tested, and, more importantly to calculate the Re_k at the roughness location. This is a Reynolds number calculated with ρ , μ , and U evaluated at the roughness height (k):

$$Re_k = \frac{\rho_k U_k k}{\mu_k} \quad (3.6)$$

This is found to be an useful parameter to define the extent of the roughness effects on a supersonic boundary layer. For instance, Morrisette was capable of singling out the effective height of a single roughness element immersed in supersonic and hypersonic boundary layers developing along flat plate or cones by plotting Re_k vs. $Re_{x,k}$ (i.e. the Reynolds number based on the roughness position from the leading edge of the tests article). He defines "effective" that roughness height above which the turbulence onset in the roughness wake does not move anymore upstream. Furthermore, by plotting $Re_{k,eff} - Re_{x,k}$ versus the edge Mach number, i.e., the freestream Mach number, he also singled out the effect of the Mach number on the distance between the roughness and the point of turbulence onset in its wake [5, and references therein]. Von Doenhoff and Braslow [33, and reference therein], instead, associating the Re_k to the roughness diameter-to-height ratio were capable of setting critical values of roughness height below which the roughness has no sensible effect on transition to turbulence. Specifically, they found that as $D/k > 10$, the data appears to asymptote to $Re_k \simeq 100$, thus concluding with a "large-D criterion" of $Re_k < 100$ for negligible impact on transition.

Table 3.4 gives the ranges of Re_k for the different test cases of the present tests campaign. The ranges account for the slight variations of total test conditions, and, more importantly, of the wall temperature. These values are found higher than expected, and the reason is given in the following Sub-section 3.3.1.

Numerical computations were also used to check the validity of the ana-



Figure 3.16: *CFD computation of the velocity field throughout the whole compression-tube (2D, only the upper half is resolved)*

lytical trends used as benchmark for the adiabatic wall temperature measurements to be presented in Section 3.5. This was done by running some simulations with the adiabatic-wall boundary condition, while the boundary conditions on pressure and temperature were still from the measurements. This check is presented and commented in Section 3.5.

3.3.1 Combined effect of favorable pressure gradient and wall temperature on a supersonic boundary-layer profile

Numerical results from the simulations of the tests highlighted a particular characteristic of the velocity profile. This characteristic is a bulge at a certain distance from the wall, wherein the velocity within the boundary layer results larger than in the freestream (first plot from the left in Fig. 3.17). It is specific to a laminar boundary layer that develops along a hot wall and is subjected to a strong-enough favorable pressure gradient.

This peculiar characteristic is due to the interaction between the density and the viscosity gradients induced by the hot wall condition [11]. The hot-wall condition means that the wall heats the flow instead of being heated by it. This implies that temperature increases in going from the freestream to the wall. Then, since the pressure is constant normally to the wall through the (thermal) boundary layer, this temperature gradient yields as well a density gradient along the same direction, but of opposite sign. That is, air becomes lighter and lighter as the distance from the wall decreases. On the other hand, since dynamic viscosity is directly proportional to temperature, the dynamic viscosity increases as the distance from the wall decreases. And so does the viscous drag. It happens that, within a certain height from the wall, the effect of the density gradient can take over the effect of the viscosity gradient. This take over forms a layer of air lighter than in the freestream, whose viscosity is not yet so high, and that is still acted upon by the same favorable streamwise pressure gradient as the freestream. Hence, the flow velocities within this layer become larger than the freestream value, and the bulge in the velocity profile is formed. Below this layer the viscosity effect becomes predominant, while, above it, the density decrease is not enough

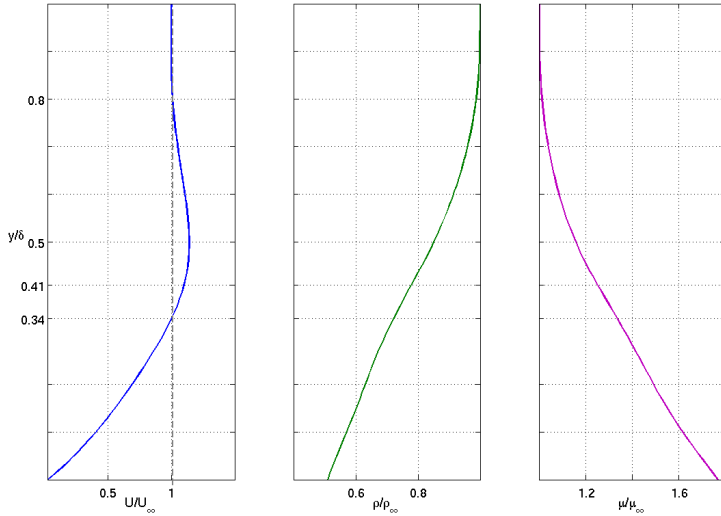


Figure 3.17: *The velocity, density, and dynamic viscosity profiles of the supersonic boundary layer along a wind-tunnel ramp as from CFD computations ($M=2.3$, $T_{wall}=28^\circ C$)*

to make a difference respect to freestream.

This mechanism is found in the present numerical results as from the plots in Fig. 3.17. The first plot from the left shows that the bulge in the velocity profile is between $\sim 80\%$ and 34% of the boundary layer thickness, and its tip is at 50% . The other two plots show that just below 80% density and dynamic viscosity start diverging from their freestream values: density decreases and viscosity increases. At 41% of the boundary layer thickness the density trend features a flex: from this point down it continues to decrease, but at a slower rate with the distance from the wall. The viscosity trend, instead, gets a slightly larger rate of increase at 50% , at the bulge tip. So the bulge features its maximum when viscosity starts increasing faster and faster, while density decreases with a slower rate. Below 34% of the boundary layer thickness, viscosity has increased enough to reestablish its predominance, and the velocity bulge extinguishes.

The presence of this bulge in the velocity profile of the boundary layer along the instrumented ramp, explains the Re_k values larger than expected, i.e. larger than for a Blasius-like, no-pressure-gradient profile in the same freestream conditions. That is, the velocity at the roughness height is larger because it falls within the bulge.



Figure 3.18: *The thin-films insert into the lower ramp of the supersonic wind tunnel*

3.4 Time-averaged heat-fluxes measurements

The heat flux measurements have been taken along and across an instrumented insert flush mounted into the lower ramp of the wind tunnel divergent section (Fig. 3.18). The sensors on this insert were sixteen thin-films arranged as in Fig. 3.19.

3.4.1 Streamwise and spanwise heat-flux trends

The heat-flux values have been calculated from the thin-films signals low-passed at 750 Hz. However, these signals showed a rather high RMS and required a further digital low-pass filtering to reduce dispersion. Many cut-off frequencies were tried and the most effective resulted $1.2/\tau_{test}$ Hz, with τ_{test} the test time, for which Fig. 3.20 shows an RMS reduction of almost $1 \text{ kW}/\text{m}^2$ respect to the original signal. This filter was then used to calculate all the heat fluxes.

The sensors arrangement shown in Fig. 3.19 allowed for heat-flux measurements in the streamwise direction, along the center-line of the ramp (from thin-film 4 to thin-film 29 through thin-films 9, 14, 26), and in the spanwise direction, across the three rows. In the latter case, we were also

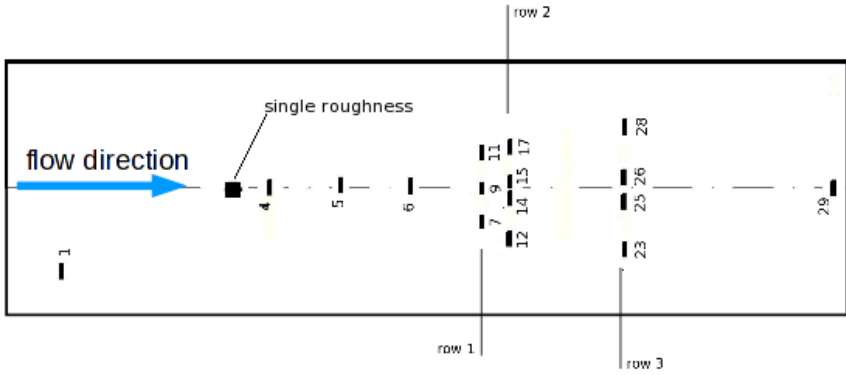


Figure 3.19: *The thin-films layout*

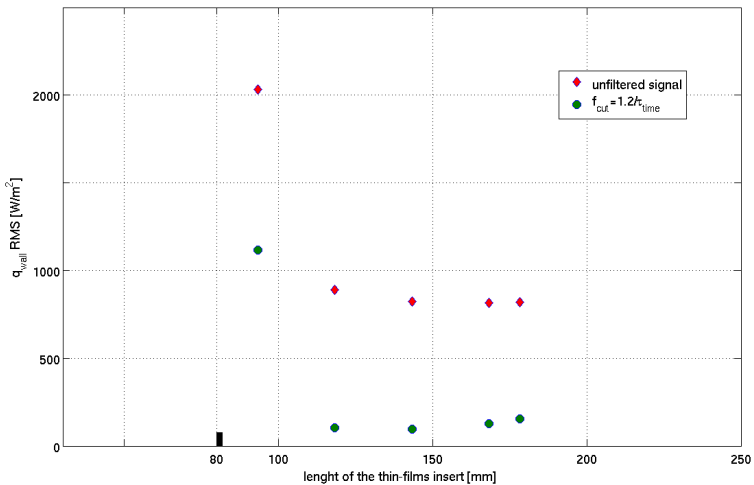


Figure 3.20: *Heat-flux RMS reduction by filtering out the signal above $\frac{1.2}{\tau_{test}}$ Hz ($T_w = 41^\circ\text{C}$, $k=1$ mm)*

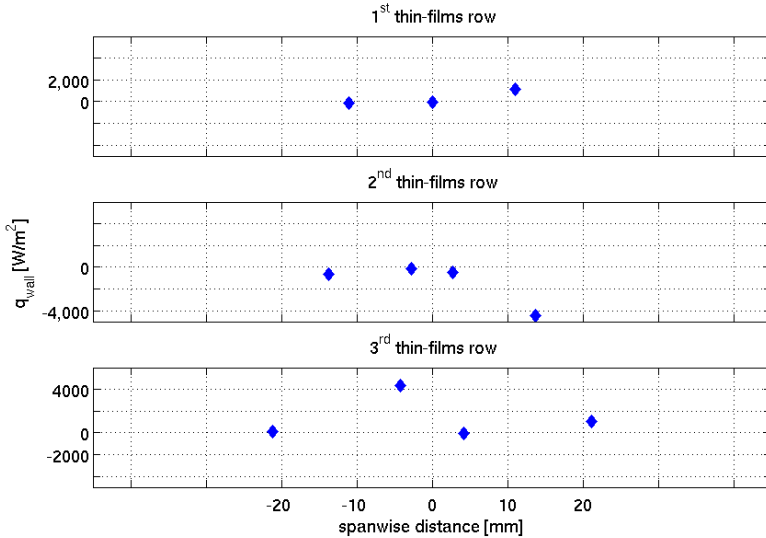


Figure 3.21: Typical heat-flux spanwise evolution on the insert without roughness ($M=2.3$, $T_w=26^\circ\text{C}$)

capable of cross-checking the correct functioning of the sensors by comparing their measurements for the no-roughness configuration, for which one expects rather comparable values from sensors on the same row. Fig. 3.21 shows a typical result of this comparison. Here thin-film 17 on the second row and thin-film 25 on third row give heat flux values very different (about 4 kW/m^2) from those by the other thin-films on the same corresponding rows. Since differences of such magnitude were found in all the tests for the same two thin-films, we concluded that those two sensors were faulty and that their measurements had to be discarded. Measurements from thin-film 1 resulted for most of the tests unreliable as well. The heat fluxes were always far higher than the measurements from the other thin-films for the clean configuration tests, and they showed no repeatability for the same flow and wall conditions. For this reason its measurements have not been included in the following heat flux streamwise trends. This was an unfortunate circumstance because thin-film 1 was the only sensor upstream of the roughness and was meant to provide reference values for the measurements of the thin-films downstream of the roughness.

The same conclusion had to be drawn for thin-film 29, but just for some tests and usually based on its frequency spectrum. In fact, even if the heat fluxes it measured were not dramatically different from those of the preceding thin-films, the comparison between the spectrum of the test signal and that of the noise showed the noise higher than or comparable to the test signal throughout almost the entire frequency spectrum. This comparison

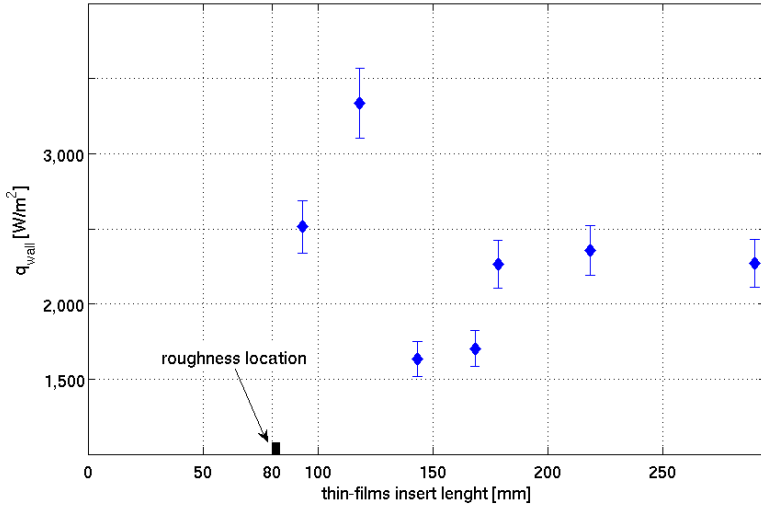


Figure 3.22: *Heat-flux streamwise evolution downstream of the 0.1-mm high single roughness ($M=2.3$, wall heating off)*

is showed in the introduction of Section 3.6. For this reason in some of the plots in the following the measurement from thin-film 29 is absent.

3.4.1.1 Streamwise heat-flux trends

The heat flux trends downstream of the roughness for the two roughness heights and the two Mach numbers tested are presented by Figs. 3.22 to 3.24. In all these three cases the heaters glued below the thin-films insert were off. Note how for the Mach-1.6 case in Fig. 3.24, the heat flux values are negative: this is because the wall is heating the flow. It is the opposite of the two Mach-2.3 cases that feature higher recovery temperatures.

Figures 3.22 and 3.24 show similar trends: the heat-flux reaches its absolute maximum just downstream of the roughness, then it goes to the absolute minimum, and further downstream levels to a constant value kept to the end of the instrumented plate. For Mach 2.3 and $k=0.1$ mm, Fig. 3.22 shows this value clearly intermediate between the absolute maximum and the minimum, while, for Mach 1.6 and $k=1$ mm, Fig. 3.24 shows it closer to the absolute minimum. In Fig. 3.23 the maximum-peak/lowest-dip combination occurs very close to the roughness. Then, the heat flux gains back the highest values and goes back down to a level close to the minimum at the location of the last reliable thin-film. This may suggest that the highest roughness for the highest Mach number tested has an effect on the flow that lasts further downstream than for the smallest roughness at the same Mach

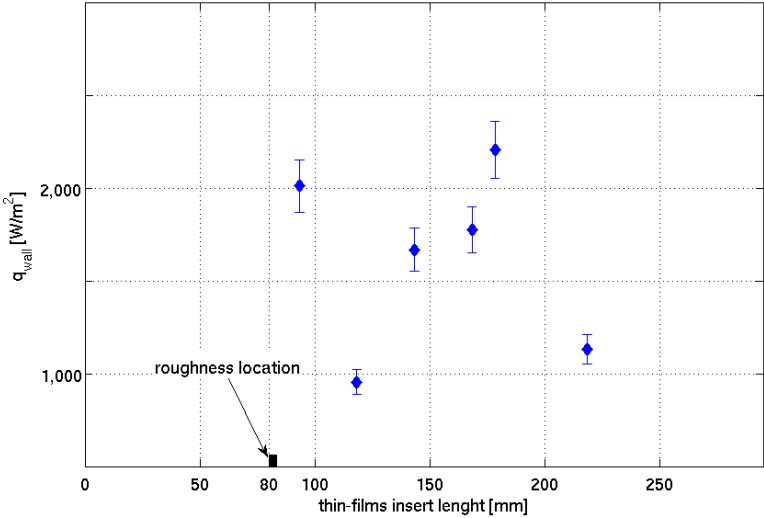


Figure 3.23: Heat-flux streamwise evolution downstream of the 1-mm high single roughness ($M=2.3$, wall heating off)

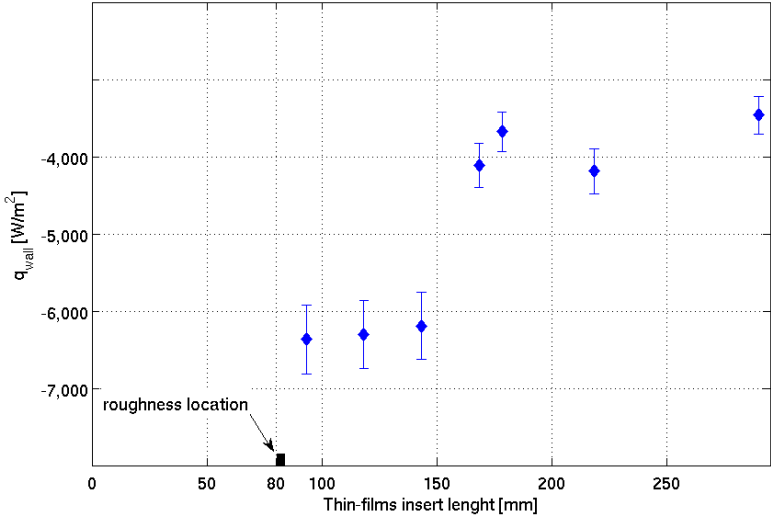


Figure 3.24: Heat-flux streamwise evolution downstream of the 1-mm high single roughness ($M=1.6$, wall heating off)

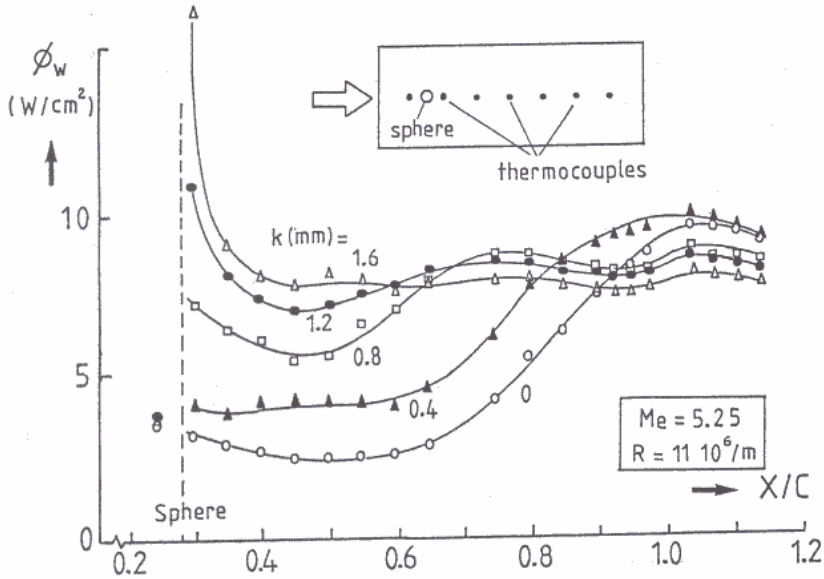


Figure 3.25: Heat-flux streamwise evolutions downstream of a spherical single roughness of varying height [10]

number, and then for the same roughness height but at a lower Mach number. In this last case, for the roughness height of 1 mm and Mach 2.3, the overall variation of heat flux is also less than for the two previous cases in Fig. 3.22 and 3.24. These trends can be compared to the results of ref. [10] for a sensors arrangement rather similar to the one of the present study (Fig. 3.25). Here we see that the heat-flux trend for $k=1.2$ mm is similar to that in Fig. 3.22 with the maximum reached just downstream of the roughness, a dip to the lowest values just downstream, and finally a plateau at a value intermediate between the maximum and the minimum. Then, the trend for $k=1.6$ mm may resemble that of Fig. 3.24, with the absolute maximum reached just downstream of the roughness and the minimum level kept along further downstream. The difference is that in Fig. 3.24 the maximum is sensed by the three thin-films closest to the roughness, while in Fig. 3.25 only by the first. This disagreement, however, may be due to the difference in the sensors spacing between the present case and the reference.

Finally, Fig. 3.26 shows the heat-flux trend for the clean insert configuration (no roughness) at Mach 2.3. This trend can be compared with those of Fig. 3.22 and 3.23 to better appreciate the roughness effect. This comparison makes evident how the heat-flux is much more constant along the insert in the clean configuration than with the roughness.

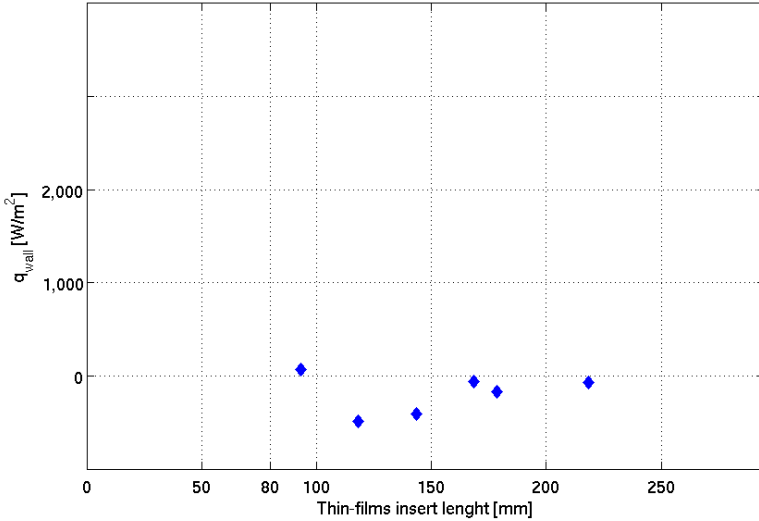


Figure 3.26: *Heat-flux streamwise evolutions along the clean insert ($M=2.3, T_w=26^\circ C$)*

3.4.1.2 Spanwise heat-flux trends

The spanwise heat flux trends across the three rows of thin-films downstream of the roughness without heating are presented by Fig. 3.27 to 3.29. (Consider again Fig. 3.19 for the schematics of the thin-films arrangement.)

The off-centered thin-films of the first two rows always sense a heat flux higher than that sensed by the central thin-film for Mach 2.3 and $k=0.1$ mm (Fig. 3.27). This is not the case for the third row, where the heat flux values from all the thin films are rather similar to each other. They are, then, not so different from the values of the central thin-films on the first and second rows. This may suggest a roughness spanwise effect confined aside from the center-line, and that fades away with the distance from the roughness.

In Fig. 3.28 the highest roughness tested at Mach 2.3, 1 mm, yields a peak heat flux for one of the most external thin-films of the first row (thin-films 7), but, also for those of the third row (thin-films 23 and 28). For the second row, instead, the maximum is on the center-line. Respect to the 0.1-mm-high roughness the difference between the heat fluxes from the external thin-films of the first row is now greater. Therefore, one may conclude that the 1-mm-high roughness sensibly affects the boundary layer flow further downstream than the 0.1-mm-high roughness. This confirms the results from the streamwise trends in Sub-section 3.4.1.1.

Finally, Fig. 3.29 shows that the largest spanwise variation occurs across

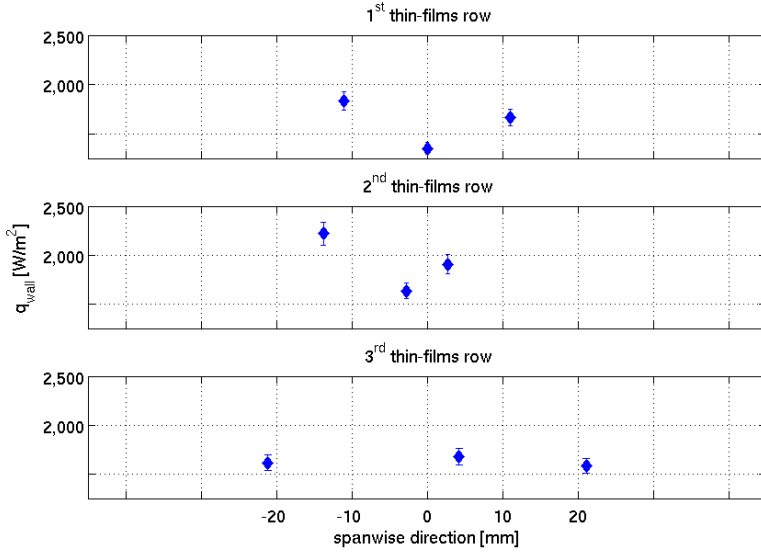


Figure 3.27: Heat-flux spanwise trends ($M=2.3$, $k=0.1$ mm, $T_w=24.5^\circ$ C)

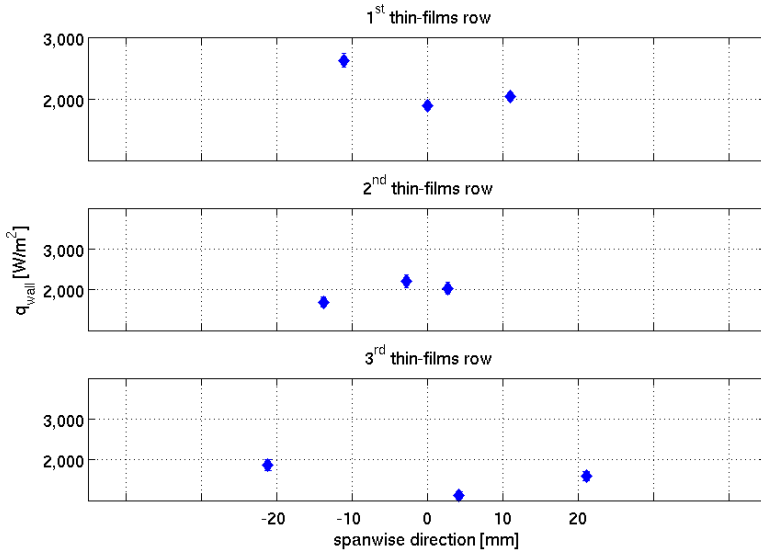


Figure 3.28: Heat-flux spanwise trends ($M=2.3$, $k=1$ mm, $T_w=15^\circ$ C)

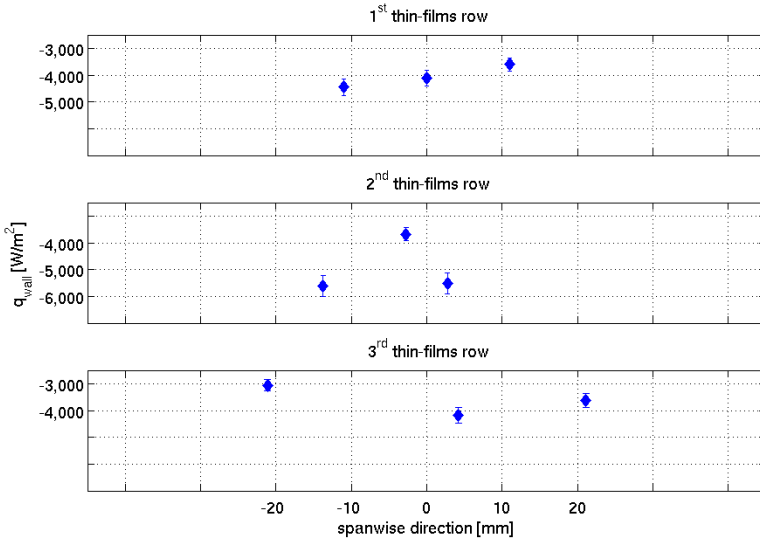


Figure 3.29: Heat-flux spanwise trends ($M=1.6$, $k=1$ mm, $T_w=26^\circ$ C)

the second row, while across the other two the heat fluxes values are comparably more uniform. Across the second row the starkest difference is among the heat flux value from thin-film 14 (just to the left of the center-line) and the very similar values from thin-film 15 (just to the right of the center-line) and from the remaining thin-film 12. Heat flux from thin-film 14 is not much different from the heat fluxes sensed across the centerline on the first and third rows, while the values from thin-films 15 and 12 are in absolute the largest, and very similar to each other. This is unexpected because thin-film 14 and 15 are both just across the center-line, while thin-film 12 is about 14 mm apart from it: one would have expected similar heat flux values at least from thin-films 14 and 15.

3.4.2 Streamwise and spanwise heat-flux trends: wall temperature effects

The thin-films insert temperature is controlled by adjustable heating elements beneath. They were used to change the wall temperature of the insert to investigate the effect on the boundary layer with or without the perturbations induced by the roughness. The maximum wall temperature was dictated by the behavior of the glue between the thin-films sheet and the metal surface of the insert as commented in Section 3.1. As a result, the wall temperature was kept below 50° C in the present test campaign.

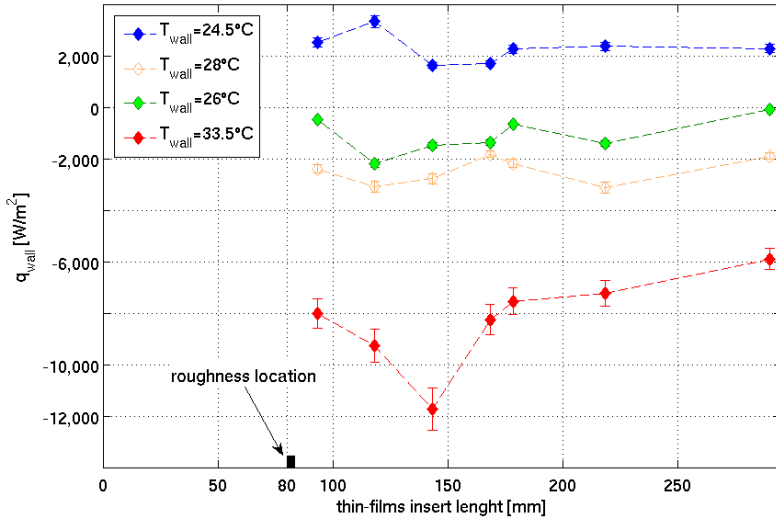


Figure 3.30: Heat-flux streamwise evolutions at different wall temperatures ($M=2.3$, roughness height 0.1 mm)

3.4.2.1 Wall temperature effects on streamwise heat flux trends

The following Figs. 3.30 to 3.32 compare the streamwise trends of the heat flux for different imposed wall temperatures, for the two roughness heights tested at Mach 2.3 and for the only one tested for Mach 1.6 ($k=1$ mm).

It is first evident from Figs. 3.30 and 3.31 for Mach 2.3 that, as the wall temperature increases, the direction of the heat flux is inverted, and it is the wall that warms the flow and not vice versa. And so much so as the wall temperature increases. On the other hand, there is always a hot-wall condition for Mach 1.6 (Fig. 3.32), whether or not the heaters are switched on. This is because the flow recovery temperature is lower than for Mach 2.3.

Fig. 3.30 shows that the absolute maximum heat flux is attained within 70 mm downstream of the roughness, at the same location for the blue, green, and yellow trends, and further downstream for the red one. The last is also the trend that shows the highest differences in heat flux along the thin-films insert. The green, yellow, and red trends do not show a plateau at the end of the instrumented insert as clear as the blue trend. Thin-film 29, the last along the insert, failed in the tests represented by the green and the yellow trends, and was rather noisy also in the test for the warmest wall temperature.

Trends in Fig. 3.31 are rather similar notwithstanding the sixteen degrees of difference between the warmest and the coldest wall temperatures. All of

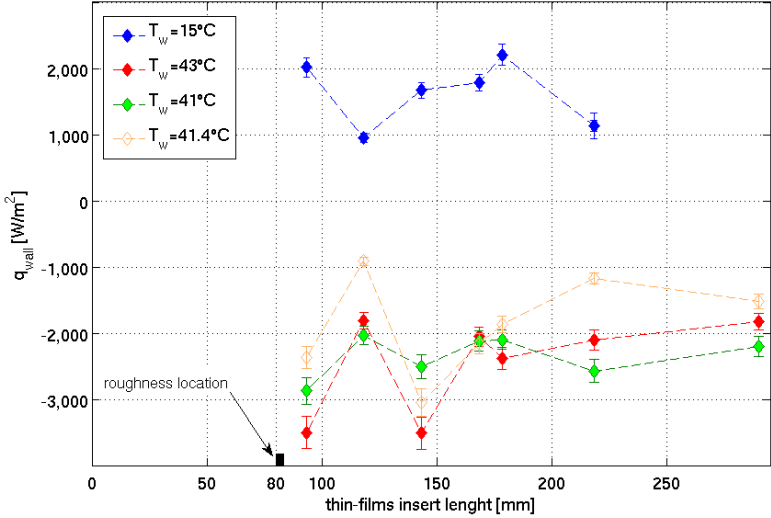


Figure 3.31: Heat-flux streamwise evolutions at different wall temperatures ($M=2.3$, roughness height 1 mm)

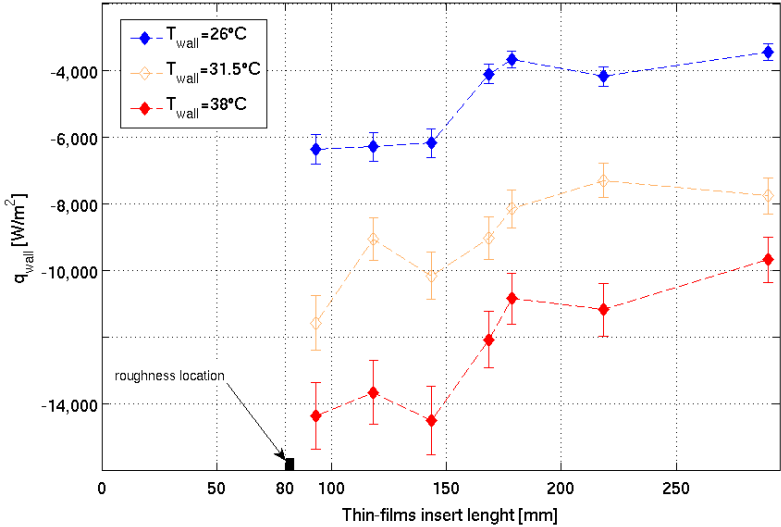


Figure 3.32: Heat-flux streamwise evolutions at different wall temperatures ($M=1.6$, roughness height 1 mm)

them show an absolute minimum at the same location, that is more or less duplicated further downstream, again at the same location for the green and red trends and for the blue and yellow ones. Differences in heat flux values at different downstream locations decrease passed about 170 mm from the insert leading edge, that is from about 90 mm from the roughness location.

Figure 3.32 presents the highest absolute heat fluxes kept along 50 mm through the first three sensors for the blue and the red trends for Mach 1.6. For the yellow trend, then, the peak is clearly only at the location closest to the roughness. However, all the three trends show the tendency to level down to a more or less constant value as from 90 mm downstream of the roughness. Consequently, these comparisons show that the heat flux trend downstream of the roughness does not change much with the wall temperature, featuring always the maximum values close downstream of the roughness and a tendency to level off moving further downstream of it. This is valid for both Mach numbers, and for both roughness heights tested at Mach 2.3.

One may note from Fig. 3.30 and 3.31 that, for the same Mach number, the higher roughness produces the peak heat flux always at the closest location, while the 0.1-mm-high roughness produces it further downstream. For the same roughness height (1 mm), but for a different Mach number (Fig. 3.31 and 3.32), the most evident difference seems to be the persistence of the maximum heat flux through the first three sensors only for Mach 1.6, while for Mach 2.3 the second sensor always shows a minimum. However, one should also consider the differences in wall temperature among the tests at Mach 2.3 and 1.6, and among those at Mach 2.3 and $k=0.1$ and 1 mm. They are not negligible, and an optimal comparison would have required the same wall temperature for different Mach numbers or roughness heights.

3.4.2.2 Wall temperature effects on spanwise heat flux trends

The spanwise variation of the thermal quantities were measured for the three rows of thin-films for the different wall temperatures imposed. The temperature color code of the symbols in a plot is the same as for the corresponding streamwise trend. The heaters-off tests, already commented in Sub-section 3.4.1.2, are included as the benchmark for the estimation of the wall temperature effects.

Figure 3.33 shows, for Mach 2.3 and $k=0.1$ mm, that the differences among the heat fluxes sensed across the first row tend to decrease with the temperature: the maximum difference is 0.8 kW/m^2 for the coldest case and reduces to 0.2 and 0.3 kW/m^2 for the other two highest wall temperatures. On the other hand, the trend across the second row seems to be preserved at the higher wall temperatures: thin-film 14 senses always the lowest (absolute) heat flux, while the most external one always the highest. Finally on the third row the uniformity found for the coldest wall is lost when temperature arises, and the differences in heat fluxes values become more sensible

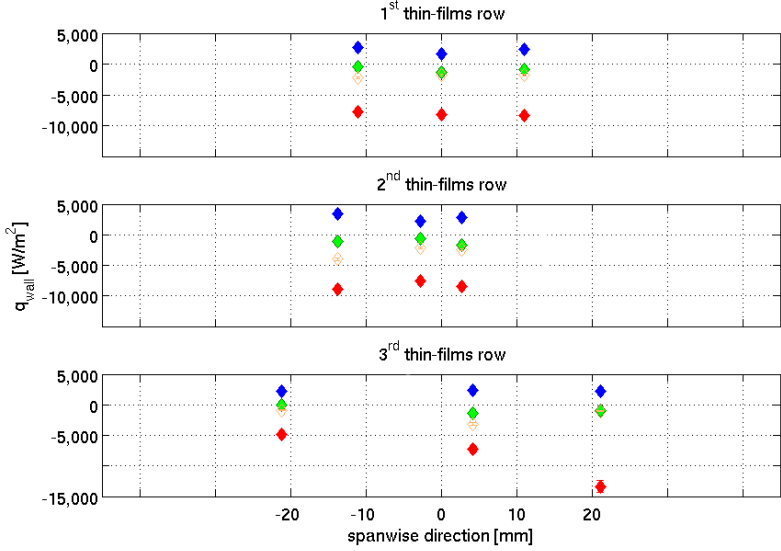


Figure 3.33: Heat-flux spanwise trends at different wall temperatures ($M=2.3$, $k=0.1$ mm)

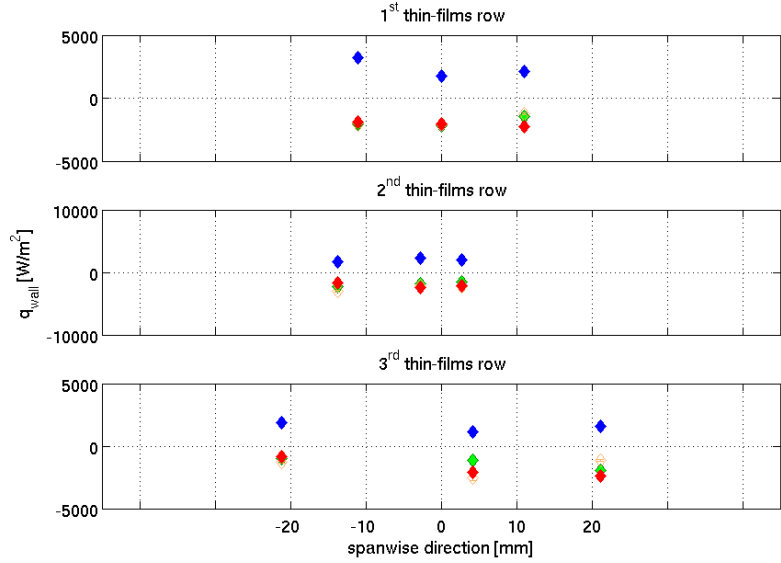


Figure 3.34: Heat-flux spanwise trends at different wall temperatures ($M=2.3$, $k=1$ mm)

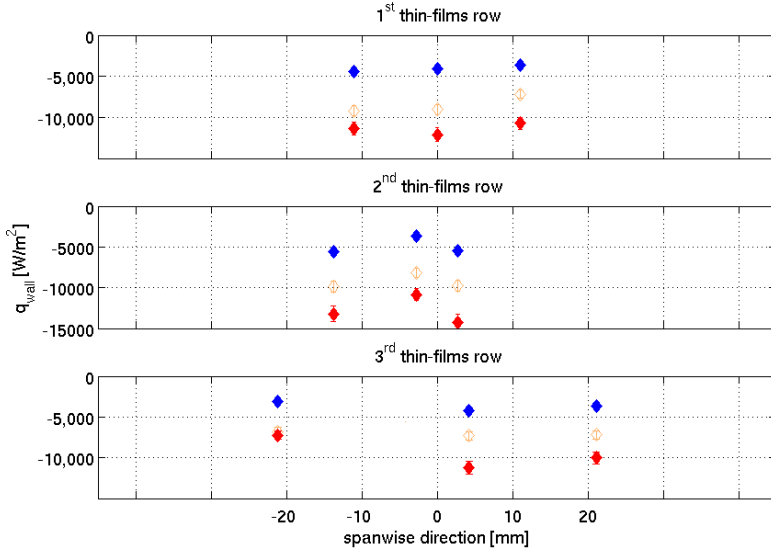


Figure 3.35: Heat-flux spanwise trends at different wall temperatures ($M=1.6$, $k=1$ mm)

with it. Note, however, how the heat flux from the rightmost thin-film on the third row is very much higher than the average between the other two at the highest wall temperature; and only for that temperature. This may be a sign that thin-film 28 did not work correctly for that particular test, thus the trend evinced from the other two heat flux values may be the more probable. Then, there would not be much difference with the trend for the intermediate wall temperature.

The wall temperature rise applied to the 1-mm-roughness Mach-2.3 case seems to level off the differences among the heat flux values sensed across the first row (Fig. 3.34): in the coldest case this is 1 kW/m^2 and becomes less than 0.1 kW/m^2 for the warmest case. It is not so for the second row, instead, where the spanwise trend of the coldest case is replicated without much difference at the highest wall temperatures. Finally, on the third row the temperature increase turns the heat flux value of the leftmost thin-film from the highest to the lowest across the row.

For the Mach-1.6 tests, the temperature rise does not alter substantially the trends across the first and the second rows (Fig. 3.35). For the first row the difference between the maximum and the minimum values increases with the temperature from 0.5 kW/m^2 to more than 1 kW/m^2 . This happens on the second row only passing from the coldest wall case to the warmest one. On the third row basically the same spanwise trend is found for the coldest and the warmest wall cases, while for the intermediate temperature case the

trend becomes more uniform. The difference between the maximum and the minimum values in the former two cases increases with the wall temperature.

In conclusion, at Mach 2.3 the wall temperature affects the first row of thin-films in the same way for both roughness heights, that is, leveling their heat flux values. On the second row is also common that the wall temperature does not change the spanwise trend found for the heaters-off case. Finally, the wall temperature seems to have a larger effect on the heat flux trends with the high roughness than with the small one across the third row. The comparison at different Mach numbers for the 1-mm-high roughness brings out the most evident difference: at Mach 1.6 also the first row trend is not affected by the wall temperature rise and not just the second row trend as for Mach 2.3. Of course, regarding the cross-comparisons between different Mach numbers and different roughness heights, the warning about wall-temperature uniformity among tests made in the preceding for the streamwise trends is still valid, and thus has still to be considered when drawing conclusions.

3.5 Time-averaged adiabatic-wall temperature measurements

The adiabatic-wall temperature trends have been used to check the state of the boundary layer downstream of the roughness elements by comparing the experimental results with analytical values characteristic of the laminar or the turbulent states.

The estimation of the adiabatic-wall temperature out of the heat-flux and wall temperature measurements has been possible thanks to the heaters that allowed the raise of the wall temperature. Five different wall temperatures have been set for each test case, i.e., for each combination of roughness height and Mach number.

This estimation as been made through the interpolation of the experimental results on a (q_w, T_w) graph. In fact, the heat flux values changed with the wall temperature and the expected trend of this change is linear as from

$$q_w = h(T_{ad} - T_w) \quad (3.7)$$

The pairs (q_w, T_w) from the five tests provided a sufficient amount of points to reproduce such linear trend. Then, the adiabatic-wall temperature has been estimated as the temperature at which this linear trend crossed the abscissa of the (q_w, T_w) graph. That is, the temperature for which the heat flux is zero. This procedure is illustrated by Figs. 3.36 and 3.37. Fig. 3.36 shows a rather clear decreasing linear trend for $q_w = q_w(T_w)$. But except for one point that gives a higher heat flux for a wall temperature practically the same as that of another in-line pair. This situation occurred twice, that is, for two different wall temperatures and in two different test cases. Since these outliers showed up in the trends of all the thin-films for the same two wall temperatures, we concluded that the tests for those two wall temperatures had to be discarded because the measurement chain failed somehow. Fig. 3.37 shows how with the linear trend clearly identified the interpolation of the adiabatic wall temperature becomes straightforward.

In this way the adiabatic wall temperature was estimated for all thin-films in the streamwise direction. However, the T_{ad} value from thin-film 29 resulted abnormally high in all the cases and was discarded. An abnormal behavior of this sensor was in effect regularly detected at the beginning of each test day, however it revealed in full only in the T_{ad} results.

3.5.1 Adiabatic-wall temperature trends along the thin-films insert

Figures 3.38 to 3.41 show the adiabatic-wall temperature trends for the four configurations tested. For those configurations with the roughness, the roughness position is also indicated. Each experimental trend is complemented by two lines that represent the analytical trends of the flow recovery

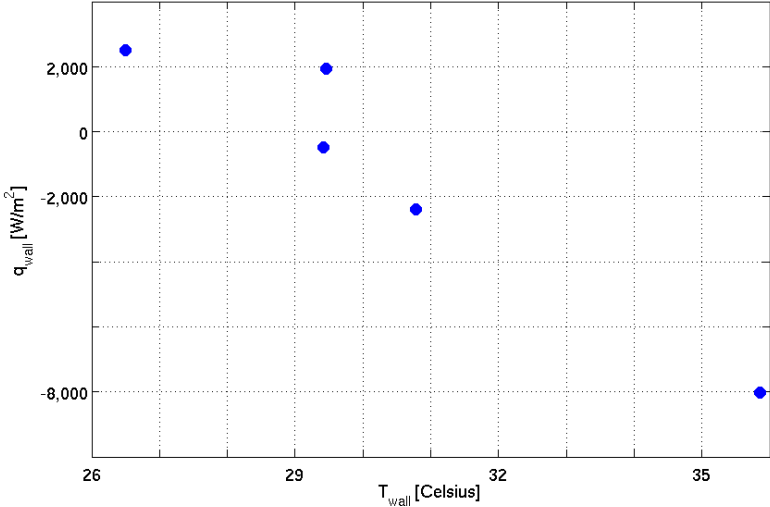


Figure 3.36: The (q_w, T_w) pairs from five tests at different wall temperatures for thin-film nr. 4 ($M=2.3$, clean configuration)

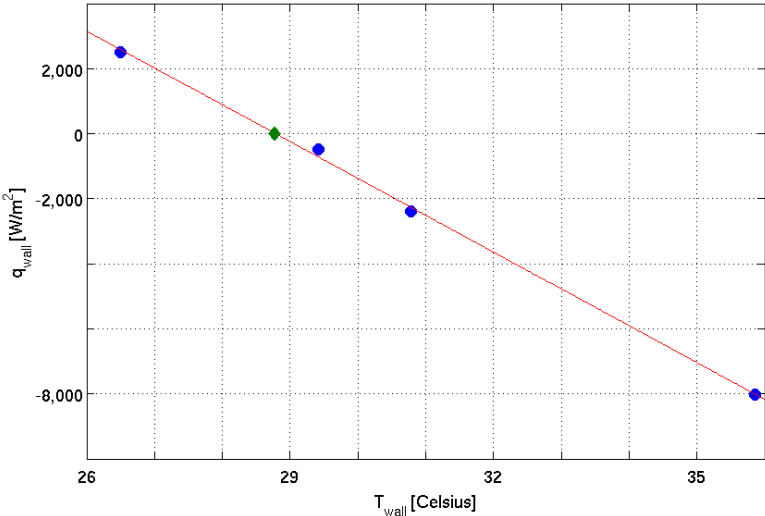


Figure 3.37: The (q_w, T_w) pairs and the interpolated T_{ad} value for thin-film nr. 4 ($M=2.3$, clean configuration)

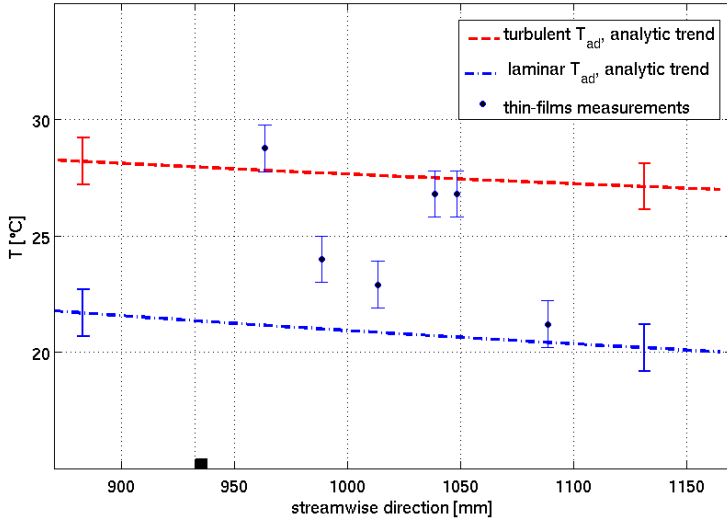


Figure 3.38: *The experimental adiabatic-wall temperature trend along the thin-films insert ($M=2.3$, $k=0.1$ mm)*

temperature for laminar and fully turbulent boundary layers, respectively. These trends are calculated from the definition of recovery temperature [e.g., 34]

$$T_r = T_\infty + r \frac{U_\infty^2}{2C_P} \quad (3.8)$$

in which $r = r(Pr, M)$ and $Pr = Pr(T)$, and T_∞ is the static freestream temperature. Comparing the experimental trend with these analytical trends enables the evaluation of the roughness effectiveness as turbulence trigger.

Figure 3.41 shows two more trends of adiabatic-wall temperature, again one for a laminar boundary layer, the other for a fully turbulent one. These trends are the results of CFD computations performed to validate the analytical trends. As one can see the agreement between the analytical and the numerical turbulent trends is rather good; less so between the analytical and the numerical laminar trends. In this latter case the CFD result ended up fluctuating across an average trend, and the error bars, present only for this trend, account for the amplitude of such fluctuations.

Also the experimental points show an error bar; the way the uncertainty on the T_{ad} value has been calculated is the subject of the following Sub-section.

Figure 3.38 shows that T_{ad} peaks to a turbulent value just downstream of the roughness, then decreases towards laminar values, gains back turbulent

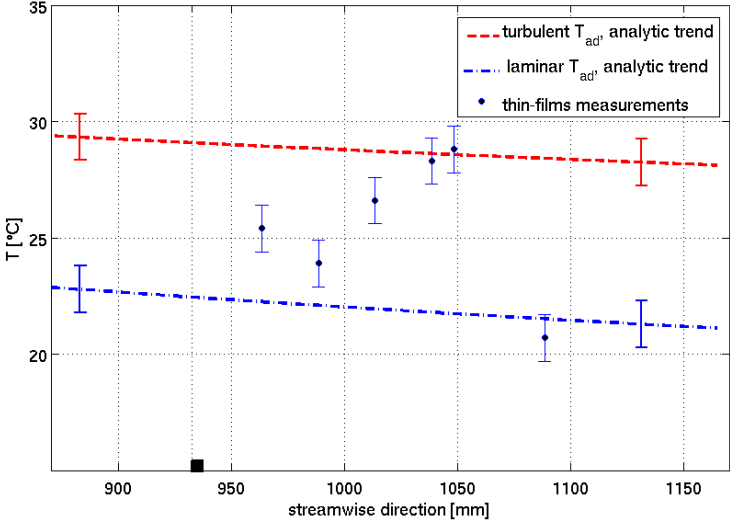


Figure 3.39: The experimental adiabatic-wall temperature trend along the thin-films insert ($M=2.3$, $k=1$ mm)

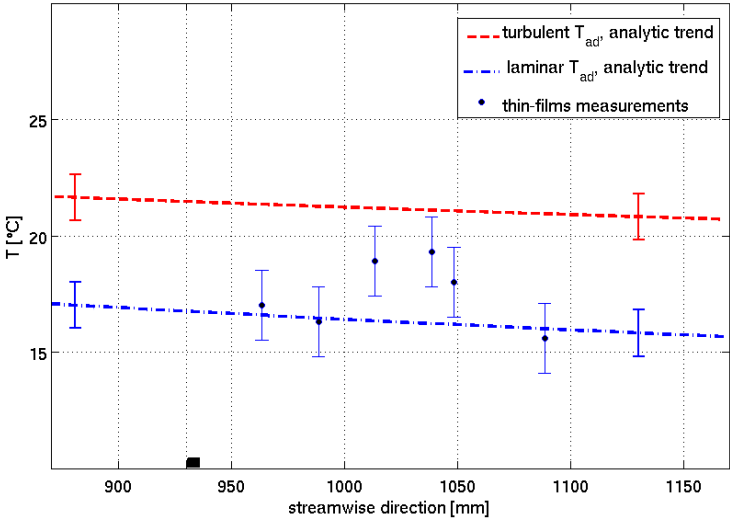


Figure 3.40: The experimental adiabatic-wall temperature trend along the thin-films insert ($M=1.6$, $k=1$ mm)

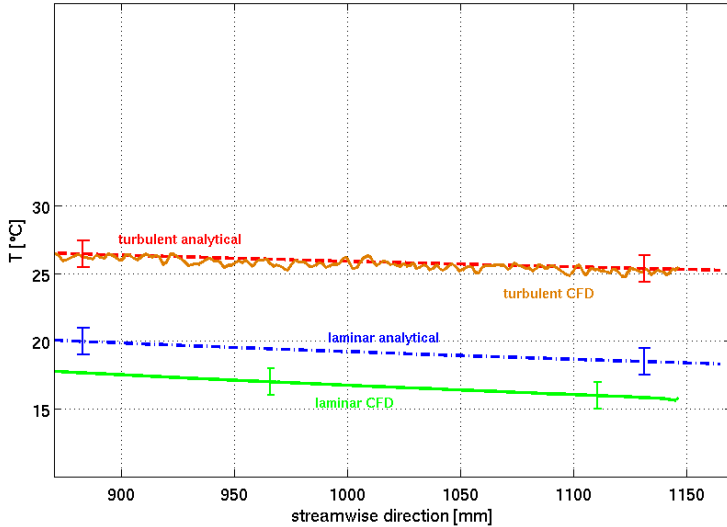


Figure 3.41: Comparison among analytical and 2D-CFD numerical adiabatic-wall temperature trends along the thin-films insert ($M=2.3$)

values, and finally, dips to a definitely laminar value. Figure 3.39, instead, for the same Mach number but $k=1$ mm, shows T_{ad} gradually increasing towards turbulent values downstream of the roughness element. These values are attained at the same positions as in Fig. 3.38, and are followed by a decrease to a laminar value for the last sensor, again as for $k=0.1$ mm.

For the Mach-1.6 case (Fig. 3.40), instead, the roughness effect on the boundary layer flow seems to be weaker than for Mach 2.3, in the sense that turbulent values are just approached and never reached. Furthermore, this effect is also delayed to more downstream positions, since the first two sensors downstream of the roughness still give laminar values, unlike for Mach 2.3 in Fig. 3.39. However, the T_{ad} value at the most downstream location is still clearly laminar like for Mach 2.3.

3.5.2 Uncertainty estimation of the adiabatic-wall temperature measurements

The uncertainty on the adiabatic-wall temperature estimation is calculated from the uncertainty on the heat flux measurements. The interpolation line that determines the T_{ad} value can change its slope if one accounts for the heat flux uncertainty, thus shifting the T_{ad} value. And the maximum possible shift of this value is taken as a conservative estimation of the uncertainty on the value of the adiabatic-wall temperature. This procedure, depicted in

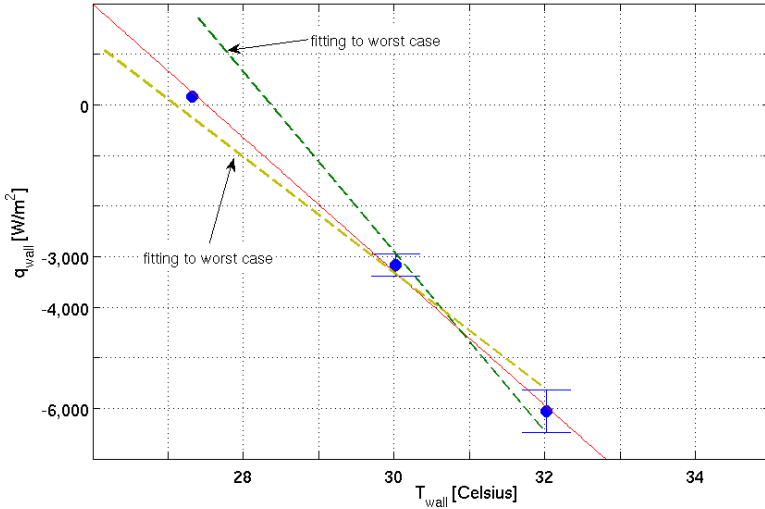


Figure 3.42: Estimation of the uncertainty on the adiabatic-wall temperature value

Fig. 3.42, has been repeated for each test case and the resulting uncertainties appear as error bars in Figs. 3.38 to 3.40.

3.5.3 Stanton number streamwise trends

With the heat fluxes and the adiabatic-wall temperatures from measurements, the Stanton number can be calculated at each sensor location. This is a dimensionless number that is frequently used to describe aerodynamic heating in high-speed flows; it is defined as [35]:

$$St = \frac{\dot{q}_w}{\rho_\infty U_\infty (h_{ad} - h_w)} \quad (3.9)$$

where $h = C_p \cdot T$ is the static enthalpy.

For the present calculations of the Stanton number at each sensor location \dot{q}_w , T_{ad} , and T_w are from the measurements, while ρ_∞ and U_∞ are from the CFD computations.

The Stanton numbers so obtained are checked against analytical trends for laminar and turbulent boundary-layer flows calculated with the reference-temperature method. This method is found to be rather accurate for Stanton number values, thus it is currently used [35]. But it is rigorously valid only for flat-plate flows, i.e. flows without pressure gradients. This is not the case for the present experimental study, because the boundary layer along the instrumented insert experiences a favorable pressure gradient from its

very beginning in the subsonic part of the wind tunnel throughout the whole divergent (see Fig. 3.3). To, at least, mitigate this inconsistency, 2D-CFD numerical values and measured values are used for the calculation of these analytical trends.

Following the definitions in ref. [35] the analytical expression of the Stanton number for a laminar boundary layer is:

$$St_{lam} = \frac{0.332}{\sqrt{Re_x^* Pr^{*\frac{2}{3}}}} \quad (3.10)$$

where the apex * means that the Reynolds number and the Prandtl number are calculated with the reference-temperature value instead of the freestream temperature value. The reference temperature is also used to calculate C_p for Eq. 3.9. This reference-temperature, T^* , is then defined as:

$$\frac{T^*}{T_\infty} = 1 + 0.0032M_\infty^2 + 0.58\left(\frac{T_w}{T_\infty} - 1\right) \quad (3.11)$$

For a fully-turbulent boundary layer flow, instead, the analytical Stanton number is expressed as:

$$St_{turb} = \frac{0.0592}{2s(Re_x^*)^{0.2}} \quad (3.12)$$

where $s = 0.825$ as from ref. [36], as suggested in ref. [35].

Figure 3.43 shows the Stanton number trends for $k=1$ mm and Mach 2.3; each trend corresponds to a given wall temperature. The error bars account for the measurement uncertainty on the heat flux and the adiabatic-wall temperature. Here it appears that all the trends tend to collapse on a common value for the same sensor; except for the very first thin-film at the lowest wall-temperature case.

The Stanton number trends for the other cases are not shown because, due to the relative scarce difference among the wall temperatures set and the adiabatic-wall value, they have been judged misleading. In effect, one can note that the sheer definition of the Stanton number (Eq. 3.9) predicts a theoretically indeterminate value as $T_w \rightarrow T_{ad}$. In fact in this case the denominator goes to zero and so does the numerator \dot{q}_w because the heat flux tends to vanish as the wall temperature approaches the adiabatic-wall temperature. Actually, the indeterminate value would be if both numerator and denominator tended to zero in the same way: in case the numerator does it slower, the Stanton number would tend to infinity, if faster, it would tend to nil. In conclusion, if the wall temperature is close enough to the adiabatic-wall value, the Stanton number may assume values less and less trustful. This was the case for the tests at Mach 2.3 and $k=0.1$ mm, for which the difference $T_{ad} - T_w$ was as low as less than one degree. These low differences led to very high Stanton numbers, far above the turbulent level, and were taken as due just to this shortcoming of the Stanton number

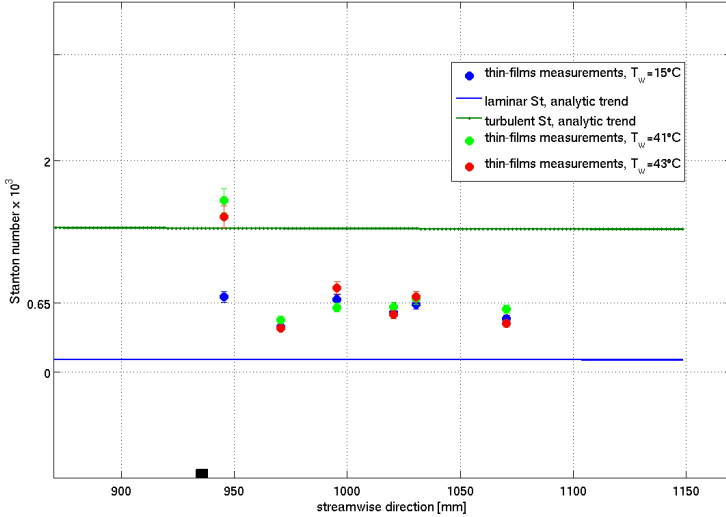


Figure 3.43: *Experimental Stanton number trends along the thin-films insert ($M=2.3$, $k=1$ mm)*

parameter. Moreover, these trends do not even collapse to each other as expected and seen in Fig. 3.43.

Also the experimental Stanton numbers at Mach 1.6 are found above the turbulent levels for all the sensors. However, they are closer to the turbulent analytical trend than for Mach 2.3 and $k=0.1$ mm. And the different values for a given sensor, corresponding to each wall temperature, are also much less spread out. Moreover, in this case wall temperatures are farer from the adiabatic-wall value than for Mach=2.3 and $k=0.1$ mm. It is then possible that the analytical model fails to give values accurate enough and predicts a turbulent level too low. In fact, one should bear in mind that the reference-temperature method is valid only for boundary layer flows without any pressure gradient, whereas this is not so for both present Mach number cases. And for Mach 1.6 the CFD-calculated favorable pressure gradient along the instrumented insert was stronger than for Mach 2.3.

In the end, the Stanton number analysis predicts convection heating of “transitional“ intensity for the cases at Mach 2.3 and $k=1$ mm, i.e. intermediate between the laminar- and turbulent-flow intensities. For the remaining cases the prediction is too clouded by the proximity of the wall temperatures to the adiabatic-wall value, or, possibly, by the inaccuracy of the zero-pressure-gradient analytical model to be considered physically sounding, thus trustworthy.

3.6 Time-resolved wall-temperature measurements

The thin-films signals high-passed above 100 Hz and sampled at 1 MHz have been used for frequency analyses. These were aimed at detailing in different ways and depths the flow evolution downstream of the roughness element. Different techniques have been applied, each for a given goal: plots of smoothed FFT-ed signals have been used to detail the spatial evolution of the temperature fluctuations for the different Mach numbers, roughness heights, and wall temperatures (Sub-section 3.6.1); signals RMS stream-wise evolutions have been plotted against the insert length to highlight the overall fluctuations behaviors (Sub-section 3.6.2); spectrograms (i.e., three-dimensional plots of fluctuation amplitude versus frequency and time) have been made to detail the time evolution of the fluctuations frequency content through the test duration (Sub-section 3.6.3).

The goodness of the high-passed test signals was checked test by test by comparing their frequency spectrum with the one of the signals acquired in quiescent conditions. These acquisitions were made before each blow-down with the wall temperature already set to the test value. In these conditions, then, the sensors measured only what can be considered as electronic noise.

Figure 3.44 shows typical signal and noise frequency spectra of a well-behaving thin-film. It is evident that the signal is not overwhelmed by the noise, since it keeps an amplitude comfortably higher than that of the noise throughout the entire frequency range.

The spectra presented in this Section will span a frequency range from 100 Hz up to 250 kHz. This was the range allowed by the Data Acquisition System and is kept to show the widest frequency range possible. This is done despite the fact that the thin-films electronics allowed a frequency resolution up to 60 kHz. For other analyses presented in this Section all the signals were further high-passed above 200 Hz.

3.6.1 Frequency analysis of the wall-temperature fluctuations

The comparisons between the spectra at the lowest and that at the highest wall temperatures have been performed to estimate the wall temperature effects on the spectra of the temperature fluctuations. These spectra are smoothed by the application of a Savitzky-Golay 5th-order filter¹ to the original signal for the sake of clarity.

Figure 3.45, for the clean configuration at Mach 2.3, shows a clear amplitude decrease with the frequency for all the sensors. At 20 kHz all the signals have a drop of one order of magnitude. Thin-films 12 and 23 show a broken line at around 300 Hz: in this range they have the noise larger than

¹ *sgolayfilt* in the MATLAB[®] Signal Processing Toolbox, version R2007b

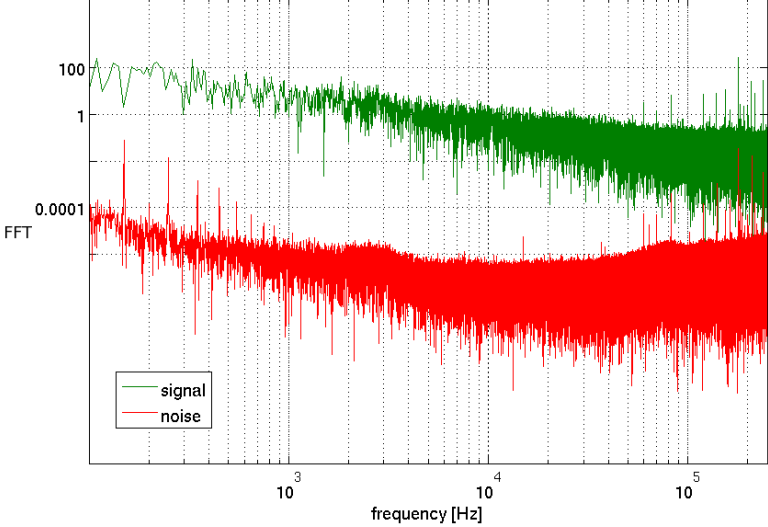


Figure 3.44: Typical signal and noise frequency spectra of a thin-film correctly working ($M=2.3, k=1$ mm)

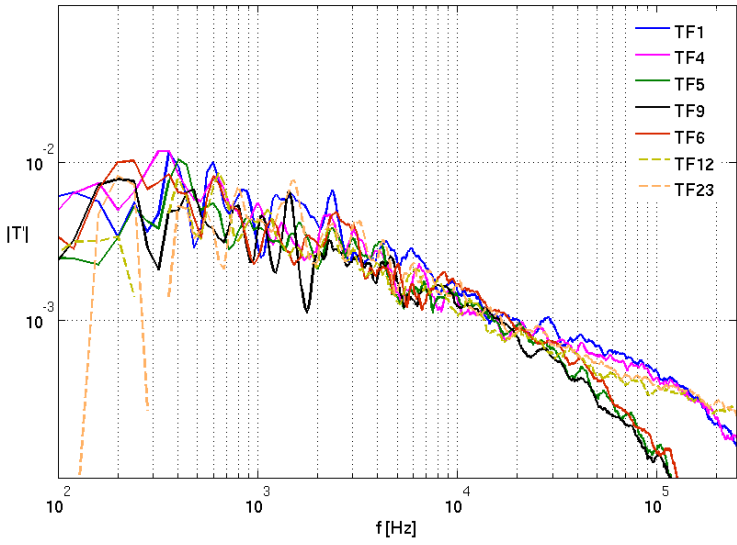


Figure 3.45: Frequency spectrum streamwise evolution ($M=2.3$, clean configuration, coldest T_{wall})

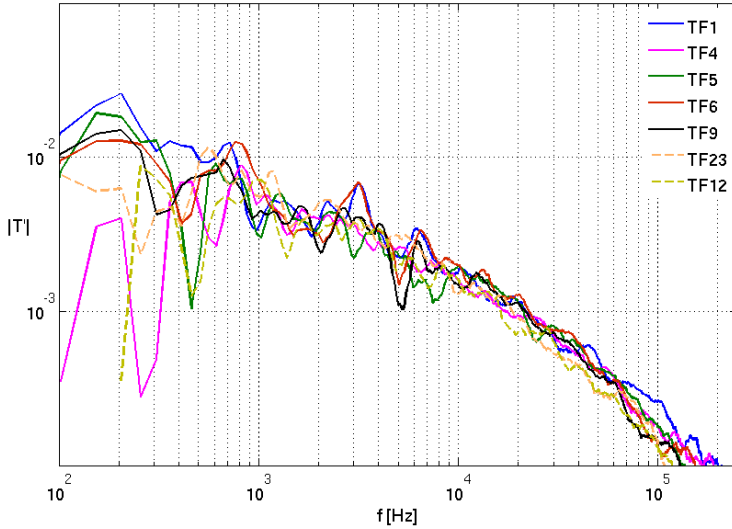


Figure 3.46: *Frequency spectrum streamwise evolution ($M=2.3$, clean configuration, warmest T_{wall})*

the signal, thus their spectrum is not reported. All the signals have their highest peaks between 200 and 600 Hz, and only thin-films 1 and 23 feature another high peak at about 2.5 and 1.5 kHz, respectively. Above 30 kHz thin-films 5, 6, and 9 show a slope steeper than that of the other thin-films.

For the same configuration, but the warmest wall temperature, Fig. 3.46 shows the amplitudes of most of the spectra increasing respect to the coldest wall-temperature case, especially at the lowest frequencies; thin-film 4 is the most remarkable exception. The frequencies of some of the highest peaks are slightly lower than in Fig. 3.45, but the frequency range within which all the main peaks lay is now up to about 900 Hz. Again respect to the coldest-wall case thin-films 1 and 6 have their peak moved from about 2.5 kHz to 3 kHz, and the one at about 6 kHz gains in amplitude. Finally, the slope of all the spectra stays the same at the highest frequencies, unlike in Fig. 3.46, and the total number of peaks decreases respect to the coldest wall case.

For the 0.1-mm-high roughness at Mach 2.3, Fig. 3.47 shows that the spectra are rather similar to those of Fig. 3.45 in terms of fluctuation amplitude, but more peaks appear at lower frequencies. The spectrum of thin-film 4 is less excited than for the clean configuration below 1 kHz. Thin-films 5, 6, and 9 have the largest peak at about 350 Hz, and another peak at 3 kHz. The general slope of their spectra with the frequency is not much different from that in Fig. 3.45.

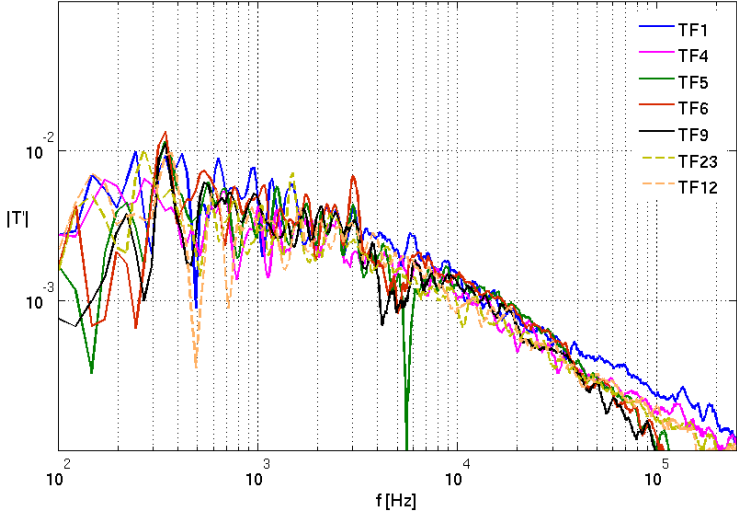


Figure 3.47: *Frequency spectrum streamwise evolution ($M=2.3$, $k=0.1$ mm, coldest T_{wall})*

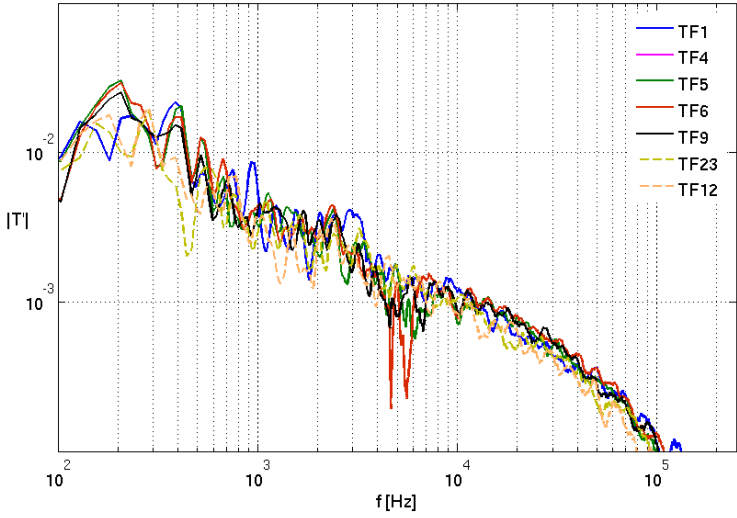


Figure 3.48: *Frequency spectrum streamwise evolution ($M=2.3$, $k=0.1$ mm, warmest T_{wall})*

The comparison between Figs. 3.47 and 3.48, for the coldest and the

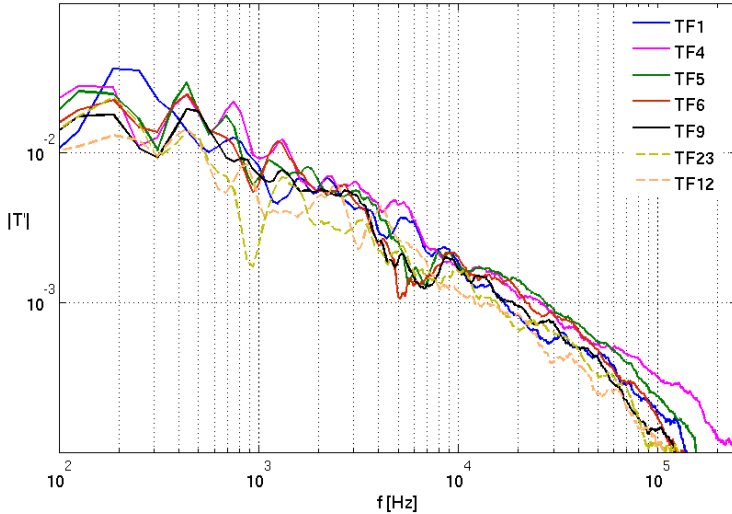


Figure 3.49: *Frequency spectrum streamwise evolution ($M=2.3$, $k=1$ mm, coldest $T_{wall}=15^\circ$ C)*

warmest wall, respectively, shows the amplitude shifting up with the wall temperature as for the clean insert. The highest peak appears at a lower frequency in Fig. 3.48 (200 Hz instead of 350 Hz), still for thin-films 5, 6, and 9. Above 1 kHz the amplitudes seem to decrease slightly with the wall temperature.

Figure 3.49 compared to Fig. 3.47 shows that for the higher roughness at Mach 2.3 there are higher amplitudes throughout the whole frequency range. But this may not be an effect of the roughness, because it happens also for thin-film 1 upstream of it. Also the wall temperatures of these two plots are rather different. Note the same relatively high peak at about 450 Hz for thin-films 4, 5, 6, and comparably less prominent for thin-film 9. However, the maximum peak is for thin-film 1 at 200 Hz. Thin-film 4, the closest sensor downstream of the roughness, has the highest peaks above 600 Hz: at about 750, 1400, 3000, and 5000 Hz. With thin-films 5 and 6 its spectrum features also a kind of plateau between 10 and 20 kHz that is not visible in Fig. 3.47. The spectra slope increases as well with the roughness height, whilst the number of peaks with comparable amplitude decreases with it at the lowest frequencies in all the spectra.

The wall temperature effect on the flow downstream of the 1-mm-high roughness is shown by the comparison between Figs. 3.50 and 3.49: fluctuation amplitudes are generally lower respect to the coldest-wall case. This makes the spectra slope less steep than for the coldest-wall case. Thin-film 5 peaks the highest throughout the spectrum at a frequency about 100 Hz

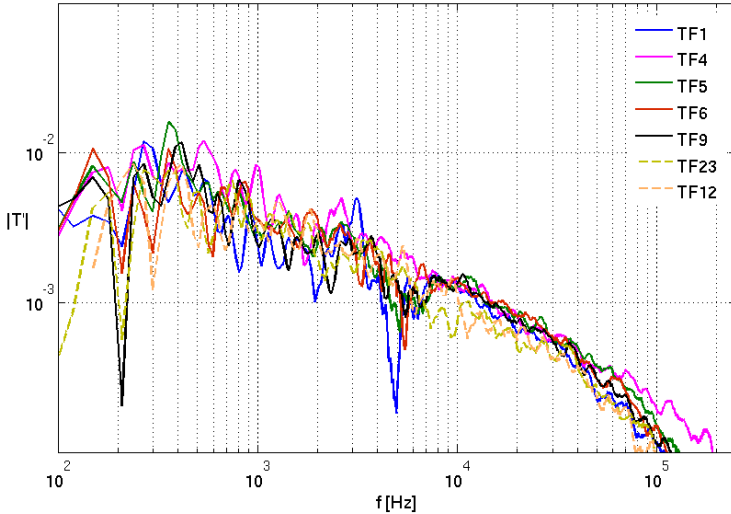


Figure 3.50: *Frequency spectrum streamwise evolution ($M=2.3$, $k=1$ mm, warmest $T_{wall}=43^\circ$ C)*

less than for the coldest-wall case. Thin-film 4 still features the highest peaks above 500 Hz; at about 550, 750, 1000, 1400, 2600 Hz. The plateau between 10 and 20 kHz as for the coldest-wall case is no more evident. The number of peaks increases as well with the wall temperature. Respect to the warmest-wall case for $k=0.1$ mm, the spectra are generally less excited below 400 Hz and have comparable amplitudes elsewhere. The slopes of the spectra do not change much between the two plots except for the decrease starting after 1 kHz in Fig. 3.48.

Finally, for the Mach 1.6 case, Fig. 3.51 shows that there is a peak at about 300 Hz for all the thin-films, except 9, and that the trends are rather similar to each other, with the exception of thin-films 9. Spectra of thin-films 1, 23, and 12 have a very similar slope for $f > 10$ kHz.

The comparison between Fig. 3.49 and 3.51 shows that for the same roughness height but a lower Mach number the fluctuation amplitudes are lower throughout the whole spectrum. And this happens despite the higher wall temperature. However, spectra features more peaks for Mach 1.6 than for Mach 2.3. Thin-film 4 is still the sensor featuring the most excited spectrum.

The wall temperature effects on the temperature fluctuations downstream of the 1-mm-high roughness at Mach 1.6 are illustrated by the comparison between Figs. 3.51 and 3.52. Fluctuation amplitudes do not change much with the 12-degree increase in wall temperature, except for thin-film 9. The general slope of the spectra does not change much neither. Thin-films 9 and 6 now show both a sensible dip at about 5 kHz, whilst for the coldest

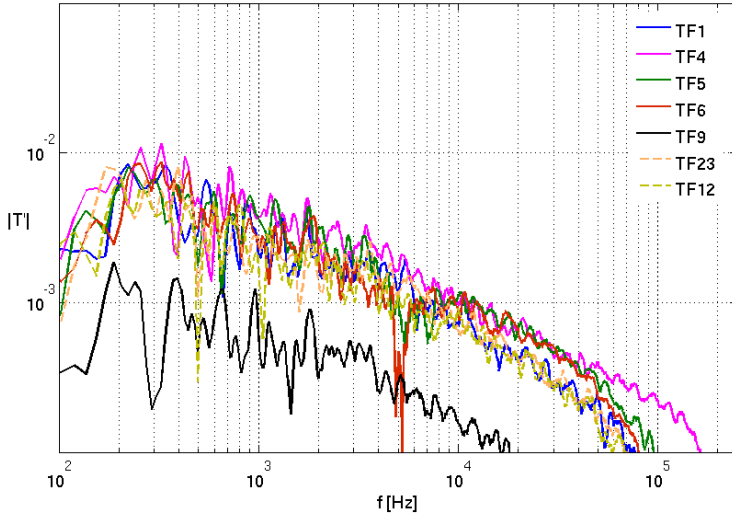


Figure 3.51: Frequency spectrum streamwise evolution ($M=1.6$, $k=1$ mm, coldest $T_{wall}=26^\circ$ C)

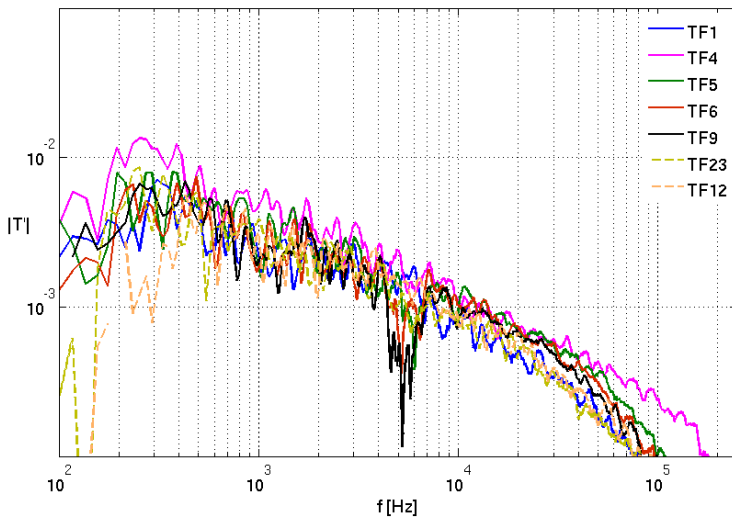


Figure 3.52: Frequency spectrum streamwise evolution ($M=1.6$, $k=1$ mm, warmest $T_{wall}=38^\circ$ C)

case only thin-film 6 does. Thin-film 4 is still the most excited sensor, still

between 200 and 400 Hz.

In the end, one can see that there are few features in the frequency spectra recurring whatever the case tested: main peaks appear always below a certain frequency generally lower than 1 kHz; above 20 kHz most of the spectra show their amplitudes decreased of one order of magnitude from the peak values; this decrease becomes of two orders of magnitude above 100 kHz.

The effect of the roughness at Mach 2.3 with the heaters off, is rather feeble passing from the clean configuration to the roughness 0.1-mm high. Amplitudes stay generally at the same level, and the frequencies of the main peaks do not change sensibly. A difference can be the appearance of a peak at 3 kHz for thin-film 6 and, less pronounced, for thin-film 5. More remarkable is that thin-film 4, the closest sensor downstream of the roughness, is less excited below 1 kHz than for the clean configuration case. On the other hand, as the roughness height is 1 mm, the amplitudes become the highest among all the coldest-wall cases throughout the whole frequency range, and the general negative slope of the spectra becomes steeper.

The most evident Mach-number effect on the heaters-off cases for the 1-mm-high roughness are all the amplitudes decreasing sensibly as the Mach number goes from 2.3 to 1.6. Then, for the lowest Mach number, peaks repeat more frequently along the spectrum of all the signals.

The main wall-temperature effect on the clean and 0.1-mm-high roughness configurations is an increase of the amplitudes at frequencies below 1 kHz. But this is not the case for the 1-mm-high roughness configuration, for which there is a general decrease of fluctuation amplitudes in passing from 15 to 43 Celsius. And the total number of peaks in the spectra increases for the 1-mm-high roughness configuration, while it stay practically the same for $k=0.1$ mm and goes down for the clean configuration. A slight decrease in amplitude is, actually, also seen for the 0.1-mm-high roughness above 1 kHz. This, then, may suggest that the roughness height hinders the effect of wall temperature starting from the highest frequencies downward. However, for the same roughness height of 1 mm the fluctuation amplitudes at Mach 1.6 do not differ much between the coldest-wall and the warmest-wall cases (and the wall temperature increases of 12 degrees Celsius in this case). Thus, if the roughness really plays a role in the wall temperature effect, this also seems to depend on the Mach number.

3.6.2 Signals RMS streamwise evolution

The Root Mean Square (RMS) of the thin-films signals have been calculated to give an overall estimation of the effects on the wall-temperature unsteadiness of the parameters varied during the test campaign (Mach number, roughness height, wall temperature).

RMS is also useful to assess the general repeatability of the noise from test to test, and this assessment is firstly presented for two wall temperatures

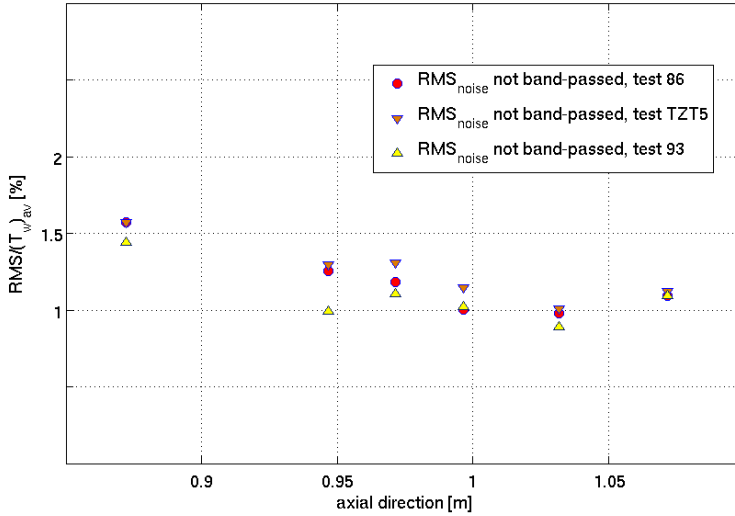


Figure 3.53: *Three streamwise evolutions of noise RMS from the beginning of different tests ($M=2.3$, $T_{wall} \simeq 25^\circ C$)*

representative of the lowest and the highest values tested.

The other RMS plots presented in this Sub-section are for a frequency band of $[0.1 \div 20]$ kHz . This range has been chosen because of the results of the cross-correlation analysis to be showed in the following. These results, in fact, sounded only in that range of frequencies. Note, then, how the spectra presented in the preceding Sub-section show all the signal amplitudes at 20 kHz at least ten times less than the corresponding peak values. Hence, the great part of the signal power is within this range of frequencies. This is finally confirmed by Fig. 3.55 where the filtered and unfiltered signals are plotted along with each other for the clean plate configuration at Mach 2.3. There appears how the RMS values from both signals are very close to each other.

3.6.2.1 Noise RMS evolution

Figures 3.53 and 3.54 collect each three trends of noise RMS. This is showed dimensionless with respect to the average wall temperature of the insert and in percentage.

For each thin-film one can see that the RMS levels from the three different tests are rather similar, being the maximum difference in Fig. 3.53 $\simeq 0.3\%$ for thin-film 4 among the value of test 93 and those of tests TZT5 and 86, which are almost coincident. The maximum difference reduces to $\simeq 0.2\%$ in Fig. 3.54 for thin-film 1. This means that the RMS of the noise is acceptably

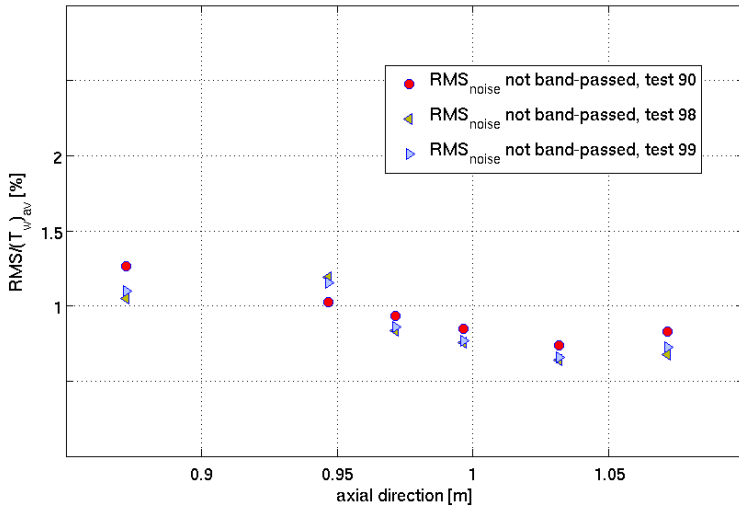


Figure 3.54: Three streamwise evolutions of noise RMS from the beginning of different tests ($M=2.3$, $T_{wall} \simeq 41^\circ C$)

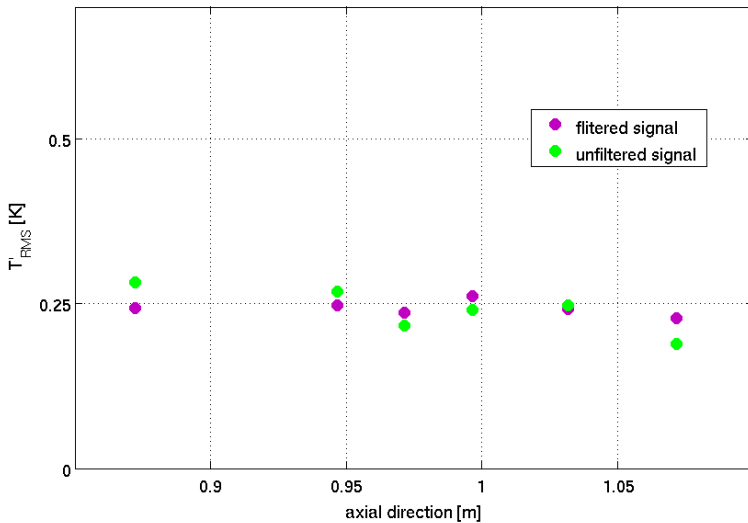


Figure 3.55: Streamwise evolutions of filtered and unfiltered RMS ($M=2.3$, clean configuration, $T_{wall} = 26^\circ C$)

repeatable from test to test, so that the electronics worked in the same correct way in all the tests treated.

3.6.2.2 Streamwise evolution of wall-temperature fluctuations

Here are presented the RMS streamwise trends at different wall temperatures, for different Mach numbers, and for both roughness heights tested.

These RMS have been calculated in the frequency domain exploiting the Parseval's theorem [37, pp. 492-493] that allowed the cleaning of the signal RMS from the electronic-noise influence. This theorem states that the integral of the signal power spectral density per unit time over a range of frequencies is equal to the mean square amplitude of the signal within that range of frequencies. Thus, the test signal is here automatically cleaned from electronic noise by applying this integration to the power spectral densities per unit time resulting from the subtraction of the noise spectrum from the signal spectrum, i.e., those presented in previous Sub-section 3.6.1. This results in a procedure for noise elimination neater and more consistent than subtracting directly the noise RMS from the signal RMS both calculated separately in the time domain.

All the plots henceforth show not only values from the sensors so far used for the streamwise trends, but also values from the others on the three rows (\times , \star , $*$). They give an estimation of the RMS spanwise trend, or can be representative of the value from the sensor along the plate when this was not available (e.g., thin-film 9 on the first row). The streamwise position is given respect to the leading edge of the ramp, that is, the bleed slot lip (see Fig. 2.2)

Figure 3.56 is for the clean configuration at Mach 2.3 and shows a rather constant RMS trend along the plate, and also across the sensor rows except for one thin-film on the second row.

Then RMS values in Fig. 3.57 show the effect of the 0.1-mm-high roughness at Mach 2.3: the RMS just downstream of the roughness is lower than the value upstream of it, it goes up back to it at about $x=1$ m, it overshoots this value, and goes back to a lower value further downstream. Unlike the central sensors, the lateral thin-films on first and second rows do not show any RMS increase respect to the sensors just downstream of the roughness; on the opposite, their RMS are slightly lower. Then, one of the sensors on the third row overshoots, while the other gives an RMS coincident with that from the central sensor. For comparison in the plot is reported the value 0.25 K along which the RMSs of the clean configuration evolve. It seems that the roughness effect is confined to the very central sensors aligned downstream of it, especially from 1 to 1.05 m, while away from the centerline (1.1 cm on both sides and across both the first and the second rows) the differences respect to the clean configuration are less sensible.

Figure 3.58, for $k=0.1$ mm and the highest wall temperature tested, shows that the RMS is as sensible to changes in wall temperature as to show prac-

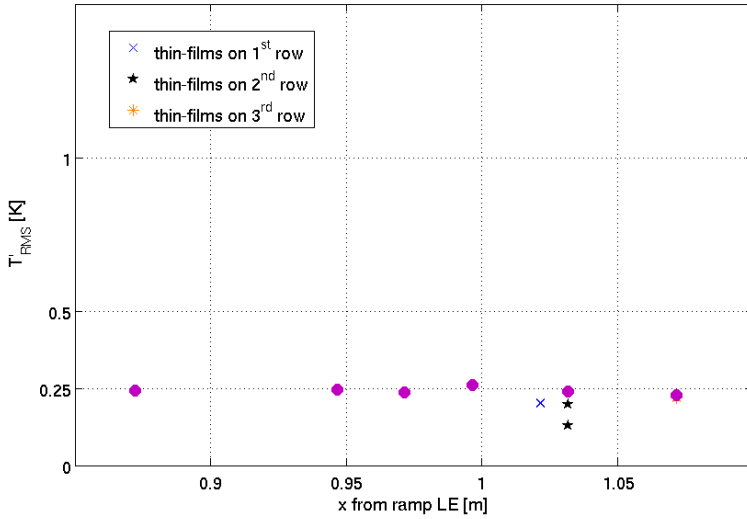


Figure 3.56: *Thin-films RMS streamwise evolution ($M=2.3$, clean insert, $T_{wall} = 26^\circ C$, $f_{LP} = 20$ kHz)*

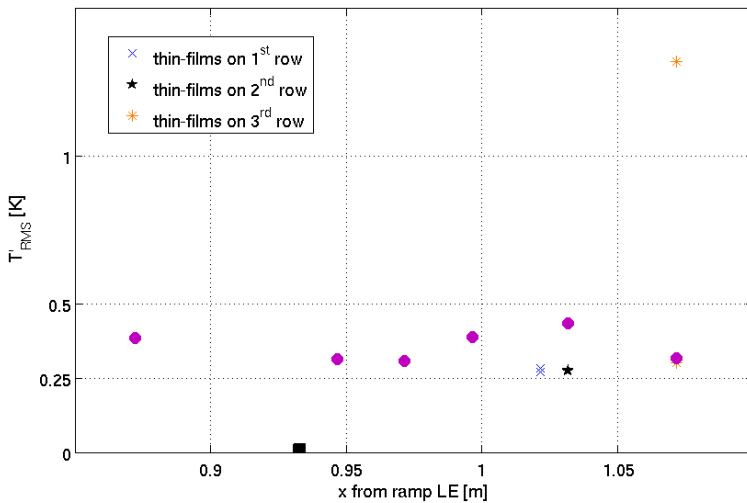


Figure 3.57: *Thin-films RMS streamwise evolution ($M=2.3$, $k=0.1$ mm, $T_{wall} = 26^\circ C$, $f_{LP} = 20$ kHz)*

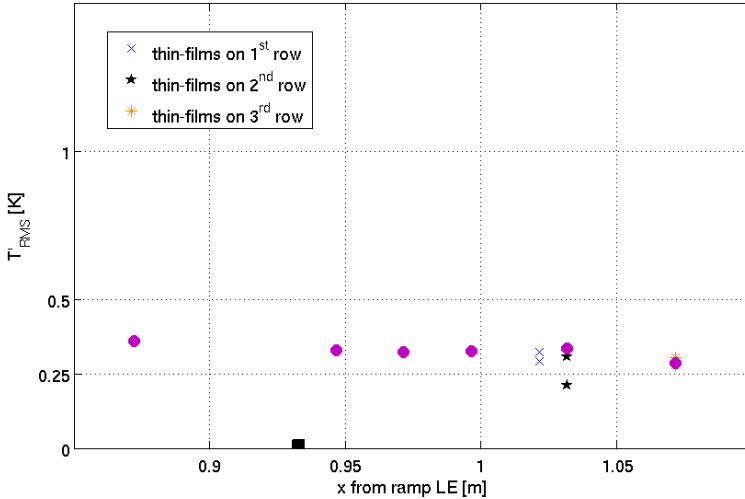


Figure 3.58: *Thin-films RMS streamwise evolution ($M=2.3$, $k=0.1$ mm, $T_{wall} = 33.5^\circ\text{C}$, $f_{LP} = 20$ kHz)*

tically no roughness effect for an increase of 7.5 Celsius. In fact there is no more any RMS increase between 1 and 1.05 m. The last sensor, however, keeps showing an RMS lower than that of thin-film 1 upstream of the roughness. Spanwise, for the highest wall temperature, the external sensors confirm the constant RMS value found streamwise, except one on the second row (\star) that has it lower; no sensor on the third row overshoots the values from the others, this time. The wall temperature has, then, practically erased the RMS increase at the locations of the fourth and the fifth sensors in Fig. 3.57.

Figures 3.59 and 3.60 show the RMS of the temperature fluctuations at Mach 2.3, with the roughness 1-mm high, and at the lowest and the highest wall temperatures, respectively.

The comparison between these two plots shows that the temperature increase makes only a very slight difference in the RMS values; also for the thin-film upstream of the roughness. But more noteworthy respect to the previous cases is the effect of the highest roughness: the RMS of the temperature fluctuations decreases monotonically with the distance from the roughness, downstream of which now the RMS peak appears. This happens for both wall temperatures. This trend, then, is practically the opposite of that for the 0.1-mm-high roughness, for which the RMS increases with the distance from the roughness up to a certain point. Spanwise, finally, one can note that the differences in RMS across the second row reduces sensibly with the temperature.

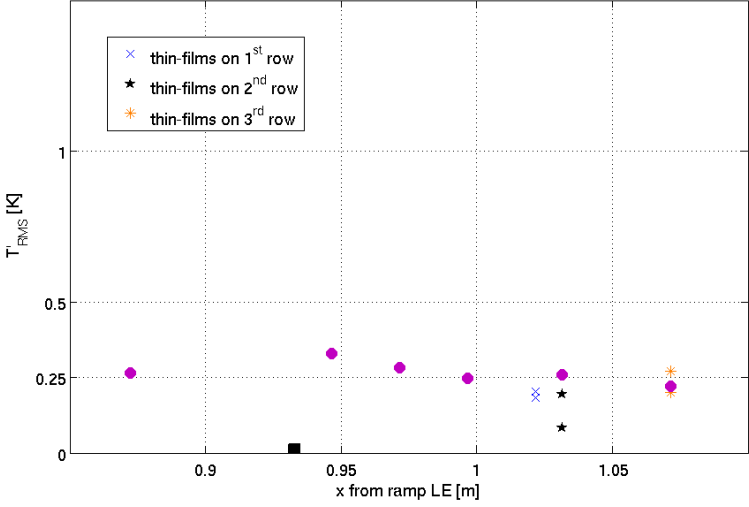


Figure 3.59: *Thin-films RMS streamwise evolution ($M=2.3$, $k=1$ mm , $T_{wall} = 15^{\circ}C$, $f_{LP} = 20$ kHz)*

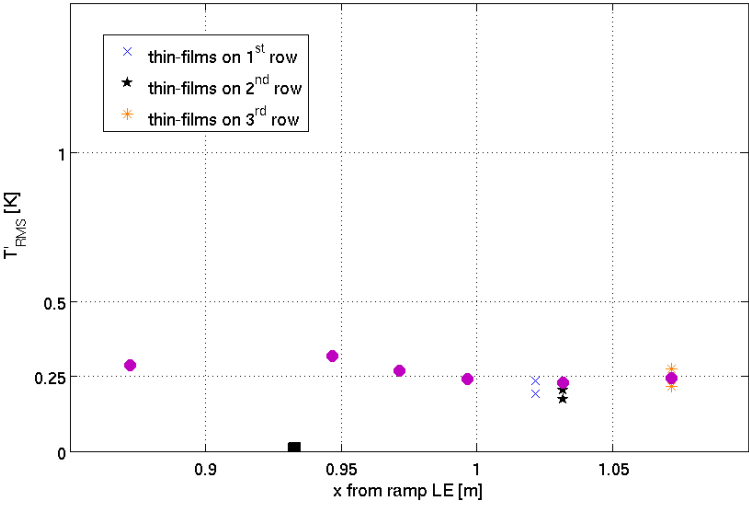


Figure 3.60: *Thin-films RMS streamwise evolution ($M=2.3$, $k=1$ mm , $T_{wall} = 42.5^{\circ}C$, $f_{LP} = 20$ kHz)*

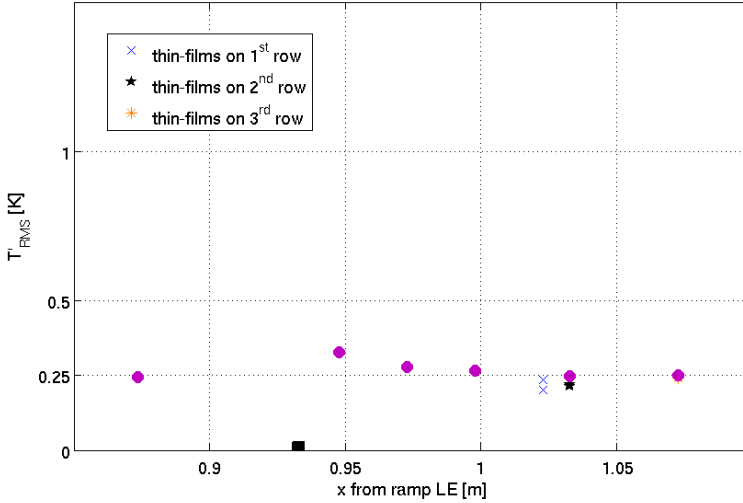


Figure 3.61: *Thin-films RMS streamwise evolution ($M=1.6$, $k=1$ mm , $T_{wall} = 26^{\circ}C$, $f_{LP} = 20$ kHz)*

The same comparison between RMS trends at different wall temperatures is proposed for the Mach 1.6 cases by Figs. 3.61 and 3.62.

As far as the wall-temperature effect is concerned, there is no difference respect to the Mach 2.3 case: again the 1-mm-high roughness makes the RMS decrease monotonically along the insert, be it the wall temperature the highest or the lowest. It is as well evident from both trends that the absolute maximum is reached just downstream of the roughness, and that the RMS trends end their monotonic decrease close to the value of thin-film 1 for both wall temperatures. The RMS values from the external sensors across the rows confirm the general streamwise trend. On the second and third rows they are practically coincident with the value from the central thin-film.

In the end, signals RMS have yielded new insights in the general effect of roughness and wall temperature on the temperature fluctuations. The roughness effect is found to revert increasing the roughness height from 0.1 mm to 1 mm at the lowest wall temperatures and at Mach 2.3. For $k=0.1$ mm the lowest RMS values are closer to the roughness and tend to increase along the insert. While for $k=1$ mm the RMS peaks just downstream of the roughness to decrease monotonically to a value equal to or lower than that upstream of the roughness. Wall temperature, instead, is found capable of affecting the streamwise RMS trend only for the smallest roughness at Mach 2.3. Interestingly enough, this happens even if for $k=0.1$ mm and Mach 2.3 the difference between the maximum and minimum wall temperatures tested

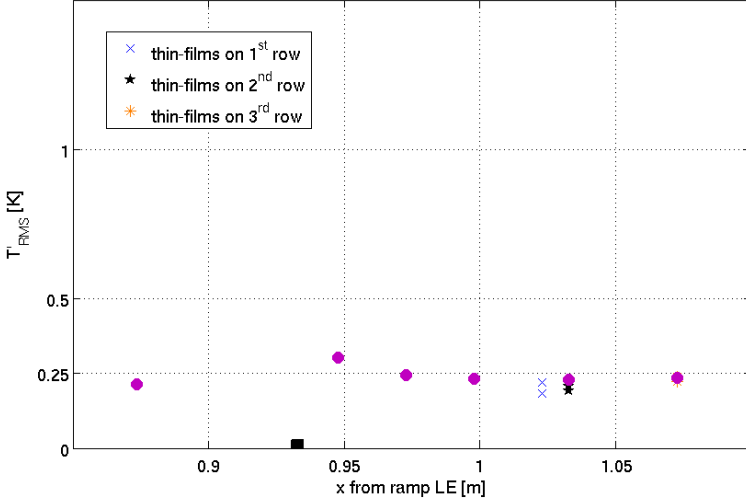


Figure 3.62: *Thin-films RMS streamwise evolution ($M=1.6$, $k=1$ mm , $T_{wall} = 38^\circ C$, $f_{LP} = 20$ kHz)*

is the lowest among the three test cases presented.

Regarding the Mach number effect for $k=1$ mm, the same streamwise trend as for Mach 2.3 is also found at Mach 1.6.

A second general result is that the RMS amplitude evolves practically always around the same average value of 0.25 K. And this happens whatever the Mach number, the roughness height (or presence), and the wall temperature. This, then, seemed the most significant value to be compared to literature data. These data are found in refs. [38, 39].

Laufer and Vrebalovich [38] present hot-wire measurements of temperature fluctuations within a supersonic laminar boundary layer with $M_\infty = 2.2$, and $Re_u = 77000$ in^{-1} in the frame of a study on natural stability and transition. Kistler [39], instead, presents the same type of data, but for a supersonic turbulent boundary layer with $M_\infty = 1.72, 3.56, 4.67$, and $Re_\theta \simeq 30000$. In ref. [38] temperature fluctuations in the laminar boundary layer tend to a value of $T'/T_\infty \simeq 0.0005$ as the distance to the wall reduces, and have their amplitude peak at $T'/T_\infty \simeq 0.0016$. These fluctuations are due to the Tollmien-Schlichting waves present within the boundary layer still laminar. In ref. [39], on the other hand, temperature fluctuations tend to about 0.03 as the distance to the wall reduces, but the quantity that describes them is not T'/T_∞ but a function of T' , T_∞ , T_w , and T_0 . This quantity has been reduced to T'/T_∞ with the freestream and wall values of the present tests to allow the comparison, it becomes: $T'/T_\infty \simeq 0.032$ for Mach 2.3 and 0.016 for Mach 1.6. Kistler finds that these turbulent temperature fluctuations are

produced by the transport of the temperature field by the turbulent velocity fluctuations.

Now, the RMS value of 0.25 K divided by T_∞ taken at the roughness position becomes 0.00165 for Mach 2.3 and 0.00127 for Mach 1.6. It is evident, then, that both values are one order of magnitude less than Kistler's turbulent values, and that the value for Mach 2.3 is practically equal to the peak of the temperature fluctuations induced by TS-wave in ref. [38]. This comparison, in the end, makes conclude that the wall temperature fluctuations do not show a turbulent character, but, at least for Mach 2.3, they are more akin to fluctuations due to instabilities still developing within a laminar boundary layer.

3.6.3 Wall-temperature fluctuations evolution in the (frequency,time) domain

Spectra throughout the test time have been plotted for each signal from each thin-film to find the time evolution of the wall temperature fluctuations spectral content. This particular plot is called a spectrogram. A typical spectrogram is presented in Fig. 3.63, and is a surface describing the amplitude of the fluctuation versus the time and the frequency. The fluctuation amplitude is also reported by a color scale as the one shown in Figs. 3.64 and 3.65. The FFT plots presented in Sub-section 3.6.1 can be seen as the view along the time axis of a spectrogram, thus they 'integrate' over the test time the frequency content of a signal. Only in a spectrogram, then, one can see whether a frequency peak has been just a single occurrence or repeats during the test time.

For the best clarity, in the following the spectrograms surface will not be shown three-dimensionally as in Fig. 3.63 but from the top view as in Figs. 3.64 and 3.65: time and frequency will be the plot axes, while the color scale will illustrate the fluctuation amplitude. This amplitude in general depends on the size of the window by which the signals samples are treated, and usually has to depend on the test duration to have the best plot resolution. However, the tests here analyzed have different durations, thus for the sake of a meaningful comparison, a fixed window has been used for all of them. This resulted in some spectrograms appearing coarser than others. Moreover, a frequency resolution of 50 Hz has been used to avoid too long times for the generation of the plots.

3.6.3.1 Roughness height and Mach number effects on the time evolution of T' frequency content

Figure 3.64 shows the spectrogram of the signal of thin-film 5 for the clean insert-configuration. It is evident how frequency peaks do not occur throughout the entire test time, but they appear at given instants and without any apparent regularity. Another evidence is that the peaks are mostly con-

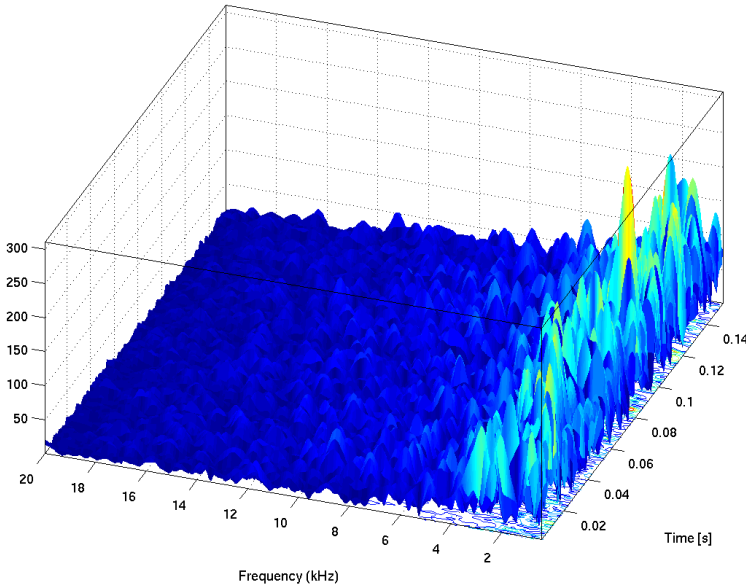


Figure 3.63: *Typical spectrogram of an unsteady signal: $A = A(f, t)$*

centrated below a threshold value during the test time, while above it they become rarer and rarer; in Fig. 3.64 this frequency is about 4 kHz. Above about 17 kHz the fluctuation amplitudes reduce to at least 1/3 of the peak value.

Figure 3.64 can be compared to Fig. 3.65 to single out the effect of the 0.1-mm-high roughness for a wall temperature practically the same. And this effect is indeed scarce: except for some more frequent activity at frequencies higher than 4 kHz, and a relative increase in the number of main peaks below the same threshold, there are no other differences. Note as well how the main peaks keep the same amplitudes as in the clean insert case.

The spectrograms of the signals from the remaining sensors have all the same features as of thin-film 5 spectrogram, thus their comparisons yield the same conclusions. That is, the 0.1-mm-high roughness does not change sensibly the fluctuations evolution in frequency and time respect to the clean insert configuration. This is so except for thin-film 14 whose signals are analyzed in the next two Figs. 3.66 and 3.67. This time differences are evident in: the generalized increase in the spectrum of frequencies excited; their higher frequency in time; and the larger number of main peaks. The fluctuations highest amplitude, however, does not change much with the roughness.

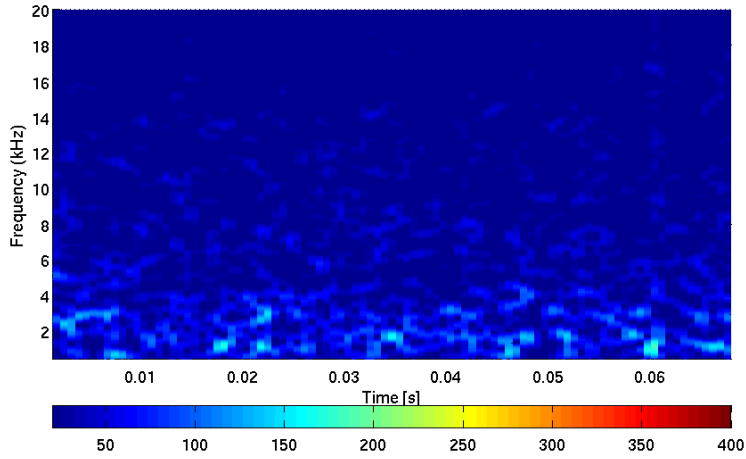


Figure 3.64: Spectrogram of TF nr. 5 signal ($M=2.3$, clean insert, $T_w=27^\circ C$)

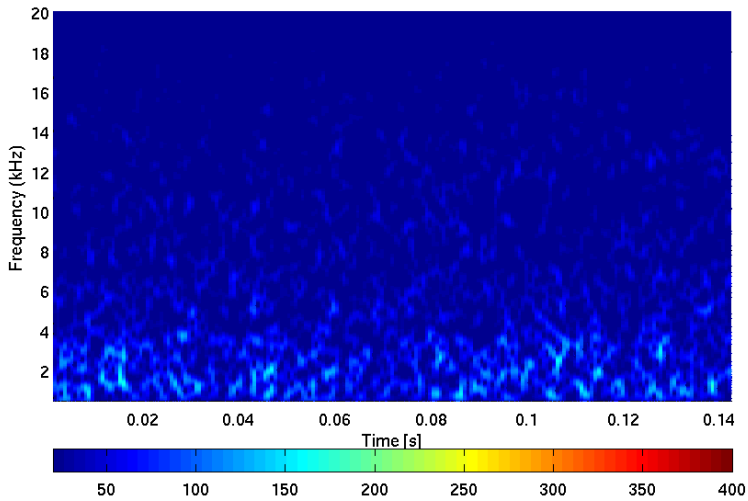


Figure 3.65: Spectrogram of TF nr. 5 signal ($M=2.3$, $k=0.1$ mm, $T_w=28^\circ C$)

Next is the comparison between the clean configuration and the 1-mm-high roughness configuration at Mach 2.3 for practically the same wall temperature. Figures 3.68 and 3.69 show the effect of the highest roughness

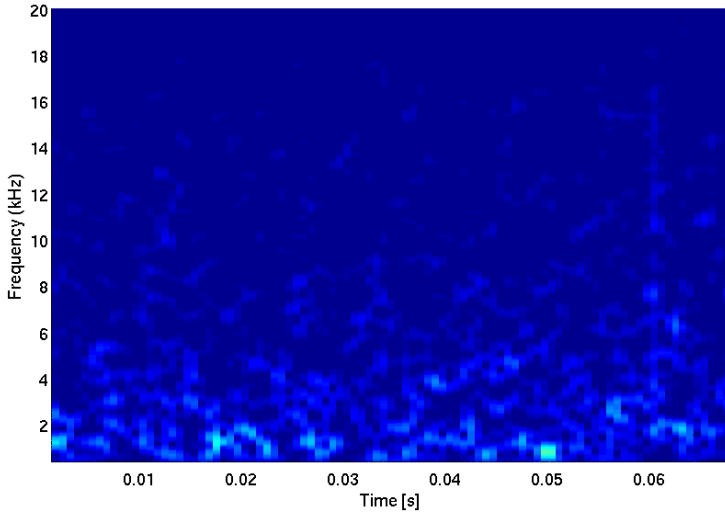


Figure 3.66: Spectrogram of TF nr. 14 signal ($M=2.3$, clean insert, $T_w=27^\circ C$)

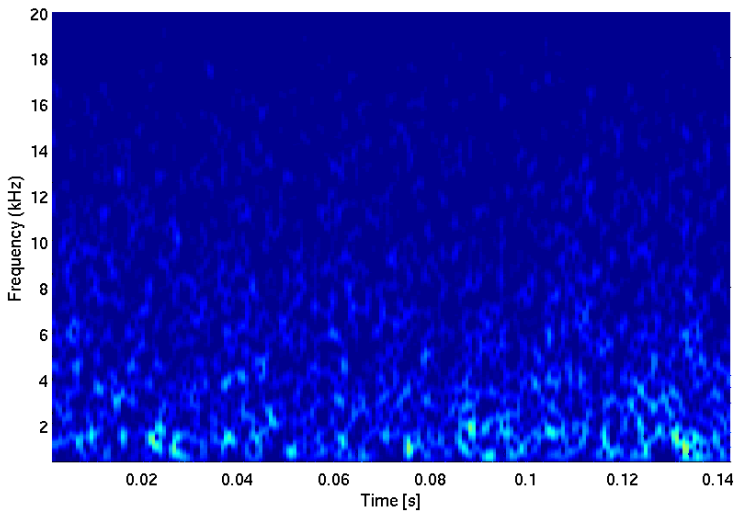


Figure 3.67: Spectrogram of TF nr. 14 signal ($M=2.3$, $k=0.1$ mm, $T_w=28^\circ C$)

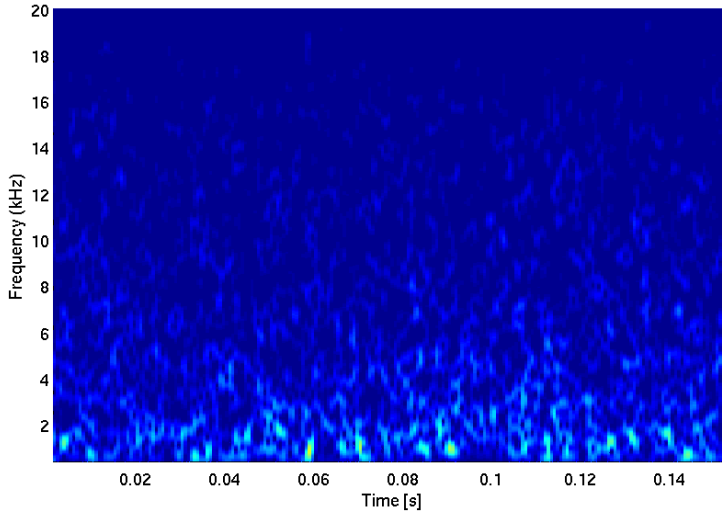


Figure 3.68: Spectrogram of TF nr. 4 signal ($M=2.3$, clean insert, $T_w=41^\circ C$)

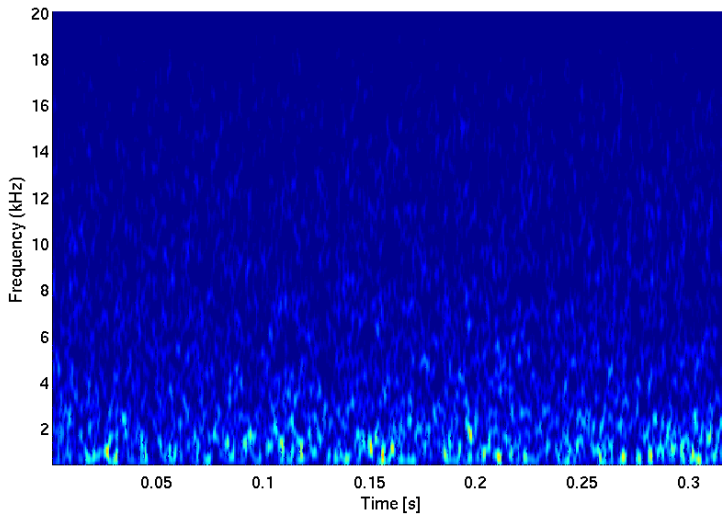


Figure 3.69: Spectrogram of TF nr. 4 signal ($M=2.3$, $k=1$ mm, $T_w=41.5^\circ C$)

tested on the signal from the thin-film closest to the roughness.

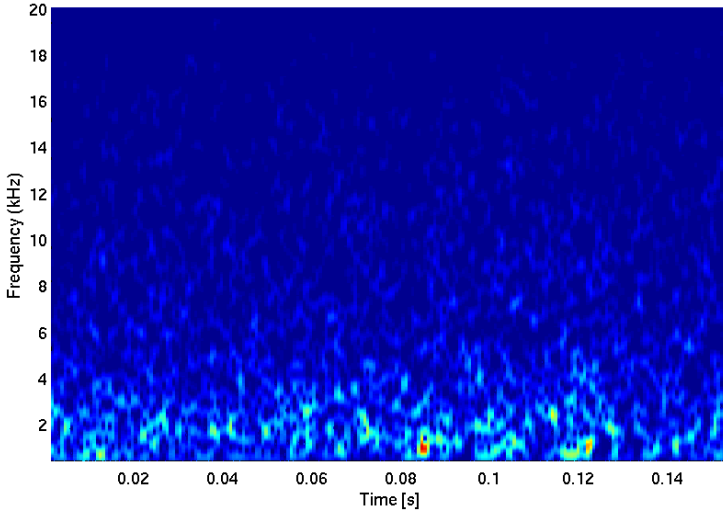


Figure 3.70: *Spectrogram of TF nr. 6 signal ($M=2.3$, clean insert, $T_w=41^\circ C$)*

Figure 3.69 shows more main peaks below about 4 kHz than Fig. 3.68, and more activity above the same threshold. Also in this case the highest amplitudes do not change with the roughness presence. Thus, the highest roughness increases the range of excited frequencies of the signal of the thin-film closest to it, while increasing as well the presence of main peaks throughout the test time. As for the other spectrograms, finally, these main peaks do not show any evident regularity in their appearance through the test time.

The comparison between the spectrograms from thin-film 6 (Figs. 3.70 and 3.71) is representative of the comparisons for all the thin-films downstream of thin-film 4. One can see that the presence of the roughness: reduces the band of the most excited frequencies, from about 5 kHz to about 3 kHz; reduces the intensity of the main peaks; and reduces the value of the lowest frequency excited. It seems to reduce the presence in time of a given peak, as well: there seem to be more peaks aligned in time along a given frequency with the clean insert than with the roughness. These effects are the opposite of what found for the 0.1-mm-high roughness.

Finally, the effect of the 1-mm-high roughness at Mach 1.6 is presented by Figs. 3.72 and 3.73. The tests with the most similar wall temperature values are chosen for the comparison to highlight the roughness effect. Spectrograms are for thin-film 5, but conclusions can be extended to thin-films 4 and 6 as well. In these figures one can see that a higher frequency spectrum is excited through the test time with the roughness, even if the amplitudes of

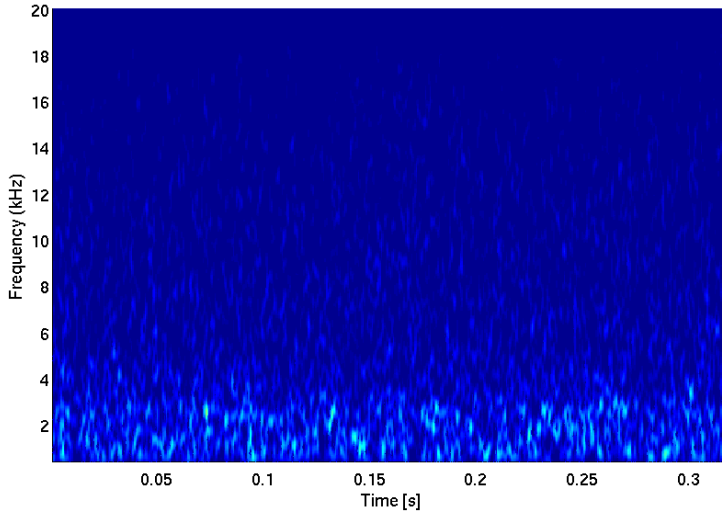


Figure 3.71: Spectrogram of TF nr. 6 signal ($M=2.3$, $k=1$ mm, $T_w=41.5^\circ C$)

these peaks do not increase respect to the clean-insert case. The main peaks stay below about 4 kHz but are more present in time with the roughness than with the clean-insert.

The spectrogram from thin-film 14, on the second row of sensors, instead, is representative of what happens downstream of thin-film 6. Starting from roughly 90 mm from the roughness, the roughness effect essentially fades, and the spectrograms in Figs. 3.74 and 3.75 look rather similar to each other. The roughness presence, however, still yields more activity between about 2 kHz and 6 kHz. The frequency around which the main peaks stay through the test time seems lowered by the presence of the roughness.

3.6.3.2 Wall-temperature effects on the time evolution of T' frequency content

The analysis of the signals spectrograms brought out two general effects of wall temperature: the range of excited frequencies is enlarged, and peaks repetition in time is increased. However, these features may not appear all together, and, more important, do not appear at all in the spectrograms of some sensors for some test conditions. Figures 3.76 and 3.77 show how an increase of $9^\circ C$ in wall temperature yields an increase in the repetition in time of main peaks, but range-wise the excited frequencies are more or less the same as for the coldest wall.

The following Figs. 3.78 and 3.79 for the Mach-1.6 case, instead, show no

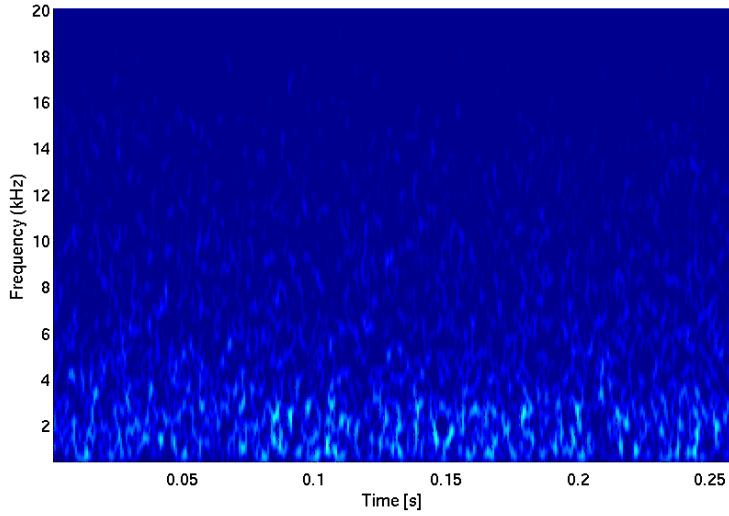


Figure 3.72: Spectrogram of TF nr. 5 signal ($M=1.6$, clean insert, $T_w=27^\circ C$)

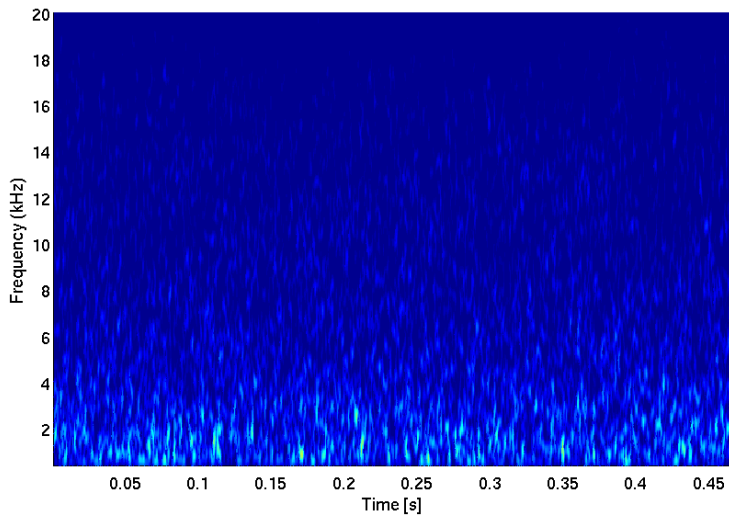


Figure 3.73: Spectrogram of thin-film 5 signal ($M=1.6$, $k=1$ mm, $T_w=26^\circ C$)

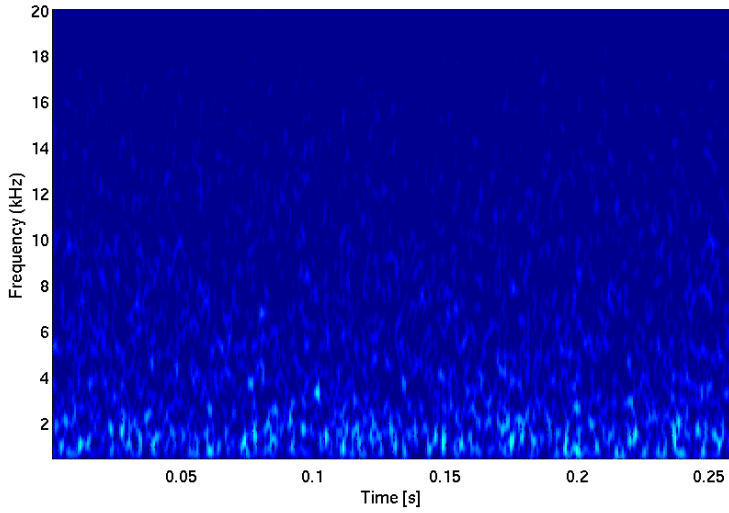


Figure 3.74: Spectrogram of TF nr. 14 signal ($M=1.6$, clean insert, $T_w=27^\circ C$)

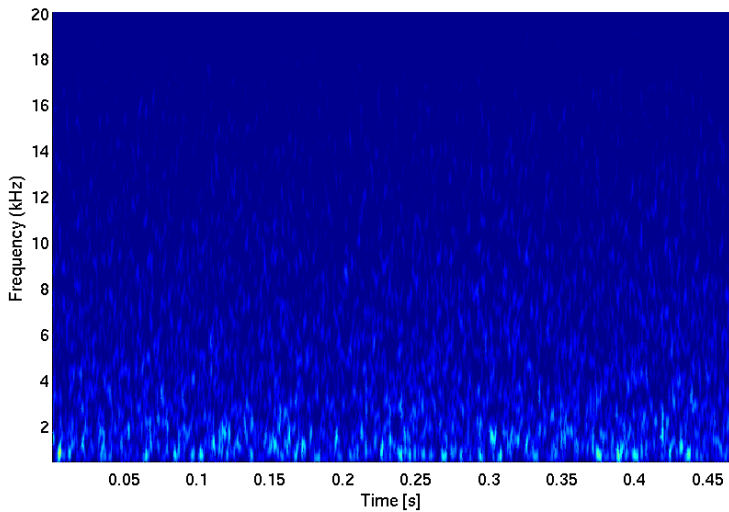


Figure 3.75: Spectrogram of TF nr. 14 signal ($M=1.6$, $k=1$ mm, $T_w=26^\circ C$)

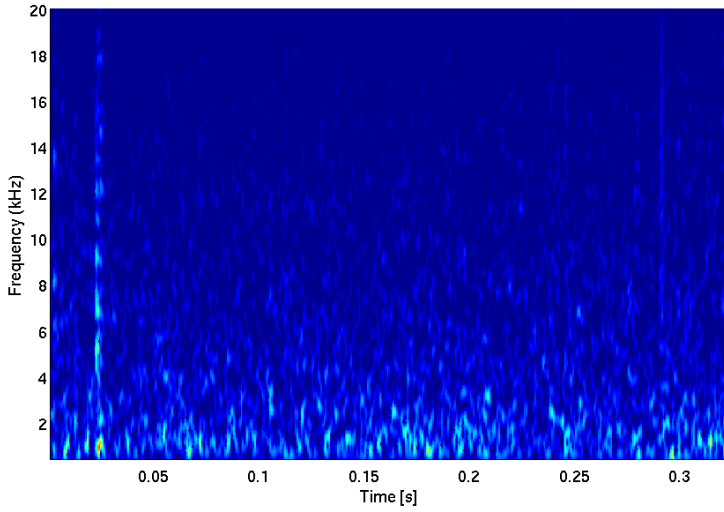


Figure 3.76: Spectrogram of TF nr. 4 signal ($M=2.3$, $k=0.1$ mm, $T_w=24.5^\circ$ C)

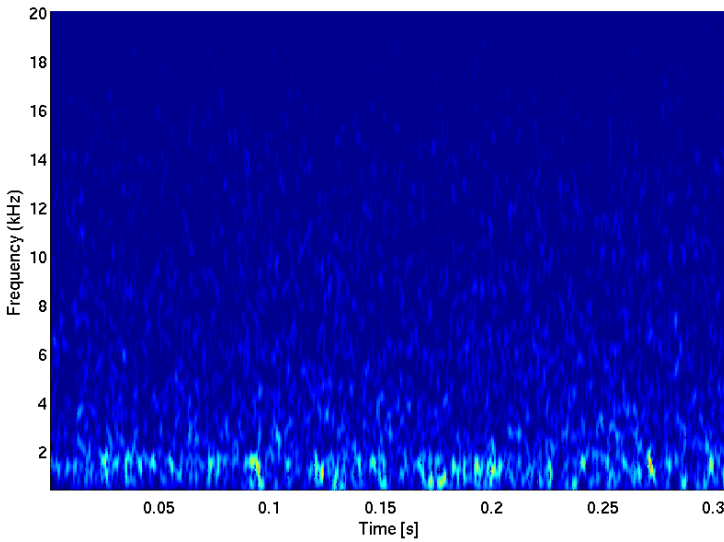


Figure 3.77: Spectrogram of TF nr. 4 signal ($M=2.3$, $k=0.1$ mm, $T_w=33.5^\circ$ C)

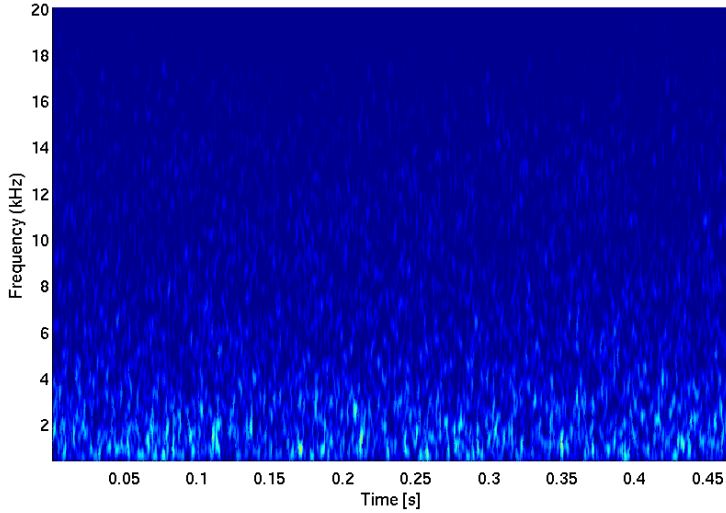


Figure 3.78: Spectrogram of TF nr. 5 signal ($M=1.6$, $k=1$ mm, $T_w=26^\circ C$)

sensible differences in the spectrograms of thin-film 5 upon a wall temperature change of $14^\circ C$.

This was the generalized behavior of the three sensors closest to the roughness, and also of thin-films 6 and 9 for the 1-mm-high roughness case at Mach 2.3.

3.6.3.3 Wall-temperature fluctuations evolution in the (frequency,time) domain: conclusions

The spectrograms presented in this Sub-section shed light on the time evolution of the frequency content of the thin-film signals, thus complementing the analyses made in Sub-section 3.6.2 and adding some new information.

It is evident how the spectrograms presented for the 0.1-mm-high roughness Mach-2.3 case confirm the conclusions drawn from the comparison between Figs. 3.56 and 3.57, that is, only on the second row of sensors (thin-film 14) a sensible difference respect to the clean-insert case is found; the other streamwise-oriented sensors yield the same fluctuation intensity as without roughness. The same confirmation comes from the spectrograms for the 1-mm-high roughness at Mach 2.3. Here again the important difference among the fluctuations intensity at the location closest to the wall and that of all the others is highlighted clearly as by the RMS trend in Fig. 3.59.

Finally, the spectrograms for the Mach-1.6 case also confirm the corresponding RMS trends (Fig. 3.61): the roughness effect is confined down to

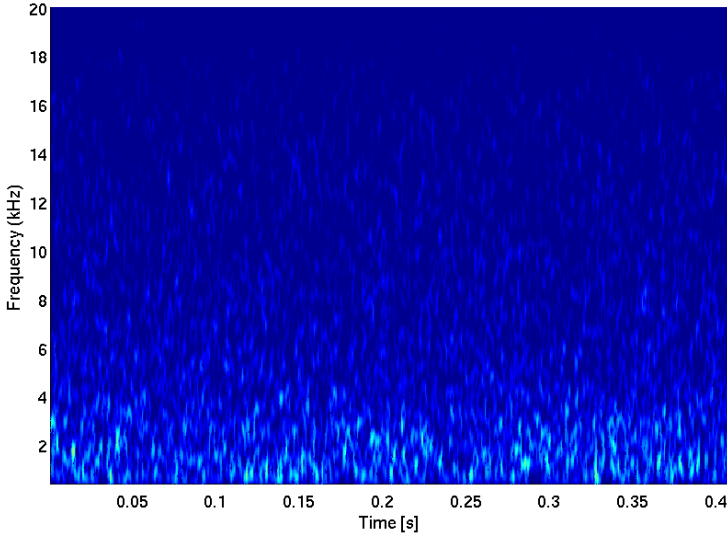


Figure 3.79: Spectrogram of TF nr. 5 signal ($M=1.6$, $k=1$ mm, $T_w=38^\circ$ C)

thin-film 6, so that downstream of it changes respect to the clean-insert configuration are not sensible.

The main difference among the cases above mentioned was generally an increased amount of peaks along the test time for those signals with larger fluctuation intensities, while the fluctuation amplitudes were almost the same. The range of excited frequencies broadened, as well, but generally main peaks never moved up in the spectrum respect to the less excited case. The same evidences come from the higher wall-temperature cases. Thus, one may tentatively conclude that both roughness and wall temperature increase the overall intensity of the wall-temperature fluctuations in the same way, that is, just by increasing in time the amount of peaks at frequencies already excited in the clean and/or coldest-wall cases.

The generalized irregular appearance of frequency peaks along the test time is the peculiar information from the spectrogram analysis. Even if in some cases the main peaks look aligned along a given frequency, or appear within a rather restricted band of frequencies, a clear repetition pattern in time is hard to find. Another aspect brought out by the spectrograms is that frequencies above 20 kHz stay unexcited throughout the entire test time, relatively to the lower ones.

3.7 Cross-correlation analysis of thin-films signals

The high-passed signals used in the previous Section for the spectral analysis have also been processed for cross-correlation analysis. This analysis aims at detecting possible phenomena passing through the boundary layer flow along the instrumented insert. More important, it provides a propagation velocity for these phenomena, in the form of the ratio of the distance between two sensors and the lag time between their signals.

Meaningful results from the cross-correlations were output only after filtering out the signals below 500 Hz and above 20 kHz.

Cross-correlations were calculated also for no-flow signals and for signals during the wind-tunnel starting phase as a check of the validity of the results. This was done to rule out any false match possibly coming from electronic noise, or coming from facility noise detectable also in the early phase of the wind tunnel flow. Figures 3.80 and 3.81 show the difference among cross-correlation outputs from no-flow signals (also representative of signals from the wind-tunnel transient starting-phase) and cross-correlation outputs from test-time signals. For the no-flow cases either the lag time is 0 s (top plot), that is no passing-phenomenon is detected, or there are many lag times equally possible (bottom plot). In the case of the in-flow signals, instead, a single clear peak is always present and yields a lag time different from zero. Hence, one can conclude that the cross-correlation outputs found from the signals taken during the test time come from phenomena happening only during the test time.

3.7.1 Cross-correlation results

Figure 3.82 shows the propagation velocities found for different wall temperatures tested at Mach 2.3 with the clean insert. The wall temperature value is color-scaled from blue (the lowest) to red (the highest) through green and yellow. The propagation velocity is calculated for each pair of consecutive thin-films along the instrumented insert, and this is why it is shown by a horizontal segment: this segment extends between the two thin films of the pair. The plot is complemented by the streamwise evolutions of freestream velocity and speed of sound (both from CFD) as visual benchmarks.

It is evident how the same propagation velocity value recurs across four pairs of thin-films starting from 0.95 m, that is thin-film pairs 5-4, 6-5, 9-6, 14-9. This value varies slightly or not at all with the wall temperature. The remaining pairs of thin-films give much more changing values, especially the first pair between thin-films 1 and 4. This situation is replicated for all the other configurations tested as shown by Figs. 3.83 and 3.84, for the 1-mm-high roughness cases at Mach 2.3 and 1.6, respectively (the former is also representative of the 0.1-mm-high roughness case at the same Mach number).

The propagation velocity value is $0.8 \cdot u_\infty$ for both Mach numbers, and is

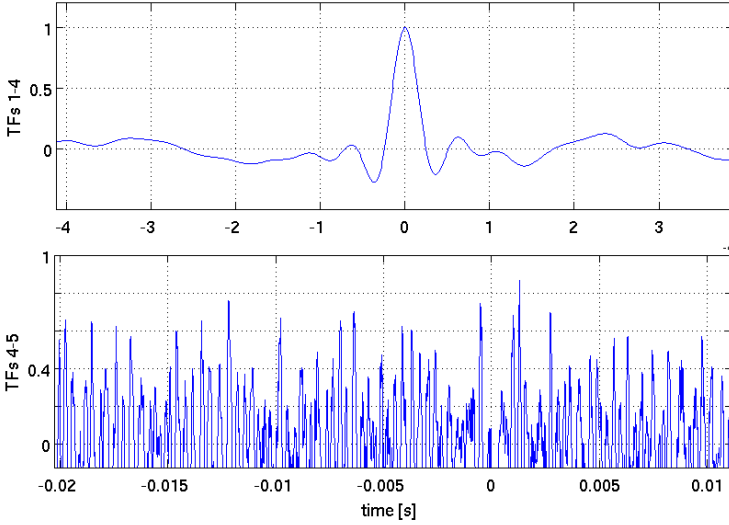


Figure 3.80: Typical cross-correlation outputs from no-flow signals (signal band pass= $[0.5 \div 20]$ kHz)

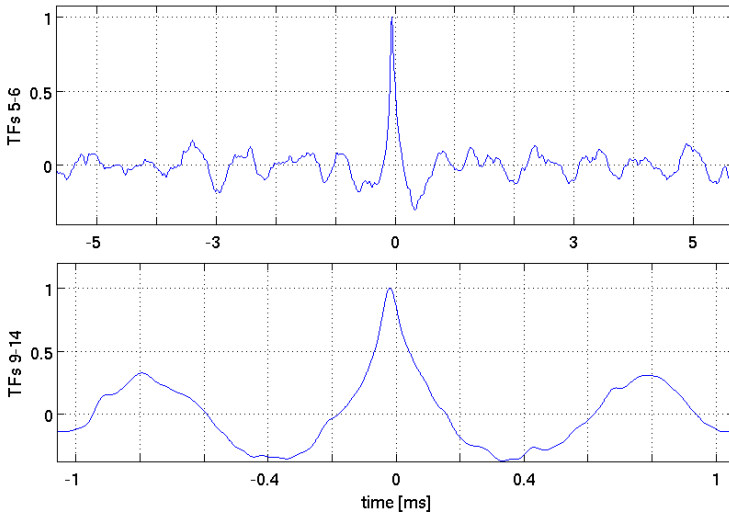


Figure 3.81: Typical cross-correlation outputs from signals at Mach 2.3 in clean-insert configuration (signal band pass= $[0.5 \div 20]$ kHz)

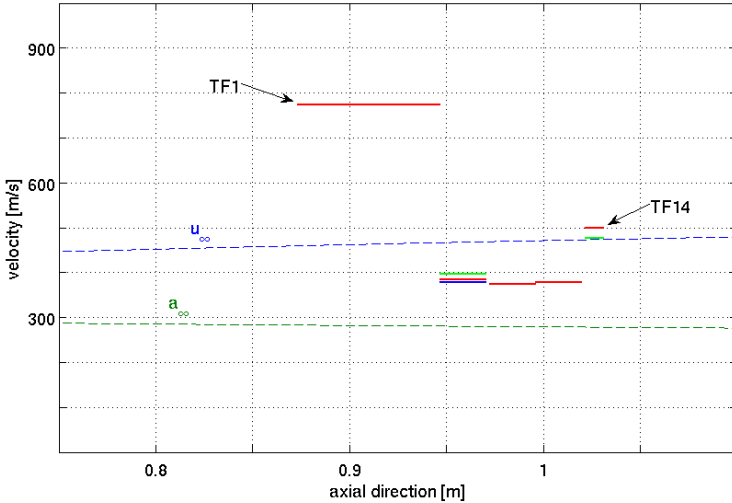


Figure 3.84: Propagation velocities from the cross-correlations between pairs of signals from thin-films along the insert (Mach 1.6, $h = 0.1$ mm)

not sensibly affected by wall temperature or roughness presence or height. This makes it hard to conclude that it is the propagation velocity of a phenomenon generated by the roughness.

As written in the introduction, signal cross correlations were also performed in no-flow conditions and at the starting of the wind tunnel, before and during the establishment of the supersonic flow within the divergent. They yielded no result similar to what found in Figs. 3.82 to 3.84. Thus some other hypotheses for the nature of this phenomenon were investigated.

First, pure acoustic noise from some fixed source within the wind tunnel has been considered, but readily ruled out because the propagation velocity is larger than the speed of sound at which acoustic noise would propagate. Also noise from a fixed source but close on the side(s) of the instrumented insert can be discarded, because it was not found compatible with the propagation velocities measured by the different sensors along the insert.

Secondly, vortical structures flow within the freestream were considered. In view of the internal structure of the compression tube between the air-feeding line and the nozzle convergent, one may suppose that some vortices may be generated there, and then likely convected downstream throughout the wind tunnel throat into the divergent, as to cause acoustic disturbances traveling above and along the thin-films. However, the vortices convection velocity is likely to be the freestream velocity, thus the absolute velocity respect to the thin-films should be the sum of the sound velocity and the freestream velocity, and, consequently, the propagation velocity of such a

disturbance would be larger than the freestream value, which is not the present case.

Finally, an electronic problem that happens only during the test is rather unlikely.

In conclusion, the phenomenon that has generated the cross-correlation peaks has not been clearly identified for the moment, but one could fairly conclude that it is not due to the presence of the roughness nor to the wall temperature value.

3.8 Time-resolved wall-pressure measurements

The unsteady pressure measurements were performed in order to characterize the pressure fluctuations in the boundary layer of the supersonic flow field under analysis. Unlike for the wall-temperature measurements, for these measurements also the 0.1-mm-high roughness was tested at Mach 1.6. In all the tests high-frequency pressure signals were acquired at seven locations, all downstream of the roughness elements. The surface flush mounted pressure sensors were placed $3.5d$, $25.5d$, $46d$, $58.5d$, $71d$ and $86d$ away from the roughness element. Measurements were made at two locations on both sides $\pm 2d$ away from the centerline to observe the spanwise variation of unsteady pressure fluctuations far downstream of the roughness element. The position of the roughness element respect to the measurement locations is depicted in Fig. 3.85.

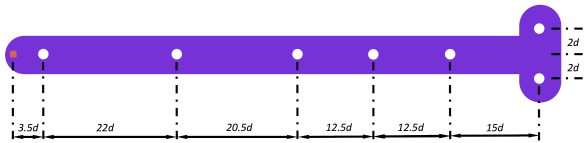


Figure 3.85: *The PCB insert mounted into the lower ramp of the supersonic wind tunnel*

Piezo-electric pressure transducers of the type 132A31 with resonance frequency of 1 MHz were used for time-resolved measurements. The signal is low-pass filtered at 250 kHz and sampled at 1 MHz. The spectral analysis of the high frequency signal has been performed to characterize the unsteadiness in the boundary layer of the supersonic flow over the flat plate. Fourier and Welch spectra of the pressure signal at each measurement location and for every flow condition tested were extracted. The excited frequencies were extracted in the mean and overall spectra. Furthermore, the temporal spectra of each signal throughout the test duration have been analyzed by means of spectrograms. The intermittent excitations become visible by such an analysis.

Among the eight PCBs, the one in the middle of the spanwise row went irresponsive during the first test and therefore is not reported in Fig. 3.85. However, the other PCB sensors, except PCB 3, gave too low signal-to-noise ratios for certain acquisitions. Hence, results are here presented only for PCB 3, which resulted the only one with a trustworthy signal for all test conditions.

3.8.1 Fourier analysis of unsteady pressure signal

3.8.1.1 Broadband spectrum up to 250 kHz

The frequency spectra of the PCB signals were calculated to understand the development of flow unsteadiness along the wake of the roughness element. The spectra were first investigated for their broadband content. The power spectrum density levels of the unsteady pressure fluctuations are plotted for each test condition as depicted in Fig. 3.86. No spectra exhibit Kolmogorov decay of $(-5/3)$ for the fully turbulent boundary layer. Hence the state of the boundary layer downstream of the roughness element cannot be concluded from the broadband FFT analysis. The boundary layer state may either be laminar or transitional. Moreover, no distinctive frequency excitation has been observed on the unsteady pressure spectra beyond 10 kHz.

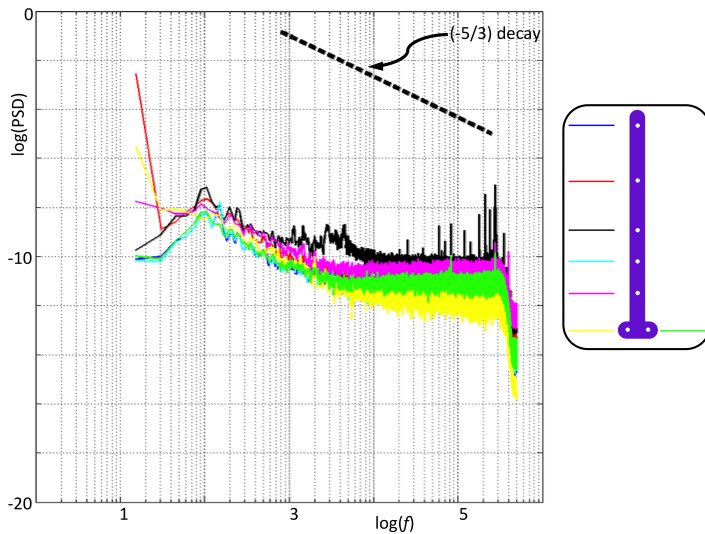


Figure 3.86: The broadband spectra of PCB sensors for the test at $M=2.3$ with 0.1 mm roughness

3.8.1.2 Narrow band spectrum up to 15 kHz

The low range frequency spectrum of the pressure fluctuations is exemplified in Fig. 3.87. The pronounced individual peaks are always observed at the values lower than 6 kHz for all test conditions. An additional band of frequencies between 7 and 10 kHz was observed to be excited for test at $M=1.6$. The amplitudes of such band of peaks increase with the roughness height. On the other hand, the strength of the fluctuations below 6 kHz are better appreciated when the free stream Mach number is increased to 2.3.

Furthermore, the amplitude of the low frequency peaks have reduced when the roughness with 0.1 mm was introduced to the flow. The increase in the roughness height also led to an amplification on those frequencies. This trend in PCB spectra is further investigated by spectral analysis throughout the flow time (Spectrogram analysis) in Sub-section 3.8.1.4.

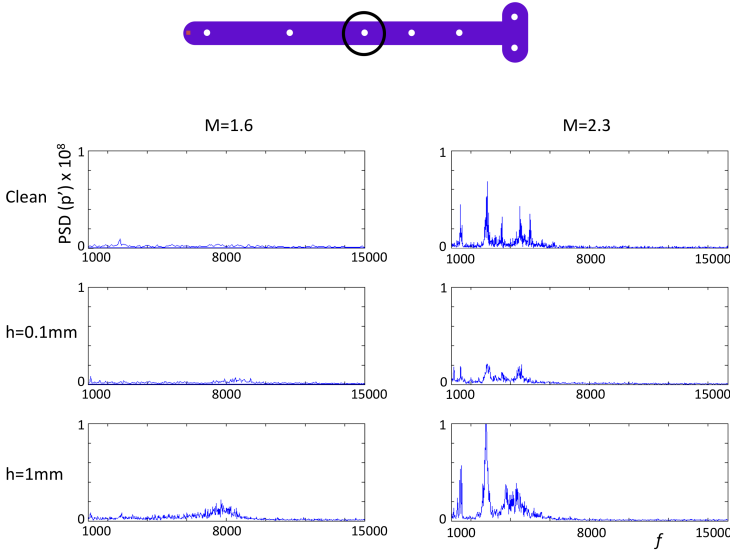


Figure 3.87: *The low frequency spectra of third PCB sensors downstream of the roughness element for all test conditions*

3.8.1.3 Quantification of unsteadiness downstream of the roughness element

The variation in the pressure unsteadiness commented in the previous section, and depicted in Fig. 3.87, was quantified by calculating the root-mean-square (RMS) of the unsteady pressure signal of the PBC gauge of interest. RMS values were calculated for each test condition and roughness height by the integration of the FFT signal for the range of frequencies $[100 \div 10000]$ Hz in the spectra. The mean levels of RMS together with the standard deviation resulting from the test repetitions are given in Table 3.5. It was observed that the introduction of the roughness element of 1 mm height resulted in an increase as high as 27% in the flow unsteadiness from the clean configuration. But the opposite was found for the 0.1-mm-high roughness. In this case, in fact, the RMS values do not increase but slightly decrease respect to the clean configuration; and for both Mach numbers. Finally, Mach-wise, the level of unsteadiness is the most pronounced for the highest free stream Mach number for all the three configurations tested.

| | | clean insert | | k=0.1 mm | | k=1 mm | |
|------------------------|-----|--------------|------|----------|------|--------|-----|
| M_∞ | | 1.6 | 2.3 | 1.6 | 2.3 | 1.6 | 2.3 |
| $RMS \times 10^{-3}$ | [V] | 1.77 | 2.18 | 1.66 | 2.11 | 2.16 | 2.8 |
| $STDEV \times 10^{-4}$ | [V] | 0.57 | 0 | 0 | 2.14 | 0.83 | 2.5 |

Table 3.5: *RMS values of the pressure fluctuations measured by PCB nr.3*

3.8.1.4 Wall-pressure fluctuations evolution in the (frequency,time) domain

The temporal evaluation of the frequency spectrum has been made as for the thin-films signals analysis. The function calculates the frequency spectrum of the signal throughout the given flow time with certain windowing and overlap. In this analysis, the window length and the overlap were chosen to be 20000 samples and 19950 samples respectively to maximize the resolution of the spectrograms. The spectrograms representing all test cases are plotted in Fig. 3.88.

The time-resolved spectra validates the trends observed in the averaged frequency analysis. The strongest unsteady activity below 6 kHz is observed for the largest roughness element for the M=2.3 test. Nevertheless, the unsteadiness is not observed continuously over the test duration but appears rather intermittently throughout it. Moreover, Fig. 3.88 depicts that the overall unsteady activity spreading the entire spectrum up to 15 kHz is gradually reduced passing from the clean plate configuration to the 1-mm-roughness configuration for Mach 2.3. That is, the excited frequencies tend to concentrate toward a defined band below 8 kHz. For M=1.6, instead, the excited frequencies at 8 kHz are amplified by increasing the roughness height, and this concentration effect of the roughness is not as clear as for Mach 2.3.

3.8.2 Conclusions on the unsteady pressure measurements

There are some general evidences that emerge from the pressure fluctuations analysis.

Figure 3.87 shows peaks at about 1.5 and 3 kHz for all the three configurations tested at Mach 2.3. Their amplitudes decrease going from the clean-insert configuration to the 0.1-mm-high roughness configuration, but increase again for 1 mm. The amplitudes for the 1-mm-high roughness are the highest among the three configurations, hence, this roughness element increased the unsteadiness within the boundary layer. This increase is confirmed by the RMS values in Table 3.5. This amplitude trend with the roughness height seems to be more general, since Fig. 3.87 shows as well that all the frequencies in the excited band for the clean-insert configuration reduce their amplitudes for the 0.1-mm-high roughness and increase

them again for the case with the high roughness. Nevertheless, all excited frequencies are below 6 kHz for all conditions at Mach 2.3.

For Mach 1.6, instead, the band of excited frequencies centers around 8 kHz in both roughness configurations. Highest amplitudes are induced by the highest roughness. In the clean configuration, instead, no bands are clearly visible, but only one peak at about 2700 Hz. For this Mach number amplitudes seem always to grow going from the clean-insert to the 0.1-mm and to the 1-mm-high roughness configurations, but this is not what found in the RMS analysis. Also for this Mach number, in fact, Table 3.5 shows the RMS slightly decreasing with the smallest roughness, respect to the clean configuration values. Probably the sole peak about 2700 Hz found for this latter configuration is responsible of this difference.

Figure 3.88 confirms the extent of the excited frequencies bands in Fig. 3.87 for both Mach numbers, and adds the evidence that they are kept throughout the whole test time. However, this happens intermittently and without any clear regularity. Furthermore, the spectrograms show how the scarce activity above these excited bands tend to concentrate within smaller and smaller time intervals as the roughness height increases. In fact, what could be described as 'threads' of frequencies along large intervals of time become more and more like 'spots' of frequencies when the roughness is present and its height increased. In other words, above 6 kHz for Mach 2.3 and 8 kHz for Mach 1.6 pressure fluctuations become rarer and rarer with the roughness height. Actually, even if with a more modest extent, this coarsening of the spectrogram is evident at all frequencies. At Mach 2.3 it happens passing from the clean-insert configuration to the 0.1-mm-high roughness, while at Mach 1.6 it happens in passing from $k=0.1$ mm to $k=1$ mm.

Finally, one can also observe in Fig. 3.88 how, for the most excited configurations, peaks are repeated during the test time more often than for the least excited configurations. This aspect is in common with the wall-temperature fluctuations analyzed in Sub-section 3.6.3.

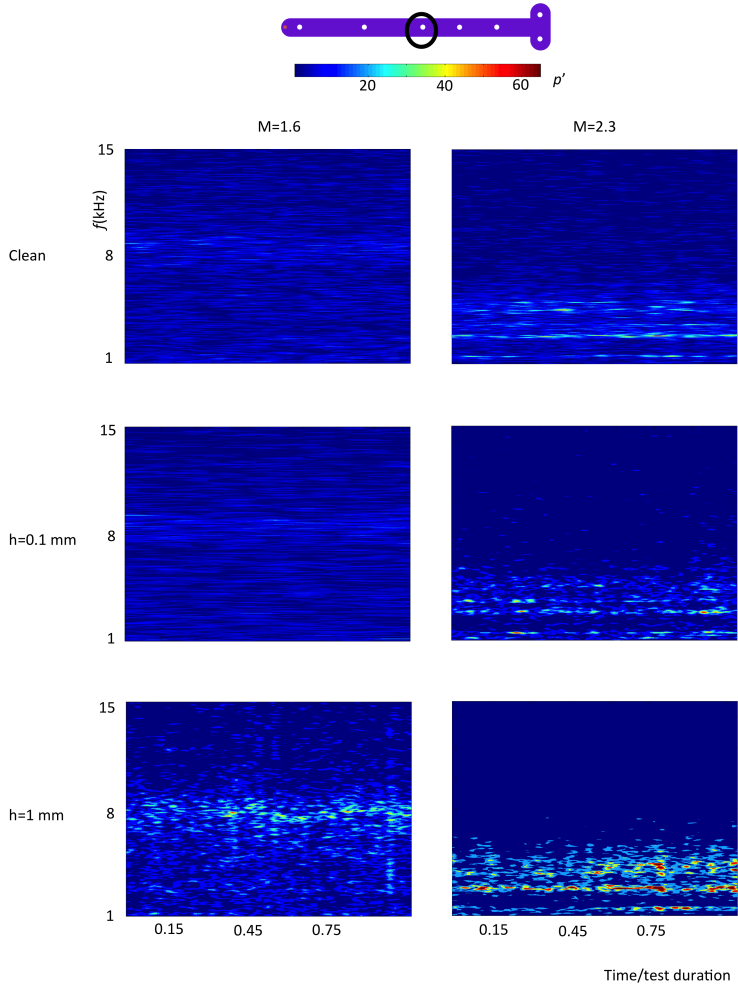


Figure 3.88: Time-resolved frequency spectra of third PCB sensor downstream of the roughness element for all test conditions

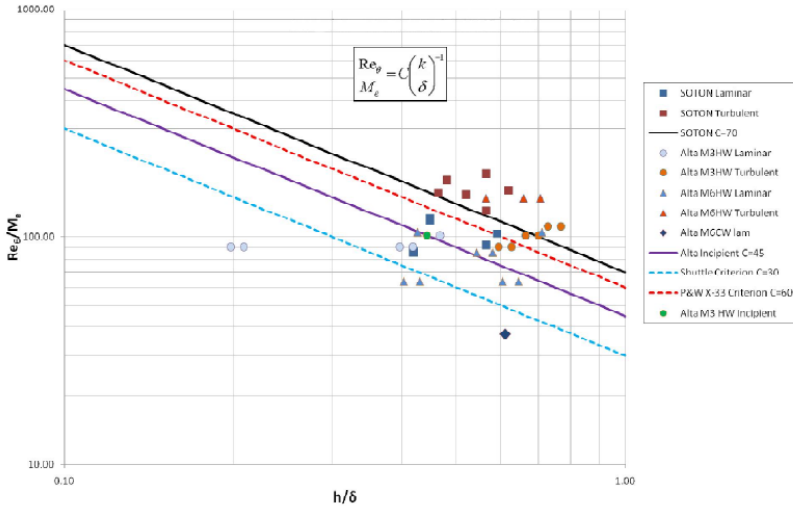


Figure 3.90: From ref. [40]: the Shuttle transition criterion applied to numerical and experimental results

is predicted to start at the location of the roughness as the test point is above the threshold of the Shuttle criterion.

The two criteria are based on the boundary layer characteristics of the test point (the momentum thickness, θ , or the physical thickness, δ), the flow properties (the density and velocity at the roughness height, ρ_k and u_k , respectively), the properties of the freestream flow (density, velocity, and Mach number, ρ_e , u_e , M_e , respectively), the wall temperature (only for the Reda criterion and through the viscosity at the wall μ_w), and the roughness height (k in Fig. 3.89 or h in Fig. 3.90). For the Reda criterion k is the average height of the surface roughness distributed on hemispherical or blunt conical surfaces (see ref. 3 in ref. [40]), while for the Shuttle criterion h is the height of a single roughness element placed on a flat wall.

As the name suggests, the Shuttle criterion has been developed from Space Shuttle in-flight and wind-tunnel data, the latter taken at Mach 6 and 8 and at high angles of attack. This criterion was developed to assess the aero-thermodynamic dangerousness of protuberances jutting out from the thermal protection system constituting the Shuttle external surfaces. In time these data have been complemented by other data from successive NASA hypersonic lifting-body programs, and the criterion was consequently updated [41, 42].

Hence, the Shuttle criterion seems better suited than the Reda criterion to describe the present results, even if it fails to account for the wall-temperature effect. However, it must be noted that none of both criteria accounts for the pressure gradient in the present tests, which, being negative

(i.e. the pressure decreases along the velocity direction), favors boundary layer stability, thus it delays transition to turbulence [e.g., 43]. More specifically, Morrisette [44] performed measurements in hypersonic flows to assess the effect of a favorable pressure gradient on transition to turbulence induced by a single roughness. His test articles were blunt-leading-edge flat plates and blunt cones. He found that the effective roughness Reynolds number (calculated with the minimum roughness height for which turbulence starts very close to the roughness) with a favorable pressure gradient was between twice and seven times the value with zero pressure gradient. This means that a roughness in a favorable pressure gradient flow has to be higher than in a no-pressure-gradient flow to trigger turbulence. For the present tests, CFD computations found the streamwise pressure gradient at the roughness location equal to -50 kPa/m for Mach 2.3, and equal to -65 kPa/m for Mach 1.6. These values correspond to a doubling of the effective roughness Reynolds number as from the data in [44].

Figures 3.91 and 3.92 show the Reda criterion and the Shuttle criterion applied to the present thin-film tests for both Mach numbers (2.3 and 1.6), both roughness heights (0.1 and 1 mm), and all the wall temperatures. Both figures report the plot limits in the corresponding ref. [40] figures by dashed grey contours as to ease visual comparison.

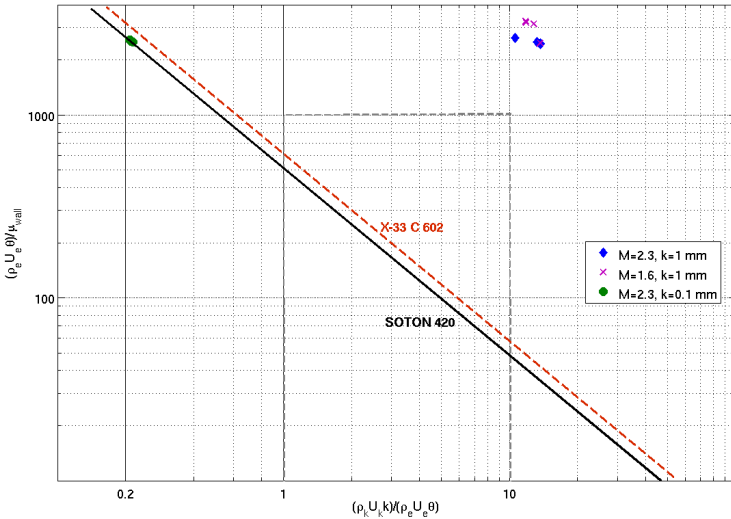


Figure 3.91: The Reda transition criterion applied to the results of the present thin-film experiments

Figure 3.91 reports only the two upmost diagonal lines in Fig. 3.89, “Reda X-33 C=602” and “Line SOTON 420”, that are sufficient to conclude on the

present tests. It is seen that the test points form two distinct groups: those for Mach 2.3 and $k=0.1$ mm cluster all just below the Reda X-33 line and practically on the SOTON line, around the abscissa 0.2; all those for $k=1$ mm, instead, are well above both lines and lay just after the abscissa 10. In the case of the first group only the Reda X-33 line seems to yield a clear conclusion, that is, the boundary layer flows at Mach 2.3 past the 0.1-mm-high roughness are still laminar. The SOTON line, instead, may suggest that they are “transitional”, i.e., in the process of becoming turbulent, since they all cluster just on the laminar/turbulent threshold, not clearly above or below. In the case of the second group, instead, there are no doubts for the prediction, because all the test-points clearly result turbulent according to both lines.

All the present test-points in Fig. 3.91 fall off Fig. 3.89 plot limits because of their higher ordinates and lower or (slightly) larger abscissas. In both these differences the higher unit Reynolds number, lower wall temperatures, different roughness heights, or the lower Mach numbers of the present tests play a role. But they are essentially due to the momentum thickness higher than that in the tests of ref. [40]. The momentum thickness at a given location along a surface is directly proportional to the distance from the leading edge of the surface, and in the present case the roughness/ramp-leading-edge distance is about 0.93 m, much higher than the value in ref. [40]. In fact, for the latter the present author has estimated a throughout length of the test article of about 0.16 m, thus the roughness/leading-edge distance has to be even less than 0.16 m. This momentum thickness, then, appears at the numerator of the ordinate and at the denominator of the abscissa, so that the present test points are lifted up and put away from Fig. 3.91 range. The latter effect is equally due to a difference in the roughness heights: the present tests are for $k=0.1$ and 1 mm, ref. [40] tests have been made for k ranging from 0.1 to 0.3 mm.

Finally, Fig. 3.92 reports all the diagonal lines in Fig. 3.90. It is clear that, whatever the threshold chosen, all of them predict a turbulent boundary layer downstream of the roughness for all the present cases.

3.9.2 Conclusions

A total of forty five tests has been performed to study the effects of a single roughness element and of the wall temperature on supersonic boundary layer flows. Tests were for freestream Mach numbers of 2.3 and 1.6. Two roughness heights were tested, 1 mm and 0.1 mm; the roughness base was $2 \times 2 \text{ mm}^2$ for both heights.

Two types of sensors were used: thin-films and piezoelectric pressure transducers (PCBs). Thin-films were used to measure the convection heat flux through the wall, and the temperature fluctuations at the wall. PCBs were used to measure pressure fluctuations at the wall. From the heat flux measurements at different wall temperatures the adiabatic wall temperature

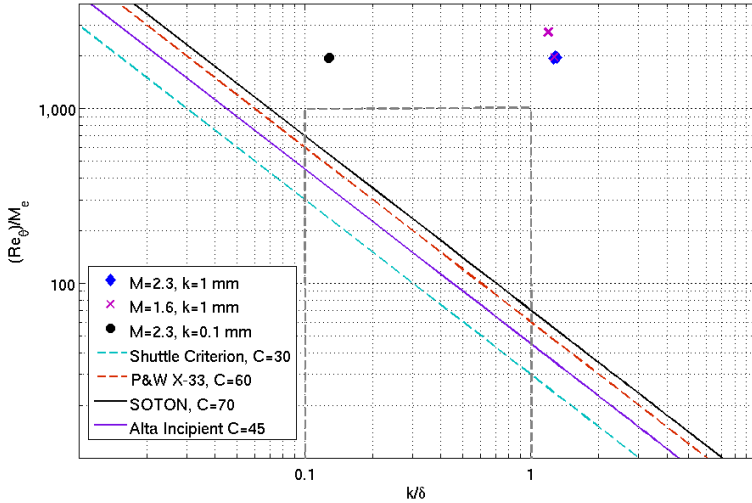


Figure 3.92: *The Shuttle transition criterion applied to the results of the present thin-film experiments*

values were obtained for each configuration tested, and were used as indicator of the state of the boundary layer. Reference values for the adiabatic wall temperature were calculated with analytical models, whose validity, in turn, was checked against CFD results.

The adiabatic wall temperature trends in Section 3.5 show that the general roughness effect on the boundary layer does not persist with the distance from the roughness. In case of the Mach-2.3 flows, in fact, the two roughness heights produce turbulent levels of adiabatic wall temperature only as peaks in two distinct locations (one of which is the closest to the roughness for the lowest roughness height), while the rest of the values is either intermediate or laminar. The Mach-1.6 flows show the same general trend, except that the peaks are just approaching turbulent levels of adiabatic wall temperature, while the others values are laminar. Moreover, none of these peaks is as close to the roughness as for Mach 2.3.

Heat flux streamwise trends in Section 3.4 confirm that the roughness effect is generally localized close to the roughness itself and does not extend downstream to the last sensor available. Then, the spanwise trends for the Mach-2.3 0.1-mm-high-roughness and the Mach-1.6 cases show that at this position the flow is also rather uniform spanwise. In turn, the remaining spanwise trends from the rows closest to the roughness confirm the most sensible effect of the roughness there, showing more appreciable spanwise heat flux changes.

The combined use of heat flux measurements and adiabatic-wall temperatures has let the calculation of the Stanton number trends along the instrumented plate. These trends, in turn, have been used to inquire the boundary layer status. They, checked against analytical values for pressure-gradient-free flows, picture a transitional boundary layer downstream of the 1-mm-high roughness at Mach 2.3 for all the wall temperatures tested. On the other hand, for the cases of the roughness 0.1-mm high at Mach 2.3, and of the roughness 1-mm high at Mach 1.6, the results of the Stanton number analysis are judged too moot to be relied upon. This is likely due to the proximity of all the wall temperatures tested at the Mach 2.3 to the adiabatic-wall value, and to the inaccuracy of the analytical model used to check the Mach-1.6 cases.

The analysis of the thin-films unsteady data has been carried out with different tools with the purpose of allowing different points of view on the same phenomena (Section 3.6); this helped confirming conclusions by more than one result. PCBs results on pressure fluctuations complement this analysis.

The frequency analysis in Sub-section 3.6.1 showed that fluctuations amplitudes increase with the wall temperature at frequencies below 1 kHz at Mach 2.3, but not for the 1-mm-high-roughness configuration. In this case, in fact, a general amplitude decrease is observed across the whole frequency range. At Mach 1.6 and 1-mm roughness, fluctuation amplitudes do not change much with wall temperature, suggesting that the Mach number may outplay roughness height and wall temperature.

The most important effect of the Mach number, passing from Mach 2.3 to Mach 1.6, was found to be a sensible amplitude decrease for the 1-mm-high roughness cases. This conclusion applies also to the pressure fluctuations measured by the PCBs; and also for the 0.1-mm-high roughness. Then, for the low Mach number, peaks are observed to repeat more frequently along the spectrum of all the thin-films signals, while they get centered around a specific frequency for the pressure fluctuations. For the same Mach 2.3, the roughness effect on the thin-films spectra respect to the clean configuration is sensible only for the largest height tested.

Finally, highest peaks appear always below a certain frequency in the spectra of the wall-temperature fluctuations, which is generally lower than 1 kHz. Above 20 kHz most of the signals amplitudes have decreased of one order of magnitude respect to their peak values, and this decrease becomes of two orders of magnitude above 100 kHz. Wall-pressure fluctuations highest peaks also appear all below a certain frequency, but this time this is 6 kHz for all the cases tested at Mach 2.3. For the cases at Mach 1.6, instead, the peaks tend to concentrate around 8 kHz leaving the rest of the spectrum relatively much more clean.

The main goal of the RMS analysis of the temperature fluctuations was to highlight their general trend along the instrumented insert. This trend is found to change in passing from the lower to the higher roughness at Mach

2.3. For the 0.1-mm-high roughness, in fact, the RMS has its lowest value closest to the roughness and its highest away from it. On the contrary, for the 1-mm-high roughness the highest RMS is closest to the roughness and decreases monotonically with the distance. The RMS streamwise trend at Mach 1.6, then, is analogous to that at Mach 2.3 for the same roughness height of 1 mm. This change is confirmed by the analysis of the signals spectrograms, which provided also a hypothesis for the mechanism of fluctuations amplitude rise. This mechanism may be the increased recurrence in time of peaks already present in the less excited signals, rather than an increase of the peaks across the frequency spectrum at a given time. Finally, intensity-wise, the comparison of the measured RMS with literature data highlighted an one-order-of-magnitude difference respect to turbulent values and a much closer proximity to laminar values for both Mach numbers.

No RMS trends resulted from the wall pressure measurements because only one sensor performed acceptably. This is the one located in the middle of the PCBs insert, and yielded RMS values with the 0.1-mm-high roughness, and for both Mach numbers tested, slightly lower than for the clean configuration. As for the wall-temperature fluctuations, the highest RMS values were reached for the 1-mm-high roughness configuration.

The peculiar information from the spectrogram analysis is that, generally, frequency peaks of comparable amplitude are irregularly intermittent throughout the test time: that is, they appear and disappear during the test at times hardly relatable to each other. This intermittency is found for the temperature fluctuations as well as for the pressure fluctuations. Also pressure fluctuations spectrograms highlight how this intermittency increases with the roughness height, but show as well how the peak amplitudes increase more than for the wall-temperature fluctuations with the roughness height and for both Mach numbers tested.

The cross-correlation analysis of Section 3.7 revealed a phenomenon likely moving along the instrumented insert at $0.8 \cdot U_\infty$ m/s in all the test cases considered; with or without the roughness. Therefore, this phenomenon cannot be directly related to the presence of the roughness.

At this point one can summarize the results from the many analyses performed, and try to conclude accordingly on the effects of single roughness and wall temperature on the status of Mach-2.3 and Mach-1.6 boundary layer flows. These analyses have stemmed from two types of data. First, the steady data that allowed the calculation of the wall heat flux, the adiabatic wall temperature, and the Stanton number. The last two quantities let an assessment on the boundary layer status, even if the Stanton number analytic trends do not account for the pressure-gradient effect. Second, the unsteady data that allowed the spectral analysis of the pressure and wall temperature fluctuations (across the whole test time and in the frequency-time domain), the cross correlations, and the calculation of their RMS trends. The latter trends checked against literature data also let an

assessment of the boundary layer status.

Furthermore, there are the two transition criteria, whose results have to be judged keeping in mind the warnings given in Sub-section 3.9.1; especially for the Reda criterion.

For the case of the roughness 1-mm high and Mach 2.3 all the analyses on the measurements converge to the same conclusion that the flow downstream of the roughness is not fully turbulent but rather "transitional", i.e., in the process of becoming turbulent. Both transition criteria, on the other hand, predict a turbulent boundary layer flow for it.

For the case of the roughness 0.1-mm high and Mach 2.3, the analyses on the measurements converge to the same conclusion as for the 1-mm-high roughness, that is the boundary layer flow downstream of the roughness is not yet turbulent but "transitional". This is now the same prediction as from the Reda criterion, but the Shuttle criterion still predicts a turbulent boundary layer downstream of the roughness. Finally, for the case of the roughness 1-mm high at Mach 1.6, the RMS and the adiabatic-wall-temperature trends give a boundary layer not turbulent and transitional in a lesser degree respect to Mach 2.3. This latter prediction is shared by both transition criteria.

The general view of a non-turbulent flow downstream of the roughness in all the cases above mentioned is then reinforced by the spectral analysis of the wall temperature fluctuations. In fact, the resulting spectra have all peaks in a defined frequency range, and their amplitudes decrease rapidly with the frequency. But this is not what is expected from a supersonic turbulent boundary layer. In this case, in fact, fluctuations amplitudes should stay comparable across a wide frequency range and should feature a less steep decay with the frequency. For instance, measurements in ref. [39] on a fully turbulent supersonic boundary layer give 90% of the turbulent energy within a frequency range stretching up to 90 kHz, while in the present cases beyond 20 kHz there is a drop in fluctuations amplitude of one order of magnitude. Then, in case of a turbulent boundary layer, one would have expected a decaying law for the frequency spectrum as $-5/3$, but all the present spectra have a decay steeper than that, which is rather found to be a characteristic of a turbulent flow in its earliest stage [e.g., 18].

In the end, all the analyses of the steady and unsteady measurements data lead to the same conclusion for the cases at Mach 2.3 for both roughness heights: their effect in conjunction to the several wall temperature values is not sufficient to trigger a fully turbulent boundary layer along the length of the instrumented insert downstream of the roughness. And this full convergence of conclusions repeats also for the case at Mach 1.6. In fact, the unsteady data analyses keep on picturing the same situation as for the Mach 2.3 cases, and the adiabatic wall trends are the closest of the lot to the laminar limit. The above conclusions are practically never the same as from the prediction criteria. This may be due to the criteria incapability to account for the favorable pressure gradient experienced by the flows in the present

tests, or to their specificity to flow and/or surface conditions too different from those of the present tests.

Chapter 4

Effects of oblique-shock-wave impingement onto a Mach-2 transitional boundary layer

The test campaign at Mach 2 to be presented in this Chapter was conceived to investigate the effect of the impingement of an oblique shock wave on a supersonic transitional boundary layer. For transitional boundary layer has to be intended the boundary layer that is in the process of becoming fully turbulent and cannot be considered anymore laminar but neither yet fully turbulent. Two types of transitional boundary layer can be distinguished: natural and induced. The natural transitional boundary layer is the boundary layer that is becoming turbulent without any major external forcing agent, but just because of the eventual growing of the instabilities that inevitably it carries within. The induced transitional boundary layer, instead, is the boundary layer that is forced to become turbulent by some external forcing agent.

The main characteristic of a naturally transitional boundary layer is the presence of turbulent spots [e.g., 45], i.e., lumps of turbulent flow completely embedded in the surrounding flow, still mainly laminar. Turbulent spots continuous birth and subsequent evolution eventually set on the fully turbulent boundary layer downstream of the location of their first appearance [e.g., 12, 45, 46]. This is why the bounds of the naturally transitional boundary layer are considered the location of appearance of the first turbulent spots and the location where a fully turbulent boundary layer is observed [e.g., 12, 47].

On the other hand, the main characteristic of a roughness element is that its effect on the flow is well confined within a specific zone of fluid downstream of it: its wake. It is observed [e.g., 8, 10, 48] that the incoming laminar boundary layer is sensibly modified within the roughness wake, so much as to possibly become turbulent at a certain distance from the roughness. This distance depends on many factors, among which the most prominent can be considered the size (height) of the roughness [5, 11, e.g., and references therein]. Since, in general, the wake of the roughness grows spanwise with the distance [e.g., 45], a turbulent wake will fill with turbulence more and more of the boundary layer as it flows along. Hence, only the wake of

the roughness can be considered as the transitional part of a boundary layer that is forced to become turbulent with a roughness element.

In the present test campaign the natural transitional boundary layer has been simulated by the flow perturbed with an electric spark released at different frequencies. In fact, it has been observed that a turbulent spot can be triggered within a laminar boundary layer in this way. This generation process is so regular as to allow the detailed studies of the spots characteristics and properties [46, 49]. However, to the author knowledge, the present tests are the first attempt to generate a turbulent spot in a supersonic boundary layer along a flat plate in such a way. Only one similar attempt [50] at hypersonic speeds on an axis-symmetric body has been found by this author in the open literature.

For the induced transitional boundary layer, then, a single roughness 1-mm high, and 2-mm wide and long has been used to generate the wake in the Mach-2 boundary layer. This roughness is actually the same as the highest roughness tested in the test campaign described in Chapter 3.

4.1 Instrumentation and apparati for the generation of electric sparks within a supersonic boundary layer

For this test campaign the same sensors with the same electronics as for the test campaign presented in Chapter 3 have been used. For the PCBs the very same sensors in the same insert were used, whilst the thin-films insert was different from that of Chapter 3, and equipped with eleven thermocouples: four of them on the insert top and the rest on its bottom. These thermocouples were used as reference for the thin-films measurements and as gauge of the insert temperature during the continuous run of the Mach-2 facility. Figure 4.1 shows the layout of the thin-films along their insert.

The novelty of this test campaign was the use of an electric spark to perturb the supersonic boundary layer. To produce this effect new devices had to be designed and manufactured; they are presented in the following Sub-section 4.1.1.

4.1.1 Hardware for the generation of electric sparks

To release an electric spark within a boundary layer, two electrodes can be placed above the wall where the boundary layer develops [46]. Their height has to be as low as to keep them within the boundary layer, but as high as not to endanger the spark release with the proximity to the wall. A trial and error procedure in a preliminary test campaign has been used to set this optimal height. This test campaign will be discussed in the following Section 4.2.

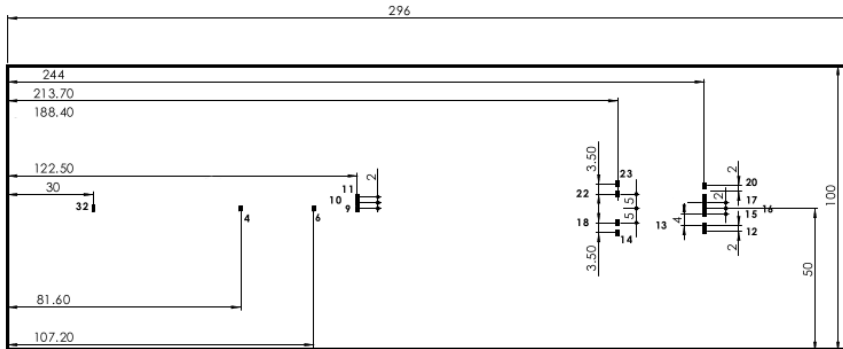


Figure 4.1: *The layout of the thin-films on the insert used for the Mach-2 test campaign (dimensions are in mm)*

The electrodes need to be powered by an electric circuit that has to build a voltage difference high enough to release the spark in the air gap between them. In the present tests two different electric circuits were used as to provide different spark release frequencies (Fig. 4.2). The first circuit was comprised of a car battery, a 40-kV car induction coil, and a frequency modulator [46] (Fig. 4.2 top). The latter was based on a 555-timer electronic circuit that generates a tunable square wave to activate the coil. Tuning the square wave resulted in tuning the spark release frequency. After devising modifications of the circuitry and a specific procedure to operate the coil, the frequency modulator was calibrated (see next Section 4.2). The frequencies 1, 10, and 20 Hz were finally selected for the tests at Mach 2. The second circuit was comprised of a 12-kV transformer powered by the main (Fig. 4.2 bottom). This configuration allowed a release frequency fixed at 100 Hz directly governed by the alternate current of the main.

The electrodes of both circuits were mounted in a plug that was flush-mounted into the wall along which the boundary layer developed. Figure 4.3 shows the plug out of the wall during the tests for the characterization of the spark shape. To avoid the spark happening behind the electrodes tips, or even in the bulk of the plug, the cables to the electrodes had to be electrically insulated, and the plug had to be made of a strong electrical insulator. Therefore, special high-voltage cables were used in both circuits to carry the current to the electrodes, and the plug was made of Vespel Dupont[®] SP-1, a strong electric-insulator easy to machine. Easy machining was a requirement because, as a further precaution, the plug was specifically shaped as to keep the cables as far as possible from each other, and as to have the shortest distance between the electrodes exactly at their tips. This

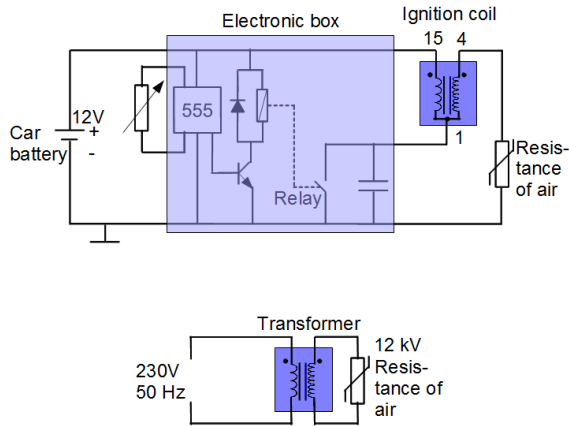


Figure 4.2: *The schematics of the two circuits used to generate the electric spark*

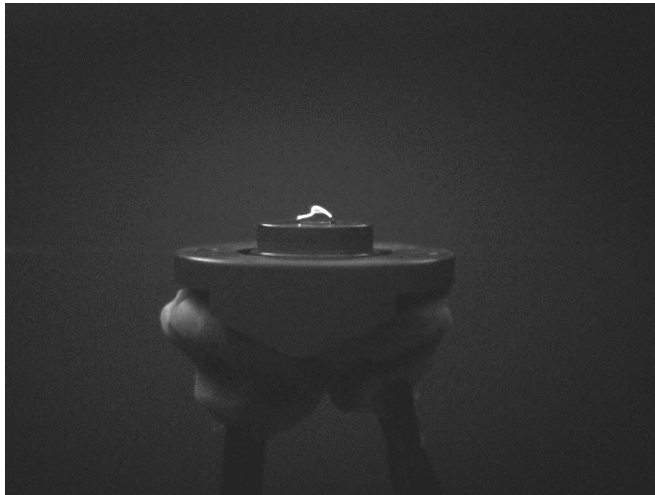


Figure 4.3: *The spark plug activated and recorded by high speed camera (the gap between the electrodes is 6 mm)*

resulted in the plug featuring two diagonal passages for the electrodes with slanted surfaces at their bottoms (Fig. 4.4).

The gap between the electrodes tips had to be chosen taking into account the wanted size of the perturbed zone within the boundary layer, and the voltage difference allowed by the circuitry. In fact, there is a relation between

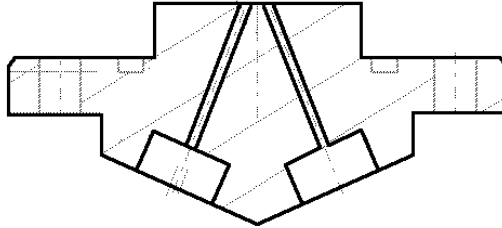


Figure 4.4: *The cross section of the spark plug with its two convergent passages for the electrodes*

the electrode gap, the air pressure, and the voltage required to generate an electric spark. This is shown in Fig. 4.5 by the Paschen law for plane-parallel electrodes. Based on literature data [46, 49] and on the electric power available to the electrodes, three gaps were chosen, 2, 4, 6 mm, and three different plugs were manufactured accordingly. All of these gaps were tested in a preliminary test campaign, and one gap was selected for the supersonic test campaign.

4.2 Preliminary test campaigns

Once all the hardware for the generation of the spark was ready, the preliminary test campaigns were carried out to: test and calibrate the frequency modulator; test the reliability of the hardware; check the effective generation of a turbulent spot within a laminar boundary layer. For the latter point three electrodes gaps were tried, and the electrodes height from the wall was varied. Finally, the validity of some of the conclusions drawn from these tests at ambient pressure was checked for Mach-2-like low pressures by a further test campaign in a vacuum chamber.

The calibration of the frequency modulator has been made by visualizing the spark releases at a given modulator position with the Phantom high-speed camera (Fig. 4.3). Once calibrated, the modulator was capable to span a frequency range from 1 Hz to 20 Hz. During a series of such tests following the wind tunnel test campaign the power released by the spark to the air

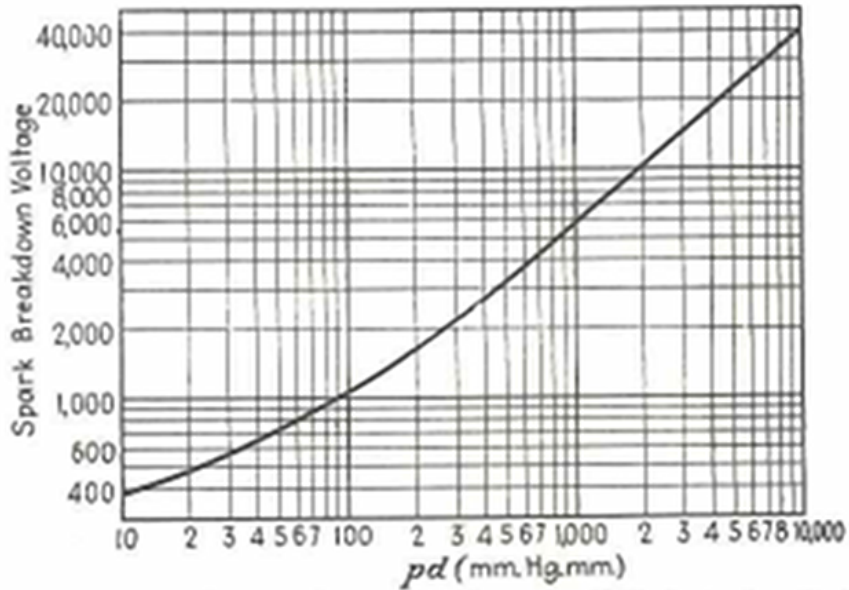


Figure 4.5: The relation between electrodes tip gap (d), pressure (p), and voltage for spark release (Paschen law)[51]

was also estimated by measurements of voltage across and current along the cables connecting the electrodes to the battery-coil and the transformer circuits. The sampling frequency of these measurements was 1 GHz as to sufficiently resolve the very short characteristic time of the spark release. The measured peak power produced by the battery-coil circuit was 8.5 kW, and the corresponding energy release 100 mJ. The cumulative peak power produced by the transformer circuit was 124 kW with a corresponding energy release to the flow of 250 mJ. This power is cumulative in the sense that is the sum of nine distinct, major power-peaks that happened during one spark release. Their powers ranged from a minimum of 10.4 kW to a maximum of 13 kW. Both energy releases have the same order of magnitude because their times are different: the power from the battery-coil circuit was released to the flow in $30 \mu s$, while the power from the transformer circuit relative to each of the nine peaks was released in $2 \mu s$; the order of magnitude of these times is confirmed by [51]. So, in the end, the transformer circuit input about 2.5 times more energy into the flow than the batter-coil circuit.

To check the hardware reliability and its effectiveness on a boundary layer flow, a test campaign was carried out in the low-speed wind tunnel shown in Fig. 4.6.

This facility, open-loop and of the suction type, features a velocity tunable from about 2 m/s up to 45 m/s, and a freestream turbulence intensity of



Figure 4.6: *A view of the low-speed wind-tunnel with the set up for smoke-sheet visualizations*

around 0.2%. The freestream velocity is adjustable by varying the speed of the facility DC-motor. Its value is obtained from the measurement of the static pressure, and for the present tests was fixed at 2 m/s.

The wind tunnel octagonal test section is 0.28-m wide and 1.3-m long with wide Plexiglass windows on four sides. These windows allowed the flow visualizations by which conclusions on the hardware effectiveness were drawn.

For these visualizations, the boundary layer flow developing along the bottom of the test section was made visible by the use of a smoke screen. This was generated by a flush-mounted slit located just downstream of the spark plug and perpendicularly to the flow direction. The bottom of the slit hosted a narrow strip of Nicrom (an alloy specifically made to maximize Joule heating) connected in series to a DC power generator. The slit was filled before each test with a thin layer of grease, which, once the DC generator was on, rapidly vaporized into the boundary layer flow. This vaporization resulted in a smoke sheet as wide as the slit that flowed downstream just above the wall. Finally, this smoke sheet was made visible by bottom illumination. (Figs. 4.6 and 4.7).

The visualizations revealed that the spark has indeed an effect on the boundary layer, and that it appears downstream of the slit, along the horizontal line through the electrodes location, or slightly displaced to its left (Fig. 4.8). This result is in accordance with ref. [46], which reports that the

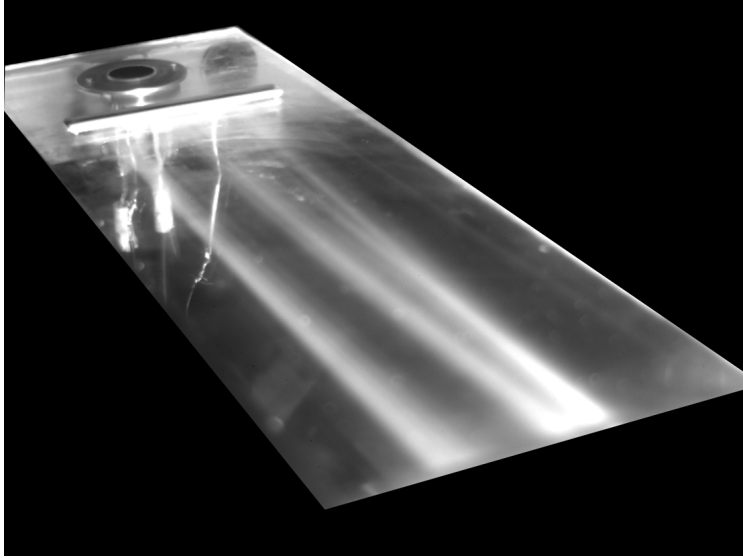


Figure 4.7: *A view of the smoke sheet generated on the bottom of the low-speed wind-tunnel test section. The cabling for electrodes and Nicrom heater is visible through the transparent bottom*

spots are not generated just at the spark location, but always further downstream. The distance between the slit and the location of the spark-induced perturbation was found to increase with the spark frequency.

The spark effect on the smoke sheet was found depending heavily on the electrodes height from the wall. A difference of plus 3 mm above the optimal value, or flush mounting, resulted in no visible effect at all. Hence, the fact that no perturbation is seen on the smoke screen leads to the conclusion that no perturbation at all was generated by the spark within the boundary layer. In the case of the flush mounting, then, it was soon evident during the characterization of the spark how a release very close to the plug surface was to be avoided. In fact, the spark regularly burned away a rather consistent amount of material from the surface within the electrodes with the consequence of piercing a preferred path across the electrodes bases that short-circuited the electrodes tips. In so doing, the spark in air extinguished. In the end the optimal height of the electrodes was found to be 0.7 mm, and was adopted for the tests at Mach 2.

Another evidence from the visualizations was that the appearance of the disturbance on the smoke sheet was synchronized with the spark release at the lowest frequencies. As the spark frequency increased, however, this aspect was more difficult to single out from the visualizations.

Regarding the best gap between the electrodes, the heaviest effects on the smoke sheet have been found with that of 6 mm; with both the battery-coil

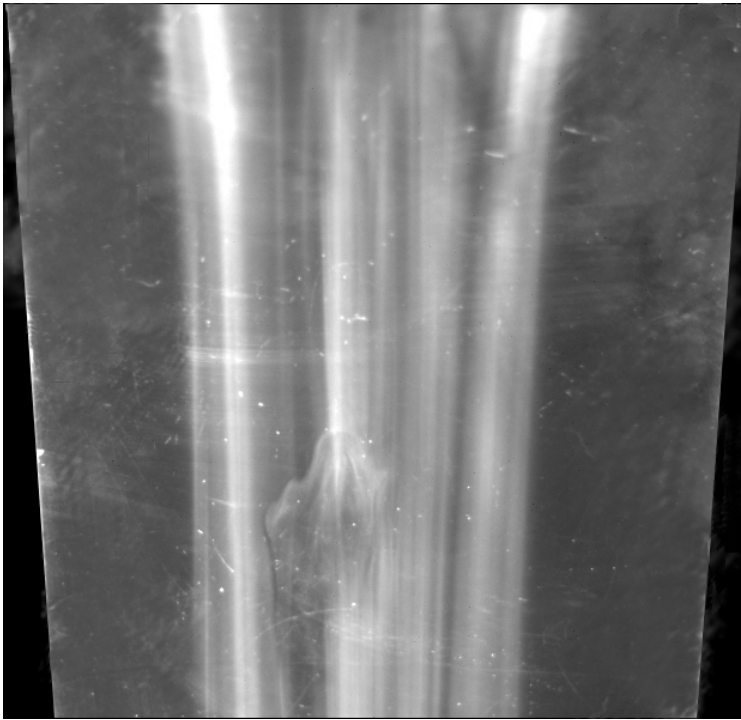


Figure 4.8: *The effect of one spark release on the smoke sheet (spark frequency=1 Hz, electrode gap=6 mm, the flow comes from above)*

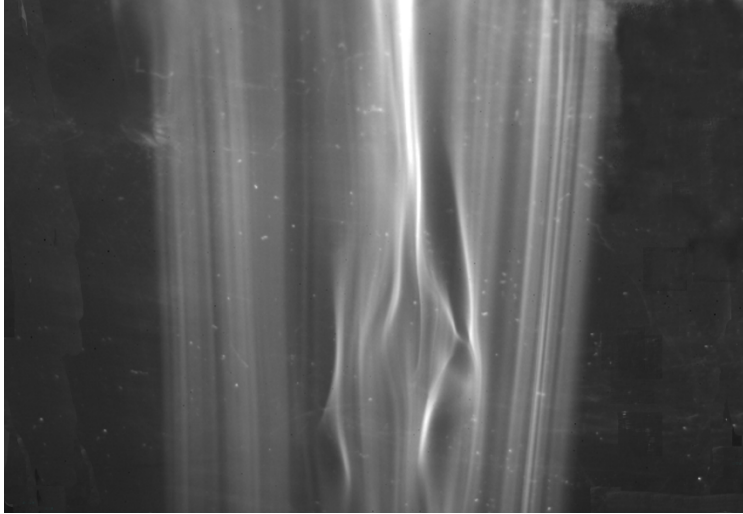


Figure 4.9: *The effect of one transformer burst on the smoke sheet (spark frequency= 100 Hz, electrode gap=6 mm, the flow comes from above)*

circuit and the transformer circuit. Figure 4.9 shows the top view of the effect on the smoke sheet of an impulsive activation of the transformer (“burst-mode”, that is, the transformer was turned on and just after turned off). It is seen that the central part of the smoke sheet is distorted as to feature dark zones from where smoke disappeared and brighter zones where the smoke seemed to concentrate. And these brighter zones show sinuous filaments of smoke. But, most importantly, all this happens in a well defined zone of the sheet, whose surroundings stay unaffected. It is found that this finiteness is the outmost feature of a turbulent spot, which can be idealized as a lump of turbulent flow surrounded by an otherwise laminar flow [e.g., 12, 45, 46, 49, 52].

Figure 4.10, then, shows a side view of the effects of the spark generated by the battery-coil circuit. In this test the spark frequency was not kept fixed, but continuously increased from 1 to 8 Hz, and Fig. 4.10 captures the flow field at 8 Hz. The same dark and bright zones as in Fig. 4.9 are present, and again the visible part of the smoke sheet bordering the perturbed flow stays laminar. But, in this picture one can also appreciate the extension normal to the wall of the spark-induced perturbation, i.e. its three-dimensional character. Fig. 4.10, in fact, shows filaments of smoke lifted up from the smoke sheet. These filaments are also sinuous like those in the top view of Fig. 4.9.

To have a better idea of the nature of the perturbations visualized in Figs. 4.9 and 4.10, one can compare them to the visualization in Fig. 4.11. This picture shows a fully turbulent boundary layer naturally occurring

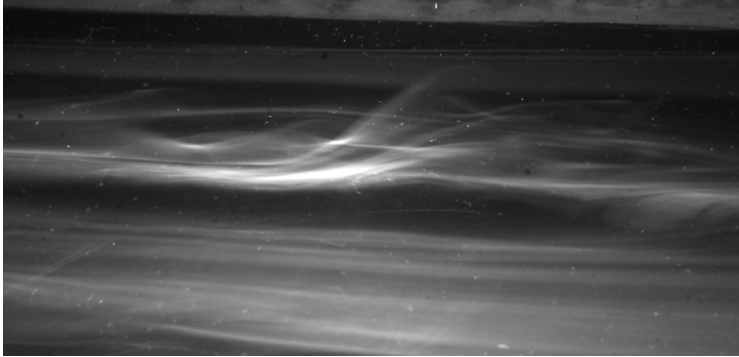


Figure 4.10: *The effect of sparks generated by the battery-coil circuit on the smoke sheet (spark frequency continuously increased from 1 to 8 Hz, electrode gap=6 mm)*

along the bottom wall of the test section. Natural transition to turbulence was achieved by continuously increasing the freestream velocity of the wind tunnel. The increase was slow as to allow the camera to capture the initial effect of turbulence on the smoke sheet. In fact, once the turbulent boundary layer was fully established, the whole smoke sheet was cleared from the wall, and no visualization was possible anymore.

Even if the zoom of the image is not as in Figs. 4.9 and 4.10, in Fig. 4.11 one can still detect the presence of zones cleared by the smoke aside to zones where the smoke seems denser (thus resulting brighter). Where the smoke is still visible, sinuous filaments are seen aligned to the main flow direction, instead of the regular laminar streaklines in Fig. 4.7.

One can conclude from this comparison that the spark effects on the smoke sheet in Figs. 4.9 and 4.10 present the same features as the turbulent boundary layer naturally occurring in the same wind tunnel, except for the fact that they are bounded in space. Furthermore, the images in ref. [53] show the core of a turbulent spot featuring dark zones bounded by brighter ones that highlight sinuous filaments of fluid. The visualizations in [53] were made by a smoke wire, i.e. a spanwise-mounted wire from which smoke streaks parallel to the flow direction originated. The freestream velocity of the flow was 5.3 m/s.

Accurate measurements would have been needed to find out whether the perturbations shown in Figs. 4.9 and 4.10 were real turbulent spots or not. Notably, measurements of velocity average and fluctuation values [e.g., 12, 46].

In conclusion, the results from this preliminary test campaign are the identification of: the best electrodes gap as 6 mm; the optimal electrodes height from the wall as 0.7 mm; the successful calibration and testing of the new hardware. In the end, the visualizations showed, at least, that the

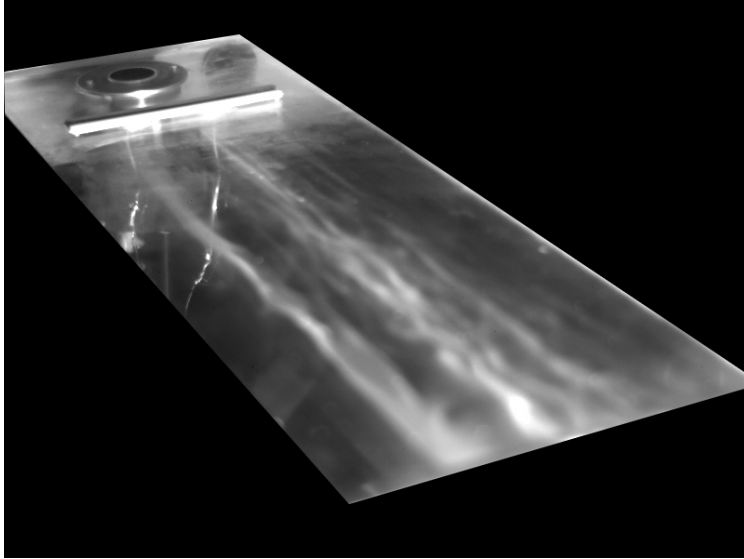


Figure 4.11: *Smoke sheet visualization of the naturally-occurring turbulent boundary layer along the bottom of the L2A low-speed wind tunnel*

spark had a clear effect on the boundary layer flow. Even if this cannot be surely considered as a fully developed turbulent spot, this effect was judged enough for the validation of the two set-ups for the spark generation and for their use for tests at Mach 2.

The last check on the spark-generating apparatus consisted in testing them at low static pressures, comparable to or lower than those of the Mach-2 flow of the tests. In fact, the Paschen law (Fig. 4.5) states clearly a dependency of the voltage on the air pressure, and the tests above presented were carried out at ambient pressure, while those at Mach 2 feature a much lower static pressure. This is not only because of the supersonic expansion that the air flow undergoes, but also because of the characteristics of the continuous-flow facility used. As explained in the following Sub-section 4.3.1, this wind tunnel pumps out air from the flow within it in order to keep safe compressor operations. It follows that the combination of supersonic expansion and low mass of air brings the static pressure in the test section to values of the order of 10^3 Pa (see Table 4.1).

The set up in Fig. 4.12 was used to replicate these low pressure values. The plug with the electrodes was placed inside a sealed chamber, wherein vacuum was made by the use of a vacuum pump. The effect of the pump was controlled by a pressure calibrator, so that different pressures were possible to set. At each pressure the spark was released and filmed by the high-speed camera. The camera movies allowed the check of any major changes respect

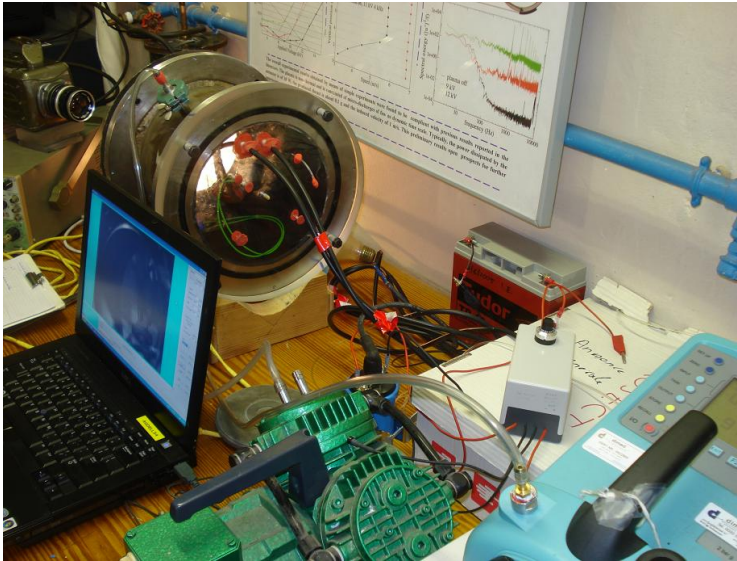


Figure 4.12: *The spark plug within the vacuum chamber for testing at very low pressures*

to the ambient-pressure tests, and the individuation of the effects of the low pressure.

Figure 4.13 show the sequence of three high-speed camera pictures of the spark released within the vacuum chamber at three different static pressures: ambient, 0.5 atm, and 0.01 atm (from left to right; note that in the rightmost picture the view angle is more slanted than in the other two). These pictures confirmed that the spark was correctly released also at pressures lower than ambient, but show as well that its characteristics changed. Notably, the color of the spark changes from orange to violet going from ambient to 0.01 atm, and, perhaps more importantly, the spark becomes thicker as the pressure decreases to the lowest value.

A possible explanation for the change in color is in the total mass of air within the vacuum chamber decreasing with the pressure decrease. In fact, the power released by the spark to the air within the electrodes is independent of air pressure, but is received by less and less molecules of air as the pressure goes down. Therefore these fewer molecules are more energized than those excited at higher pressures, and emit light at a higher frequency. This higher-frequency emission results in the spark color shifting toward the upper edge of the visible spectrum, i.e. the violet.

Probably, then, this reduction of air mass with decreasing pressure is also responsible for the spark thickening.

The pressure decrease had no effect on the frequency of the spark release,

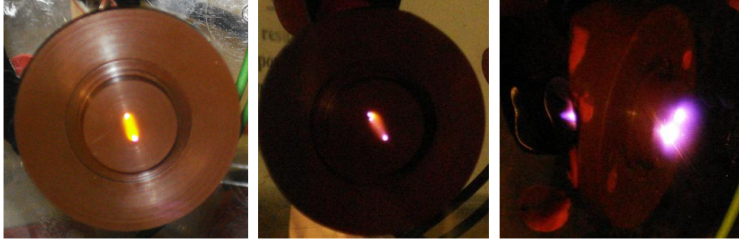


Figure 4.13: *The spark released at three different static pressures: ambient, 0.5 atm, 0.01 atm, from left to right*

but a sensible effect on the duration of the spark glow. However, the latter was present only for the spark generated by the battery-coil circuit. This effect is presented in Fig. 4.14 and consisted in a general increase of the spark glow duration as pressure decreased from ambient (1000 mbar) to 0.1 atm (100 mbar). Then, from this pressure down, only at a release frequency of 20 Hz the spark duration came back to the value of the ambient pressure (1000 mbar), while for the other two frequencies it stayed higher. As from Table 4.1 in the following, 10 mbar (0.01 atm), i.e. 1000 Pa, is the static pressure expected in the Mach 2 test section. Note that the times in Fig. 4.14 are two order of magnitudes larger than the times of the spark energy release, but they refer to two different phenomena: the energy release to air is the cause of the spark glow, i.e. of the spark visibility. The glow is generated by the vibrational relaxation of the air molecules, and this does not stop with the energy release, but continues after it as long as the whole vibrational energy in the frequencies of the visible light is exhausted. The order of magnitude of the spark glow in Fig. 4.14 is typical of spark plugs for automotive use [e.g., 54].

Finally, another noticeable low-pressure effect was at the rear of the plug, where cables connect to the electrodes; it is visible in the third image of Fig. 4.13. There appears that a spark is released between the cables at the same time as between the electrodes. It is possible that, due to the low pressure, the voltage difference across the two cables has become enough to release the spark. Figure 4.5 shows, in fact, how a decrease of air pressure of two orders of magnitude (from 1 bar to 10 mbar) for the same distance between electrodes, can reduce the voltage for spark release from 40 kV to 1 kV. This second spark was not synchronized to the main spark, but appeared sporadically. Nonetheless, more electrically-insulating material was added at the connections between the electric cables and the electrodes for the tests at Mach 2.

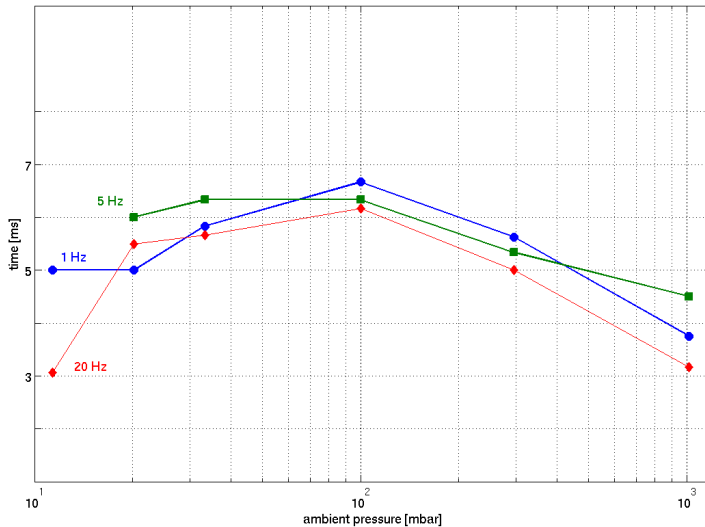


Figure 4.14: *The duration of the spark glow generated by the battery-coil circuit versus air pressure*

4.3 Mach-2 test campaign

The test campaign at Mach 2 has comprised one hundred tests, by which the effects on the laminar boundary layer of the single roughness and of the release of the electric spark have been studied. One roughness height was tested, 1 mm, and four spark release frequencies, 1, 10, 20, 100 Hz. Tests for both roughness and spark have been carried out with and without the impingement of a 41° -oblique shock wave as to highlight its effects on the transitional boundary layer. Schlieren movies (Fig. 4.15) were shot for each test by a high-speed camera to visualize the location and (possibly) some effects of the oblique shock on the boundary layer.

The cause of the untidiness of the shock appearance in Fig. 4.15 may be the vibrations of the shock generator that were evident during the tests. Another explanation (or a complement to the previous one) may come from the three-dimensionality of the shock around the wedge that generated it. In fact, the wedge was not spanning the full test section, but left some space between its lateral borders and the later wall of the test section. In this way the shock generated by the wedge was not exactly two-dimensional, and its lateral evolution may have been captured and super-imposed on its main two-dimensional shape.

The post processing of the measurements did not pose any more difficulties than for the test campaign described in Chapter 3, as far as the roughness

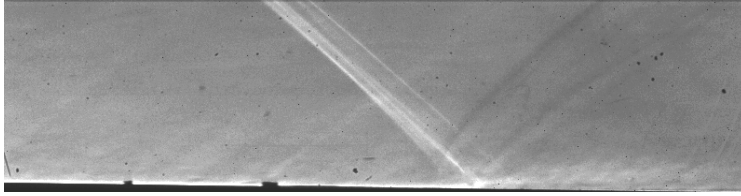


Figure 4.15: *Schlieren visualization of an oblique shock wave impinging downstream of the roughness position (the electrodes for the spark tests are also visible upstream of the roughness)*

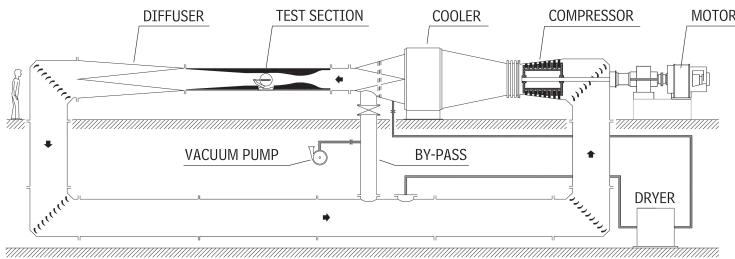


Figure 4.16: *The Mach-2 S-1 Wind tunnel*

tests were concerned. But it was more cumbersome for the tests with the spark. In fact, in these tests Electro-Magnetic Interference between the spark-releasing circuit and the thin-films and piezoelectric pressure sensors (PCBs) showed up and polluted heavily the signals of these sensors. The procedure by which this problem has been dealt with is detailed in 4.3.2 for the thin-film signals. PCBs signals, in fact, resulted too noisy even in the no-spark tests to be recovered in any way, and they all had to be discarded. Therefore, in this Mach-2 test campaign conclusions are drawn just from the thin-film measurements.

4.3.1 Mach-2 facility and experimental set-up

The test campaign at Mach 2 was carried out in the continuous transonic and supersonic S-1 wind tunnel of the von Karman Institute for Fluid Dynamics (Fig. 4.16). The wind tunnel is a closed-circuit continuous-flow facility driven by a 615-kW motor compressor. Mach 2 in the test section is achieved by a contoured convergent-divergent 2-D nozzle. A variable-incidence boom can be used to position a shock generator in the test section (Fig. 4.17). And this is the shock generator used for the present shock-wave/boundary-layer interaction tests.

In order to avoid vapor condensation during the expansion to supersonic velocities, the air recirculating in the wind tunnel is dried by a dedicated



Figure 4.17: *The test section with the shock generator, and the convergent-divergent 2-D nozzle for Mach 2*

device (Fig. 4.16). This prevents damages to the test article or the wind tunnel walls by droplets impact. Compressor motor limitations make the amount of air treated limited, thus a vacuum pump has to regulate it. This is the cause of the rather low values of static and total pressures available for testing that are reported in Table 4.1.

The test section has optical access for Schlieren and shadowgraph visualizations. This set up is comprised of a 55-Watt lamp as light source, and two parabolic mirrors. These mirrors directed through a systems of focusing lens the Schlieren image onto the SR-CMOS sensing element of a Phantom v7.0 high-speed camera. This camera is capable to acquire images at a frequency up to 100000 pictures per second, depending on the selected picture size and on the recording duration. Schlieren visualizations have been used in the test campaign to film the effects of the roughness on the boundary layer.

General test conditions for supersonic experiments in S-1 are given in Table 4.1.

The experiments were carried out along a 550-mm-long 400-mm-wide plate instrumented with the thin-films and PCBs already described in Section 4.1, and grouped in two distinct inserts. For practical reasons (due to the continuous nature of the wind tunnel and the time required to set it at regime) both the thin-films insert and the PCBs insert were kept mounted side by side through the entire campaign (Fig. 4.18). Each insert had a

| PARAMETER | SYMBOL | UNIT | TYPICAL VALUES |
|---------------------------|--------|-----------|----------------|
| Total pressure | p_0 | $10^3 Pa$ | 9...25 |
| Static pressure | p | $10^3 Pa$ | 1...3.3 |
| Total temperature | T_0 | K | 300 |
| Static temperature | T | K | 160 |
| Reynolds number per meter | Re | $10^6/m$ | 1...2.5 |

Table 4.1: *S-1 main test conditions for $M = 2$*



Figure 4.18: *The layout of the two instrumented inserts on the plate (the PCBs insert is on the left, the thin-films insert is on the right)*

dedicated electrodes plug or single roughness, both mounted at the same distance from the plate leading edge (Fig. 4.19). In this way one had only to switch cables for the spark circuits and for the Data Acquisition System to switch from one measurement to the other without stopping the facility. When testing with the spark no single roughness was installed, while the electrodes plugs stayed mounted in testing the single roughness. The roughness height was 1 mm, the highest tested in the test campaign of Chapter 3.

4.3.2 Thin-film data processing

For the Mach-2 test campaign the unsteady data, acquired at 1 MHz, from the thin-films have been post-processed. No steady values of the wall tem-



Figure 4.19: *Zoomed view on the two instrumented inserts on the plate: each of them has a dedicated electrodes plug or roughness*

perature, and thus convective heat fluxes, were measured, as done in the tests of Chapter 3. This was because the Mach-2 wind tunnel is a continuous-flow facility. Thus, the continuous convection heating reduces the difference between the recovery temperature of the flow and the wall temperature more and more as the wind tunnel is set to regime and test time goes on. In so doing, the wall temperature tends rapidly to the adiabatic (recovery) value. In this case, not only there is no much interest in measuring the wall heat flux because it is near zero, but the thin-films themselves feature an increasing error in their measurements, so that the measured values would also feature a large uncertainty. Therefore, only the unsteady data have been judged of interest and thus post-processed.

The post processing consisted in extracting the RMS and the spectrograms of the wall temperature fluctuations with the same procedure described in Chapter 3, Section 3.6, that is, subtracting from the test signal the electronic noise. However, for this test campaign it has not been possible to acquire the noise at the beginning of each test, as done in the test campaign of Chapter 3, because of the wind tunnel modus operandi. Hence, the electronic noise has been acquired at the end of the test campaign in a series of fifteen dry tests with the whole set up re-build on a bench.

From the point of view of signal processing, no differences existed between the roughness tests in this Mach-2 test campaign and those in the Mach-1.6 and -2.3 test campaign of Chapter 3. On the other hand, the presence of the

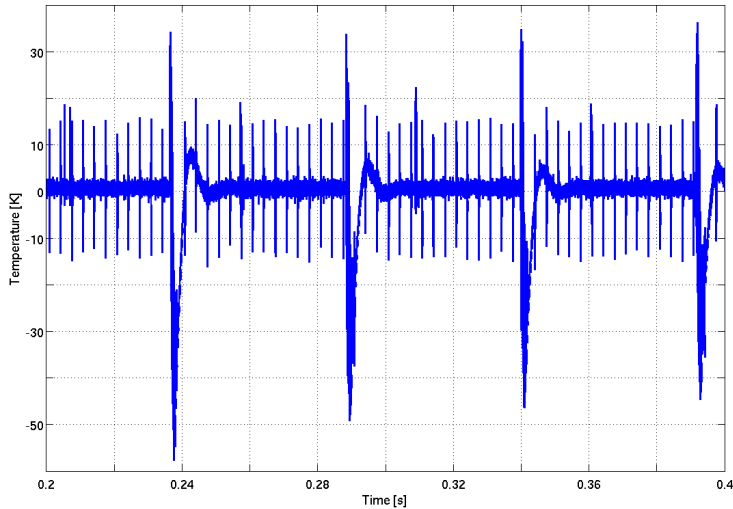


Figure 4.20: *Example of thin-film signal affected by the Electro-Magnetic Interference of the spark release ($f_{spark} = 20$ Hz, no shock wave impinging)*

electric spark introduced a new source of noise in all the sensors signals, and this further noise had to be treated specifically. The signals, in fact, resulted heavily polluted by Electro-Magnetic Interference (EMI) from the electric spark itself and the circuits that generated it. This pollution showed up in the time series of signals and noise as very high peaks at the spark releasing frequency and as many other peaks at its harmonic frequencies. Electro-Magnetic-Interference was present no matter the spark releasing frequency. Figure 4.20 shows an example of this pollution. There appear clearly main peaks each 0.05 seconds, and, between them, series of relatively smaller peaks regularly spaced of 0.0033 s. That is, the main peaks have a frequency of 20 Hz, and the smaller ones of 300 Hz. These peaks are just followed by a dip of equal intensity. This intensity, in turn, stays practically constant throughout the entire test time. The main peaks have a characteristic shape wherein the signal recovers from the dip with an overshoot of the mean value followed by a second less ample overshoot in the opposite direction.

To better appreciate the frequency extent of the Electro-Magnetic Interference, the following Fig. 4.21 shows the spectrum of the signal in Fig. 4.20. There appears how peaks repeat regularly beyond 20 Hz and up to about 700 Hz, equally spaced of about 20 Hz. The maximum amplitude is at 100 Hz, being also the peaks at lower frequencies smaller. However, this result is misleading, since the unsteady signals are analogically high-passed above 100 Hz before being acquired. Hence, the intensities of the peaks below 100

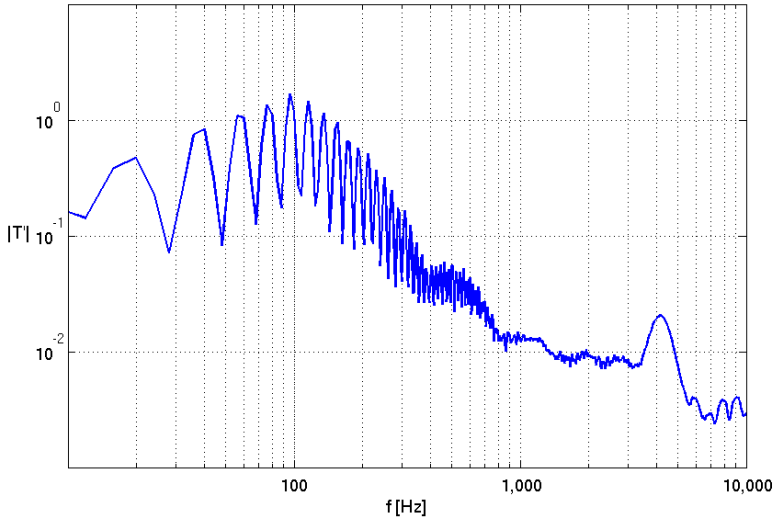


Figure 4.21: *Example of the spectrum of a thin-film signal affected by the Electro-Magnetic Interference of the spark release ($f_{spark} = 20$ Hz, no shock wave impinging)*

Hz have to be considered much higher than shown, because the low-pass filter greatly diminishes them. (Actually, the filter should have zeroed them, and this may give an idea of their original intensity.) As for the presence of the high-pass filter, one may conclude that the highest peak in the spectrum may well be below 100 Hz, as likely if the main frequency is 20 Hz.

It is evident from Figs. 4.20 and 4.21 that the electromagnetic interference is so heavy that has to be removed from the signals to have meaningful measurements. In order to do so, it was decided to modify directly the time series of the signal and noise, removing all those portions where the peaks appeared. Then the remaining portions, unaffected by the interference, were sewed together as to re-establish the continuity of the time series. As a by-product, the usable time series ended up being shorter than the original.

The removal of the peaks has been accomplished by the use of a threshold for the amplitude of the signal. If the amplitude at a given time was above or equal to the threshold, the corresponding data point was eliminated, if it fell below, it was maintained. The threshold value (A_{median}) was set as a multiple of the median of the amplitude throughout the entire test time. The median was chosen as statistic quantity because of its better robustness (respect to the mean value, e.g. [55, 56]) to the effect of outliers in the data sample. These outliers in the present case are the EMI peaks. Different threshold values were tried, and in the end $3 \cdot A_{median}$ resulted the

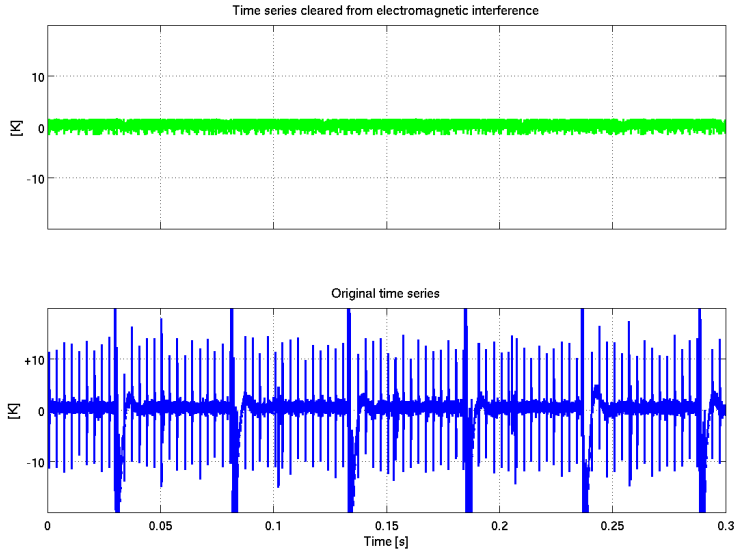


Figure 4.22: Example of the effect on a thin-film time series of EMI removal ($f_{spark} = 20$ Hz, no shock wave impinging)

best compromise between cleaning effectiveness and integrity of the original signal. Figure 4.22 shows the effect of this treatment on a time series from a thin-film measurement, and the following Fig. 4.23 shows the effect on the frequency spectrum.

Figure 4.22 shows how all the most evident peaks of the original time series have gone away by the peak-removal algorithm. Just a light “dent” is still visible in the place of each major peaks. In effect, the spectrum of the cleaned signal in Fig. 4.23 still features major peaks at low frequencies, being the first one at 22 Hz instead of 20 Hz. This slight shift in the frequency of the first peak may well be due to the slight shortening of the time series after the application of the peak-removal algorithm. The number of major peaks in the original time series and of “dents” in the cleaned one is the same, but the latter repeats through a time interval slightly shorter than the original one, consequently, the “dents” frequency results slightly higher than the peaks frequency. However, the tail of harmonics of this peak is shorter than for the original signal in Fig. 4.21, since it disappears around 500 Hz instead of going through 1000 Hz. This means that at least at frequencies equal or higher than 500 Hz the cleaning has been effective. Moreover, the frequencies below 100 Hz were not considered of interest in the first place (thence, the analog high-pass filter), thus it does not matter if harmonics are still present there. Finally, also to be noted, is the general

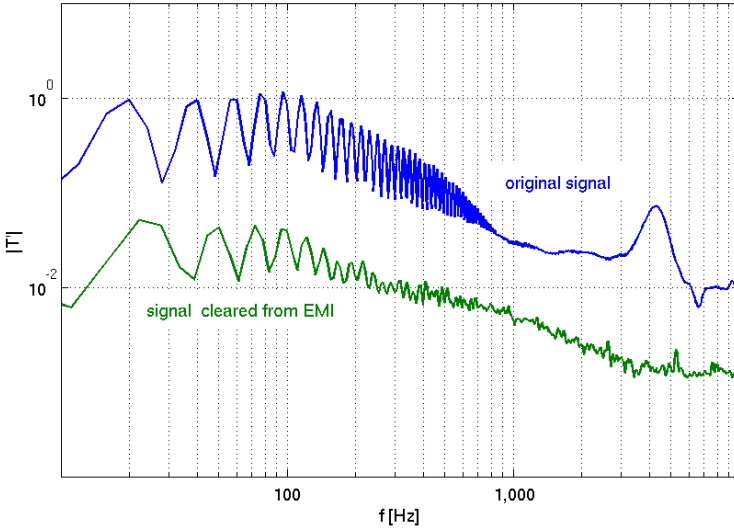


Figure 4.23: *Example of the effect on the spectrum of a thin-film signal of EMI removal ($f_{spark} = 20$ Hz, no shock wave impinging)*

lower fluctuation amplitudes of the cleaned signal respect to the original one, and the disappearing of the bulge at 4200 Hz that, apparently, was also due to EMI.

The type of signal cleaning above presented was applied to both the signal from the experiments and the signals from the dry tests, i.e. the electronic noise. After these applications, the electronic noise was subtracted from the measurement signals in the frequency domain, and RMS trends and spectrograms were obtained directly from the resulting signal (as done in Section 3.6 for the previous test campaign). This process of subtraction determined automatically the frequency range of RMS and spectrograms as that range wherein the signal was larger than the noise. This range was practically the whole resolved spectrum just for some sensors and in some tests. More often it was a band of some tens of kHz, whose width and starting value depended on the sensor and the spark frequency. To allow comparisons among the different tests, then, a common frequency range had to be chosen, and its lower bound happened to be 20 kHz. As a result of this choice a great part of the lower frequencies was cut out, and were left only those frequencies for which the EMI was already feeble, and the cleaning procedure more effective. Hence, the results of the spark tests in the following Sub-sections, and so the conclusions drawn from them, can be considered, at least, not severely clouded by Electro-Magnetic Interference.

4.3.3 Effects of oblique-shock-wave impingement on the wake of a single roughness element

Two series of tests have been carried out: with and without oblique-shock impingement. They were repeated for the insert without the roughness and with the roughness. In this way the measurements allowed the estimation of: the effect of the roughness respect to the no-roughness configuration; the effect of the shock impingement on the no-roughness configuration; and the effect of the shock impingement on the roughness wake. Comparing the latter two cases, one can find out whether the roughness presence makes a difference or not in the effect of the shock impingement. It should be noted that the no-roughness case cannot be strictly regarded as a real flat-plate case because of the presence of the electrodes upstream of the instrumented insert. In fact, as stated in the preceding, the electrodes were kept mounted for practical reasons even when not needed. These electrodes were 0.7 mm high above the wall, thus not much smaller than the 1-mm-high single roughness.

The single roughness is located 26 cm from the leading edge of the flat plate, and this distance corresponds to a $Re_{x_k} = 5.2 \cdot 10^5$, since the unit Reynolds number of the experiments is $2 \cdot 10^6 [m^{-1}]$. The roughness Reynolds number, i.e., the Reynolds number calculated with the flow properties at the roughness height is $Re_k = 570$. The roughness height relates to the local laminar boundary-layer as $k^*/\delta^* \approx 0.85$ and $k^*/\delta \approx 0.42$.

4.3.3.1 Streamwise evolution of wall-temperature fluctuations

The plots in this paragraph show the RMS streamwise trend as measured by the thin-films in the same guise as in Section 3.6. Each plot features the RMS value of all those sensors correctly responding for the tests in cause. In fact, the number of these sensors was variable from test to test, thus RMS trends can be illustrated by different points for different tests. Each test has been repeated at least once to check for repeatability. However, all the signals in this test campaign resulted particularly close to the electronic noise, especially at the highest (>1000 Hz) frequencies. For this reason some of the tests had to be discarded, and the comparisons among different tests feature a rather short frequency range, at most from 100 to 600 Hz. Considering the results of the frequency analysis in Section 3.6, where the highest wall-temperature fluctuations are below 1 kHz, this short range is considered enough for a meaningful comparison among RMS trends.

Many thin-films will appear at the same position in all the plots: they were located on the instrumented insert on a single row across the flow direction (Fig. 4.18). All the distances are calculated from the insert leading edge. This is also the position of the roughness element when mounted on the insert, thus implying that, unlike for tests in Chapter 3, no sensor was located upstream of the roughness position.

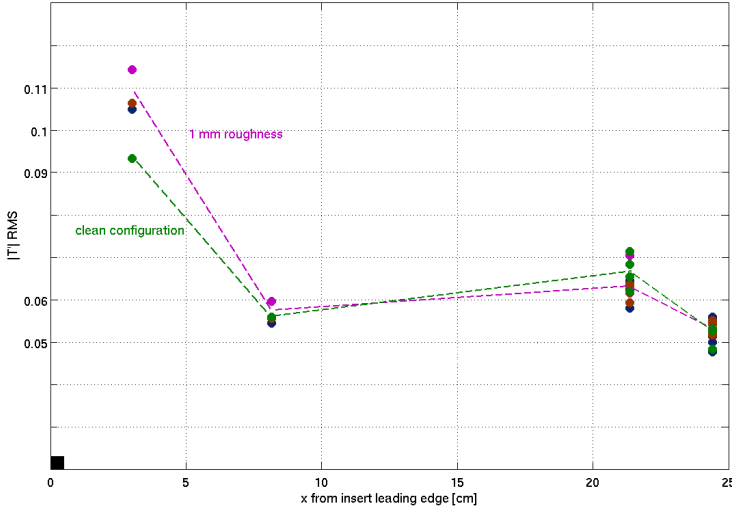


Figure 4.24: Comparison among trends of RMS wall-temperature fluctuations with (3 tests) and without (1 test) the single roughness element ($f_{LP} = 500 \text{ Hz}$)

Figure 4.24 shows the comparison among three RMS trends downstream of the roughness element and one RMS trend along the clean insert. Among the three sets of points for the roughness case two are very close to each other (blue and brown) while the third (violet) has just the first two points, and one of the second row, at a higher amplitude. The comparison with the clean insert trend shows how the only sensible difference in amplitude is for the thin-film closest to the roughness position, i.e. the first one from the left. In fact, this sensor measures in all the three tests an RMS value higher than that of the clean configuration, whilst, further downstream, starting from the very second thin-film, differences are negligible. One can conclude, then, that the roughness effect on the Mach-2 boundary layer extends less than 8 cm behind the roughness position and is negligible further downstream.

Also to be noted for the clean configuration is the sensible difference among the RMS by the first thin-film and the RMS by all the others: if all the latter are between 0.05 and 0.07 K, the RMS of the first is at 0.093 K. This difference may be due to the presence of the electrodes that may act as two single roughness elements. Since they are 3.15 cm upstream of the roughness position, it may still be only the first thin-film that senses their presence as for the single roughness configuration.

Figure 4.25 compares the no-roughness trend of Fig. 4.24 with one trend for the same configuration but with shock wave impingement. The plot

reports the impingement location observed in a Schlieren movie and the one from inviscid theory for oblique shock waves. Note how the observed location is ahead of the location from inviscid theory. This is in accordance with Schlieren observations in ref. [57], where an experimental campaign similar to the present one was carried out for a turbulent boundary layer at freestream Mach numbers of 3.8 and 3.9.

The shock wave impingement appears to have two opposite effects on the wall-temperature fluctuations, depending on the position respect to the impingement location. In fact, the RMS values increase across the observed and the theoretical impingement locations, but decrease further downstream. Moreover, this decrease is to a value that stays practically constant till the end of the instrumented insert. This decrease happens abruptly between the 2.6 cm that separates the second thin-film from the third one.

Figure 4.26, then, is the same as Fig. 4.25 but for the 1-mm roughness configuration, and features more than one test per each case. This Figure shows the same general effect of the shock wave impingement as for the no-roughness case: RMS values are increased between the observed and the theoretical impingement positions and decreased just downstream to a common average value. For the tests in Fig. 4.26 more sensors than for the test in Fig. 4.25 were available, thus RMS values are slightly spread across the rows. Nonetheless, the mean value stays practically the same streamwise. And, notwithstanding the difference of 100 Hz in resolved frequency range, this value is practically the same as of the no-roughness case.

These similarities among roughness and no-roughness cases, in the general trends, and in the RMS values at the end of the instrumented insert, support the conclusion about the roughness effectiveness drawn from the trends without shock wave impingement (Fig. 4.24). That is, the roughness effect does not go a long way downstream, thus along the majority of the instrumented insert the oblique-shock impingement has the same effect on the boundary layer flow with or without the single roughness.

To comment the general effect of the oblique-shock, one may say that it appears reversed depending on the position respect to the impingement point. Just across this point the oblique shock increases the RMS of the wall-temperature fluctuations, but, downstream of it, it decreases them to a constant value. This behavior can be explained by the intrinsic unsteadiness of the flow around the impinging point [57–60, e.g., and references therein], and by the presence of a separation bubble just downstream of it.

In fact, a laminar boundary layer developing along a rigid surface hit by a shock wave can be strongly modified by the ensuing interaction between the abrupt pressure change (due to the shock) and its momentum gradient normal to the wall [e.g., 11, 61–63]. It happens that the pressure rise downstream of the shock is transmitted upstream through the inner subsonic part of the boundary layer. This, then, finds itself flowing against an adverse pressure gradient, therefore, it slows down and thickens below the

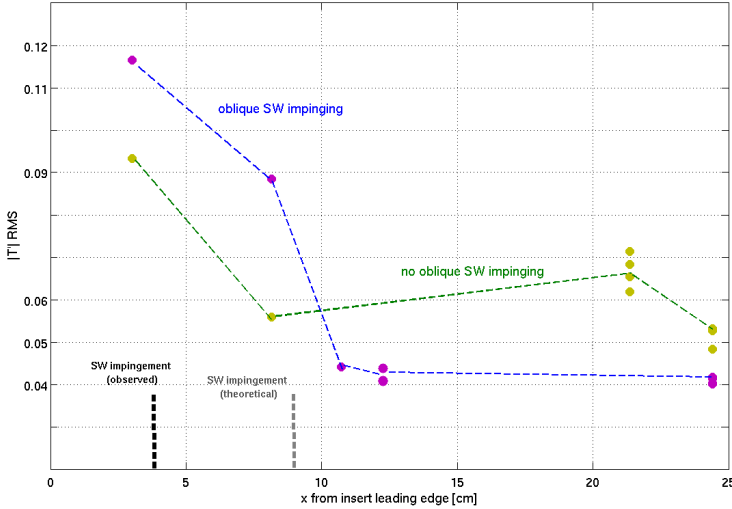


Figure 4.25: Comparison among trends of RMS wall-temperature fluctuations with and without shock wave impingement (no-roughness configuration, $f_{LP} = 600 \text{ Hz}$)

impingement point. If the shock is sufficiently strong, the adverse pressure in conjunction with viscosity is capable of stopping altogether the flow in the subsonic part of the boundary layer, and of reverting its direction. In so doing a separation bubble is formed, in which a part of the boundary layer flow is trapped and turns around as to have its direction at the wall opposite to the direction of the main flow. The rest of the boundary layer flow adjusts to the presence of the bubble by detaching from the surface, flowing above the bubble, and reattaching further downstream of it. A sketch of this flow field is reported in Fig. 4.27 [61]. In this illustration one can note how the characteristic static pressure trend across the separation zone features a plateau across the apex of the separation bubble. This characteristic is also reported in ref. [60], where the separation bubble in a turbulent boundary layer is caused by a frustum around an axial-symmetric body invested by different supersonic flows.

More importantly, in [60] pressure fluctuations at the wall have also been measured across the impingement location and downstream of it (Fig. 4 in [60]) and their trends show a large peak at the shock impingement position followed by a decrease to a plateau level in the fully-separated zone between the shock and the frustum. That is, the same trend as of the wall-temperature RMS in Figs. 4.25 and 4.26. Computations in ref. [64] confirm lower pressure fluctuations at the wall below the separation bubble respect

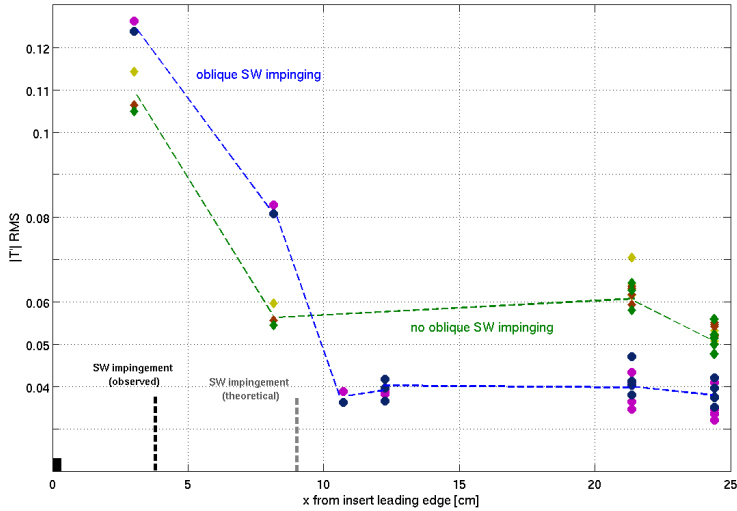


Figure 4.26: Comparison among trends of RMS wall-temperature fluctuations with (2 tests) and without (3 tests) shock wave impingement (1-mm roughness, $f_{LP} = 500$ Hz)

to upstream values; also in this case the supersonic boundary layer studied is turbulent. Finally, a sharp peak in wall-heat-flux fluctuations about 3 cm upstream of the theoretical impingement point has been measured in ref. [57] by thin films in a Mach-3.9 turbulent boundary layer flow. This latter reference is particularly valuable because the same type of sensor as of the present study has been used. And it may help elucidating a further aspect of the present results. In fact, one recognizes that, in the end, in Figs. 4.25 and 4.26 the sole change induced by the shock-wave impingement in all the RMS trends is the higher RMS value of the second thin-film from the left. In fact RMS of the most upstream thin-film were already the highest in both configurations. At this point one can note that the distance between the second thin-film and the theoretical impingement point (taken as reference in [57]) is about 1 cm, much closer to the 3 cm of [57] than the most upstream thin-film. (Furthermore, it is in ref. [57] that the observed impingement point was ahead of the theoretical one). Hence, it may be that is the second thin-film sensing the most of the shock impingement effect in the present experiments instead of the first one.

In conclusion, one can say that the wall-temperature RMS trends in Figs. 4.25 and 4.26 give the same picture of a shock-impingement-induced zone of boundary layer separation as the wall pressure fluctuations in refs. [60, 64]. There are concordances also with the results in ref. [57] about the im-

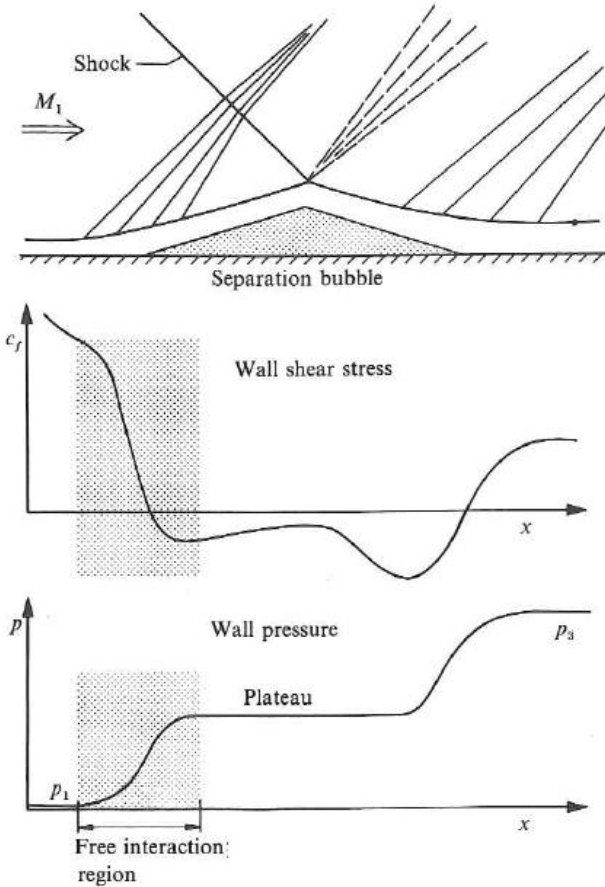


Figure 4.27: Sketch of shock-wave/laminar-boundary-layer interaction in case of separation with skin friction coefficient and static pressure evolutions [61]

pingement position and the highest peak across it. But less so respect to their wall-heat-flux RMS trends below the separation bubble. In fact, they show a second peak followed by a decrease to a plateau level, and a further increase at the reattachment point. In the present results this second peak is not found, and the reattachment appears to happen beyond the instrumented insert (see also Fig. 4.15). These differences may be due to the higher number of sensors in ref. [57] respect to the present case, and to the turbulent state of their boundary layer. For a turbulent boundary layer, in fact, the overall size of the shock/boundary-layer interaction zone is shorter than for a laminar boundary layer [e.g., 65–67].

Finally, one can estimate the length of the separation bubble in the present tests at about 14 cm, applying the results in ref. [68] to present test conditions (oblique shock wave angle = 41° , relative pressure jump $\simeq 1.77$, $Re_u = 2.1 \cdot 10^6$). This value compares rather well with the extension of the constant-RMS zones in Figs. 4.25 and 4.26, that is, about 13.5 cm (from about 11 cm to 24.5 cm). However this latter dimension should be considered as the minimum length of the bubble, since no sensor was available further downstream of 24.5 cm.

4.3.3.2 Wall-temperature fluctuations evolution in the (frequency,time) domain

Spectrograms have been extracted from the thin-film unsteady data also for the Mach-2 tests as for the measurements presented in Chapter 3. They are here presented to complement the RMS trends in the study of the shock wave impingement effect on the configurations with and without the roughness.

Figure 4.28 shows, for the clean insert configuration, the comparison between the spectrograms of the most upstream thin film along the insert. The top plot is the spectrogram of the signal from the test without oblique shock wave impingement, the bottom plot is the spectrogram from the test with shock wave impingement. Data are from the same tests as of the RMS trends in Fig. 4.25. As a first result, Fig. 4.28 shows clearly how the highest fluctuation amplitudes are only for the case with shock wave, thus confirming the RMS results. But, it is also interesting how these high amplitudes appear grouped in intervals throughout the test time, and how these intervals have variable extent. Counting from the interval at the beginning of the test, one can even find a sequence of three of these intervals regularly spaced to each other of about 0.17 s. They are the widest in time and feature the highest amplitudes. This grouping is, in other words, an intermittent appearance in the thin-film signal of time intervals where the wall-temperature fluctuations have the highest amplitudes. This, in turn, implies intermittency of the largest effect of shock-impingement on the flow at the thin-film location.

Figure 4.29 is the same as Fig. 4.28 but for thin-film nr. 4, the sensor just downstream of thin-film nr. 32. The spectrograms here just confirm the same picture as for thin-film nr. 32: the highest amplitudes appear only with the shock-wave impinging, and are still grouped in intervals throughout the test time. Actually, for this sensor the grouping in time of high-amplitude zones is more evident than for thin-film nr. 32, because they alternate with zones of amplitude lower than those in thin-film nr. 32 spectrogram. In this case, a regular repetition of about 0.07 s is recognizable only for the high-amplitude intervals between 0.2 and 0.5 s. Hence this repetition is shorter and at a higher-frequency than for the most upstream thin-film.

Finally, Fig. 4.30 presents the same comparison as the previous two figures, but for a thin-film laying on the last row (the only other location where comparison is possible). At this position it is evident how the spectrogram

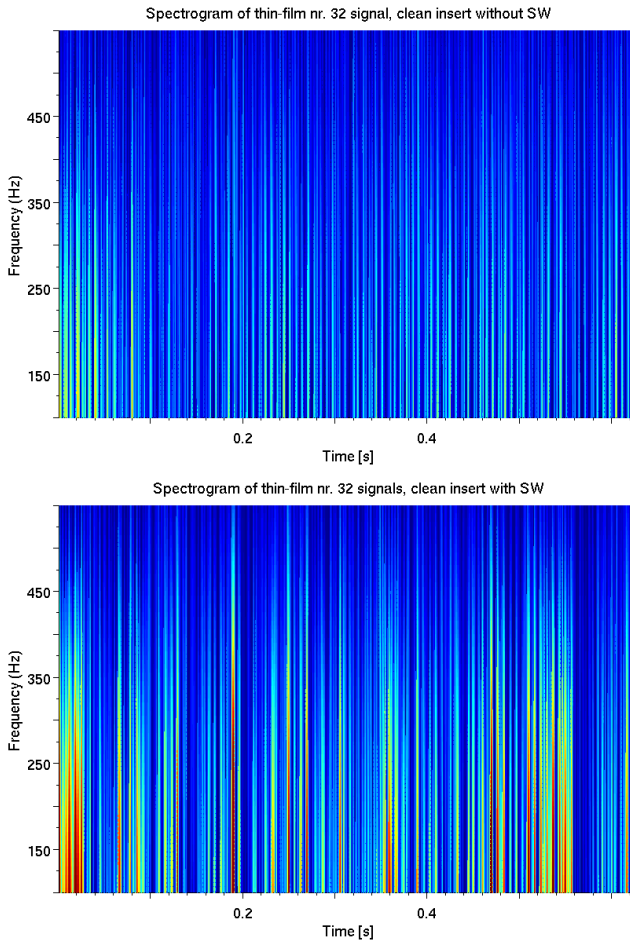


Figure 4.28: Comparison between the spectrograms of the signal by the most upstream thin-film (nr. 32): shock impingement vs. no shock impingement

of the case without shock impingement features slightly higher amplitudes than the spectrogram of the case with shock impingement, thus confirming the picture from the RMS trends. And, as a further confirmation of the RMS trends, thin-film nr. 15 also shows much lower fluctuation amplitudes respect to the two most upstream sensors for the case with shock impingement. Moreover, Fig. 4.30 shows no apparent grouping of high-amplitude zones throughout the test time. In fact, the overall occurrence of amplitude peaks is rather similar to that for the no impingement case. This leads to the conclusion that the intermittency of large-amplitude zones in the spectro-

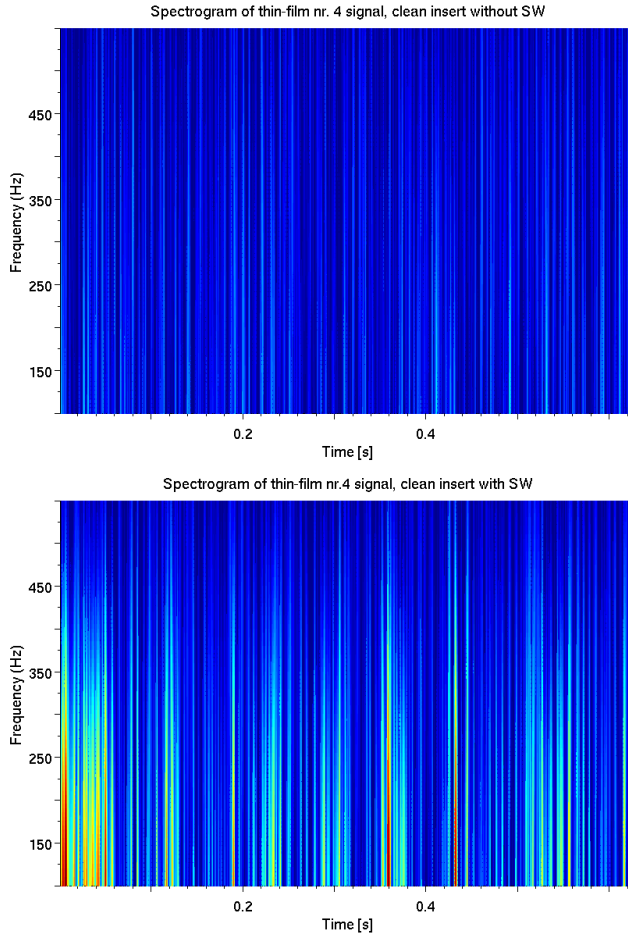


Figure 4.29: Comparison between the spectrograms of the signal by the second most upstream thin-film (nr. 4): shock impingement vs. no shock impingement

grams is limited to sensors around the impingement position, and disappears in the spectrograms by the sensors below the separation bubble located at least 16 cm downstream of the theoretical impingement point.

A space-limited effect of shock impingement onto a supersonic boundary layer has been also measured in ref. [57] (and references therein). In this reference, intermittency was found in the heat-flux time evolution in the form of “disturbed-level” and “undisturbed-level” heat fluxes alternating in time in the zone of the highest heat-flux RMS value. “Disturbed-level” is a level of heat flux compatible with the most severe shock impingement effect,

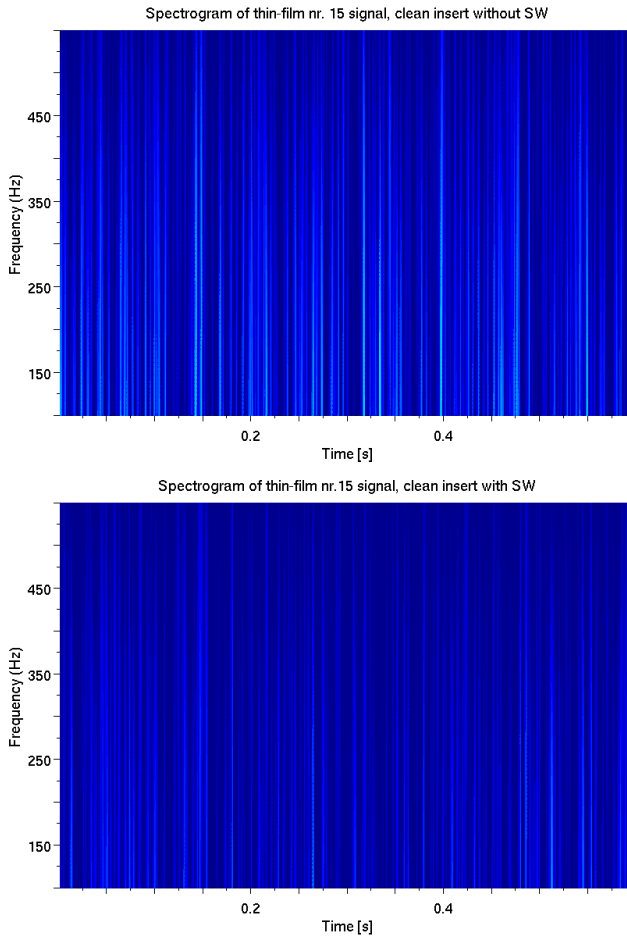


Figure 4.30: Comparison between the spectrograms of the signal by a thin-film on the last row (nr. 15): shock impingement vs. no shock impingement

whilst “undisturbed-level” is compatible with a normal turbulent boundary layer. Further downstream of where the highest RMS was sensed no intermittency was found. They explain the localization of intermittency across the shock impingement by offering the large-scale shock-system oscillations as its cause. These oscillations in turn, affect just the boundary layer flow across the shock impingement point, so that the intermittency is measured only by the sensors around it. Furthermore, in [58] Kistler found a distinctive “on-off character” in the unsteady pressure signal just near the separation point, and no more away downstream. This signal looked as a square-wave, appearing at a frequency considerably less than 1 kHz, super-

imposed to white noise, whose high frequencies had larger amplitudes at the plateau of the square wave.

At this point the case with the 1-mm-high roughness is presented. Figure 4.31 shows the comparison between the spectrograms of thin-film nr. 32 with and without shock impingement. Data are from the same tests as of the RMS trends in Fig. 4.26, and this comparison is representative of the comparisons possible among all the tests for the same thin-film.

Figure 4.31 shows that more frequencies are excited with the shock impingement than without, and for longer intervals, but the amplitudes with and without the shock impingement stay rather comparable. And this latter aspect makes more difficult than for the clean configuration to single out the intermittency of the high-amplitude zones. Figure 4.32 shows the spectrogram for thin-film nr. 4. Here it is even more difficult than in Fig. 4.31 to find intermittency. Most of the spectrogram for the shock-impingement case, in fact, is very similar to that for the no-shock impingement case. Even if one considers the time intervals around 0.44 and 0.52 s (that are just slightly larger than for the no-shock impingement case), the intermittency appearance is much less neat than in the spectrogram by the same thin-film for the clean configuration.

To repeat completely the set of three comparisons already made for the no-roughness case, Fig. 4.33 presents the comparison for thin-film nr. 15 on the last row. This figure does not show much difference respect to the clean insert case: the highest amplitudes appear in the spectrogram for the case without shock impingement, and there is no distinguishable sign of intermittency in the spectrogram for the case with shock impingement.

In conclusion, according to the present experimental results, the roughness has had an effect on the frequency-time evolution of the wall-temperature fluctuations, but this effect is limited to the proximity of the shock impingement point. This can be considered as a further confirmation of the result found in the preceding RMS analysis, where the roughness effect was found confined within the region of the two most upstream sensors. This effect consisted in keeping the overall frequency-time evolution of the fluctuations with and without the shock impingement much more similar to each other than in the clean insert case. In this respect, one may conclude that the effect of the roughness in the present tests stayed strong enough within the first 10 cm of the wake as to be still recognizable through the shock impingement point.

To a similar conclusion came the CFD computations in [69] for a Mach-2.5 laminar boundary layer past a single roughness element. In this numerical study the impingement of an oblique shock wave was simulated onto the wake of the single roughness, and 2-D maps of static temperature, wall-temperature normal gradient, and wall pressure fluctuations, as well as streamwise skin friction coefficient trends, were calculated. The general result was that the wake survives through the shock impingement point. In fact, wall-temperature normal gradient and wall pressure fluctuations

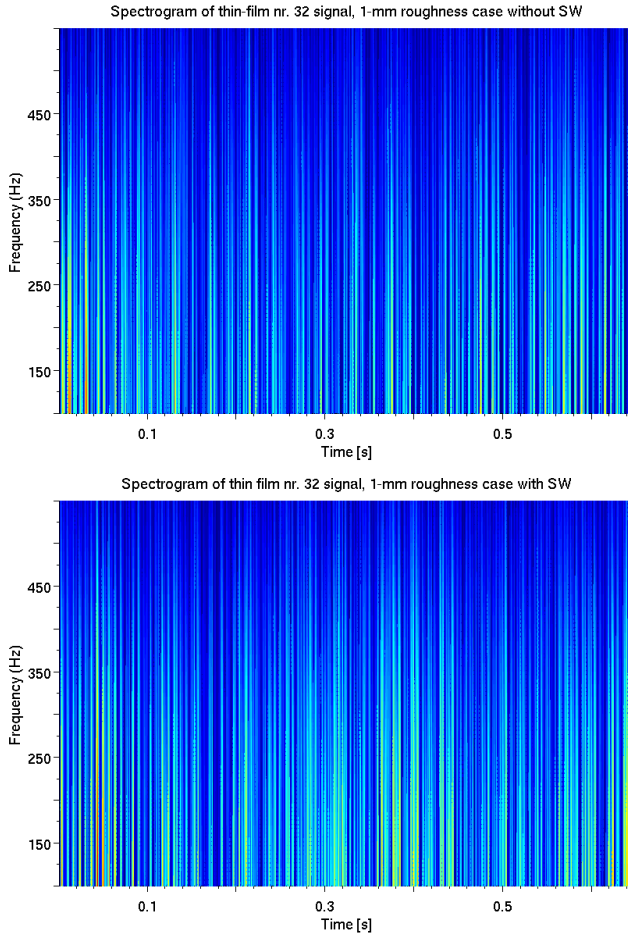


Figure 4.31: Comparison between the spectrograms of the signal by the most upstream thin-film (nr. 32), 1-mm-high roughness case: no shock impingement vs. shock impingement

within the part of the wake across the impingement point were found to stay at values comparable to those without shock impingement. Furthermore, the pressure fluctuations map in [69] shows a streamwise decrease in intensity aligned along the roughness centerline just after the impingement point respect to the values for the no-impingement case. This finding may support the present RMS measurements that revealed the same trend for the wall-temperature fluctuations.

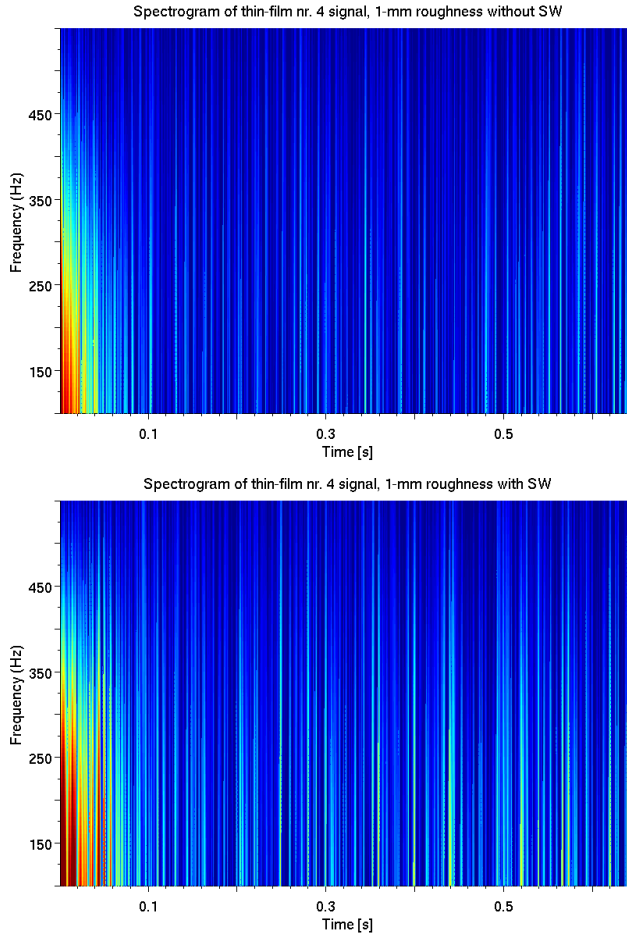


Figure 4.32: Comparison between the spectrograms of the signal by the second most upstream thin-film (nr. 4), 1-mm-high roughness case: no shock impingement vs. shock impingement

4.3.4 Effects of an electric spark within a supersonic laminar boundary layer with and without oblique-shock-wave impingement

As for the experiments without spark release, also for the tests with the spark release the number of available thin-films was varying from test to test. And also the signal was larger than the noise only within a band of frequencies.

For quite a few tests the number of sensors was not enough to produce

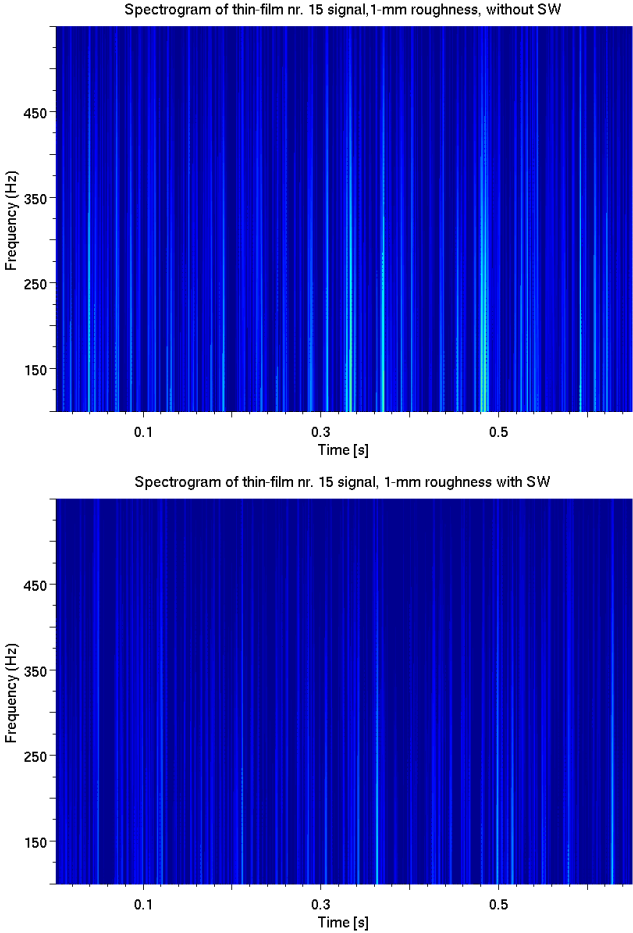


Figure 4.33: Comparison between the spectrograms of the signal by a thin-film on the last row (nr. 15), 1-mm-high roughness case: no shock impingement vs. shock impingement

meaningful trends. Therefore, it was decided to show only those tests for which at least one thin-film was functioning on each location throughout the whole instrumented insert. For this reason only the comparison between the 100-Hz and a reference case without any spark effect is presented in Sub-section 4.3.4.1 for the case without shock impingement. The reference case was a 1-Hz-spark case in which the spark was wrongly released 0.32 s before the measurements start, that is, too early to still measure its effect on the supersonic boundary layer flow.

More tests with shock impingement were successful. As many as to allow

the comparison of all the four frequencies selected with a sufficient amount of thin-films. To have this comparison as fair as possible, only the RMS values measured by the same set of thin-films are shown in all the plots.

The transformer was operated in two different modes for the tests at 100 Hz: the “burst-mode” and the “long-mode”. The difference consists in the duration of the disturbance to the flow, i.e. in the time the transformer was kept on. For the “burst-mode”, the first 0.3 s of the test time, for the “long-mode”, the whole test time. Only the test in “burst mode” was successful for the configuration without shock impingement, but, only the test in long mode was successful for the configuration with shock impingement. Therefore, no direct comparison between these two tests can be done.

The bands of frequencies wherein all the signals were comparable was 20 to 60 kHz, thus on the upper end of the instrumentation capability. This range is different from that of the tests without spark in Sub-section 4.3.3, so no significant direct comparison among those trends is possible.

Each plot starts its abscissa from the location of the electrodes between which the spark is released. This location is 3.2 cm ahead of the instrumented insert (22.65 cm from the plate leading edge), and this is why there was no sensor upstream of the electrodes.

4.3.4.1 Streamwise evolution of wall-temperature fluctuations

Figure 4.34 shows the comparison between two RMS trends of wall-temperature fluctuations. One trend is for the spark released at 100 Hz and the other is for a reference state without spark effect. The spark at 100 Hz was released by the circuit with the transformer operated in burst mode.

The reference trend develops around the average value of 0.06 K, except for two points, one on the first row and the other one on the last row of thin-films. One of these points is the maximum value, about 0.11 K, at 12.2 cm from the insert leading edge, that is, at 15.6 cm from the spark release location. In the case of the 100-Hz spark-release frequency the picture is different. The RMS trend has its peak (0.14 K) at the position closest to the electrodes, its second highest value (0.12 K) at the measurement point just downstream of it, and values mostly between 0.6 and 0.8 K from the third measurement point on. This is so except for the second thin-film on the first row, at 15.6 cm from the electrodes, that sensed an RMS of 0.09 K. Hence, for 100 Hz, the highest spark-release frequency, the highest wall-temperature fluctuations were sensed more upstream than for the reference case. However, downstream of 10 cm from the insert leading edge, RMS values for both cases are very much comparable, and, except for two outliers in the reference case, and one in the 100-Hz case, also rather constant streamwise. This may induce the conclusion that the effect of the spark released at 100 Hz, and in one burst, is limited to the proximity of the electrodes and does not survive more than 13 cm behind them.

Next Fig. 4.35 shows the comparison among the RMS trends produced

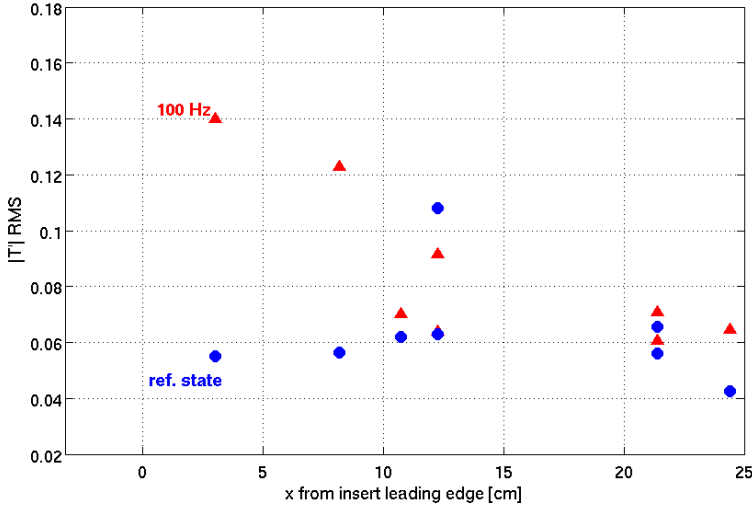


Figure 4.34: Comparison between the RMS trends of the wall-temperature fluctuations for $f_{spark} = 100$ Hz and for a reference state ($f \in [20/div60]$ kHz)

by sparks released at 1, 10, 20, and 100 Hz for the tests with the shock wave impingement. The single spark for the 1-Hz test was released 0.36 s after the test start. For the 10- and 20-Hz cases the sparks were released at the beginning of the test. Finally, the transformer for the 100-Hz case was started at the beginning of the test, and was kept on until its end (long mode).

Figure 4.35 shows clearly how the RMS trends for the three lower frequencies, 1, 10, 20 Hz, are practically coincident to each other. These trends develop along the instrumented insert between the extreme values 0.04 and 0.12 K, but mostly around the value 0.07 K. This latter value is only slightly larger than the average value around which evolves the reference RMS trend in Fig. 4.34 (0.06 K). On the other hand, the RMS trend for the 100-Hz case shows the largest values throughout the whole instrumented insert, except at 21.4 cm, where it is lower than but still comparable to the values of the other trends. The maximum RMS value is reached at the location of the second sensor (0.51 K), and decreases sensibly from there, to finally evolve around 0.2 K (except at 21.4 cm). This means that the largest RMS differences among the 100-Hz case and the others are by the two most upstream sensors, those closest to the electrodes, and near the theoretical and observed shock impingement positions.

The relative streamwise constancy of the RMS values from the 1-, 10-, and 20-Hz cases highlights the absence of the shock impingement effect on

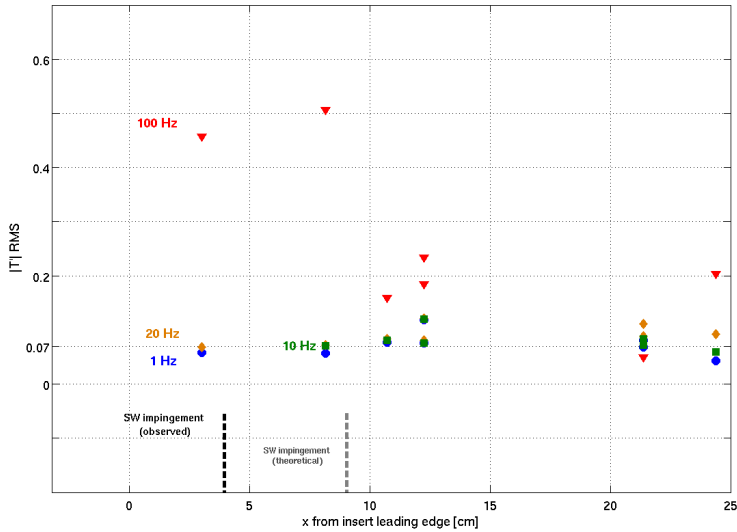


Figure 4.35: Comparison between the RMS trends of the wall-temperature fluctuations for $f_{spark} = 1, 10, 20, 100$ Hz and with shock wave impingement

the wall-temperature fluctuations found in Sub-section 4.3.3. This can be explained by the fact that the RMS is calculated in a range of frequencies that goes from 20 to 60 kHz. If the impingement effect on the fluctuations RMS is due to impingement position instabilities as from refs. [57–60], one can well expect that these instabilities have not a frequency of the order of tens of kilohertz. This consideration make suppose that also the high RMS trends for the 100-Hz case at the positions across the impingement location are not due to the shock but only to the electric spark. This supposition will be worked out in the following Sub-section 4.3.4.2, where signal evolutions in the (frequency,time) domain are shown by the use of the spectrograms.

4.3.4.2 Wall-temperature fluctuations evolution in the (frequency,time) domain

As well as for the shock-impingement tests made with and without the roughness element, spectrograms are presented also for the tests made with the spark. They will complement the information from the RMS trends also for this batch of tests.

Figure 4.36 shows the comparison between the spectrograms of the most upstream thin-film (nr. 32) for the reference case and for the 100-Hz case. As said in the preceding, in the latter case the transformer is used in "burst mode", and the duration of the burst appears clearly in Fig. 4.36 from

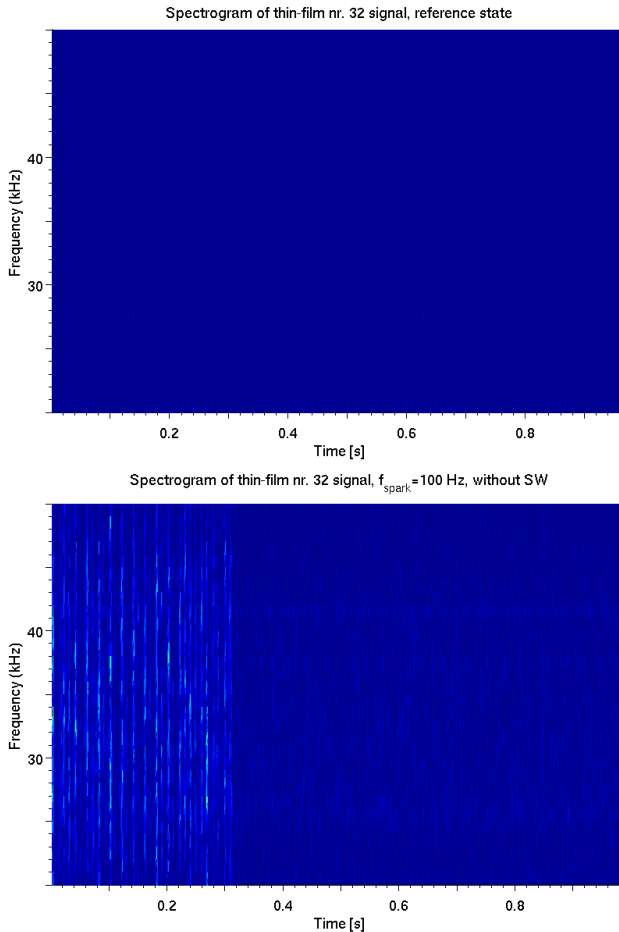


Figure 4.36: Comparison between the spectrograms of the signal by the most upstream thin-film (nr. 32): 100-Hz spark vs. no-spark-effect reference state; no shock impingement (transformer operated in “burst mode”)

0 s to to 0.36 s. There also appears how the signal spectrum becomes practically equal to that of the reference case just after the end of the “burst mode”. During this mode, then, the spectrum is excited regularly each 0.01 s throughout the resolved range; this time spacing corresponds to the frequency of the spark release, 100 Hz.

The following Fig. 4.37 is the same as Fig. 4.36 but for a sensor on the second row, at 21.4 cm from the insert leading edge (thin-film nr. 22). This comparison confirms the results from the RMS trends: at this distance from the electrodes the signal spectra from the two cases have become very similar

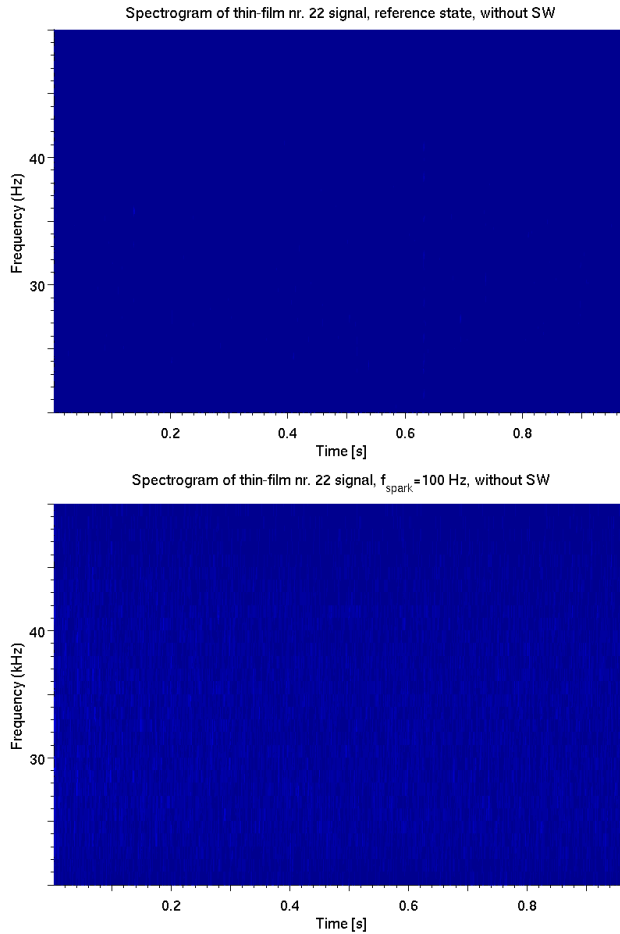


Figure 4.37: Comparison between the spectrograms of the signal by a thin-film on the second row (nr. 22): 100-Hz spark vs. no-spark-effect reference state; no shock impingement (transformer operated in “burst mode”)

to each other.

Now Fig. 4.38 shows the comparison among the spectrograms of thin-film nr. 4, for all the four spark frequencies. This sensor is the one measuring the highest RMS in Fig. 4.35.

The most excited spectrum is clearly for the 100-Hz case, and, like in Fig. 4.36, this excitation is equally spaced through the test time of 0.01 s, i.e. the frequency of the spark release. However, note how the largest amplitudes appear below about 37 kHz and are larger than in Fig. 4.36. Also in the other three frequency cases one can distinguish clearly the spark release

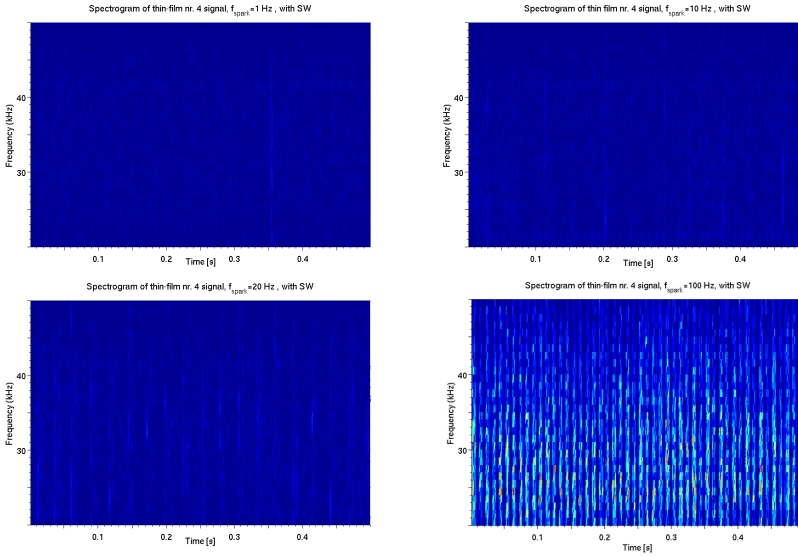


Figure 4.38: Comparison between the spectrograms of the signal by the second most upstream thin-film (nr. 4); spark frequencies are 1, 10, 20, 100 Hz (tests with shock impingement; transformer operated throughout the test time)

from the time spacing between two adjacent excited bands. However, in all these cases the amplitudes of such excitation are far lower than for the 100-Hz case. Moreover, they also look to last less, considering the width of the colored bands respect to that for the 100-Hz case. The evidence of higher fluctuation amplitudes for the 100-Hz case can be explained by the measurements of energy release presented in Section 4.2, where the transformer resulted yielding about 2.5 times more energy to the flow than the battery-coil circuit.

Finally, the spectrogram of thin-film nr. 32 in Fig. 4.39, for the 100-Hz case, is not different from that of thin-film nr. 4. That is, the highest excitation of the whole frequency spectrum is timed on the spark release throughout the test time. Both these evidences imply that the fluctuation high amplitudes in the zone across the shock impingement are produced by the spark and not by the instabilities of the shock position as found in Sub-section 4.3.3. This finding supports the conclusion drawn from the RMS trends for the 1-, 10-, and 20-Hz cases that the shock impingement has no characteristic frequency above 20 kHz, thus it leaves no trace in the frequency band here resolved.

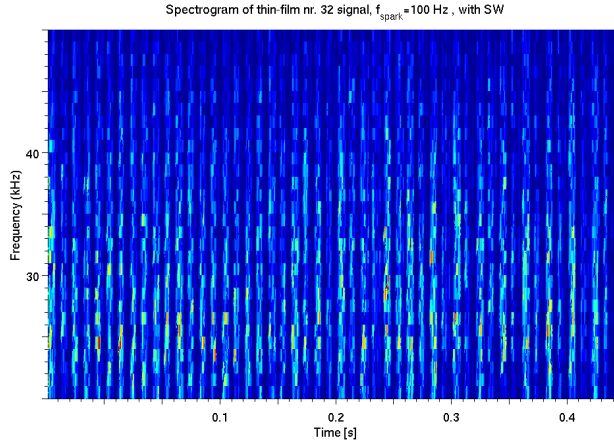


Figure 4.39: *The spectrogram of the signal by the most upstream thin-film (nr. 32); spark frequency=100 Hz; with shock impingement (transformer operated throughout the test time)*

4.4 Conclusions

This Chapter has described the test campaigns made at Mach 2 to investigate the effects of the impingement of an oblique shock wave on a supersonic transitional laminar boundary layer. The transitional boundary layer consisted in the wake of a single roughness with dimensions $h \times w \times l = 1 \times 2 \times 2 \text{ mm}^3$, and in the laminar boundary layer perturbed by the release of electric sparks.

The comparison of wall-temperature RMS trends with and without the single roughness, and without shock impingement, showed that the effect of the 1-mm-high 2-mm-wide roughness on the laminar boundary layer does not extend further downstream of 8 cm. This implies that the effect of the shock impingement on the roughness wake beyond this distance is essentially the same as for the clean configuration. This effect has been found to be twofold depending on the position respect to the shock impingement point. In fact, in the zone across this point the RMS of the wall-temperature fluctuations are higher than without shock impingement, whereas they become lower further downstream. The RMS increase in the zone across the shock impingement is larger for the clean configuration than for the roughness configuration, especially for the most upstream thin-film. But, beyond 10 cm from the leading edge of the instrumented insert the RMS trend for both configurations falls practically to the same constant value.

The explanation offered for this wall-temperature RMS trends is the intrinsic instability of the shock impingement position, and the presence of a recirculation bubble downstream of it. The instability of the impingement

position can be responsible for the high RMS of the two most upstream sensors (and, possibly, more of the second one than of the first one). Whereas the recirculation bubble can be responsible for the lower RMS from all the other sensors, above which it may extend downstream of the impingement point. The streamwise extent of this bubble, as evinced from the RMS measurements, compares well with estimated values from literature.

The spectrograms of the signals from the thin-films across the shock impingement position helped elucidating an aspect not evident in the RMS trends. This is the intermittency throughout the test time of the shock impingement effect for the clean configuration. In fact, the spectrograms of the most upstream thin-films show time intervals within which the frequency spectrum is excited, interposed between intervals wherein the spectrum feature the lowest amplitudes. All the same, this is not so for the 1-mm single roughness case. In this case, in fact, there are no such evident intervals, and the spectrograms of the two most upstream thin-films, for the cases with and without shock impingement are much more similar to each other. This leads to the conclusion that the roughness has an effect on the shock/boundary-layer interaction in the form of preserving most of the character of its wake through the shock impingement position. At least, more than a laminar boundary layer is capable to do.

To disturb the supersonic boundary layer with the electric spark, a completely new set-up had to be conceived, designed, and tested. This type of disturbance was chosen because literature data showed it capable of producing turbulent spots, i.e., the major feature of a natural transitional boundary layer. However, the majority of the literature refers to subsonic, low-velocity flow regimes, and only one to a supersonic case, which is, nonetheless, different in many respects from the case here under study. This lead us to adapt for the present test campaign the set-up used for incompressible-flow experiments as found in the open literature.

The smoke-sheet visualizations obtained in the preliminary test campaign at low velocity, checked against the available literature on the subject, gave, at least, positive hints on the set-up effectiveness in producing turbulent spots. These hints were judged enough to try the same set-up to simulate a naturally transitional supersonic boundary layer for the Mach-2 test campaign.

After the specific post-processing required by the signals acquired with the spark on, the RMS trends and the spectrograms of the wall-temperature fluctuations in the Mach-2 boundary layer flow were produced and inspected to look for the spark effects. In the tests without shock impingement, and for the spark released at 100 Hz in one burst, this effect was found in localized RMS values higher than for the reference, no-spark-effect, case. The highest RMS were measured at the positions of the two most upstream thin-films, while further downstream the RMS rapidly decreased to the values of the reference case. The spectrograms showed how the frequency spectrum of the most upstream thin-film was excited in synchrony with the spark release,

and how it became very much like that of the no-spark reference state, after the spark release ceased. No sensible differences between the spectrograms with and without the spark were found for the most downstream sensor, thus confirming the conclusion from the RMS trend that the spark effect is localized close to the electrodes.

The wall-temperature RMS trends from the tests with shock-wave impinging revealed that the sparks released at 1, 10, or 20 Hz had the same effect on the supersonic laminar boundary layer. In fact, these three trends are practically coincident to each other. Furthermore, they evolve closely around an average value not very different from that of the no-shock-impingement case. On the other hand, the RMS produced by the spark released at 100 Hz (in this case kept on during the whole test time), are always larger at almost each thin-film location. But, again, like for the test without shock impingement, the largest differences are found at the two most upstream thin-film positions.

The evidence that RMS values for the 1-, 10-, 20-Hz spark-release frequency with shock impingement, and RMS values for the no-spark-effect reference case without shock impingement are comparable throughout the instrumented insert can lead to two conclusions. The first conclusion is that these three spark release frequencies are in the same way scarcely effective in disturbing the supersonic laminar boundary layer; at least less so than the 100-Hz release frequency. The second conclusion is that there is no evidence by the most upstream thin-films of a shock impingement effect, unlike for the roughness case and its relative clean-insert reference case. This can be due to the difference in resolved frequency range: 20 to 60 kHz for the tests with the spark; 100 to 600-Hz, at most, for the tests without spark. Hence, if the high RMS values across the shock impingement position are due to its intrinsic unsteadiness, the present results show that this unsteadiness, at Mach 2 and unit Reynolds number one million, features its highest frequency contents below 20 kHz. This conclusion is supported by Kistler [58] that found the “on-off character” of the pressure unsteady signal, measured across the shock impingement position, at a frequency well below 1 kHz.

The above conclusion may lead to consider the RMS maxima for both 100-Hz cases also unrelated to the shock impingement. And, actually, this induction is supported by the information in the spectrograms of the most excited thin-films. They, in fact, clearly show how the frequency spectrum is excited periodically through the test time, and how this period corresponds to the period of the spark release. Between two adjacent excitation times, or at the end of the “burst mode”, instead, the spectra feature regularly the minimum amplitudes. This confirms that the high RMS values are strongly linked to the release of the spark.

In the end, the conclusions from the tests with the electric sparks can be summarized as: the most effective spark-release frequency is 100 Hz, but its effect is limited, at most, within 13 cm downstream of the electrodes; the effect of the shock impingement is not detectable in the frequency range

resolved, thus it has its fullest frequency content below 20 kHz.

Chapter 5

Conclusions

The present research has addressed the qualification of a multiple-Mach-number supersonic wind tunnel, the experimental study of the effects of single-roughness elements on supersonic boundary layers, and the experimental study of the oblique shock wave impingement onto two types of supersonic transitional boundary layer. The multiple-Mach-number supersonic wind tunnel was a blow-down facility comprised of a squared-cross-section Laval nozzle with a variable-angle divergent part. Two single roughness elements have been tested at Mach 2.3 and 1.6, both with the same width and length, but with different heights. A 41° -oblique shock wave was made impinge onto the not-yet-turbulent supersonic wake of a single roughness element, and onto a supersonic laminar boundary layer perturbed by electric sparks. The investigation of the roughness effects has been carried out through a test campaign in the qualified multiple-Mach-number supersonic wind tunnel. The investigation on the effects of the shock wave impingement has been carried out in a continuous-flow Mach-2 wind tunnel. This latter investigation has comprised also a preliminary test campaign in a low-speed wind tunnel to qualify the hardware for the generation of the electric sparks. The qualification of the multiple-Mach-number wind tunnel

has consisted in the verification of its correct start in a range of supersonic Mach numbers, and in the assessment of the freestream disturbances intensity and frequency spectrum. These two tasks have been accomplished by the measurement of the static pressure evolution along the wind tunnel divergent in a range of Mach numbers, and the numerical computation of the two-dimensional flow within the whole wind tunnel in a range of Mach numbers.

These measurements and computations have provided the following findings:

- the supersonic wind tunnel performs a shock-free supersonic expansion in the Mach range between 1.6 and 2.3
- the design of the wind tunnel suction slots avoids successfully the formation of a recirculation bubble in the proximity of the flow stagnation point

- the freestream mass-flow fluctuations have intensities of 0.63% of the mass-flow mean value for $M_\infty = 1.7$ and of 1.14% for $M_\infty = 1.9$. These values are in line with typical supersonic wind tunnel values, and are acceptable for the study of boundary layer induced transition to turbulence

The experimental investigation of single roughness effects on supersonic laminar boundary layers has consisted on the study of the steady and unsteady characteristics of the flow in the roughness wake at different wall temperatures. This study has been accomplished by:

- time-averaged wall heat-flux measurements at different wall temperatures
- time-averaged adiabatic-wall temperature calculations
- wall-temperature fluctuations measurements at different wall temperatures
- wall-pressure fluctuations measurements

The time-averaged effect of the roughness on the supersonic boundary layer consists in increased absolute convective heat-flux intensities and adiabatic-wall temperature values. This effect is localized close downstream of the roughness, and does not propagate further downstream, neither streamwise nor spanwise. The general effect of wall temperature rise is an increase of wall-temperature fluctuation amplitudes below 1 kHz, unless the higher roughness is present. As far as the sole Mach effect is considered, wall-temperature and pressure fluctuations decrease their amplitudes downstream of the higher roughness as the Mach number decreases. This is also the case for wall-pressure fluctuations downstream of the lower roughness. Wall-temperature and -pressure fluctuations change their spectral character downstream of the higher roughness as the Mach number decreases. That is, peaks of wall-temperature fluctuations repeat more frequently along the frequency spectrum, while peaks of wall-pressure fluctuations center around a specific frequency. The evolution of the RMS of the wall-temperature fluctuations at the higher Mach number changes with the roughness height. As the roughness is the lower, the RMS has its lowest value closest to the roughness, and its highest values away from it. As the roughness is the higher, the RMS has its highest value closest to the roughness, and decreases monotonically with the distance. This latter trend is also found at the lower Mach number. However, in all the cases the maximum RMS amplitudes stay well below turbulent levels, and much closer to laminar ones. The frequency-time evolution of the wall-temperature and -pressure fluctuations at a given position is characterized by the recurrence in time of roughly the same excited frequencies throughout the whole test time. This recurrence was found

higher for those tests where higher RMS was measured. Only for the wall-pressure fluctuations at the lower Mach number this higher recurrence was coupled with a peak amplitude increase. The RMS of the wall-pressure fluctuations, by the sole pressure transducers that performed acceptably, increases with the Mach number for both roughness heights and for the clean insert. Then, downstream of the lower single roughness the RMS is found to be slightly lower than for the clean configuration at both Mach numbers. A phenomenon moving at 80% of the freestream velocity appears from the cross-correlations of the wall-temperature time-resolved signals

These experimental evidences lead to the following conclusions:

- the combined effect of roughness presence and wall temperature rise is not sufficient to trigger a fully turbulent boundary layer within the extension of the instrumented inserts. And this is for both Mach numbers and both roughness heights tested, and at all the wall temperatures set
- a possible explanation for the main mechanism of RMS increase experienced by wall-temperature fluctuations downstream of the single roughness can be the higher repetition through the whole test time of (more or less) the same excited spectrum, instead of the appearance of higher peaks in the spectrum at given moments within the test time. This is not so for the wall-pressure fluctuations that feature the appearance of such peaks especially with the higher roughness
- there is no dependency of the phenomenon moving at 80% of the freestream velocity on the presence of the roughness element for both Mach numbers tried and for all the wall temperatures tested

The experimental investigation of the effects of the impingement of an oblique shock-wave onto supersonic transitional boundary layers has consisted in the study of the unsteady characteristics of the flow across and downstream of the shock impingement position. This study has been accomplished by:

- measurements of wall-temperature fluctuations
- the use of the higher single roughness element as of the previous test campaign to generate a transitional wake
- the release of electric sparks at different frequencies to simulate a naturally transitional supersonic boundary layer

The effect of the single roughness on the laminar boundary layer is confined close to the roughness location in absence of the shock impingement. The effect of the shock impingement on the clean configuration and on the

roughness configuration is two-fold depending on the position respect to the shock impingement point: in the zone across it, the RMS of the wall-temperature fluctuations becomes higher than without shock impingement; in the zone downstream of it the wall-temperature fluctuations become lower than without shock impingement. The RMS increase in the zone across the shock impingement is larger for the clean configuration than for the roughness configuration, but beyond one third of the instrumented insert length it falls practically to the same constant value for both configurations. The shock impingement effect on the wall-temperature fluctuations measured for the clean configuration is intermittent in time. This intermittency is highlighted in the fluctuations frequency-time maps by the alternation of periods where the spectra are most excited with periods where the spectra are most unexcited. This intermittency is not found for the roughness configuration.

The effect of an electric spark released at 100 Hz in one burst within the laminar boundary layer without shock impingement is localized close downstream of the release point. This effect is found in the RMS of the wall-temperature fluctuations increased above the reference no-spark values. Further downstream of the release point the RMS values collapse to the reference ones. The frequency spectrum of the wall-temperature fluctuations is excited in synchrony with the spark release, and as long as the spark is released. The effects on the wall-temperature fluctuations RMS of electric sparks released at 1, 10, or 20 Hz within the laminar boundary layer impinged upon by an oblique shock-wave are practically the same. These effects do not change sensibly the RMS values respect to the clean-plate, no-spark, no-shock-impingement case. The effect on the wall-temperature fluctuations of an electric spark released throughout the whole test time at 100 Hz, and within the laminar boundary layer impinged upon by the oblique shock wave, consists in a generalized RMS increase along the whole instrumented insert. However, the largest increases are localized close to the spark release point. No intermittency of the shock impingement effect is found in the wall-temperature fluctuations for any of the tests made with electric sparks.

The experimental evidences from the case of the single-roughness supersonic wake lead to the following conclusions:

- the single roughness element has an effect on the Mach-2 laminar boundary layer limited in space. This effect is not enough to trigger a fully turbulent boundary layer in its wake
- a recirculation bubble can be present along the clean plate just downstream of the shock impingement position and up to or beyond the end of the instrumented insert. It can be the cause of the RMS decrease respect to the reference no-shock-impingement case for both clean and roughness configurations
- the instability of the impingement position can be responsible for the

high RMS sensed just across it

- the wall-temperature fluctuations in the roughness wake preserves their frequency-time characteristics through the shock impingement position more than in the laminar boundary layer

and the experimental evidences from the spark-perturbed supersonic laminar-boundary-layer case lead to the following conclusions:

- among the four spark release frequencies tested, the most effective is the highest, 100 Hz. Its effect on the wall-temperature fluctuations last as long as the spark is released, and is synchronized with it. The largest effect is localized in the space close downstream of the release point
- the unsteadiness of the shock impingement position features its frequency content below 20 kHz

This work has provided a significant contribution on two research topics relevant to the design of turbulence triggers for high-speed aero-engine intake design. A multiple-Mach-number wind tunnel has been designed built and qualified to address the first topic. The experimental research on the steady and unsteady effects of a single roughness element on two supersonic boundary layers at different wall temperatures has reported original findings on the flow mechanisms that develop within the roughness wake. Prediction tools, based on literature data and analytical models, are used to conclude about the effectiveness of the two roughness heights tested in triggering a fully turbulent boundary layer flow. The unsteady evolution of the flow across and downstream of the impingement point of an oblique shock wave was measured in a Mach-2 laminar boundary layer to address the second topic. The observed evolution of wall-temperature fluctuations highlighted the differences and the commonalities between the two types of boundary layer investigated, and should serve to design effective turbulence triggers when boundary-layer/shock interaction is considered.

Bibliography

- [1] J. D. Mattingly and H. von Ohain. *Elements of Propulsion: Gas Turbines and Rockets*. AIAA Education Series, 2006. 1
- [2] J. Seddon and E. L. Goldsmith. *Intake Aerodynamics*. William Collins Sons & Co. Ltd., UK, 1985. 1
- [3] W. H. Heiser and D. T. Pratt. *Hypersonic Airbreathing Propulsion*. AIAA Education Series, 1994. 1
- [4] G. V. Lachmann. *Boundary Layer and Flow Control*. Pergamon Press, UK, 1961. 1
- [5] S.P. Schenider. Survey of boundary-layer transition for hypersonic applications, 2011. 1, 2, 3, 27, 29, 52, 127
- [6] R. A. van den Braembussche. *Measurement Techniques in Fluid Dynamics*. von Karman Institute for Fluid Dynamics, second edition, September 2001. 2, 49
- [7] R.S. Figliola and D. E. Beasley. *Theory and Design of Mechanical Measurements*. John Wiley and Sons, 1991. 2, 48
- [8] E. Reshotko. Boundary-layer stability and transition. *Annual Review of Fluid Mechanics*, 8:311–349, 1976. 2, 127
- [9] W. Saric. Flight experiments and supersonic quiet wind tunnels. In *Advances in Laminar-Turbulent Transition Modelling*, number 151 in AVT. RTO-AVT-VKI, VKI, June 2008. 2, 9
- [10] D. Arnal. Laminar-turbulent transition problems in supersonic and hypersonic flows. In *AGARD-R-761*, 1988. 3, 34, 60, 127
- [11] H. Schlichting. *Boundary Layer Theory*. McGraw-Hill Book Company, Inc., USA, 1987. 3, 53, 127, 152
- [12] R. Narasimha. The laminar-turbulent transition zone in the boundary layer. *Prog. Aerospace Sci.*, 22:29–80, 1985. 3, 127, 136, 137
- [13] S. R. Pate. Effects of wind tunnel disturbances on boundary-layer transition with emphasis on radiated noise: A review. In *11th Aerodynamic Testing Conference, Colorado Springs, Colorado/March 18-20*, 1980. 7

- [14] S. P. Schneider. Numerical analysis of the bleed slot design of the purdue mach 6 wind tunnel. In *AIAA-2005-91*, 2005. 9, 10
- [15] N. Lin, H. Reed, and W. Saric. Effect of leading edge geometry on boundary-layer receptivity to freestream sound. In *Stability, Transition and Turbulence*. Springer-Verlag, New York, 1991. 10
- [16] S. R. Pate. Radiated aerodynamic noise effects on boundary-layer transition in supersonic and hypersonic wind tunnels. *AIAA Journal*, 7:Nr. 3, 1969. 13
- [17] E. Reshotko. Roughness-induced transition, transient growth in 3-d and supersonic flow. In *AVT 151 Lecture Series on Advances in laminar-turbulent transition modelling*. RTO-AVT-VKI, 2008. 13
- [18] P. A. Davidson. *Turbulence*. Oxford University Press, 2004. 14, 124
- [19] W.D. Harvey. Influence of free-stream disturbances on boundary-layer transition. Technical report, NASA, 1978. 25
- [20] V. A. Lebiga and V. N. Zinoviev. Fluctuations characteristics of flows in test sections of high-speed wind tunnels. *AGARD CP 585*, 31:1–9, 1996. 27
- [21] S.W. Rienstra and A. Hirschberg. An introduction to acoustics, August 2013. 30
- [22] J. Anthoine. Introduction to aeroacoustic vki cn 176, January 2004. 31
- [23] J. Panda and R. G. Seasholtz. Investigation of density fluctuations in supersonic free jets and correlations with generated noise. In AIAA/CEAS, editor, *6th AIAA/CEAS Aeroacoustics Conference*. AIAA, June 2000. 31
- [24] S. P. Schneider. Development of hypersonic quiet tunnels. *Journal of Spacecraft and Rockets*, 45:641–664, 2008. 33
- [25] K. F. Stetson. Hypersonic boundary layer transition. In *The Second Joint Europe/US Short Course in Hypersonics*, 1989. 34
- [26] L. Krishnan and N. D. Sandham. Effect of mach number on the structure of turbulent spots. *Journal of Fluid Mechanics*, 566:225–234, 2006. 40
- [27] H. Bottini, F. Jivraj, A. Strub, S. Paris, C. O. Asma, and D. G. Fletcher. Inducer-induced transition in hypersonic boundary layers. In *Aerospace and Meeting and Exhibit*, number 2007-0537 in AIAA. AIAA and CIRA, 2007. 40

- [28] Vasiliki Iliopoulou. *High Frequency Gas Temperature and Surface Heat Flux Measurements*. PhD thesis, von Karman Institute for Fluid Dynamics and Universite Catholique de Louvain-la-Neuve (UCL), 2005. 43
- [29] V. Pinilla, R. J. Anthony, J. P. Solano, and G. Paniagua. Adiabatic wall temperature evaluation in a high speed turbine. *J. Heat Transfer*, 134(9):091601–091610, September 2012. 44
- [30] A. Holden. *The Nature of Solids*. Columbia University Press, 1965. 45
- [31] H. J. Gray and A. Isaacs. *A New Dictionary of Physics*. Longman Group Ltd., 1975. 45
- [32] 45, 49
- [33] J. D. Crouch. Modeling transition physics for laminar flow control. In *38th Fluid Dynamics Conference and Exhibit*, number AIAA 2008-3832. AIAA, September 2008. 52
- [34] J.D. Jr Anderson. *Fundamentals of Aerodynamics*. McGraw-Hill, 2nd edition edition, 1991. 72
- [35] J.D. Jr Anderson. *Hypersonic and High Temperature Gas Dynamics*. McGraw-Hill, 1989. 75, 76
- [36] E. R. van Driest. The problem of aerodynamic heating. In *National Summer Meeting, Aerodynamic Heating: Aerodynamic Aspects Session*, June 18-21 1956. 76
- [37] various authors. *Numerical Receipts in Fortran 77*. Cambridge Press, 1992. 88
- [38] J. Laufer and T. Vrebalovich. Stability and transition of supersonic laminar boundary layer on an insulated flat plate. *J. of Fluid Mech.*, 9:257–299, 1960. 93, 94
- [39] A. L. Kistler. Fluctuation measurements in a supersonic turbulent boundary layer. *The Physics of Fluids*, 2(1):290–296, 1959. 93, 124
- [40] A. Passaro and D. Baccarella. Roughness induced transition in hypersonic regime over a flat plate. In *17th AIAA International Space Planes and Hypersonic Systems and Technologies Conference, San Francisco, California, USA*, number AIAA 2011-2375. AIAA, April 2011. 117, 118, 119, 120
- [41] S. A. Berry, T. J. Horvath, F. A. Greene, G. R. Kinder, and K. C. Wang. Overview of boundary layer transition research in support of orbiter return to flight. In *9th AIAA/ASME Joint Thermophysics and Heat Transfer Conference*, number 2006-2918. AIAA, June 2006. 117, 118

- [42] R. A. King, M. A. Kegerise, and S. A. Berry. Version 2 of the protuberance correlations for the shuttle-orbiter boundary layer transition tool. Technical Report TP-2009-215951, NASA, December 2009. 118
- [43] L. M. Mack. Boundary-layer linear stability theory. Technical Report R 709, AGARD, 1984. 119
- [44] E. L. Morrisette. Roughness induced transition criteria for space shuttle-type vehicles. *J. of Spacecraft and Rockets*, 13(2):118–120, 1976. 119
- [45] H. W. Emmons. The laminar turbulent transition in a boundary layer—part i. *Journal of Aeronautical Sciences*, 18(7):490–498, 1951. 127, 136
- [46] I. Wygnanski, M. Sokolov, and D. Friedman. On a turbulent 'spot' in a laminar boundary layer. *J. Fluid Mech.*, 78:785–819, 1976. 127, 128, 129, 131, 133, 136, 137
- [47] J. J. Riley and M. Gad-el Hak. The dynamics of turbulent spots. In *Frontiers in Fluid Dynamics*, 1985. 127
- [48] J. J. Bertin. *Hypersonic Aerothermodynamics*. American Institute of Aeronautics and Astronautics, 1994. 127
- [49] M. Sokolov, Antonia R.A., and Chambers A.J. A turbulent spot in a two-dimensional duct. *J. Fluid Mech.*, 166:211–225, 1986. 128, 131, 136
- [50] S. P. Schenider, K. M. Casper, and S. J. Beresh. Spanwise growth of the turbulent spot pressure-fluctuation field in a hypersonic boundary layer. In *41th AIAA Fluid Dynamics Conference and Exhibit*. AIAA, 2011. 128
- [51] J. D. Cobine. *Gaseous conductors: theory and engineering applications*. Dover Publications, 1958. 132
- [52] J. W. Elder. An experimental investigation of turbulent spots and breakdown to turbulence. *J. Fluid Mech.*, 9:235–246, 1962. 136
- [53] F. W. Chambers and S. W. Thomas. Turbulent spots, wave packets, and growth. *Phys. Fluids*, 26:1160–1162, 1983. 137
- [54] 140
- [55] P. K. Janert. *Gnuplot in Action*. Manning, 2010. 147
- [56] 147
- [57] M. Hayashi, S. Aso, and A. Tan. Fluctuation of heat transfer in shock wave/ turbulent boundary layer interaction. *AIAA Journal*, 27(4):399–404, April 1989. 152, 154, 155, 158, 166

- [58] A. L. Kistler. Fluctuating wall pressure under a separated supersonic flow. *The Journal Of The Acoustical Society Of America*, 36(3):543–550, March 1964. 159, 172
- [59] A. Hamed. Flow separation layer in shock interactions speeds wave boundary at hypersonic. Contractor Report 4274, NASA, February 1990.
- [60] C. F. Coe and W. J. Chyu. Pressure-fluctuation inputs and response of panels underlying attached and separated supersonic turbulent boundary layers. technical memorandum X-62,489, NASA, September 1972. 152, 153, 154, 166
- [61] E. Katzer. On the lengthscales of shock/laminar boundary layer interaction. *J. Fluid Mech.*, 206:477–496, 1989. 152, 153, 155
- [62] T. C. Adamson and A. F. Messiter. Analysis of two-dimensional interactions between shock waves and boundary layers. *Ann. Rev. Fluid Mech.*, 12:103–138, 1980.
- [63] E. Stanewsky. Shock-boundary layer interaction in transonic and supersonic flows. In *Transonic Flow In Turbomachinery*, VKI Lecture Series. von Karman Institute for Fluid Dynamics, May 1973. 152
- [64] Y. Na and P. Moin. The structure of wall-pressure fluctuations in turbulent boundary layers with adverse pressure gradient and separation. *J. Fluid Mech.*, 377:347–373, 1998. 153, 154
- [65] J. Delery and J. G. Marvin. Shock wave-boundary layer interaction. In E. Reshotko, editor, *AGARD AG 280*, 1986. 155
- [66] H. W. Liepmann, A. Roshko, and S. Dhawan. On reflection of shock waves from boundary layers. Technical Report TR 1100, NACA, 1952.
- [67] D. R. Chapman, D. M. Kuehn, and H. K. Larson. Investigation of separated flows in supersonic and subsonic streams with emphasis on the effect of transition. Technical Report NACA-TR-1356, NACA, 1958. 155
- [68] Y. Yao, L. Krishnan, N. D. Sandham, and G. T. Roberts. The effect of mach number on unstable disturbances in shock-bl interactions. *Physics of Fluids*, 19:054104–1–054104–15, 2007. 156
- [69] N. DeTullio and N. D. Sandham. Comparison of experiments and les for turbulent spots in compressible flows. Technical Report 4.2.3, University of Southampton, March 2013. 160, 161